Enhancing the Sensitivity for Ultra-High Energy Down-Going Neutrino Detection with the Pierre Auger Observatory

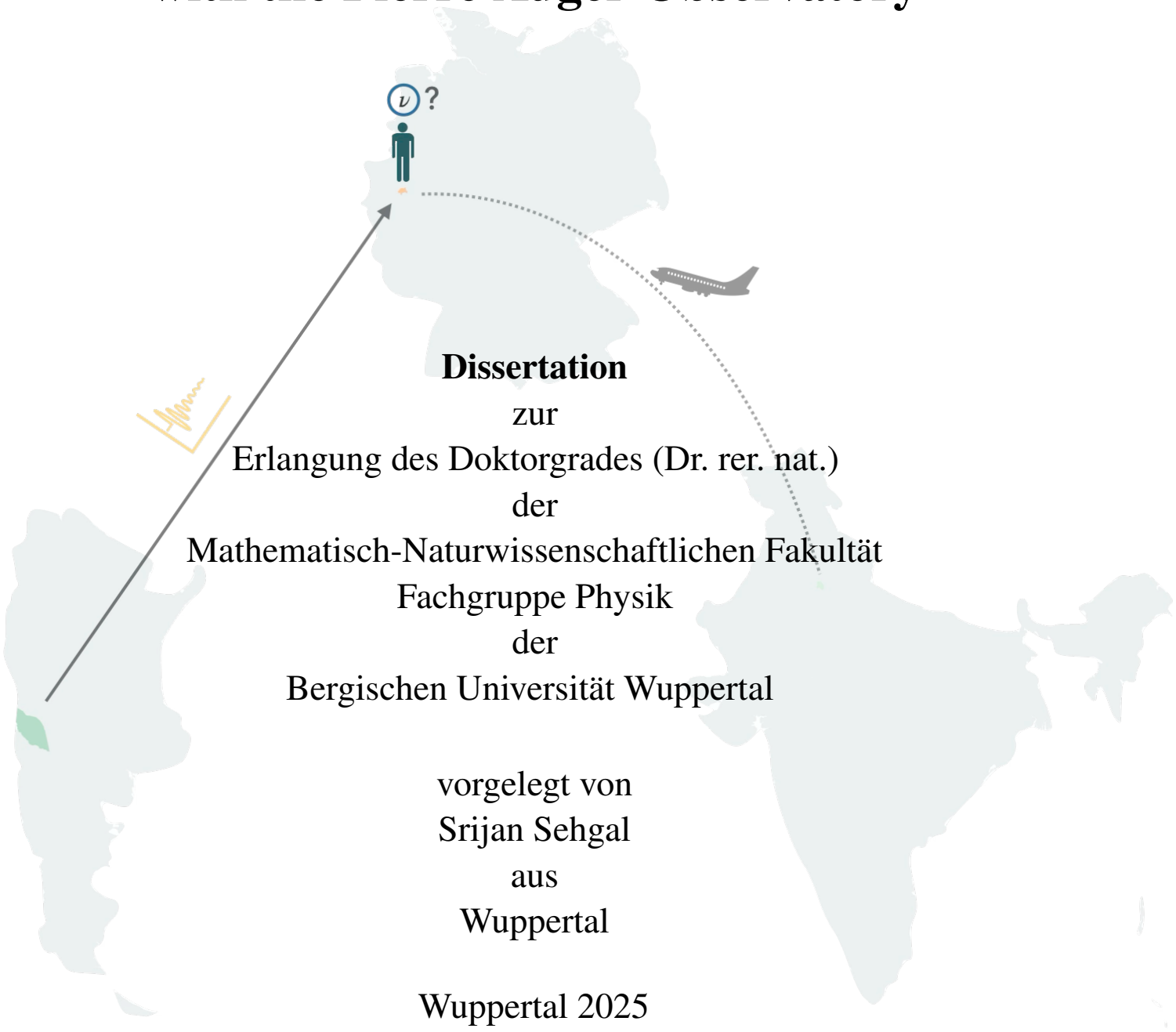

Dissertation

zur

Erlangung des Doktorgrades (Dr. rer. nat.)

der

Mathematisch-Naturwissenschaftlichen Fakultät

Fachgruppe Physik

der

Bergischen Universität Wuppertal

vorgelegt von

Srijan Sehgal

aus

Wuppertal

Wuppertal 2025

Angefertigt mit Genehmigung der Mathematisch-Naturwissenschaftlichen Fakultät der Bergischen Universität Wuppertal

1. Gutachter: Prof. Dr. Karl-Heinz Kampert
2. Gutachter: Prof. Dr. Jaime Alvarez Muñiz

Tag der Promotion:
Erscheinungsjahr:

Acknowledgements

When I was in eighth grade, I was asked what I wanted to be when I grow up. I said I wanted to be an astronomer. This was immediately followed by a second question, ah, So you want to go to space ? I said No, I want to look at it. In the end it turned out that I did a little bit of both. I went to Germany which was outer space for me and I looked at stars via an experiment in Argentina. This thesis is a result of that journey.

It took a village to raise this thesis. A crowded one at that with teachers, family and friends without whom this would not have been possible.

The first people to thank are the teachers I have had during my time working on this thesis. It took me a few years to realize how lucky I was to be given an opportunity to write this thesis under the tutelage of Prof. Dr. Karl-Heinz Kampert. The way Prof. Kampert lets PhD students operate on their own terms is something that made my time here enjoyable and his group a perfect fit. He has been a constant source of inspiration and motivation. To have him in your corner backing you up be it regarding the content of this thesis or calling the mayor of Wuppertal to make sure I am not kicked out of the country (true story) made all the difference.

I would also like to thank Prof. Dr. Jaime Alvarez Muñiz for agreeing to be my second de facto supervisor. His guidance and support has been invaluable. While sitting in his office in Santiago de Compostela, he has always been an email and Zoom call away, answering my repeated questions anytime. Thank you, I could not have asked for more. Like I said to you, I am yet to get the time and opportunity to complete my Camino to your office, but I am sure I will get there soon.

I have been blessed with even more great teachers who I need to thank. Dr. Julian Rautenberg, who I might have talked to for countless hours (always in five minute intervals) about the most trivial of things be it life or work. He always has a smile on his face and a solution to every problem or should I say challenge. Dr. Christian Pauly for being my next door office neighbour, who I bugged regarding the lab exercises all these years. Prof. Dr. Klaus Helbing for just being a fellow Bonner reminding me of my first home in Germany. Others in the Pierre Auger Collaboration like Prof. Dr. Enrique Zas, Prof. Dr. Piera Ghia and Prof. Dr. Alan Watson who have might not have been directly involved in this thesis but with their pertinent questions and supportive statements in some way helped me during the journey.

The second are my family. If a 15-year-old boy who left his home was not spared at the border during the partition of India, I would not have been here. My grandfather, Shanti Sarup

Sehgal, who was my biggest supporter has shaped my life in multiple ways. He inculcated two things in me, the desire to succeed and to have fun while doing it. My grandmother Kusum Sehgal, who our family lost way too early but her spirit and memory lives on. Both of you continue to inspire me. My parents, Ravi and Rajni Sehgal, thank you for teaching me the value of hard work and sacrifice. You both cut short your dreams to make sure me and my brother could chase ours, I hope I can honour it. Without your constant support and sacrifices, I would not have been able to come to Germany and write this thesis. Thanks to my brother Sambhav for always providing me with the much-needed sports related distractions that kept me sane.

I have a big family who have always checked up on my well-being and have been a constant source of support. Thank you Binu and Renu bua for always being there for me. Thank you Indu masi, Neeru masi and Vipin mama for always checking up on me. A big thanks to all my aunts and uncles. In India the first cousins are like siblings and I have been lucky to have a bunch of them. Thank you to all of them, Ashish Bhaiya, Rinki bhaji, Divya di, Ankita di, Suhina di, Sadhika, Kartik, Jeevanshu, Chesta and Vanya for always making those short escapes to India my favourite times of the year. A special thanks to Kritika di or Dr. Kritika Khanna, you gave me one of the most valuable advice I have ever received, to not do the PhD if I just wanted the doctor title, but to do it if I wanted to learn something new. I hope I have done justice to that advice.

My family now also includes my girlfriend Lélia Nagel. I am glad that I met you right before I started my thesis. Having a real doctor by my side who has dedicated her life to help others constantly grounds me. You have been a constant source of support and motivation. You have been my rock and my biggest cheerleader. Thank you for always being there for me and for making me a better person. I cannot wait to spend more time with you and make more memories.

Lastly, I have been blessed with a wonderful set of friends who have been my family away from home. Thank you to Svenja for being my best friend through the seven years I have been in Germany. We might not live in the same city any more, but you are always just a phone call away. Thank you to Prakhar, Amitayus, Lex, Rieka, Jan and Naseem for always keeping tabs on me and making sure I am doing fine. Starting this thesis during the pandemic was not easy but having the best roommates in the world in Steve and Fiona made it a lot of fun. A simple hi in the kitchen or a beer in the garden was all I needed to keep going.

A special thanks to Dr. Jannis Pawlowsky, Dr. Leonel Morejon and Fabian Becker for helping with the editing of this thesis. Thank you to Michael Schimp for always answering my various questions and solving my problems without which this thesis would have never been completed. A big thanks to the whole Astroteilchen group for the academic and moral support and all the laughs we have shared.

“राह में मुश्किल होगी हजार,
तुम दो कदम बढाओ तो सही,
हो जाएगा हर सपना साकार,
तुम चलो तो सही, तुम चलो तो सही।
मुश्किल है पर इतना भी नहीं,
कि तू कर ना सके,
दूर है मंजिल लेकिन इतनी भी नहीं,
कि तु पा ना सके,
तुम चलो तो सही, तुम चलो तो सही।...”

- Narendra Verma

Contents

CHAPTER 1

Introduction

Figure 1.1: Window to the inner workings of the Universe is only half opened.

The need to understand how something works or why something is?, is ingrained in every human. While attempting to find answers for these questions one either answers them conclusively or finds oneself asking additional questions stemming from the original. One such question which bothered physicists at the beginning of the 20th century and eventually led to the field of *astro-particle physics* was of so-called "atmosphere electricity" or ionization of air. After the pioneering discoveries by Theodor Wulf [1] and Victor Hess [2] who found

the increase of this ionization rate with altitude and theorized the origin of this radiation to be not Earth but something above our atmosphere, the name *cosmic rays* was coined by Robert Millikan who believed these rays were originating from primary photons. This hypothesis was rejected by the measurements done by Jacob Clay [3, 4] in 1927 who observed a latitude dependence of the intensity of cosmic rays (CRs) concluding this to be a deflection of the primary CRs by the geomagnetic field of the Earth which indicated that these rays must be charged particles. After this came the efforts of B. Rossi [5], German group [6] and P. Auger [7] all independently discovering coincident signals in separated Geiger counters which they explained by the counters being struck by an extensive particle shower triggered by a primary CR. The phenomenon was named *sciami* by Rossi, *Luftschauer* by the German group and "les grandes gerbes" by Auger and his collaborators. Auger went one step further and estimated the primary energy of the CR via his superior setup giving rise to some questions about CRs which are yet unanswered, how are they created and where are they coming from. One of the known sources which is the Sun is too close to explain some other high energy CRs constantly hitting the Earth's atmosphere. Since then the field has only expanded with numerous experiments set up to characterize these CRs.

The biggest of these experiments which looks for ultra-high energy cosmic rays (UHECRs) exists in 3000 km^2 patch of Argentinian pampa just outside Malargüe called the Pierre Auger Observatory [8]. It uses a combination of 1660 water Cherenkov tanks which form the Surface Detector (SD) of the Observatory and observe the air shower particles arriving at the ground along with Fluorescence Telescopes which can look at the development of shower as it travels through the atmosphere. Built primarily to answer the question of the cut-off of the cosmic ray spectrum interpreted as Greisen–Zatsepin–Kuzmi (GZK) limit (or GZK cut-off), the Observatory has provided immense contributions not only in the field of CRs but also in the fields of Geophysics (elves) [9], Dark matter (composition) [10] and multi-messenger physics (neutrino & photon searches) [11, 12]. Currently, the SD is undergoing an upgrade which will add a scintillator and radio antenna on top of the water Cherenkov tanks further increasing the sensitivity of the Observatory especially to the composition of the cosmic rays.

The non-electrical neutrality of the incoming CRs provides one of the biggest hindrance for finding their sources. This means that CRs do not travel in straight lines from their sources and are affected by the magnetic fields. They can also interact with the matter along the way [13, 14]. Combined with the fact that the possible sources are light-years away from us, without knowing the magnetic fields of the Universe it is very hard to detect the sources of CRs. Ultra high energy neutrinos (UHEνs) can help in this challenging search for the sources of CRs [15]. Being electrically neutral and having a very low interaction cross-section these particles can travel large distances unaffected by the intervening matter and magnetic fields. Several scenarios which are discussed later in section 2.1.4 describe how the UHEνs can be produced by cosmic-rays and can tell us about their sources. Moreover, UHEνs are also interesting as they can help constrain or explain different production and propagation scenarios for various sources helping us see known astrophysical and cosmogenic objects in a new way. The success of the IceCube Neutrino Observatory, a neutrino detection experiment located at the South Pole, in measuring the first astrophysical neutrinos and indications

of the first steady source NGC 1068 [16] and transient source [17] have reinvigorated the astroparticle field. The Pierre Auger Observatory has also contributed to the search for UHEνs by trying to detect the extensive air showers (EASs) that can be induced by them. With its stellar sensitivity at high energy, searches at Pierre Auger Observatory have provided some of the strictest upper limits on the diffuse flux of UHEνs [18]. This has already led to constrains on various hypothesized models explaining cosmogenic neutrino production.

The last decade with the successes of LIGO/VIRGO [19] in measuring the first gravitational waves and IceCube in detecting the first astrophysical neutrinos has also rekindled a field which displays the true spirit of harmony in science and is called multi-messenger astronomy. The aim of the field is to establish a network that can coalesce all the information available through various messengers via which we can see the Universe and maximise the resources and experiments available at Earth. This also allows us to understand the sources better since the observation or non-observation of different messengers can help constrain the mechanisms behind their functioning. The beginning of this field can be traced back to the observation of the first cosmic rays in conjunction with solar flares, signifying the important role of a cosmic ray observatory like the Pierre Auger Observatory to multi-messenger astronomy. One of the most important success stories of this field is the August 2017 detection of the neutron star merger [20] first by the LIGO/VIRGO detector since the Gravitational waves are the fastest messengers and then 1.7s later by the Fermi Gamma ray space telescope and INTEGRAL. 11 hours later already alerted by these two experiments the optical counterpart was detected by multiple telescopes like Las Campanas Observatory and the Hubble Space Telescope. The event was also further seen in Ultraviolet (Neil Gehrels Swift Observatory), X-ray (Chandra X-ray Observatory) and radio (Karl G. Jansky Very Large Array). The non observation of neutrinos by both the IceCube and the Pierre Auger Observatory helped reach the important conclusion about the orientation of the jets which is hypothesized to be off-axis i.e. not pointing directly towards the Earth. Since neutrinos and gravitational waves are the fastest of the messengers to reach the Earth, alerts issued by IceCube and LIGO/VIRGO are regularly used to follow up the events with other experiments. Subsequent observations of the blazar TXS 0506+056 [21] with IceCube, FERMI-LAT and MAGIC and the observations of neutrinos from the plane of the Milky Way galaxy [22] have helped establish the continued importance of multi-messenger astronomy.

In this thesis performance of one of the upgrades of the Pierre Auger Observatory done in 2013 is evaluated in the context of neutrino search. This upgrade consisted of introducing new triggers called Time-over-Threshold-deconvolved (ToTd) and Multiplicity-of-Positive-Steps (MoPS) to reduce the muonic background and effectively decrease the energy threshold for the array. Such triggers can be particularly important in the context of neutrino searches between zenith angle of 60°-75° since they help in getting a better signal background separation. The effect of these triggers for both the search of a diffused neutrino flux and point like sources of neutrinos is investigated. The thesis also focuses on maximising the previously done neutrino searches in the zenith region 60°-75° by investigating and updating the analysis presented in [18, 23].

The thesis is structured as follows: The next chapter 2 gives the theoretical background

for UHECRs and UHEνs and other important messengers in regard to the Pierre Auger Observatory. It also aims to discuss the various theoretical scenarios involved in their production and propagation. The chapter also aims to summarize the important recent results for these messengers and the various interesting open questions for them. Chapter 3 describes the phenomenon of EASs which is used to indirectly detect both the CRs and neutrinos at the Pierre Auger Observatory. To continue with understanding the detection in a more experimental context the following chapter 4 gives a detailed description of the Pierre Auger Observatory. The objective of the chapter is to try to give an exhaustive description of all the tools at the Pierre Auger Observatory necessary to detect neutrinos with a particular focus on the SD which is of primary concern for the analysis presented in this thesis. A small section is also dedicated to the recently completed AugerPrime upgrade and the exciting potential it offers especially for multi-messenger searches.

The second part of the thesis is dedicated to the neutrino search in the zenith angular region $\in 60^{\circ}$-75°, Down-going low (DG_{low}). This part begins with chapter 5 that gives a description of the neutrino search in the zenith angular range 60°-75° which is also the primary focus region for this thesis. The chapter is dedicated to provide a complete description of the choices made for the analysis with the proper reasoning. A *blind* search is performed i.e. the analysis is finalized before the recorded data is used to search for neutrinos. It reports the areas of potential improvements and also communicates the observed improvements to the neutrino identification with the new triggers. The following chapter 6 discusses the sensitivity of the Pierre Auger Observatory to neutrinos in the investigated zenith angle range. The recorded data is searched to look for neutrinos and due to the non-observance of any neutrino like events, the corresponding upper limits to the diffuse flux of UHEνs are presented with a focus on the observed improvements with the new triggers. The observatory can also detect showers in zenith angle range $\in 75^{\circ}$-90°, Down-going high (DG_{high}) and up-going showers in the zenith angular region $\in 90^{\circ}$-95°, Earth-skimming (ES) with the SD and $\in 90^{\circ}$-180° with the fluorescence telescopes, but these searches are not performed in this thesis and only their final results are included for comparison and to provide a holistic feel for the neutrino search at Pierre Auger Observatory.

The last part of this thesis presents the sensitivity of the Pierre Auger Observatory to point like sources of UHEνs in chapter 7. Due to the non-observance of any neutrinos in the recorded data at the Pierre Auger Observatory an upper limit for point like sources of UHEνs is also shown to be improved with the inclusion of new triggers in the analysis. The limit set by this analysis is also used to calculate an upper limit on the expected neutrino flux for some interesting point source neutrino candidates. All the important results are then finally summarized in chapter 8 and a short outlook on the future directions for the analysis and the neutrino search at the Pierre Auger Observatory is put forward. The dissertation is completed by five appendices. The first contains accompanying technical information for neutrino simulations, the second describes the independent work done in this thesis to compare the various hadronic interaction models for neutrino simulations and the third consists of detailed information about few of the interesting events observed during the analysis. The fourth appendix contains the results of the discrimination analysis performed in this thesis and the

fifth contains a technical overview of the changes made to implement the DG_{high} neutrino search within the software framework of the Pierre Auger Observatory.

CHAPTER 2

Ultra High Energy Cosmic Rays and Neutrinos

2.1 Ultra High Energy Cosmic Rays

2.1.1 History

CRs have been a source of investigation for more than a century now. Even before the balloon flight by Victor Hess, it was Henry Becquerel, the discoverer of radioactivity, who believed that the *atmospheric electricity* (ionization of air) was due to the radioactive substances present on Earth. In such a scenario the ionization rate should decrease the higher up you go in the atmosphere. The first measurements disproving this theory were performed by Theodor Wulf in 1909 with his own developed electrometer. His measurements published in the *Physikalische Zeitschrift* indicated a slight decrease in the level of radiation at the top of the Eiffel Tower than compared to its base but not nearly as much as predicted by the absorption of radiation in 300 m of air. Unfortunately, the measurements were not widely accepted, and it would take three years till Victor Hess, via his several balloon flights, provided irrefutable measurements corroborating Wulf's observations.

Between 1911 and 1912 Victor Hess performed nine (2 in 1911 and 7 in 1912) balloon flights going as high as 5350 m a.s.l to measure the dependence of ionization rate to altitude. He carried with him three Wulf electrometers, two tuned for γ rays and the third tuned for β rays which along with α rays were the only three known radioactive decays. His measurements published in the Proceedings of the Viennese Academy of Sciences [2], [24] showed that the radiation level decreased slightly up to a certain altitude ($\sim$1 km) but after this height, the radiation increased significantly and at the highest flown altitudes reached levels about twice in comparison to the ones at sea level. Some of his measurements were done during the night and one during a partial solar eclipse which further made him rule out the Sun as a source of this radiation. With further confirmations via the measurements by Werner Kolhörster in 1914 and Robert Millikan, in 1925, Victor Hess was awarded the Nobel

Prize in Physics in 1936.

CRs were still presumed to be gamma rays. This supposition was quickly negated by the efforts of Jacob Clay, who via his measurements of the CR intensity at different latitudes while sailing from Java to the Netherlands in 1927 [3], showed that the geomagnetic field had a significant effect on the intensity. Further observations of the *East-West* effect, the directional dependent intensity due to the charge of the primary CRs as predicted by Bruno Rossi [25] by various experiments [26] [27] concluded that the intensity was greater from the west, proving that CR primaries have a positive charge.

Today we use the term CRs to describe the highly energetic charged particles travelling at very high speeds through space. The Earth is constantly bombarded by CRs, some originating from the Sun but most of them from outside our Solar System. In more than 100 years since Victor Hess's balloon flights, we have gathered a lot more information and have achieved a better understanding of CRs. We have detected CRs up to energies $\sim 10^{20}$electronvolts (eV) [28] which is an impressive feat since at these energies the expected flux drops below one particle per km^2 per century. We know a lot more about the composition of the CRs and have also proposed models explaining their origin and their journey to Earth. CRs continue to be a source of fascination. Some of the achievements are summarized below along with some unanswered questions about CRs.

2.1.2 Origin

To understand the sources of CRs one needs to understand the mechanisms that could impart huge amounts of energies to the tiny particles that actually reach the Earth. We already know that the low energy CRs which reach our Earth are predominantly coming from the Sun. The evidence for this comes from the observation of an increase in these with a coincidence to the violent activity of the sun. Most of the CRs and UHECRs, $E > 10^{18}$eV, do not exhibit this temporal coincidence and are thought to have originated in our Galaxy or beyond respectively. Two different mechanisms could explain how the CR particles obtain such high energies and travel over large distances: *bottom-up* [29–31] and *top-down* [32, 33]. The *top-down* approach assumes that the UHECRs are produced due to the decay or annihilation of extremely massive or exotic particles. Both of these mechanisms have been investigated with various experiments including the Pierre Auger Observatory 4. With the current observations, the top-down models face significant challenges. The extremely high energies required for the annihilation of the hypothesized exotic particles and the lack of evidence for their existence make it very difficult to both verify and rule out the top-down mechanism. The continued improvement in understanding of astroparticle physics and the early universe makes the study of UHECRs an exciting and active area for research with the mystery of their origin and propagation still waiting for a solution.

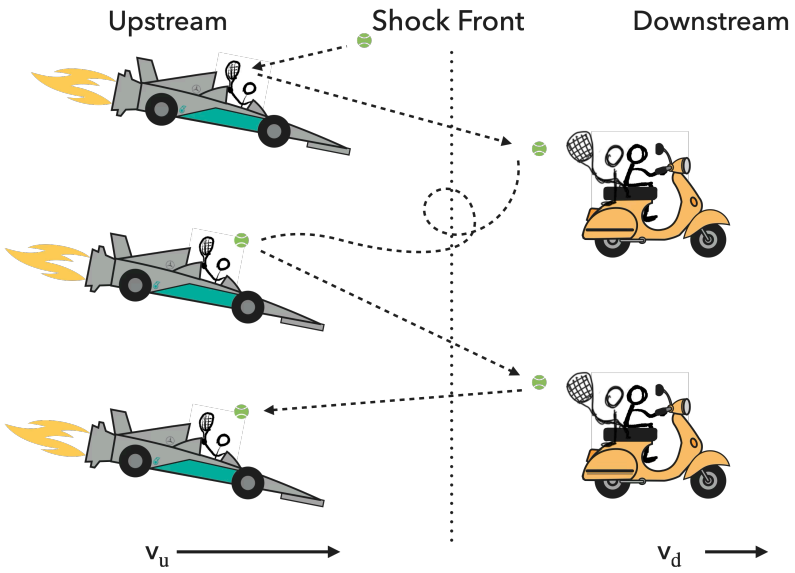

Figure 2.1: An illustration to depict the diffusive shock acceleration mechanism and the possible trajectory in the plasma like shock front region. Figure inspired from work by M. Scholer.

Bottom-up scenario

There are many proposed ways in which CRs could get accelerated by astrophysical sources. One of the most widely accepted descriptions that can explain most of the observed CRs that originate from our Galaxy is the diffusive shock acceleration also known as Fermi acceleration [34]. Qualitatively one can explain Fermi acceleration as follows: High energy violent phenomena such as a massive star reaching the end of its life cycle and undergoing a supernova explosion can produce an intense shockwave which propagates outwards towards the star's outer layers. As the shock wave progresses and moves through the interstellar medium (ISM) it sweeps up and compresses the surrounding gas and magnetic fields creating a region of very high pressure and magnetic turbulence known as the shock front. The charged particles can get trapped in such a shock front and repeatedly cross over this region of magnetic turbulence experiencing magnetic irregularities and constantly changing direction under magnetic confinement thus experiencing electric fields each time they cross which accelerate them to higher energies. An illustration is shown in Fig. 2.1. The shock front is turbulent, and particles can cross it multiple times, gaining energy at each passage. Eventually, some particles can acquire enough energy to escape the shock region and travel the required distances to reach the Earth. Such an interpretation can explain the CRs originating in our Galaxy ($<10^{15}$eV) and point towards supernovae and its remnants as potential sources but to explain the UHECRs ($>10^{19}$eV) we need other sources and mechanisms. The energy that can be produced by the accelerator is limited by the gyroradius of the accelerator. This has been illustrated by Hillas [29] where he illustrated the potential sources of CRs on a plot of magnetic field strength vs size. A modified version of his original plot with the inclusion of

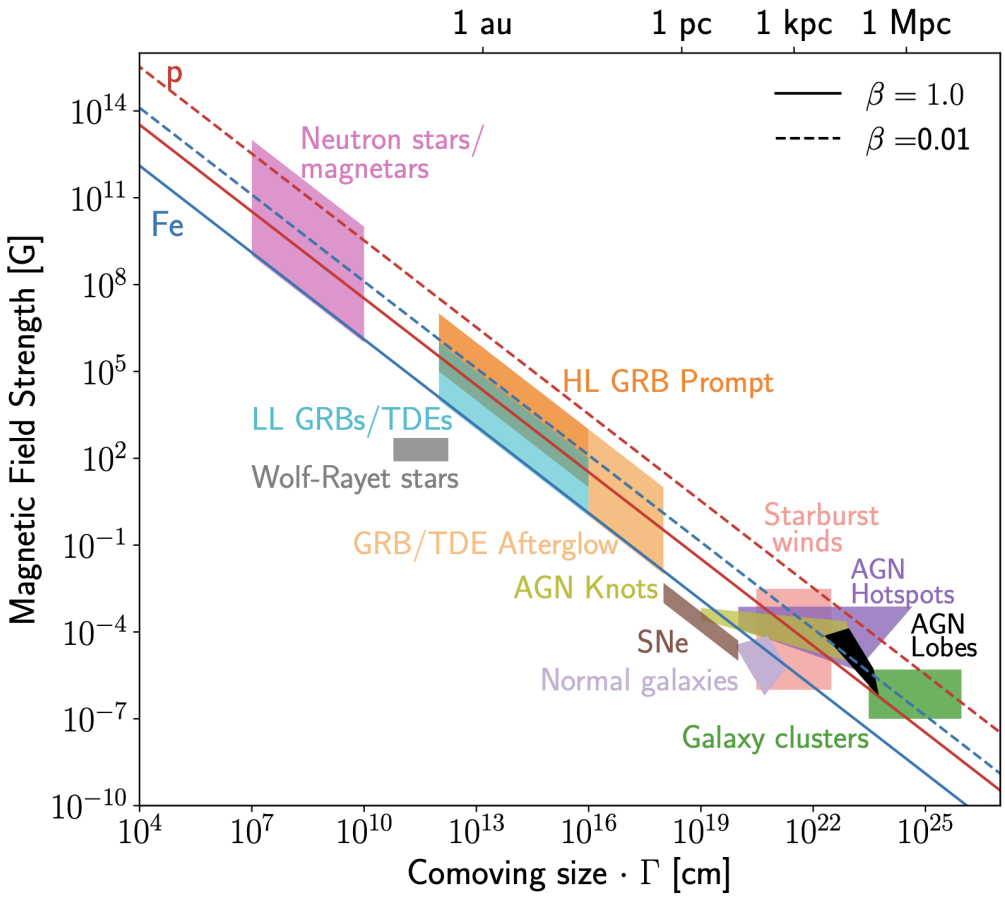

Figure 2.2: An updated version of Hillas plot. Different source classes are plotted according to their radial size, R (abscissa), and magnetic field strength, B. The solid and dashed lines indicate the lower limits above which confinement of protons (red) and iron (blue) nuclei with energy 10^{20}eV are possible. The solid and dashed lines indicate different shock velocities. Taken from [37].

modern sources is shown in Fig. 2.2. Another limitation to the energy of the CRs produced by different sources is the energy budget that an accelerator must possess. This has been estimated in [35] under the assumption that UHECRs are primarily extragalactic protons and at Auger [36] via the measurements of the CR spectrum.

Other accelerating mechanisms are as follows:

1. Supernova Remnants: Interactions of CRs with the magnetic fields within the remnants could lead to further acceleration [38].

2. Active Galactic Nucleis (AGNs): These are regions in the centre of galaxies that are capable of producing highly energetic particles. The source of this capability is theorized to be powered by supermassive black holes. The extreme conditions near the black holes such as strong magnetic fields and high-energy jets could accelerate UHECRs. [39]

3. Magnetar Outbursts: Magnetars are neutron stars having a magnetic field ~1000 times that of a normal neutron star. They are known to produce magnetically powered bursts which could potentially accelerate particles to UHECR level energies. [40]

4. Pulsar Wind Nebulae: Rapidly rotating neutron stars, also known as Pulsars emit beams of electromagnetic radiation. Such beams can collide with the ISM creating a pulsar wind nebulae, a region similar to a shock wave front and can lead to production of UHECRs. [41]

5. Galaxy Clusters: These are regions of galaxy populations bound together by gravity. These highly dense structures can accelerate particles either by themselves or via the shock waves associated with a potential merging of different galaxy clusters. [42, 43]

6. Relativistic shocks: Other types of astrophysical shocks such as those occurring in gamma-ray bursts or colliding stellar winds could also create scenarios that could accelerate particles to UHECR level energies. [44, 45]

The validity of all such hypothesized mechanisms could be checked by corroborating their spectral index predictions with those observed by the experiments.

Top-down scenario

This is an alternative approach to explaining UHECRs. The main idea behind these models is that the UHECRs are produced due to the decay or interaction of hypothetical, supermassive, or exotic particles that were produced in the early universe. Some of the proposed hypotheses are mentioned below:

1. Supermassive Dark Matter Particles: This is an extension of a concept that was first proposed to explain dark matter. In this hypothesis, it is assumed that dark matter is composed of long-lived supermassive particles. If such particles exist they could potentially decay and produce UHECRs. [46, 47]

2. Cosmic Strings: These are one-dimensional topological defects that could have formed during phase transitions in the early Universe. The decay of these massive strings could also lead to the production of UHECRs. [48, 49]

3. Other Topological effects: These include defects like monopoles or domain walls which could also produce exotic particles which can further decay into UHECRs. [50]

There are other scenarios such as the breakdown of Lorentz invariance which attack the problem of UHECR acceleration by suggesting a new mechanism for their production rather than their propagation. Some of these models can be constrained by again looking at the flux of the UHECRs [51]. There are also experiments that try to directly look for these exotic particles [52, 53]. So far, no evidence has been found to support the existence of these particles.

2.1.3 Propagation

Production is just one part of the life of CRs or UHECRs. To get detected on Earth the CRs and UHECRs have to travel large distances through ISM during which they can suffer various losses which ultimately affect the spectrum we see on Earth. Some main processes include

losses by ionization due to collision with ISM, Synchrotron Radiation which can lead to the emission of high energy photons and, consequently, energy loss for the CR particle and through collisions with low-energy photons from radiation fields leading to breakage of CR nuclei also known as Photo-disintegration. Other propagation losses such as Bremsstrahlung and Inverse Compton Scattering due to interactions with the Cosmic Microwave Background (CMB), are the reasons high energy CR electrons cannot propagate large distances. A few other mechanisms include Adiabatic Energy Loss which affects the energy density due to expansion, Scattering due to magnetic diffusion or even an escape of UHECRs from our Galaxy can all affect the spectrum of CRs and UHECRs we see at Earth. One of the critical phenomena to understand CR propagation and to realize a theoretical limit to the energy of UHECRs is the GZK cutoff. This is discussed in more detail below.

GZK Limit

The GZK cutoff was first proposed by Kenneth Greisen, an American physicist in 1966 in a paper titled "End to the Cosmic-Ray Spectrum?" [54]. He discussed the potential energy loss of high-energy CRs due to interactions with the CMB and calculated a threshold energy above which CRs, in his case protons, would lose energy through interactions with CMB. In the same year, two Soviet physicists, Georgiy Zatsepin and Vadim Kuzmin, arrived at a similar prediction. Their calculations published in their paper "Upper Limit of the Spectrum of Cosmic Rays" [55] were consistent with Griesen's work and reinforced the concept of the GZK cutoff. The energy cutoff calculated is about 5 x 10^{19} eV or about 8 joules. The dominant mechanisms via which the proton can interact with the photons of the CMB are given below.

$$\begin{aligned} p + \gamma_{\mathrm{CMB}} &\longrightarrow \Delta^{+}(1232) \longrightarrow n + \pi^{+} \qquad & N + \gamma_{\mathrm{CMB}} &\longrightarrow N' + \pi^{\pm} \\ &\longrightarrow \Delta^{+}(1232) \longrightarrow p + \pi^{0} & &\longrightarrow N' + \pi^{0}\,, \end{aligned} \tag{2.1}$$

where N is the nucleon involved in the interaction and N' is the final state nucleon which could be same or different depending on the initial nucleon. These processes are also called "Photo-pion Production". The thresholds for these reactions or the energy of the photon are of the order of ~a few hundred Megaelectron volt (MeV = 10^{6}eV) for protons and a few gigaelectron volt (GeV = 10^{9}eV) per nucleon for other nuclei in the rest frame of the proton and nucleon respectively. In the context of the CMB which have an E ~ 10^{-4}eV, the predicted cutoff for protons is 50 Exa-electron-volt (EeV = 10^{18}eV) whereas for heavy nuclei it can range from about 80 EeV to several hundred EeV depending on the mass of the incident nucleus in the lab frame (relevant for astrophysical observations). However, for heavier nuclei the cross-section for photon absorption (Giant Dipole Resonance) peaks at 10-30MeV in the nuclear rest frame making photo-disintegration the dominant process over Photo-pion production for energy loss. The mean free path which represents the average distance a CR particle can travel before undergoing a significant interaction depends on

the initial energy, interaction cross-section and the number density of target photons. For a UHE protons interacting with the CMB, the mean free path is about ~50-100 Mpc. This leads to the outcome that if a ultra high energy (UHE) proton with energy above the GZK cutoff travels over a distance larger than 50Mpc then such a proton will suffer catastrophic losses and will not be observed in the UHE regime. This consequence doesn't hold for heavy nuclei since for similar energies Photo-pion production is not the dominant process via which they can lose energy. For UHECRs composed of heavy nuclei (e.g., iron, uranium), the dominant energy loss process during their propagation through the universe which is photo-disintegration can be described as:

$$\begin{aligned} p + \gamma_{\mathrm{CMB}} &\longrightarrow n + \pi^{+} \\ (A, Z) + \gamma_{\mathrm{CMB}} &\longrightarrow (A - n, Z - n') + nN, \end{aligned} \tag{2.2}$$

with $n\,(n')$ being the number of stripped nucleons (protons). The mean free path for photo-disintegration for a photon field such as the CMB is similar to that of photo-pion production. Even though, the Pierre Auger Observatory observes a suppression in the CR spectrum above the GZK cutoff [56], it does not claim it to be just due to GZK limit. It has also observed CRs above the GZK cutoff. This issue along with its implications is discussed later in section 2.1.4. One of the other consequences arising from the interaction with the CMB is the interaction of ultra high energy photons (UHEγs, E > 10^{15}eV) to produce electron-positron pairs, $\gamma_{\mathrm{UHE}} + \gamma_{\mathrm{CMB}} \longrightarrow e^{+} + e^{-}$. This is an important consequence that alters both the expected UHECR spectrum and the CR spectrum at Earth. The interaction leads to pile up of detectable diffuse gamma-ray background at lower energies and a softer UHECR spectrum is expected at higher energies which is dominated by contributions from hadrons. It also just leaves neutrinos as one of the few known UHE particles that can point back directly to their sources over long distances. The production of these high energy neutrinos arising from the pions produced during the Photo-pion interaction or via the neutrons produced during photo-disintegration is discussed later in section 2.2.

2.1.4 Latest results

The study of CRs to constrain their properties and the relevant sources requires measurements at Earth. The measurements which provide valuable information are the energy spectrum or flux observed at Earth, the composition of the primary CRs, their arrival direction and other relevant observations such as measurement of other messengers like as high energy photons and neutrons. These measurements and their implications are discussed in more detail below. The high energy neutrinos, relevant for this thesis are discussed in a separate section.

Cosmic Ray spectrum

The CR spectrum measured by several experiments on Earth is summarized in Fig. 2.3. Extending in energy from a few 100 MeV (solar CRs) it spans about 12 orders of magnitude

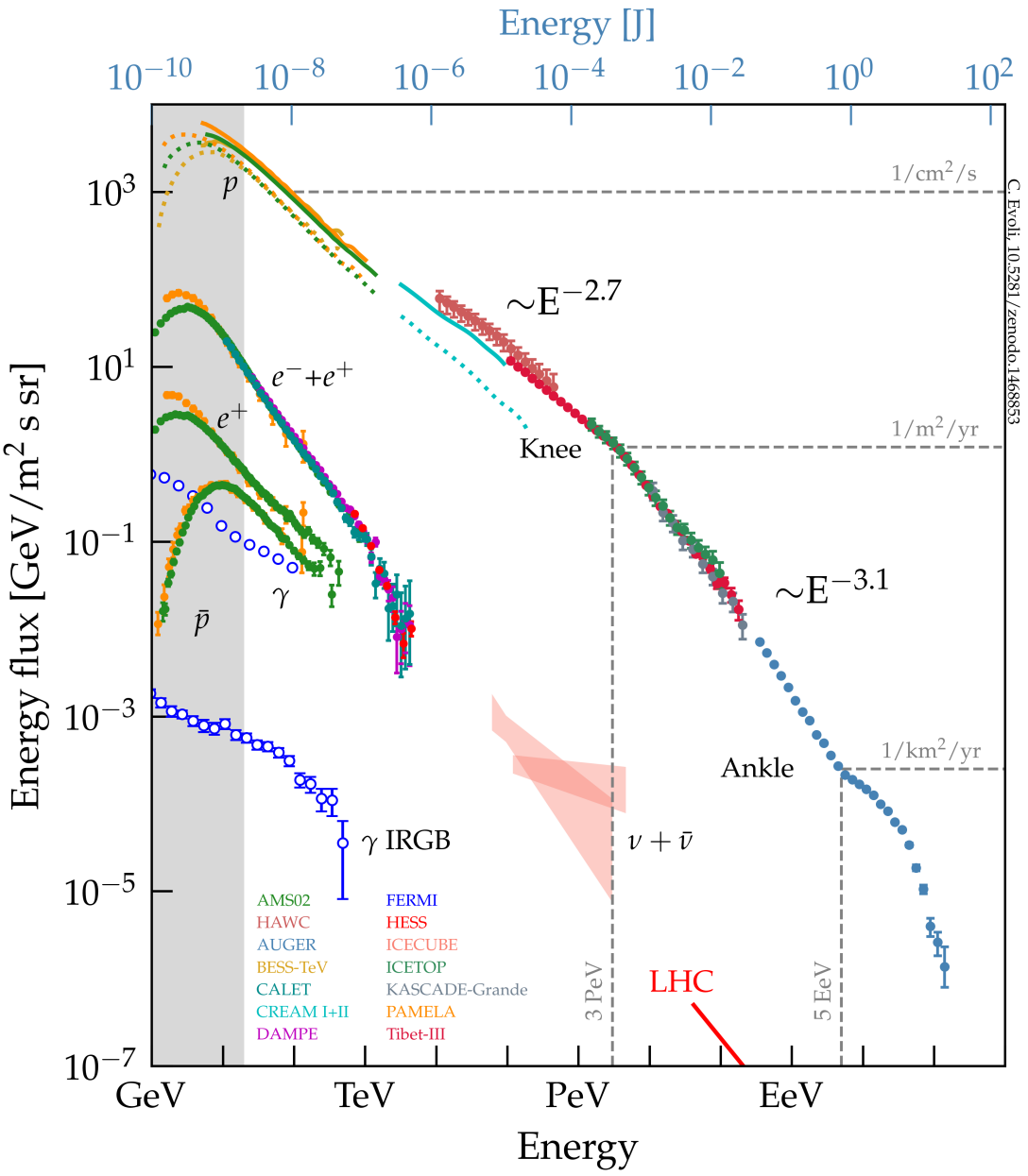

Figure 2.3: Cosmic flux vs Energy spectrum. The colour indicates the experiment used to record the flux. At lower energies we have much detailed information about the composition. At high energies only the all particle spectrum is shown due to low flux. Also shown is the gamma ray spectrum recorded by FERMI and the neutrino flux measurement by IceCube. Taken from [57].

up to the most energetic observed CRs above 10^{20}eV. The flux decreases with increasing energy and follows a varying power law description:

$$\frac{dN}{dE} \propto E^{-\gamma}, \tag{2.3}$$

where γ is the spectral index. The spectral index varies between 2.7 to 3.3 as measurements are made for higher energies. This signifies a decrease in the observed flux as the energy increases. The flux falls from $\sim 1\text{m}^{-2}\text{s}^{-1}$ at 10^{11}eV to $\sim 1\text{m}^{-2}\text{yr}^{-1}$ at 10^{16}eV to about $\sim 1\text{km}^{-2}\text{yr}^{-1}$ at 10^{19}eV. Such a steep fall also poses challenges for the experimental design and the corresponding size. This further affects the detection mechanisms employed to measure this spectrum, due to the very low flux expected at high energies, the measurements of the direct primaries become nearly impossible and an indirect detection using the property of the CR to trigger an air shower in our atmosphere is employed. This phenomenon and how it is used to measure CRs is discussed in the next chapter 3.

Below 10^{13}eV CRs from the Sun dominate the spectrum. The galactic or extragalactic CRs of these energies cannot enter our solar system because of a variety of reasons. These include a combination of the Heliosphere, termination shock and solar modulation which block the low energy CRs. The Heliosphere which is a region influenced by the Sun's magnetic field and solar wind acts as a protective bubble around the solar system. Beyond the Heliosphere, the solar wind interacts with the ISM creating a region of termination shock which can cause scattering and deflection for incoming low energy CRs. Additionally, the solar activity cycle can cause changes to the Heliosphere which in turn also affects the incoming CRs. Beyond a few GeVs the Sun as a source of CRs drops off due to reaching its maximum acceleration potential. Between 10^{13}eV and 10^{18}eV the spectrum is dominated by CRs of galactic origin. This has been verified by comparing the spectral indices of the proposed acceleration mechanisms with the measured spectrum as mentioned before. A second proof also comes from the composition of the CRs observed in these energies, but this is discussed later. *Supernovae* and *supernovae remnants* remain the most promising sources which could explain their origin. The spectral index, $\gamma \sim 2.7$ gives a good description of this region. Around $\sim 5 \times 10^{15}$ one observes a steepening of the spectrum known as the *knee*. At this point γ changes from 2.7 to 3.1. This is attributed to the galactic accelerators reaching their maximum potential for accelerating protons. Above the knee, the sources are expected to reach their maximum potential for other heavier particles until galactic sources cannot accelerate CRs any further. This point is thought to be the origin of the second knee at $\sim 10^{17}$eV. At this point the γ changes from 3.1 to 3.3. This is theorized to be a transition region in which the spectrum is believed to change from one of galactic origin to extragalactic origin. This region ends at about $\sim 10^{18}$eV whereon the spectrum hardens noticeably to a $\gamma \sim 2.6$, originating what is referred to as the *ankle*. Further, with increasing energy the spectrum again steepens to $\gamma \sim 5.1$ reaching an eventual cutoff. The suppression of flux at these energies and the cutoff is still not properly understood yet and could be due to the following possibilities:

1. **GZK Limit:** One of the most prevalent ideas behind the suppression and the cutoff is the GZK mechanism which was discussed above. Due to the observations of CRs above the cutoff of $\sim 10^{18.5}$eV by the Pierre Auger Observatory and a non-observance of expected

composition (non-proton primaries) and neutrino flux (GZK pion decay), GZK as the only reason for the observed cutoff in the spectrum is currently disfavoured. However, tensions between the composition measurements of the Pierre Auger Observatory and the Telescope Array (TA) [58], the second-largest CR observatory, make this topic still a subject of debate.

2. **Maximum Rigidity:** In this scenario, the cutoff is due to the sources of the extragalactic CRs reaching their maximum potential for acceleration for different particles i.e. maximum rigidity. Such a scenario is already observed in the spectrum for Galactic sources (*knee*). An indirect proof of this mechanism can come from the observed composition from the *ankle* region to the cutoff. If the composition shifts from lighter to heavier nuclei this would be proof of a cutoff at the potential extragalactic sources.

3. **Photo-disintegration:** This effect was also discussed before in section 2.1.3.

It is likely that the cutoff and the suppression are not just because of one of the above-mentioned scenarios but are due to a combination of all three. In theory, GZK and Photo-disintegration could explain the observed spectrum but the non-observance of GZK neutrinos and the composition measurements gather otherwise. It also shows that even though the CR spectrum gives a very nice overview, other crucial measurements of composition and multi-messengers are equally important allies to the spectrum measurements for constraining the origin and propagation of CRs.

Cosmic Ray composition

The types of particles the CR flux at Earth is made of is called the CR composition. Such measurements with respect to energy offer a very useful insight into their origin. Direct measurement of the primaries is only possible for low energies and one e.g. is the AMS detector at the International Space Station [59]. For higher energies, the mass of the primary is reconstructed by measuring the phenomenon of EASs which is described in more detail in Chapter 3. EASs are created when high-energy CRs interact with the Earth's atmosphere producing a cascade of particles resembling a shower. Depending on the mass of the primary, the EAS induced in the atmosphere by the said primary has characteristic differences. For the same energy lighter nuclei such as protons will interact and produce an EAS much deeper in the atmosphere compared to heavy nuclei such as iron. There are various ways one could estimate the mass of the primary. The estimator used for this at the Pierre Auger Observatory is $<X_{\mathrm{max}}>$ which is the average depth at which the EAS development in the atmosphere reaches a maximum. The $<X_{\mathrm{max}}>$ values are also energy dependent, and it is observed that iron nuclei typically have values $\sim$100 g cm^{-2} lower than proton. The fluctuation in the spread, $\sigma(X_{\mathrm{max}})$, can also be used to gauge the mass. For example, fewer fluctuations are expected for iron compared to proton. Other quantities such as the lateral distribution of the shower which is just the number of particles in a shower as a function of distance from the line along the CR momentum (shower core) also shows differences based on the primaries. For heavier primaries, the distribution is broader i.e. the number of particles decreases more gradually with distance from the core compared to a narrower distribution in the case of lighter primaries. The ratio of electromagnetic to muonic components first

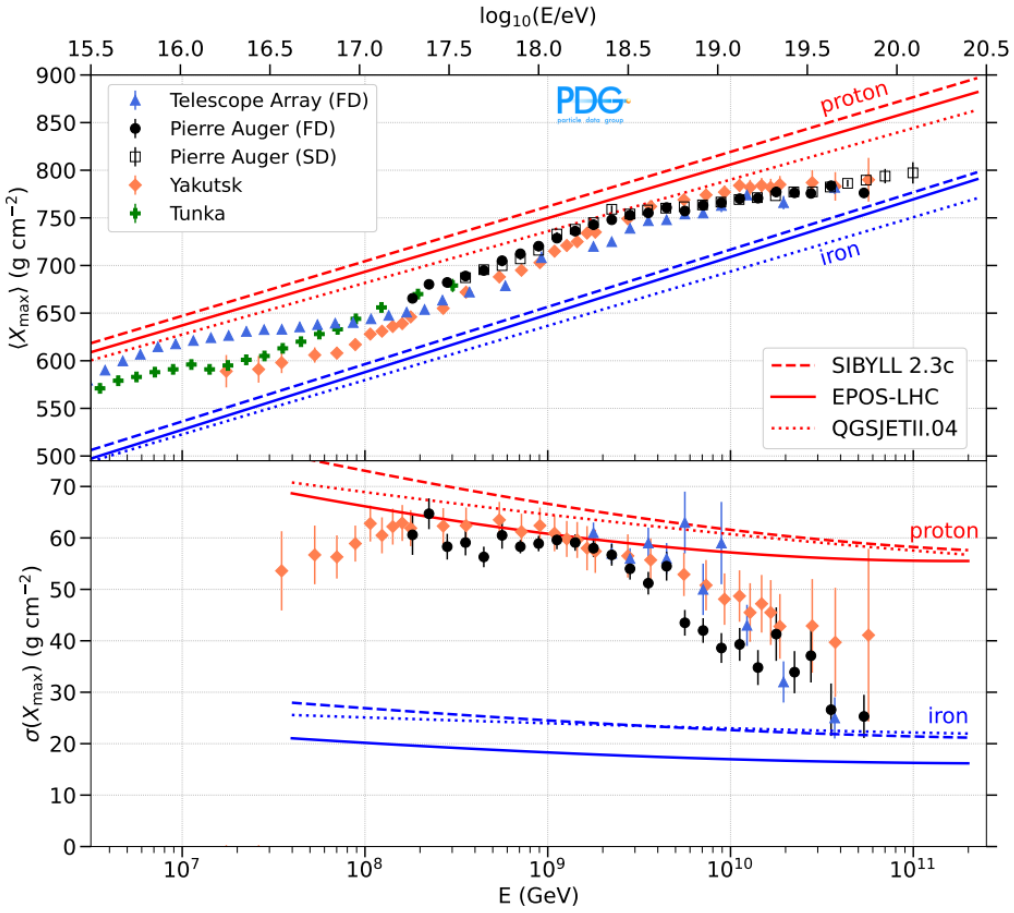

Figure 2.4: Measurements of mass composition by different experiments. $< X_{\mathrm{max}} >$ (top) and its fluctuations $\sigma < X_{\mathrm{max}} >$ (bottom). The red and blue lines are obtained from simulations with different hadronic interaction models. Taken from [61].

used by KASCADE [60] can also be used to differentiate between the primaries, the lighter primaries have a greater electromagnetic component whereas the heavier primaries have a greater muonic component in the initiated EAS.

The process of estimating the mass requires a very robust simulation that can reconstruct an EAS perfectly for a certain primary and a direct observation of X_{max}. At the Pierre Auger Observatory The Fluorescence Detector (FD), cf. section 4.1, is used to directly measure the X_{max} on an event by event basis. The recent results from the Pierre Auger Observatory are shown in Fig. 2.4. In both the figures the composition initially turns lighter and then seems to change from lighter to heavier nuclei at E ~18.5 EeV. This could be an indication of the switch from a galactic component to an extragalactic component around the *ankle* consistent with the maximum rigidity scenario as mentioned in the section above.

However, the duty cycle of the FD~14% compared to the SD ~100% leads to very limited

statistics. Currently, this problem is solved by defining a new observable described in [62] which has helped increase the number of events used to estimate the mass composition by nearly 14 times. The results for this are also shown in Fig. 2.4. Additionally, the energy dependent mass composition can be fitted simultaneously with the CR spectrum observed at the Pierre Auger Observatory with the only required assumption being about the model used to produce and propagate the CRs from the sources. Such type of analysis performed at the Pierre Auger Observatory can be found in [36]. With the current Pierre Auger Observatory measurements four different mass components are required to best describe the data with proton component completely disfavoured for the highest energies.

The future advancements of the AugerPrime [63] will further increase the capability of the Pierre Auger Observatory in measuring mass composition. The addition of a Radio Detector can present an independent measurement of the X_{max} offering an important cross-check on the FD measurement.

Cosmic Ray arrival directions

Even though the CRs are mostly charged particles and can easily get deflected by the magnetic fields [64] present in the cosmos, one can still measure the arrival directions of these CRs with the help of a good pointing resolution and estimate the direction of their origin with an understanding of these magnetic fields. The pointing resolution depends on the detector and the Pierre Auger Observatory already has an excellent pointing accuracy of $\sim 0.7^{\circ}$ [65]. The magnetic fields on the other hand are complicated to deduce and model. However, this lack of knowledge can be ignored by just looking at CRs of high energies since the expected deflections for such CRs are expected to be small. At the Pierre Auger Observatory the arrival directions of more than 2,600 CRs above 32EeV were estimated and analysed to look for potential sources of these CRs [66]. The most significant result from this study is shown in Fig. 2.5. The figure clearly shows the presence of anisotropies which are deviations from uniformity across the sky. The anisotropies are also pointed away from the Galactic centre indicating that the UHECRs have an extragalactic origin. The hypothesis is further confirmed by the increase in anisotropy with energy shown in [66]. The presence of these anisotropies not far from the Galactic spiral arm as seen in Fig. 2.5 also gives proof of an extragalactic origin of these UHECRs. Further, for low energies E> 0.03 EeV studies looking at large scale structures such as dipolar flux modulation in [67] also show a shift of the anisotropy dipole more towards the galactic centre with decreasing energy with a significance of $\sim 6\sigma$. This can again be interpreted as a transition in CR sources from Galactic to extragalactic component. Even though this result is corroborated by the measurements done by KASCADE-Grande, IceCube and IceTop due to the decrease in sensitivity of the Pierre Auger experiment for these energies the result is not conclusive yet.

Some proposed sources for these UHECRs due to observations of excess UHECRs in their surrounding regions by the Pierre Auger Observatory are presented in [69]. These include the Centaurus A region ($\sim 4\sigma$ significance), starburst galaxies ($\sim 3.8\sigma$) such as NGC4945, M83 and NGC253. The TA has also found an excess close to the Perseus-Pisces supercluster

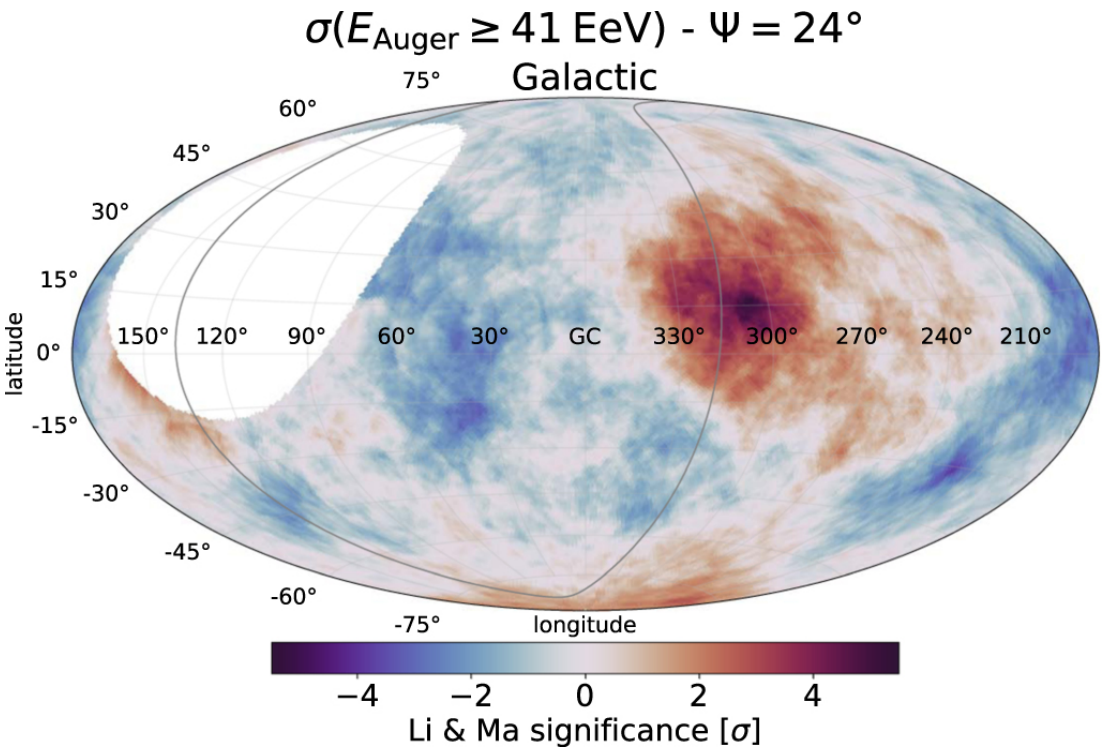

Figure 2.5: Localized excess or Li-Ma [68] significance map at energies above 41 EeV and within a top-hat search angle $\Psi = 24^{\circ}$ in Galactic coordinates. The gray line indicates the super galactic plane. Area outside the field of view of the Observatory is shown in white. The dark red areas indicate the possible source locations of extragalactic UHECRs. Taken from [66].

with a significance of $\sim 3.0 - 3.2\sigma$. However, this is still unconfirmed by the Pierre Auger Observatory which can also partly observe supercluster and remains a topic of discussion. With the continued data taking and upgrade of the Pierre Auger Observatory, the excess in the Centaurus A region is expected to reach a significance of 5σ by 2025 which could make it the first steady source of UHECRs ever observed.

Other Messengers

The scenarios for the production and propagation of CRs discussed above also predict the production of other messengers such as photons, neutrinos and neutrons. Neutrons and photons are discussed in this section and neutrinos are discussed in the next. Neutrons being neutral and thus not affected by the magnetic fields of the Universe during their propagation can be useful for arrival direction studies. They are expected to be produced at the CR source via charge exchange or other nuclear reactions near the sources. One such e.g. is a collision between an ultra-high energy proton to an ambient proton/photon. Although, neutrons can lose a significant amount of their acquired energy very quickly via β decay

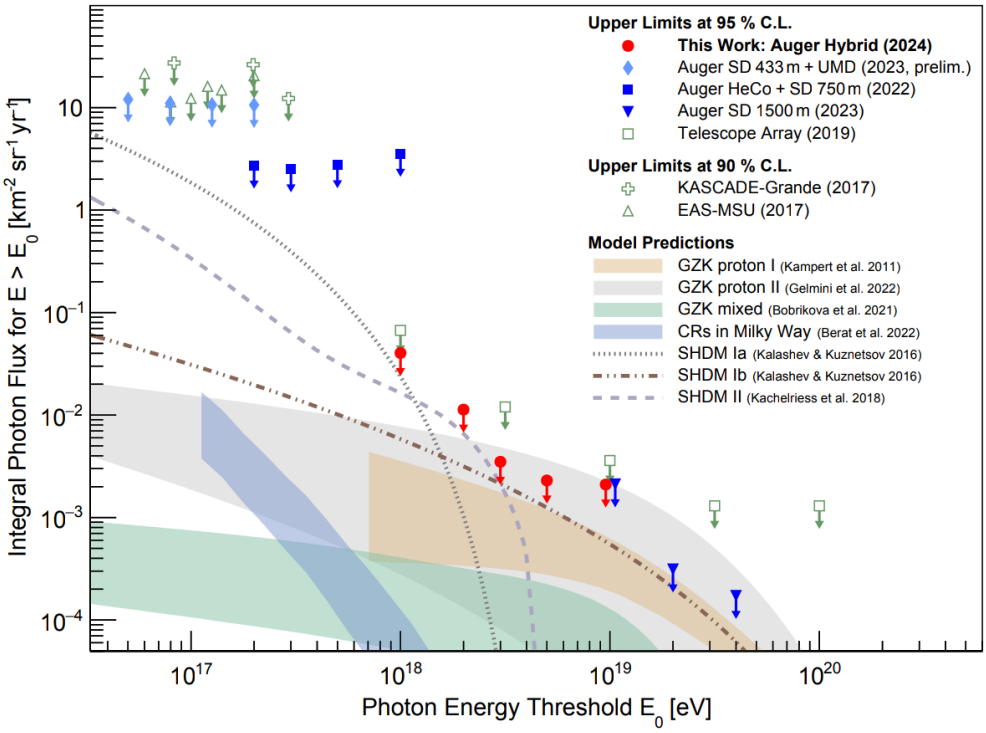

Figure 2.6: Summary of the current upper limits on the integral photon flux determined by Pierre Auger Observatory and other experiments [72].

(mean lifetime~879 s) [61] in the ultra-relativistic regime neutrons originated in our Galaxy can still make it to Earth. At Auger, a neutron produces a non-distinguishable EAS as compared to a proton. Hence, only a source catalogue correlated search can be performed at the Pierre Auger Observatory. The results of such a search are given in [70, 71]. No neutron like events have been found at Auger, but these results have already helped constrain some theorized production mechanisms for CRs. Future searches looking at transient or short-lived sources for neutrons are currently underway. Photons again offer another window to look into the origin, propagation and sources of the CRs. They can either be produced via interactions of CRs with matter or radiation fields or during propagation through interactions with the CMB as mentioned in section 2.1.3. They, along with neutrinos, can also help constrain various top-down scenarios and help paint a more complete picture of the CR landscape. Observations for high energy photons have been carried out by specialized experiments such as ground-based Cherenkov telescopes like the High Energy Stereoscopic System (HESS) [73], Fermi Gamma-ray Space Telescope [74], and the upcoming Cherenkov Telescope Array (CTA) [75]. The Pierre Auger Observatory can also contribute to this search in the ultra-high energy regime by looking for photon-induced EAS. Such EASs are expected to be different from the ones induced by CRs as they have a larger electromagnetic component and a rather small hadronic component. A more detailed description of the

signature is provided in [76].

Summary of the results of photon searches performed at the Pierre Auger Observatory is presented in Fig. 2.6 together with the predicted flux from some popular production models. Due to the non-observance of photon-like events at Auger, the collaboration has set some of the stringiest limits for expected photon flux at high energies. This has already helped constrain some top-down scenarios ultimately leading to a much better understanding of the origin of UHECRs. Further, searches will also help constrain the mystery of the cutoff. UHE photon searches are also very useful for a multimessenger approach to astronomy and these contributions are discussed more in section 2.3.

2.2 Ultra High Energy Neutrinos

2.2.1 History

Neutrino (ν) [77] (neut-neutral, ino-small) is an elementary particle belonging to the fermion class with a 1/2 spin. It was named by Enrico Fermi but first postulated by Pauli in 1930 as to not violate the conservation of energy, momentum and angular momentum in β decays. It rarely reacts in nature and only scatters via weak interaction. The neutrino was first observed in 1956 by the Cowan-Reines neutrino experiment [78] by detecting the positron annihilation of neutrons and positrons produced by antineutrinos created in a nuclear reactor. Neutrinos can have three flavours electron neutrinos (ν_e), muon neutrinos (ν_μ), or tau neutrinos (ν_τ) depending on the charged lepton (electron, muon or tau) accompanying them in their production. There are various mysteries involved with understanding this "ghost particle". One of these is the phenomenon of neutrino oscillations which is the intermixing of different neutrino flavors as they propagate through space. This has been observed in various experiments such as the Super-Kamiokande Observatory [79] and the Sudbury Neutrino Observatories [80] and was the recipient of the 2015 Nobel Prize for Physics since it was the first indication that neutrinos have some mass. This has led to various efforts to determine the mass of the three neutrinos (under Neutrino Properties in [61]). Currently, only a hierarchical differentiation can be established [81], the configuration of which is also not completely understood, and further experiments like Karlsruhe Tritium Neutrino experiment [82] are underway to solve this mystery. Also, the very mechanisms with which neutrinos can acquire mass are currently not completely understood [83].

Neutrinos arriving at Earth through astrophysical sources such as the Sun have also played an important role in increasing our understanding of CRs and physics in general. The solar neutrino observations ultimately led to the postulation and discovery of neutrino oscillations. The observations of neutrinos from SN 1987A, a type II supernova in the Large Magellanic Cloud by Kamiokande II [85] before the observation of any other messenger marked the dawn of non-solar neutrino astronomy and displayed the importance of neutrinos for multi-messenger physics. One of the most important experiments in this field has been the IceCube Observatory. Located at the South Pole it has revolutionized both neutrino and

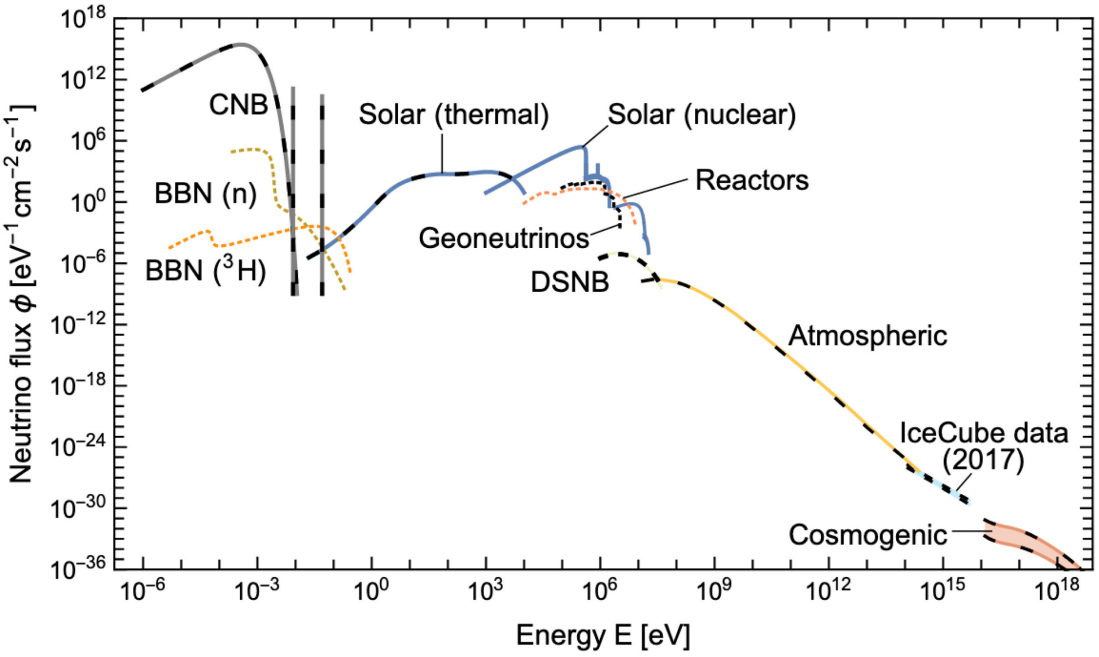

Figure 2.7: Grand Unified neutrino spectra at Earth. Taken from [84].

multi-messenger astronomy. It has led to the first detection of astrophysical neutrinos [86] and provided a measurement of their spectrum for high energies [87]. It has also contributed to the study of the neutrino oscillations [88] and could also help with ν mass hierarchy [89]. Recently, IceCube has further found indications for the first source of steady-state neutrinos in our cosmos which is the NGC1068 [16] and has also led to the groundbreaking measurement of the neutrino emission from our Galaxy [22]. These results and their implications are discussed in more detail in section 2.2.4. Its contributions to multi-messenger astronomy are also discussed later in section 2.3. For the highest of energies, the Pierre Auger Observatory remains the only facility capable of detecting neutrinos. Neutrinos can help to understand various astrophysical processes such as the Big Bang where the neutrinos are hypothesized to have decoupled one second after leading to Cosmic Neutrino Background (CNB) [90] to the nuclear processes inside stellar objects. Each such process speculates a unique neutrino spectrum which can be probed with experiments to garner their viability. Figure 2.7 shows the unified neutrino spectrum (measure and expected) with respect to energy. For this thesis, the following sections are constrained to only the neutrinos of the highest energies (UHEνs) above 10^{16} eV. How neutrinos can help decipher the mysteries of UHECRs is also discussed below.

2.2.2 Origin and Propagation

UHEνs can be broadly classified into three categories based on their origin. These are astrophysical, originating from known/hypothesized astrophysical sources, cosmogenic, ori-

ginating from the interactions of UHECRs with the CMB or the extragalactic background light (EBL) and exotic, emerging from processes such as the Big Bang, dark matter annihilation etc. The reactions for the mentioned processes are as follows:

Astrophysical Neutrinos

Astrophysical neutrinos are thought to be produced by or around known sources of UHECRs. The most important ingredients that are required to produce UHEνs are the interactions of high-energy protons and nuclei with matter or radiation fields which result in photo-meson production followed by a charged pion decay. The decay length of pions is much shorter than the distances of the sources to Earth thus they decay and give rise to secondary neutrinos.

$$\begin{aligned} p + \gamma &\longrightarrow \Delta^+(1232) \longrightarrow n + \pi^+ \\ &\longrightarrow \Delta^+(1232) \longrightarrow p + \pi^0 \end{aligned} \tag{2.4a}$$

$$p + \bar{p} \longrightarrow \pi^- + \pi^+ + \pi^0 \tag{2.4b}$$

$$\pi^0 \longrightarrow \gamma + \gamma \tag{2.5a}$$

$$\pi^+ \longrightarrow \mu^+ + \nu_\mu \longrightarrow e^+ + \nu_e + \bar{\nu}_\mu + \nu_\mu \tag{2.5b}$$

$$\pi^- \longrightarrow \mu^- + \bar{\nu}_\mu \longrightarrow e^- + \bar{\nu}_e + \nu_\mu + \bar{\nu}_\mu \tag{2.5c}$$

Other interactions such as beta decay of neutrons and nuclei ($n \longrightarrow p + e^- + \bar{\nu}_e$, $(A, Z) \longrightarrow (A, Z - 1/Z + 1) + e^{+/-} + \nu_e/\bar{\nu}_e$), electron/positron capture and β decays can also contribute to neutrino production. In most of these scenarios the expected flux ratio per flavor can be either $\nu_e : \nu_\mu : \nu_\tau = \bar{\nu}_e : \bar{\nu}_\mu : \bar{\nu}_\tau = (1 : 2 : 0)$ or (1:0:0) with no direct known process for ν_τ production at the source. However, since neutrinos can oscillate which is a consequence of the mixing between the flavor $|\nu_\alpha\rangle$ and mass eigenstates $|\nu_i\rangle$ of neutrinos, given by the following relation:

$$|\nu_\alpha\rangle = \sum_i U_{\alpha i} |\nu_i\rangle \,, \tag{2.6}$$

where $U_{\alpha i}$ is the mixing matrix formulated by Pontecorvo-Maki-Nakagawa-Sakata [92, 93]. In a standard case where three neutrino flavors are considered this matrix is a 3x3 matrix parameterized by the three mixing angles $(\theta_{12}, \theta_{23}, \theta_{13})$ and a single phase called δ_{CP}. Starting from the expected source flavor ratio one can calculate the flavor ratio at Earth by knowing the above four mentioned parameters. One example of such propagation is shown in Fig. 2.8. Since high energy tau neutrinos are not expected to be present in the atmospheric neutrino background the detection of such neutrinos at Earth could be an indication that the neutrino had an astrophysical origin.

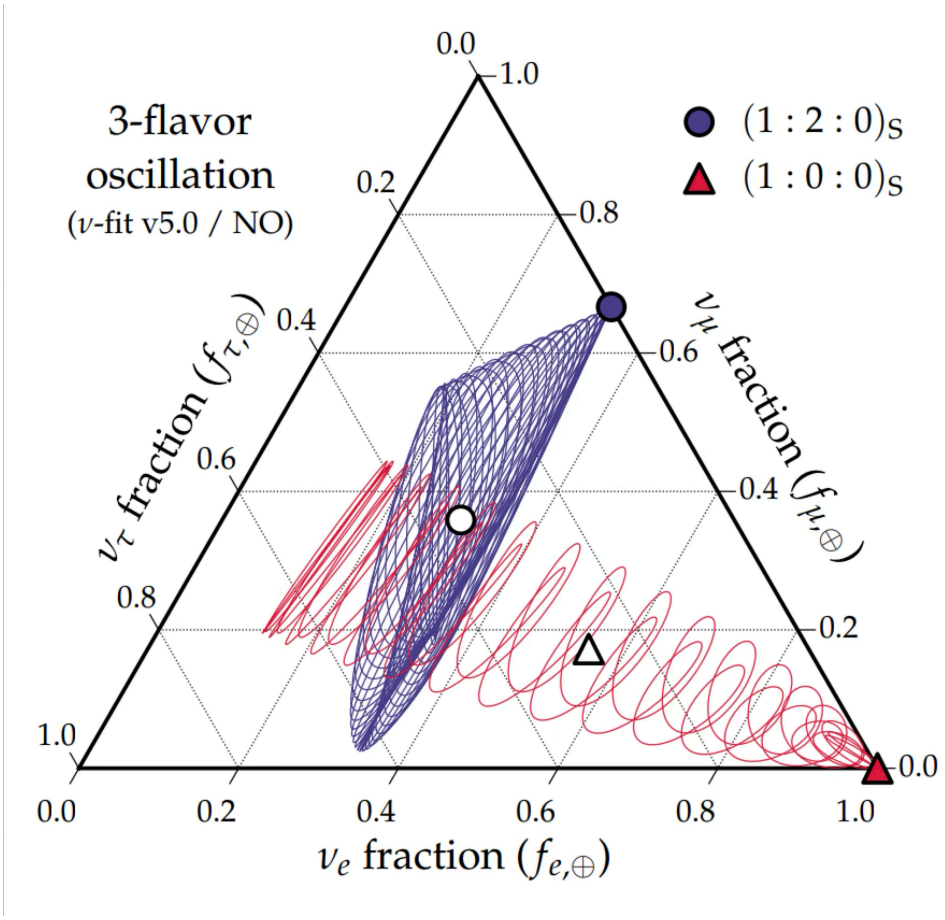

Figure 2.8: A ternary plot to show the neutrino flavor oscillations. Two different flux ratios per flavor (circle, triangle) based on different production mechanisms are shown. Flavors expected after propagation are also marked (open shapes). Taken from [91].

Another important aspect to fully understand the origin and propagation of astrophysical neutrinos is determining their expected energies. On average the energy fraction that pions can get from the CR nucleons is about 20%. These relativistic pions can then further pass on between ~20-26% depending on the flavor and type of the neutrino. Approximately, the energy fraction for the produced neutrinos concerning the gamma and nucleon is [94]:

$$\langle E_\nu \rangle \simeq \frac{1}{2} \left\langle E_\gamma \right\rangle \simeq \frac{1}{20} \langle E_N \rangle \tag{2.7}$$

Depending on the type of source and how far the said source is one can calculate the maximum energy potential for sources. With the measurement of the diffused astrophysical flux [95] by IceCube up to 10^{16}eV, these calculations can be directly constrained by measurement [96]. Since extragalactic sources can produce UHECRs up to $\sim 10^{20}$eV which is corroborated by measurements of the Pierre Auger Observatory one can calculate an upper limit to the

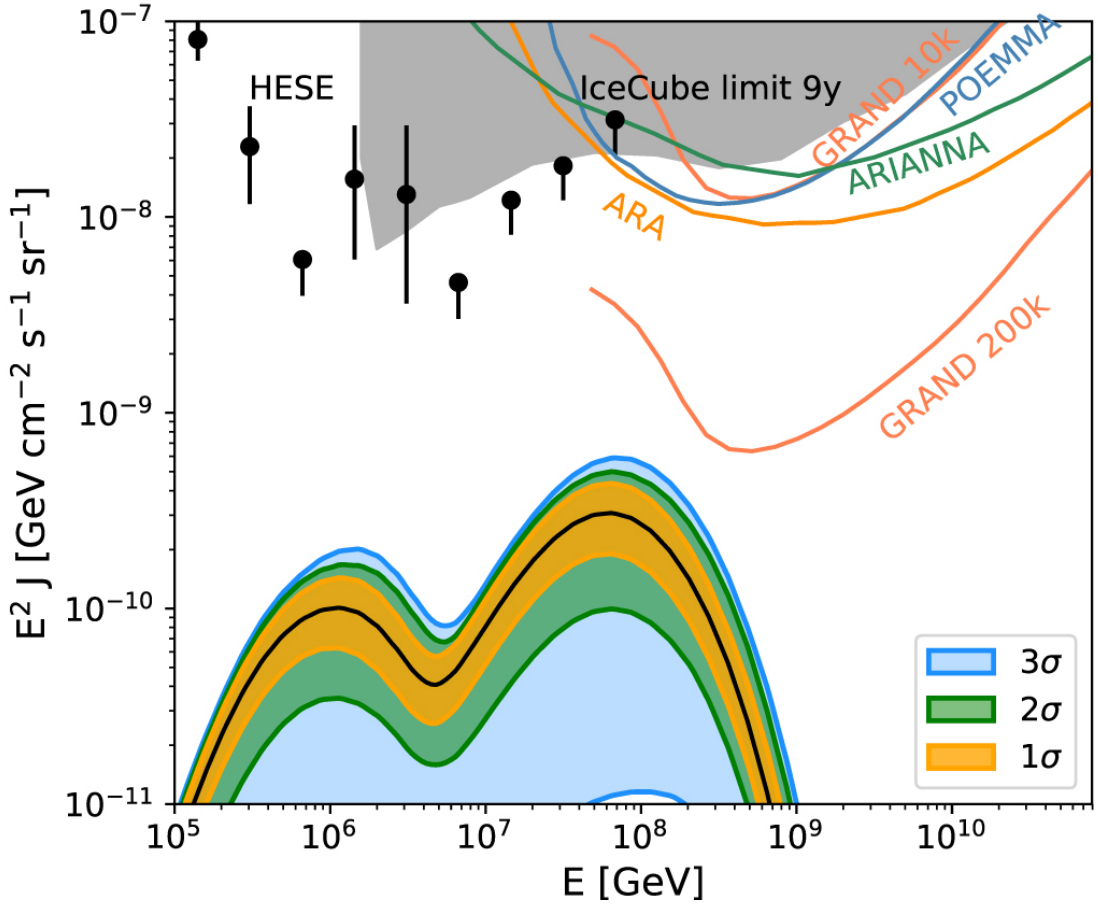

Figure 2.9: Allowed confidence ranges for cosmogenic neutrino fluxes obtained by varying the parameters regarding the source distribution and emission. The figure illustrates the two mechanisms of production of with the first peak corresponding to neutrinos from neutron decay and the peak at 10^{18}eV corresponds to neutrinos from meson decay. Taken from [100].

diffuse flux for neutrinos from some hypothesized sources such as Starburst galaxies [97], AGNs [98] and Magnetars [99]. The non-detection of UHEνs at Auger can thus also act as an important tool to constrain the production mechanisms hypothesized for these sources. The potential of this is discussed later in section 2.2.4.

Cosmogenic Neutrinos

Cosmogenic neutrinos are produced either as a consequence of the GZK mechanism discussed in section 2.1.3 or due to the interactions of UHECRs with EBL. They were first suggested by Berezinsky and Zatsepin in 1969 [101]. The processes involved are similar to those for astrophysical neutrinos albeit the proton/nuclei interact with the CMB/EBL photon instead of the photons from the radiation fields. The two main processes are the same as that for

the GZK mechanism i.e. decay of charged pions produced in photo-pion production, eq. 2.1 and the beta decay of neutrons and nuclei produced in photo-disintegration, eq. 2.2. CMB mainly affects the protons [102] during their propagation which form a large fraction of the UHECRs traversing the universe while the EBL plays an important role in the case of other nuclei [103]. Since the processes are the same, the flavor flux expectations at Earth remain the same. However, the expected energies that the cosmogenic neutrinos can acquire differ drastically as compared to astrophysical neutrinos. The energy of neutrinos produced due to interactions with CMB in the case of photo-pion production is of the order of 10^{18}eV while for the ones produced via the by-products (pions or neutrons) of photo-disintegration, it is of the order of 10^{16}eV [103]. In the case of interactions with EBL, this lowers to about 10^{15}eV and 10^{14}eV for the two types of interactions. The exact properties of the neutrinos produced are directly dependent on the parent UHECRs that produce them. The properties of UHECRs such as the total flux, composition, maximum energies, production spectrum at the sources and their cosmological evolution (adiabatic losses) are all crucial factors that affect the secondary cosmogenic neutrinos produced by these UHECRs. A collection of some examples of the expected cosmogenic neutrino fluxes for different scenarios can be found in [100, 104, 105]. One example is shown in Fig. 2.9. The two distinct humps are due to the two associated production processes with the lower one being due to the neutrinos produced in beta decay of neutrons and the higher one caused by nuclei produced via photo-disintegration.

Measurements of CR detection observatories such as the Pierre Auger Observatory can also be used to calculate an expected neutrino spectrum based on assumptions on the composition and the cosmological evolution of the sources. Neutrinos thus can act as a very important tool in constraining the composition of the incoming UHECRs and furthering their actual sources. They can also help to solve the question of the cutoff observed in the UHECR spectrum whether this is due to the GZK mechanism (proton-dominated composition) or sources reaching their maximum potential as theorized by Hillas (mixed composition). The current results regarding this important study are discussed in section 2.2.4.

Exotic Neutrinos

Neutrinos can also be produced as a result of self-annihilation or decay of dark matter particles. In dark matter annihilation scenarios, two dark matter particles come together and annihilate, leading to the production of standard model particles as a result. The specific flux of the neutrino depends on the properties of the dark matter particle. One such candidate for such a process could be a Weakly Interacting Massive Particle (WIMP), which could be its own antiparticle (a Majorana fermion). In regions with a high concentration of dark matter, such as the centres of galaxies or galaxy clusters, WIMPs can come together and annihilate into standard model particles [106]. One of the annihilation channels of interest for producing very high-energy neutrinos is the annihilation into pairs of intermediate bosons, such as W^+W^- (W-boson pair), or $Z^0 - Z^0$ (Z-boson pair). These intermediate bosons can subsequently decay into quarks, leptons, and other particles, including neutrinos. The final state neutrinos can be very high-energy, potentially reaching energies in the peta-electronvolt

(PeV) range and beyond. For dark matter decay, a stable dark matter particle is supposed to spontaneously transform to other standard model particles including neutrinos [107].

2.2.3 Neutrino Interactions and Detection

The low interaction cross-section (σ_ν) [108] of neutrinos which allows them to travel for large distances also makes them almost impossible to detect. They can pass through vast amounts of material without leaving a significant trace. While at low energies (keV-GeV) processes such as Inverse Beta Decay, resonant production etc. are used to detect neutrinos, at high energies neutrinos interact with the nucleons mainly via Deep Inelastic Scattering (DIS) in Charged Current (CC) and Neutral Current (NC) interactions. In CC interaction, a neutrino interacts with a target nucleus with an exchange of a W boson, transforming into a charged lepton corresponding to the flavor of the incoming neutrino and a hadronic cascade. The NC interaction is flavor blind and occurs with an exchange of the Z^0 boson and a nuclear recoil. Both reactions are shown in the equations below:

$$\nu_l\,(\bar{\nu}_l) + N \xrightarrow{\text{CC}} l^-\,(l^+) + X \tag{2.8a}$$

$$\nu_l\,(\bar{\nu}_l) + N \xrightarrow{\text{NC}} \nu_l\,(\bar{\nu}_l) + X \tag{2.8b}$$

The products from the CC and NC interaction i.e. a lepton and the hadronic cascade can be detected in multiple ways. Antineutrinos can also interact with atomic electrons leading to a W^- boson production called the Glashow resonance [109]. The threshold antineutrino energy for such a reaction to occur is ~6.3 PeV. This process dominates the CC and NC interaction albeit only in a small energy range. Proposed in 1959, it was first observed at the IceCube Observatory [110]. Both CC and NC when interacting with the nucleon undergo neutrino-nucleon deep inelastic scattering where the interacting neutrino scatters off individual quarks inside nucleons (protons or neutrons), leading to the fragmentation of the nucleon and the creation of hadronic (particles made of quarks) jet. At low center-of-mass energies (~TeV) accelerators can provide most of the information about the neutrino interaction with matter and the corresponding cross-section but at high energies this estimation can either only be calculated via the detection of astrophysical and cosmogenic neutrinos or via a robust theoretical estimation including quantum chromodynamics (QCD) and low energy measurements. The description of QCD at such high energies is still not completely understood. Moreover, physics beyond the Standard Model can also be introduced for these energies which can further affect the neutrino cross-section estimation [111]. For the purpose of this thesis, the neutrino cross-sections calculated in [112] are used. The reference provides an updated $\nu - N$ cross-section calculations with corresponding uncertainties, taking into account the full HERA [113] data release and combining it with the DGLAP [114–116] formalism of QCD. Based on the expected flux the cross-section and the energy of neutrinos it is easy to calculate minimum detector sizes for high-energy neutrinos. For example, for

a neutrino of energy $E_\nu \sim 1\,\mathrm{PeV} = 10^{15}\,\mathrm{eV}$, the expected flux is $\frac{d^2N_\nu}{dtdA} \sim \frac{1}{cm^2 \times 10^5 yr}$, the cross-section is $\sigma_{\nu N} \sim 10^{-8} \times \sigma_{pp} \sim 10^{-33}\mathrm{cm}^2$ and the targets can be estimated as $N_N \sim N_A \times V/cm^3$ where N_A is the Avogadro's number then the rate of expected events is given by:

$$N_\nu \sim N_N \times \sigma_{\nu N} \times \frac{d^2N_\nu}{dtdA} \sim \frac{1}{\mathrm{yr}} \times \frac{V}{1\,\mathrm{km}^3} \tag{2.9}$$

Therefore, to detect a neutrino at this energy range in a year requires a detector with a minimum size of $1\mathrm{km}^3$. The type of such large volume detectors for UHEνs depends on the particular techniques used to detect the products of neutrino interaction with nucleon.

The charged lepton can produce detectable signals via ionization, Cherenkov radiation or scintillation. Moreover, the lepton and hadrons can also trigger EASs which can be detected. Both the lepton and the hadron can lead to a cascade. Depending on the flavor of the neutrino the interaction also leads to unique signals. The electron produced in the CC interaction of ν_e produces electromagnetic cascades in the propagation medium while a muon rarely produces a cascade like signature only undergoing radiation losses. In contrast, a tau lepton produced from ν_τ can propagate without interaction for a certain distance and then lead to a cascade. For NC reactions the leptonic cascade is missing and only a hadronic cascade can be observed. Low-energy neutrinos or neutrinos produced in the atmosphere can also lead to similar cascades and act as background for high-energy neutrino searches. Depending on the location and techniques employed such background is dealt with in different ways. Some examples of different detectors based on the medium and the methodology employed for detection are as follows:

Ice and Water Cherenkov Detectors: IceCube Neutrino Observatory [118] and its predecessor AMANDA [119] are examples of in ice Cherenkov detectors. IceCube is located at the South Pole and uses a cubic-kilometer array of Antarctic ice to detect high-energy neutrinos. It consists of 80 strings carrying 60 photomultiplier detectors each situated between 1500 m and 2500 m below the surface. Neutrinos interact with the optically clear ice nuclei, producing secondary particles that emit Cherenkov radiation. The detector's photomultiplier tubes capture the Cherenkov light, allowing reconstruction of the neutrino direction and energy. Muon tracks resulting from CC interactions can also be observed. Being underground partly shields IceCube from the atmospheric muonic background which is useful for detecting down-going neutrinos. It can also use the Earth as a shield to look for TeV upward-going neutrinos. The Observatory also consists of a surface array (IceTop) of ice Cherenkov tanks which further help in atmospheric background rejection and CR studies.

Water based Cherenkov detectors have been used for neutrino detection since their discovery. Kamiokande II [120] used a large underground water tank surrounded by PMTs to observe the first astrophysical neutrinos from SN 1987A [85]. Since the required detector volume for detection of a sufficient rate of neutrinos is very large, sizeable stable natural water reservoirs are used to build such detectors. Some examples

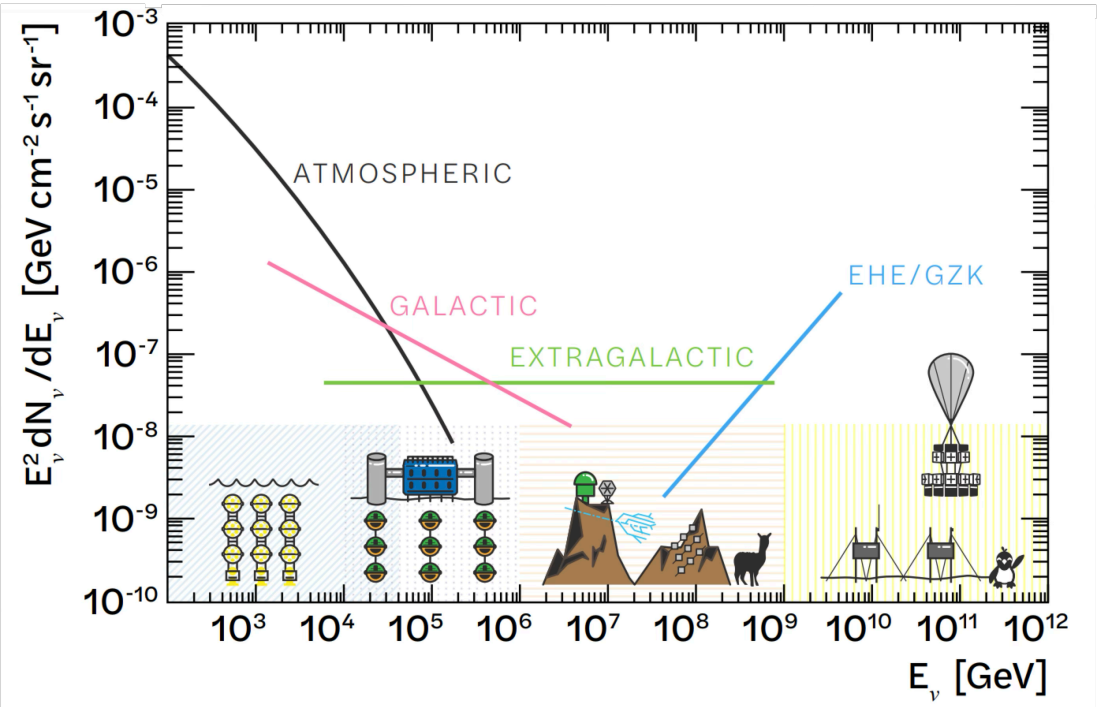

Figure 2.10: Different detection techniques for UHE neutrinos. Ice and Water based Cherenkov detectors are sensitive to atmospheric, galactic neutrinos and some extragalactic neutrinos while radio and air shower detectors are sensitive to very high energy neutrinos with other techniques filling the gaps. The spectral indices of the different components are estimations. Taken from [117].

include the ANTARES [121] and KM3Net [122] located in the Mediterranean Sea off the coast of France and Italy and the upcoming BAIKAL-GVD [123] and P-ONE [124] located in Lake Baikal, Russia and the Pacific Ocean off the coast of British Columbia, Canada respectively. The actual detector and the principle remain the same as IceCube with the only change being the medium and upgrades in detector technology depending on the advances in the field.

– **Radio Detectors:** These detectors are based on the detection of νs in dense media using the Askaryan effect [125, 126]. It is a phenomenon in which high-energy charged particles moving through a dense dielectric medium, produce coherent electromagnetic radiation in the radio frequency range. When the high-energy particles interact with the atoms and molecules in the dielectric medium, they generate a shower of secondary charged particles. As these secondary particles move through the medium they undergo a charge separation leading to the emission of coherent Cherenkov radiation in the radio frequency range. The effect typically produces radiation in the radio frequency range, from a few hundred megahertz (MHz) to several gigahertz (GHz). Experiments like ANITA [127] have tried to detect the radio emission produced when neutrinos

interact with the Antarctic ice [128]. RNO-G [129], an in ice radio antenna array, is also under construction at Summit Station in Greenland to search for neutrinos above PeV energies. The planned upgrade of IceCube, IceCube-Gen-2 [130] also plans to employ a large in ice radio array to increase its sensitivity to both astrophysical and cosmogenic neutrinos.

– **Acoustic Detectors:** The cascade of secondary particles produced in a neutrino interaction in a medium can also generate an acoustic shockwave, also known as a "thermoacoustic pulse," due to rapid heating and expansion of the medium. The resulting acoustic signal travels through the medium as a pressure wave and can be detected by sensitive acoustic sensors. Typically, large volumes of water or ice are used as the detection medium. The acoustic signal propagates through the medium and can be detected by underwater microphones (hydrophones) or other acoustic detectors. This technique has not yet yielded a neutrino observation. It has been used at ANTARES as AMADEUS [131] and at IceCube as SPATS [132] to test the acoustic properties. ANDIAMO [133] is a proposed acoustic neutrino detector that could use this technique in the future.

– **Radar Echo Detectors:** Radar Echo Telescope [134] is a detector that aims to detect neutrinos using the radar echo method. The method is based on the reflection of a transmitted radar signal by the in ice neutrino cascade which acts as a short-lived mirror. The reflected signal is then detected at a receiving antenna. This technique is currently being tested in Greenland for Cosmic ray showers and might be employed to detect neutrinos in the future.

– **Air Shower Detectors:** Even though, the typical interaction lengths of UHEνs are way larger than the atmospheric depth, neutrinos can still induce an EAS. Such EASs can develop at any point in the atmosphere, due to the interaction length of neutrinos in atmosphere ($\sim 10^5 \mathrm{g/cm^2}$) being orders of magnitude higher than the total atmospheric depth, in comparison to CRs with interaction lengths($\sim 70 \mathrm{g/cm^2}$). This offers a distinctive aspect for neutrino detection at CR observatories like the Pierre Auger Observatory. Pierre Auger Observatory uses the said property to search for EeV neutrinos. EASs and the expected signature at the Pierre Auger Observatory for both CRs and neutrinos are discussed in the next Chapter 3.

2.2.4 Latest results

Astrophysical Neutrinos

Spectrum After the measurements of astrophysical neutrinos at the IceCube Neutrino Observatory, the first plot and estimation of flux has been possible for high-energy neutrinos. The flux spectrum as measured by IceCube and other experiments is shown in Fig. 2.11. The flux was first published in 2013 [135] and has since been refined with various analyses [95]. The plot also shows the summary of the currently published analysis along with current

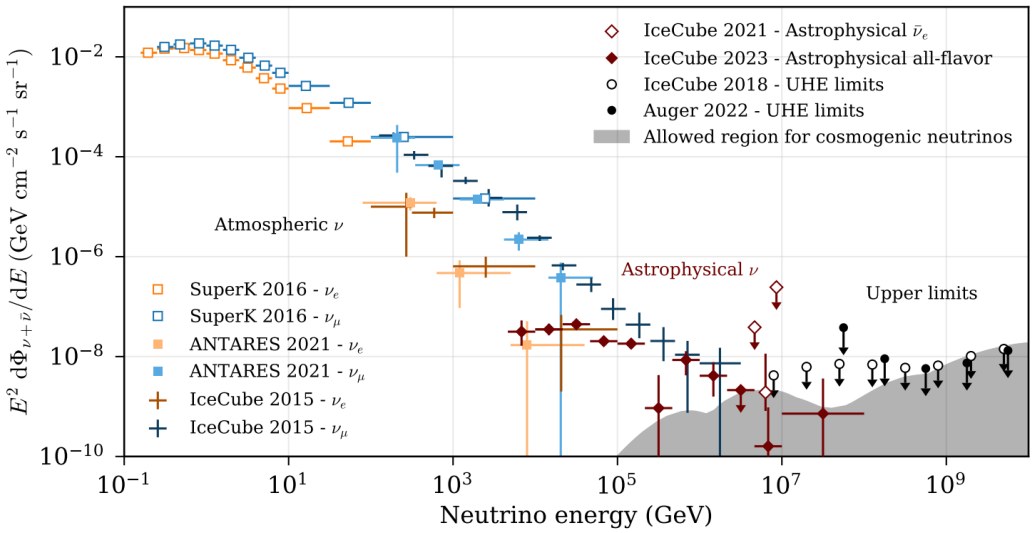

Figure 2.11: Measured neutrino flux for atmospheric and astrophysical neutrinos. At high energies for the diffuse flux of cosmogenic neutrinos there are upper limits from IceCube and the Pierre Auger Observatory. Taken from [61].

best upper limits for cosmogenic neutrino flux. The diffuse flux spectrum agrees across the various analyses within the overlapping energy regions. However, there is a slight tension between the estimate of the spectral index which is obtained after fitting the flux spectrum. The measurements are also not enough to decide on the nature of the flux across the whole energy range and more measurements in the future would help understand the neutrino spectrum in more detail.

Sources Since neutrinos arrive at Earth pointing directly back to their source, plotting the candidate astrophysical neutrino events measured by the neutrino telescopes over a sky map can localize their sources of origin. Such studies have been performed by various neutrino telescopes such as ANTARES [136], AMANDA [137], BAIKAL-GVD [138] and IceCube [16]. Only IceCube has found the most significant excess of 81 events in the TeV range, arriving from the region within 0.18 degrees of active galaxy NGC1068 (M77). The Fig. 2.12 taken from [16] shows the hottest spot along with the excess. The association of the observation to the particular source has a significance of 4.2σ. Hosting an active AGN surrounded by a dust torus makes it one of the ideal candidates for neutrino production [139, 140]. The same analysis has also pointed out other potential neutrino source candidates PKS 1424+240 and TXS 0506+056. The latter of these is also important in the context of multi-messenger physics and is discussed later.

In 2023, IceCube also published the first observation of diffuse emission of high-energy neutrinos from the galactic plane of our own galaxy, the Milky Way [22]. The result is at

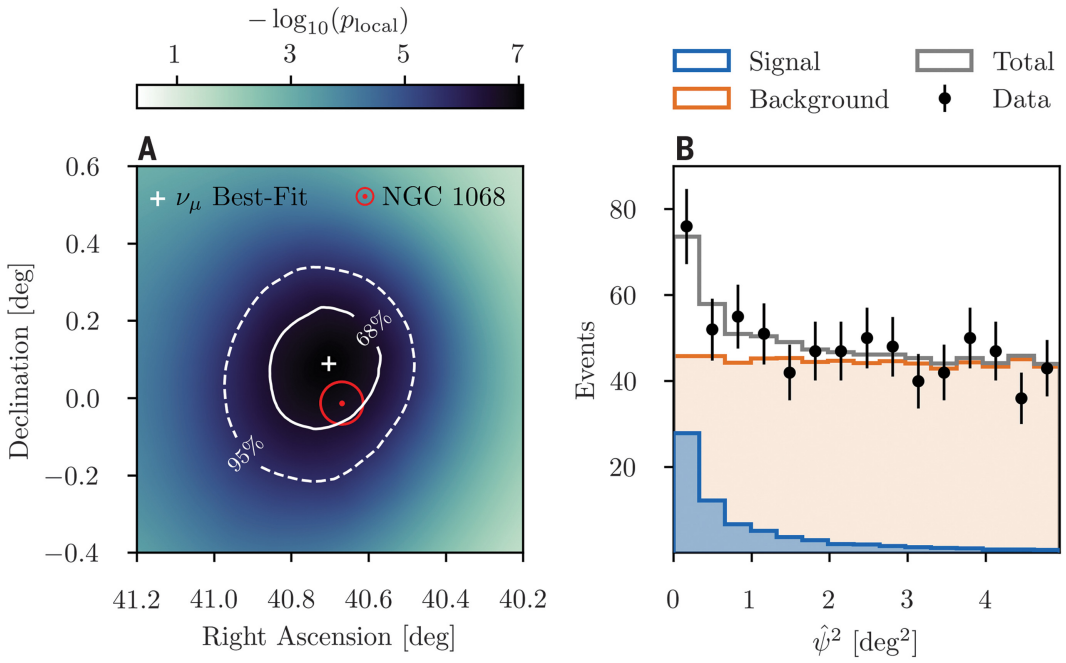

Figure 2.12: Left:The sky region around the most significant neutrino excess spot in the Northern Hemisphere close to NGC 1068. The plot shows a fine scan of the region around the hottest spot. The hotspot is marked by a yellow cross and the dot marks the position of NGC 1068. Further, the solid and dashed contours show the 68% (solid) and 95% (dashed) confidence regions of the hot spot localization. Right: The distribution of the squared angular distance between NGC 1068 and the reconstructed event direction. Taken from [16].

the 4.5σ level of significance when compared to a background-only hypothesis. However, the signal could also be due to a population of unresolved point sources near the galactic plane. This observation has opened a new way to observe our Milky Way galaxy and offers an evidence based proof confirming our understanding of both CR and neutrino physics. It also opens a new avenue for the application of multi-messenger astronomy. The Fig. 2.13 shows the plane of the Milky Way galaxy as seen by different messengers.

Cosmogenic Neutrinos

Limits Both the Pierre Auger Observatory and the IceCube neutrino Observatory have also performed searches to look for UHEνs which have a cosmogenic origin. These searches have led to some of the most stringent upper limits for such fluxes. These limits are shown in Fig. 2.14. The results from the Pierre Auger Observatory dominate for energies above 10^{18}eV and for lower energies, IceCube provides the best limits. The lack of observations can help constrain various models for high-energy neutrino production. These results can

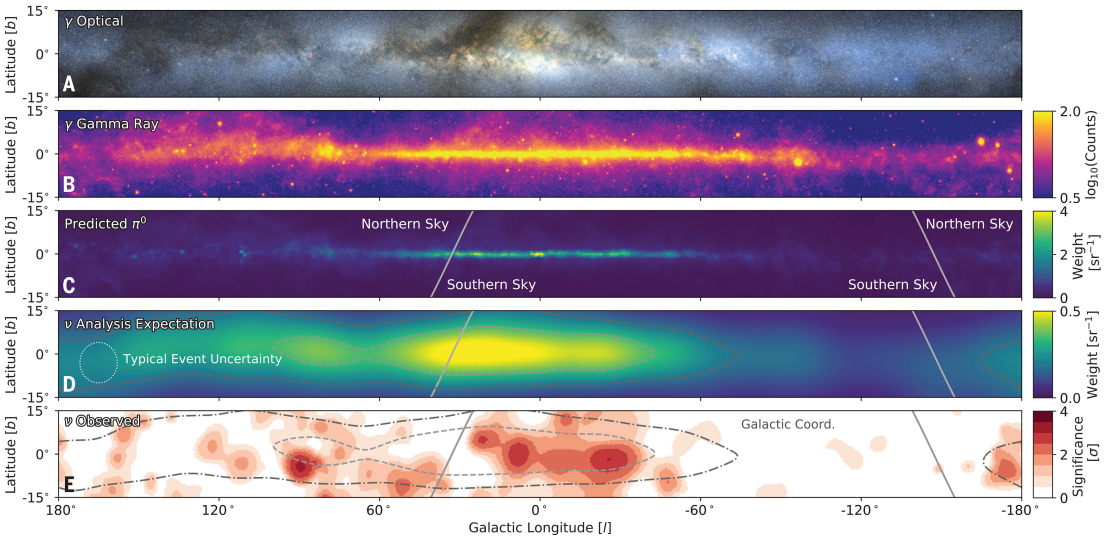

Figure 2.13: Galactic plane with different messengers. The observation of neutrinos at the bottom is the final piece added to this picture. Taken from [22].

also help better our understanding of CR physics and in particular their composition. The lack of observation of the expected neutrino flux predicted by a pure proton composition scenario for CRs is an important result in favour of mixed composition scenarios. This result further points towards the spectrum cutoff being more likely due to a maximum rigidity limit for the sources rather than a GZK limitation. The detection of cosmogenic neutrinos can help complete the picture of the neutrino and CR sky.

2.3 Multimessenger Astronomy

Combining the various messengers via which we can see the Universe can help better understand the mechanisms behind their production and propagation. By combining the observations of various dedicated experiments for gravitational waves (LIGO/VIRGO), Gamma rays (FERMI-LAT, CTA), neutrinos (IceCube) and CRs (TA, Pierre Auger Observatory) a holistic overview of an astrophysical process can be gathered. The detection from one messenger/experiment and a non-detection from another can also be informative since it helps refine our understanding or might even reveal a new phenomenon [142, 143]. One of the most important aspects of this field is a fast communication network via which all the different experiments can share their observations as fast as possible. Supernova Early Warning System [144], established in 1999 and the Astrophysical Multimessenger Observatory Network [145], created in 2013 are some examples of the networks used in multi-messenger astronomy. Some of the key observations of this field and the corresponding publications are summarized in table 2.1. As mentioned in the introduction, the Pierre Auger Observatory continues to contribute to these searches [146]. One of the best examples of this collaboration

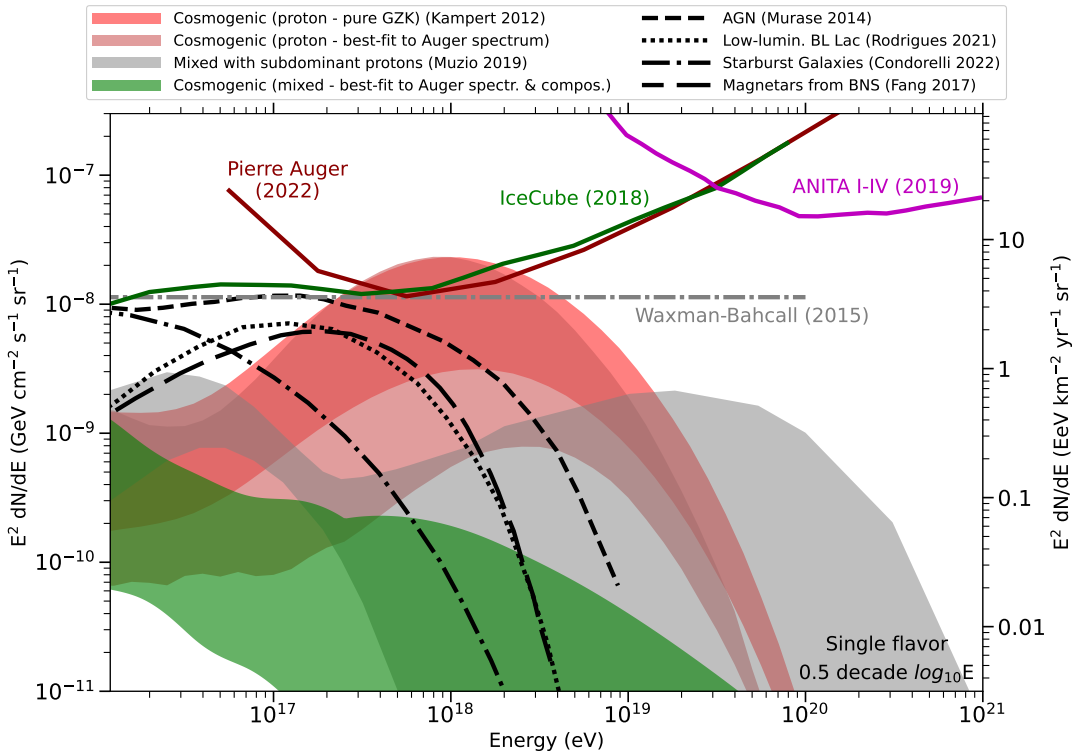

Figure 2.14: Current upper limits on the diffuse flux of neutrinos from different experiments. Only the differential limits are shown. Also shown are the expected neutrino fluxes from different theoretical predictions for comparison. Taken from [141].

is [147] where a spatial correlation search for neutrinos and CRs was performed as a joint effort between ANTARES, the IceCube Observatory, the Pierre Auger Observatory and the Telescope Array. The GW 170817 [20] multi-messenger analysis using more than 70 observatories cemented the benefits and the potential of multimessenger astronomy.

Multimessenger picture					
Astrophysical Event	Electromagnetic	Cosmic rays	Gravitational Waves	Neutrinos	Example
Solar flare	yes	yes	-	-	-
Supernova	yes	-	predicted	yes	SN1987a
Neutron star merger	yes	-	yes	predicted	GW170817
Blazar	yes	possible	-	yes	TXS 0506+056
Active galactic nucleus	yes	possible		yes	NGC1068
Tidal disruption event	yes	possible	possible	yes	AT2019dsg AT2019fdr

Table 2.1: Current status of Multimessenger observations. Adapted from [148]

CHAPTER 3

Extensive Air Showers

As mentioned in the previous chapter an EAS is a cascade of high-energy particles that is produced when an UHECR, typically a proton or a nucleus, collides with a nucleus in Earth's atmosphere. This cascade can span over hundred to thousands of meters at ground based on the energy of the initial particle and the incoming zenith angle. EASs offer the best way to look for UHECRs since the low flux of these particles make direct detection using detectors mounted on balloons or spacecrafts not feasible. The EAS can be detected at the ground via an array of detectors. To infer the properties of the CR from the EAS it creates, one needs to model and understand how an air shower develops in the atmosphere. This chapter describes the process of the initiation and the development of the shower induced by CRs and neutrinos. It also aims to describe the important characteristics of EASs which help in extracting the relevant information and the last part of this chapter is devoted to summarize the detection of the EASs using different detector systems.

3.1 Development

As the CR particle, which is predominantly a proton, collides with the nuclei of the atmosphere (N_2, O_2 etc.) it produces pions and also a few kaons. The neutral pions produced almost immediately decay to pairs of photons which in turn produce electrons via the process of pair-production. These electrons can then further produce photons via bremsstrahlung initiating a chain reaction which alternates between these two processes and forms the *electromagnetic component* of the shower. The charged pions can survive for a while but eventually decay to muon and a corresponding anti neutrino. These muons can either survive till the shower reaches the ground and form the *muonic component* or can also decay to electrons thus contributing to the electromagnetic part. The neutrinos due to their low interaction cross-section mostly survive till they reach the ground and even further. Though not causing any problem for an EAS detector such neutrinos are the biggest background for a neutrino telescope. Kaons and charged pions due to their long lifetimes can also interact with the atmospheric nuclei producing additional pions which form the *hadronic component* of the

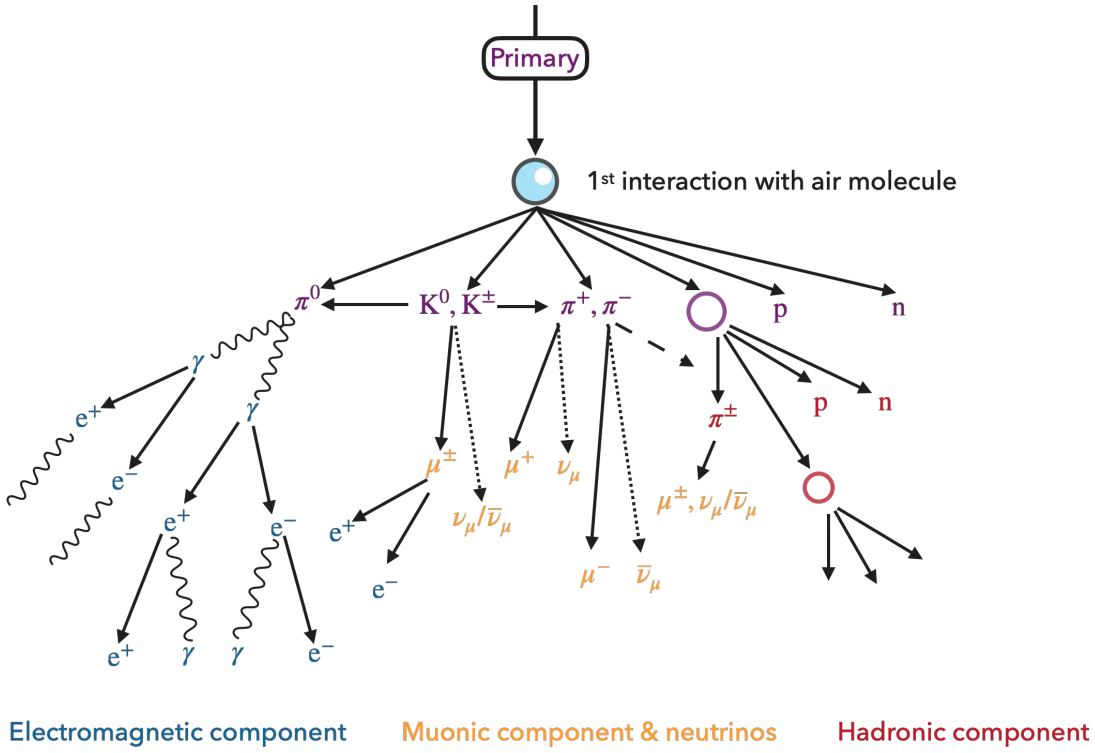

Figure 3.1: Development of an Extensive Air Shower. The figure shows the different components of an EAS and the reactions which lead to their formation.

shower. The hadronic component can further contribute to both the electromagnetic and muonic component as more the shower propagates lesser the overall hadronic component becomes. A schematic of all the reactions with the different components is presented in Fig. 3.1.

To understand the cascade of particles a detailed modelling of each component is required. These models help extract the basic properties of the cascade. A simplified model describing the electromagnetic component called the Heitler's toy model, its hadronic extension, and a generalized cascade equation are all discussed below. The specific development of a neutrino induced EAS is also discussed.

3.1.1 Heitler's Toy Model

Proposed by Heitler in 1954 [149], Heitler's Toy Model is a simplified perfect binary tree to understand and model an EAS development. The model characterizes an EAS as a perfect binary tree. In such a scenario all particles produced in a shower equally share the primary energy available at the time of their creation. At each step, which has a fixed size related to the radiation length of the medium λ, the number of particles are supposed to be doubled, with each having the same energy. The energy losses which may occur due to collisions are

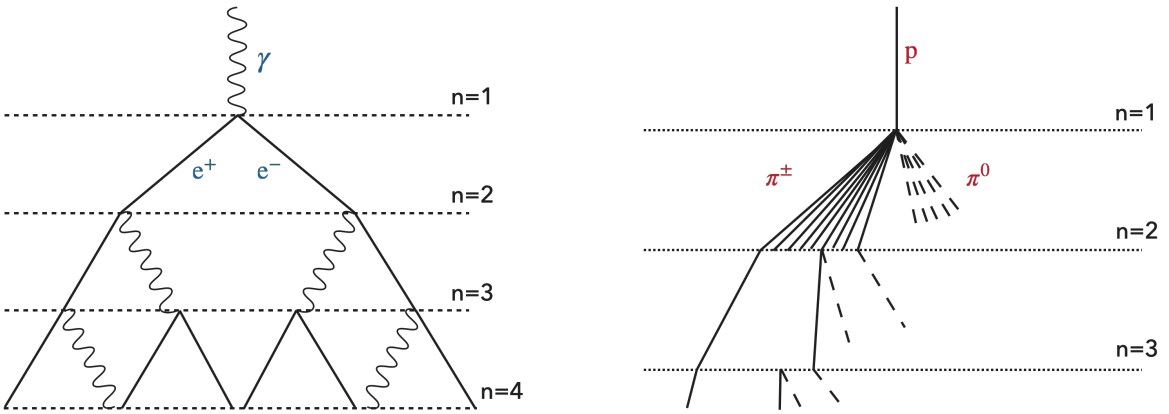

Figure 3.2: Representation of Heitler's model.

completely ignored. The shower development or splitting process is supposed to continue until a critical point where the where average collisional energy losses begin to exceed radiative losses in the medium. At the critical point, the shower has the maximum number of particles given by, $N_{\max} = E_0/E_c$, which is the ratio of the original energy (E_0) to the critical energy ($E_c \sim 87$MeV). After this point the shower keeps getting absorbed in the atmosphere. The penetration depth at this point is called the shower maximum denoted by $X_{\max}$. This can be calculated to be $X_{\max} = X_0 + \lambda_r \ln(E_0/E_c)$ where X_0 is the first interaction point in the atmosphere. A visualization of the shower development according to the Heitler's model is shown in Fig. 3.2.

Such a simplified model works quite well for estimating the properties of the electromagnetic cascades although the $N_{\max}$ estimations do not match perfectly. The reason for this is the difference in the energy loss values for electrons and photons. For hadronic cascades an extension to the model was made. Other important properties of the shower such as lateral and longitudinal spread, also require taking into account the emittance direction and losses due to collision which are not taken into account for a simplified model. These are discussed in section 3.2. Even with its shortcomings the Heitler model gives a very good estimation for electromagnetic cascades and helps clearly categorize an air shower into three phases, the growth phase, the critical point phase and the tail phase.

3.1.2 Hadronic Extension

The Heitler model was extended by Matthews [150] to characterize the hadronic cascades in an EAS. In his approximation when a hadron with Energy, E, interacts with a nucleon the total particles produced have a two-third charged component ($\pi^{\pm}$) and a one-third neutral component (π^0) with the initial energy equally divided based on the number fraction. The neutral component decays quickly and contributes its share of energy to the electromagnetic component. The charged hadrons, provided they have not reached their critical energy

in air (∼20 GeV), interact again repeating the initial process. Muons are only produced when it begins to become more likely that a charged hadron will decay rather than interact. The energy transfer for each component after n generations is given as $E_{\text{had}} = \left(\frac{2}{3}\right)^n E_0$ and $E_{\text{em}} = [1 - \left(\frac{2}{3}\right)^n] E_0$. Deeply penetrating air shower i.e. for a primary with high energy and a low cross-section in air, results in a lower number of muons produced, and observed at ground. This fact is important as based on the ratio of muons to electrons observed at ground, the type of the primary can be estimated. The number of muons (N_μ) can be estimated in this model directly from charged hadrons when their energy falls below the critical energy. For n generations one finds, $N_\mu = n_{\text{ch}}^n$ where n_{ch} is the number of charged hadrons and n can be written as $n = \frac{\ln(E_0/E_c)}{\ln(n_{\text{tot}})}$. Generalizing by eliminating generations:

$$N_\mu = \left(\frac{E_0}{E_c}\right)^\alpha, \; \alpha = \frac{\ln(n_{\text{ch}})}{\ln(n_{\text{tot}})} \tag{3.1}$$

All the parameters in this model need to be estimated using detailed simulations [151]. α has been estimated to be in the range 0.82...0.9. Other factors such as production of particles which do not decay such as baryon-anti-baryon pairs [152] can also affect the calculated values in this model. The change of the depth of the shower maximum per decade in energy also called the elongation rate is given by $D_{10} = \frac{\langle X_{\text{max}} \rangle}{d \log_{10} E_0} = 2.3\lambda_r$. The elongation rate of electromagnetic showers in air is about $\approx 85\,\text{g cm}^{-2}$. The elongation rate theorem [153] states that the upper limit to the elongation rate for hadronic showers is also D_{10}^{em} in the presence of Feynman scaling.

The first interaction with the nucleon was presented in a simplified way by Matthews as the superposition model. In this model a nucleus with mass A is assumed to be a superposition of A independent nucleons, each with energy $E_h = E_0/A$. With such an assumption one can reach the following conclusions:

$N^A_{\text{em, max}}(E_0) = AN^h_{\text{em, max}}(E_h/E_c) \approx N_{\text{em, max}}(E_0)$ i.e. the fraction of energy transferred to the electromagnetic component at shower maximum, has only an indirect dependence on the primary mass via the dependence on primary energy.

$X^A_{\text{max}}(E_0) = X_{\text{max}}(E_0/A)$. This shows how the shower maximum has an inverse dependence on the mass of the primary i.e a shower initiated by heavier nuclei will develop higher in the atmosphere compared to one initiated by lighter nuclei.

$N^A_\mu(E_0) = A\left(\frac{E_0/A}{E_c}\right)^\alpha = A^{1-\alpha}\left(\frac{E_0}{E_c}\right)^\alpha$. This shows that heavier primaries will produce a larger number of muons compared to lighter primaries. For e.g. Iron showers on average contain 40% more muons than proton showers [154].

$D_{10} = D_{10}^{\text{had}}\left(1 - \frac{d\langle lnA \rangle}{d \log_{10} E}\right)$ Since Feynman scaling is known to be violated for higher energies, the hadronic elongation rate is always less than the electromagnetic rate. Thus, an

increase in elongation rate towards 85 g cm^{-2} is a direct indication of change of the mass composition.

Simulations have shown that the superposition model gives a more realistic description of many features of the shower [155]. However, it is still not a perfect description especially for heavier nuclei. Studies with photographic emulsion techniques have tried to create a better picture of the fragmentation of heavier nuclei [156]. This field is continuously evolving with better models and theoretical predictions being worked on based on the continually increasing database of observations.

Although these models help understand the principle, a full Monte Carlo simulation and a generalized analytical solution of the cascade equations is needed to fully recreate the EAS. Even after huge amount of efforts made a few discrepancies such as the muon puzzle which is the mismatch in the number of muons predicted by the simulations in comparison to the measurements remain [157].

3.1.3 LPM effect

Another process that can directly impact the development of highly energy electromagnetic showers is the Landau-Pomeranchuk-Migdal effect [158, 159]. The LPM effect is the reduction of the bremsstrahlung and the pair-production cross-section at high energies or densities. All the above models work under the assumption that the energy range is low enough for the LPM effect to not be applicable. If the medium is dense enough or at high energies the LPM effect also becomes important to fully estimate the development of an air shower. The implications of the LPM effect for air showers implemented in simulations can be found in [160].

3.1.4 Neutrino induced EAS

The development of a neutrino induced shower in comparison to a CR shower is important in the context of this study. Understanding the differences helps to identify the unique signature at a CR observatory like the Pierre Auger. The differences in the shower development can also help increase the sensitivity of a neutrino observatory like the IceCube. Unlike a cosmic ray particle a neutrino can interact at any depth. This is due to the low neutrino cross-section at 10^{18} eV $\approx 10^{-33}$cm^2 in comparison, for e.g. the proton-nucleon cross-section which is $\approx 10^{-27}$cm^2. The cross-section also has a slight energy dependence i.e. it increases with energy. Thus, neutrino-induced showers require significantly higher neutrino energies to increase the likeliness of interaction in the atmosphere and their subsequent detection. The ultra-high energy neutrino can undergo DIS with the atmospheric nucleon via CC or NC interaction as mentioned in the last chapter. Neutrino-induced showers involve fewer particles in the initial interaction which translates to difference in the shower development in comparison to CR induced air showers. The development of the shower and the unique signature depend on the flavor of the neutrino as shown in Fig. 3.3.

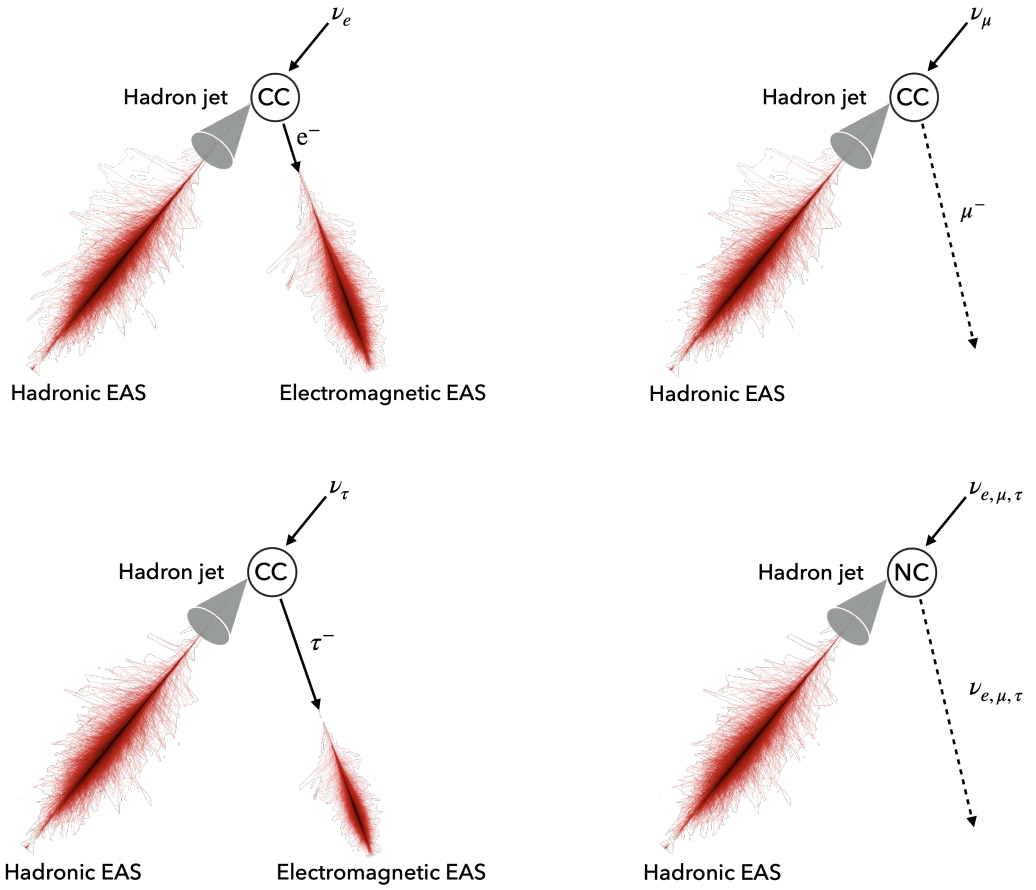

Figure 3.3: Sketch of different possible interactions of UHE neutrinos in the atmosphere.

An electron neutrino, ν_e, interacting via CC interaction produces an initial hadronic cascade which has fewer particles in comparison to a hadron-initiated shower from the CRs. The high energy electron/positron produced in the same initial interaction also produces an electromagnetic shower. At high energies the two showers are overlapped and the fraction of energy carried by the electron/positron governs the ratio of the electromagnetic to hadronic component for the shower.

A muon neutrino, ν_μ, also produces an initial hadron cascade but in contrast to the electron neutrino interaction the resulting muon has a very low probability to decay and mostly passes through the detector undetected. The energy carried by the muon which is usually a large fraction is invisible and only the hadronic cascade can be detected.

Tau neutrinos, ν_τ, have a unique and particularly interesting signature among neutrino showers. The initial interaction remains the same with the production of a hadronic cascade, but the resulting tau lepton has a decay length ≈ 10 km at 10 PeV. This means that depending on the atmospheric depth the tau encounters on its way to the ground, it can either decay and

potentially produce an electromagnetic cascade much later than the initial hadronic cascade or not decay at all. The asynchronous cascade signature is also known as "double-bang" effect and can occur both in air or a specific medium. Tau neutrinos can also be a source of upward-going air showers which can also be detected at an EAS detector. In this case the tau neutrinos can interact in the Earth's crust or in some natural obstruction like mountains around the detector leading to production of a hadronic cascade which gets absorbed and a tau lepton which can escape and produce an electromagnetic cascade in air that can be detected. The process is unique to tau neutrinos for an EAS detector since for a ν_e both the hadronic cascade and the electron is absorbed by the obstacle whereas for the muon neutrino the resulting muon is almost impossible to detect.

All three neutrino flavors can also undergo NC interactions. These also result in an initial hadronic cascade and a neutrino which usually does not interact and escapes being detected especially for an EAS detector. Thus, the signature is indistinguishable in comparison to a muon neutrino CC interaction. The probability of NC interaction is also lower than a CC interaction which also affects the overall number of EASs induced due to this channel.

3.2 Characteristics

Apart from the shower maximum and the number of muons at ground other observables are also required to fully characterize the shower and estimate the important quantities such as the mass, energy and the arrival direction of the incoming primary CR or UHEν. Fig. 3.4 gives an overall picture of the evolution of an EAS. The amount of atmosphere penetrated is measured in units of slant depth X, with a unit of g/cm^2. The first interaction depth, X_0, is the slant depth until the first interaction of the primary particle with the nucleon. The shower begins from this point on and the vector along which the shower develops from the first interaction point is called the *shower axis*. The development continues till the shower reaches a maximum which was defined earlier and is denoted by $X_{\max}$. After this point the shower depopulates which is caused by particle energy loss due to absorption or decay. The *longitudinal development profile* plotted in Fig. 3.4 gives a relation between the number of shower particle in dependence to the atmospheric depth. This relation is also called the Gaisser-Hillas function [161] parametrized as follows.

$$N(X) = N_{\max}\left(\frac{X - X_0}{X_{\max} - X_0}\right)^{\frac{X_{\max}-X_0}{\lambda}} \exp\left(\frac{X_{\max} - X_0}{\lambda}\right) \tag{3.2}$$

X_0 and λ can be estimated by fitting the profile based on the above function and depend on the composition and energy of the primary. $N_{\max}$ is the number of particles observed at $X_{\max}$. The integral of the longitudinal development profile gives an estimate of the total calorimetric energy deposited by the shower. The point where the shower axis vector intersects the ground is called the *shower core*. The shower axis is thus defined by the zenith angle θ, azimuth angle ϕ and the shower core position. If one looks at the shower head on, the large thin disc like appearance consisting of highly energetic particles is called the *shower front*. The shape

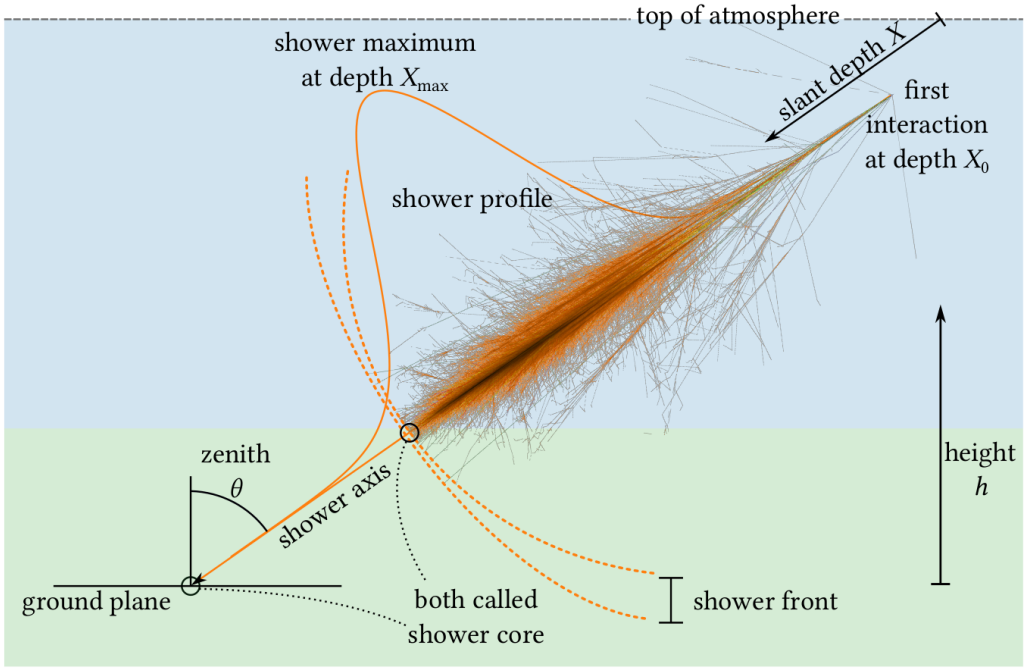

Figure 3.4: Schematic of the development of an EAS in the atmosphere. Taken from [162].

is due to the path length differences between the shower particles travelling away from the shower axis to the one travelling in the direction of the shower axis. The disc is thus thinner near the shower core and widens away from it. As the shower front intersects the ground, the density and the timing of the particles detected at the detector form what is called the *shower footprint*. It is the primary observable used by a ground level EAS detector to measure and characterize the shower. The arrival time of the particles in the footprint can help determine the shower geometry whereas the density can be used to reconstruct the energy of the primary. The density is estimated as a function of the radial distance from the shower core on the ground, by the lateral distribution function (LDF). The modern LDF function is an extension on the parameterization given by Greisen [163] and by Kamata and Nishimura [164] and is described as:

$$\rho_e(r) = \frac{N_e}{2\pi R_M^2} C(s) \left(\frac{r}{R_M}\right)^{(s-2)} \left(\frac{r}{R_M} + 1\right)^{(s-4.5)}, \tag{3.3}$$

with shower ages s and the Moliere radius $R_M = 0.0265\, X_0(Z + 1.2)$.

Another important characteristic of an EAS are its universality features first pointed out by Hillas for electromagnetic showers [165]. In this formulation the average development of an air shower is universal around the shower maximum. An individual shower can be defined by the shower age given as:

$$s = \frac{3}{1 + 2X_{max}/X} \tag{3.4}$$

This parameter is a result of the nature of the development of the cascade process which hides the initial primary dependent fluctuations [166]. Simulations have used such a universal feature to fit shower profiles reasonably well independent of the primary mass and energy [167]. Air shower universality only holds for air showers induced by gamma rays, electrons, or positrons and breaks down for a hadronic cascade. It can still be used if each individual component of the shower can be disentangled. Although, not applicable for this study, universality is an important characteristic of the shower and has been used in various CR [168] studies such as to estimation of the proton-air cross-section [169] and other CR studies.

3.3 Detection

At high energies, due to the low flux, EAS offer the best way to detect CRs. Ground based detectors can be spread over large areas offering a cost-effective way to study UHECRs. The particles arriving at ground can also be directly detected. Furthermore, the shower can be seen through different emissions such as the Cherenkov, fluorescence and radio. The different emissions which can be detected in context of EAS are described in this section along with an expected EAS signatures of a neutrino induced EAS which relates to the analysis presented in this thesis.

3.3.1 Fluorescence Detection

Atmospheric fluorescence, observable in air showers above 10^{17} eV, involves the emission of faint optical and ultraviolet (UV) light when high-energy particles from extensive air showers interact with nitrogen molecules in Earth's atmosphere. These interactions excite the nitrogen molecules, which emit UV light during de-excitation, primarily in the near-ultraviolet range. The number of photons emitted is directly proportional to the energy deposited by the shower particles, allowing researchers to estimate the primary particle's energy. At altitudes between 5 km and 10 km, the photon yield varies with height, typically producing 4–5 photons per meter per charged particle, and these photons can be detected from distances up to 35 km.

Fluorescence telescopes measure this light intensity, enabling reconstruction of the shower's longitudinal profile and energy. However, their operational duty cycle is limited as they require clear, moonless nights. Accurate reconstruction also depends on constant atmospheric monitoring to adjust for variations in light yield. Early experiments, such as those at Volcano Ranch [170] and the Fly's Eye experiment [171, 172], pioneered this detection technique. Today, it remains a crucial method used by observatories like the Pierre Auger Observatory and TA.

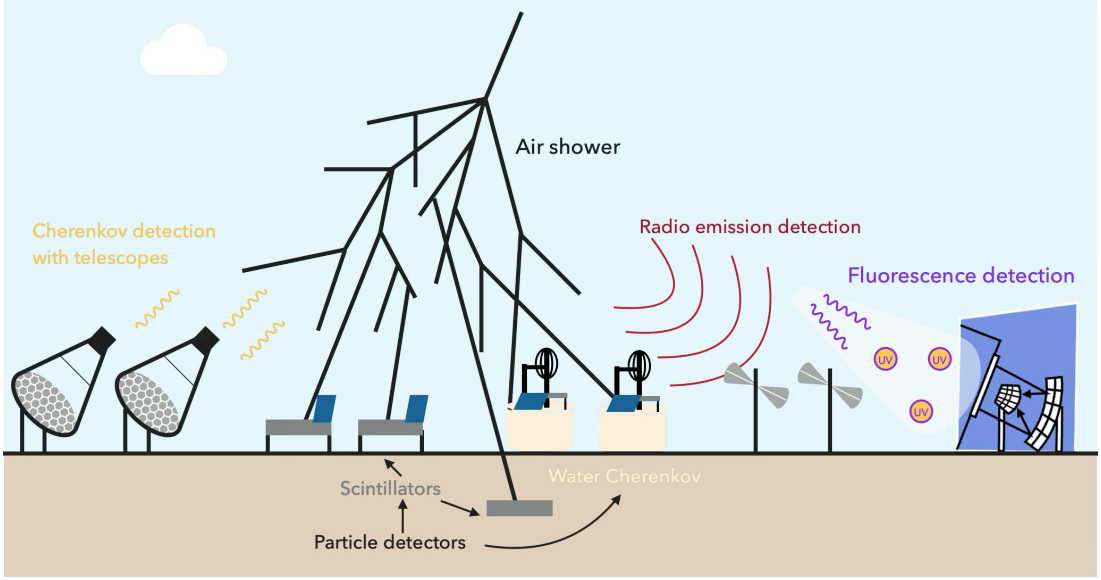

Figure 3.5: Sketch of various ways to study experimentally extensive air showers. Inspired from [177].

3.3.2 Cherenkov Detection

Charged particles moving through the atmosphere can also produce Cherenkov light [173]. The EAS can be either detected via Imaging Cherenkov telescopes (IACTs) which can detect showers between 20 GeV -100 TeV or non-imaging Cherenkov detectors can be set up akin to a ground based particle detector array. Both techniques are used for both gamma-ray astronomy and CR studies. Since the Cherenkov cone is collimated around the shower axis the detectors need to be installed with small spacing between them. For e.g. a particle at 10 km height produces a Cherenkov cone with a radius of 120 m. This property and the similar operational limitations akin to the fluorescence detection for the IACTs makes this technique impractical to detect UHECRs. The currently operational experiments using the non-imaging Cherenkov technique for EAS detection include Yakutsk [174] and Tunka [175] etc. IACTs are very popular for gamma-ray astronomy and multimessenger detections with H.E.S.S. [73], MAGIC [176] and CTA [75] currently operational.

3.3.3 Radio Detection

When an EAS travels through the atmosphere, it generates radio emissions primarily due to two mechanisms: the geomagnetic effect and the Askaryan effect. In air showers, the geomagnetic emission dominates, contributing around 85-90% of the total signal, while the Askaryan effect accounts for the remaining 10-15% [125, 178, 179]. The geomagnetic effect occurs when electrons and positrons in the shower are deflected by Earth's magnetic field, creating a dynamic current that moves at nearly the speed of light. This process generates a

forward-focused radio signal with a lateral distribution described by the NKG relation.

The strength and characteristics of the radio signal depend on the geomagnetic field's orientation and atmospheric conditions at the detector site. At distances around 100 meters from the shower core, the detected frequencies are in the MHz range [180], while near the core, they extend into the GHz range. For primary energies above 10^{17} eV, the emissions from both mechanisms overlap, with the measured electric field scaling directly with the shower's primary energy. This radio detection approach offers a valuable alternative to fluorescence and Cherenkov methods, free from the operational limitations of a restricted duty cycle.

Several radio antenna arrays are currently used for EAS detection, including LOFAR [181] and AERA [182]. The Pierre Auger Observatory is enhancing its capabilities by installing radio antennas on each unit of its particle detector array, expected to become fully operational by end of 2024. Future experiments, such as GRAND [183] and IceCube-Gen-2 [130], aim to expand this field further. Additionally, observatories like RNO-G [129] are also using this technique for neutrino detection.

3.3.4 Particle detector arrays

This is one of the oldest detection techniques used to measure and study CRs. It consists of setting up a set of particle detectors (stations) spaced by large distances, depending on the desired energy range sensitivity of the experiment which is also dependent on the altitude of the experiment. The detectors are usually arranged in a regular pattern, and they are able to detect the secondary particles of EAS at ground by searching for time coincidences between neighbouring stations. By measuring the signal and time delay between the triggered stations the incoming direction of the primary can be estimated to $0.5^\circ - 1^\circ$ of zenith angle resolution. The core position can also be determined by using the lateral distribution function (eq. 3.3) to fit the recorded signal at the surface detector array. The energy can also be estimated through the measurement of number of muons at ground or cross calibration with other detector systems. Different types of detection methods have been used to combine and act as particle detector arrays. These include Geiger counters at Harwell [184], hodoscopes at Kiel [185], scintillators at Volcano ranch [186] and water or ice based Cherenkov detectors. Currently, scintillator based surface detector arrays and water or ice based Cherenkov tanks are the popularly used EAS detection techniques.

Water/ice based Cherenkov tanks/detectors can also detect the secondary particles of EAS at ground. These are sensitive to the Cherenkov light which is produced by the charged particles while travelling through the medium of the detector. The subsequent light is measured using a photomultiplier tube (PMT). This light signature is different depending on the type of the particle and thus can effectively help in differentiating between muons and electrons. The Pierre Auger Observatory uses an array of water Cherenkov tanks in conjunction with five fluorescence detectors for EAS measurements. IceCube also contains an array of ice based Cherenkov detectors which are used for cosmic ray studies and as a veto for their underground neutrino detectors. More details about the Pierre Auger Observatory are presented in the next chapter 4

Scintillator based particle detector arrays can be used to distinguish between the different secondary particles of an EAS. These consist of scintillating material which produces detectable photons if a charged particle traverses through the material. If deployed at the surface, such detectors can act as discriminators for electron and muons whereas if deployed underground they can only detect muons. The size of the scintillating material controls the zenith angle sensitivity which typically decreases as the inclination of the shower increases. TA uses a vast array of scintillator based detectors along with three fluorescence detectors to measure EAS. The Pierre Auger Observatory is also testing an array of underground muon detectors which are situated directly below its surface array stations.

3.3.5 Towards detecting Neutrino Induced Extensive Air Showers

Neutrino induced EASs can be differentiated from a regular CR induced EASs by their unique signature. Since neutrinos can interact at any atmospheric depth only the EASs that were initiated very deep in the atmosphere can be differentiated from a CR induced shower which typically starts at the top of the atmosphere. The deeper interaction means less shower development till the shower front reaches the ground in comparison to a CR induced EAS. This difference in development can be measured by the muon to electron ratio at ground via a particle detector array. Since, the neutrinos are only expected to interact and induce an EAS if the volume of the atmosphere through which they traverse is large enough. For zenith angles less than 60° either the neutrinos are not expected to interact till they reach the ground and even if they do, due to the general amount of atmospheric volume at these angles the CR induced EASs are supposed to be indistinguishable from a neutrino shower, at least for a particle detector array at ground. This is due to the fact that the CR induced EASs have not developed enough to significantly reduce or lose their electromagnetic component. This leaves the primary distinguishing factor i.e. the muon to electron ratio the same for neutrino and CR induced EASs. The terminology used to determine the development of the shower in the atmosphere is the shower age and typically showers having a larger muonic component at ground are called *old showers* while showers having a larger electromagnetic component at ground are called *young showers*.

Thus, to detect a neutrino induced EAS using surface detector arrays the smoking gun signal is an inclined ($\approx$ zenith angle $> 60^{\circ}$) "young" shower. A perfect neutrino air shower detector should have a good angular resolution and a large electron-muon signal separation. However, these signatures are not completely background free. Such a signature can also be caused by deeply interacting CR primaries or highly energetic muons emitting bremsstrahlung photons both of which can also induce a young shower at large zenith angles. B meson could also be misidentified as a neutrino as shown in [187]. Other processes such as low energy showers coincident with an EAS could also act as background for a neutrino detection. These have been studied in detail in [23] and are negated in the analysis through the techniques developed in the reference.

CHAPTER 4

The Pierre Auger Observatory

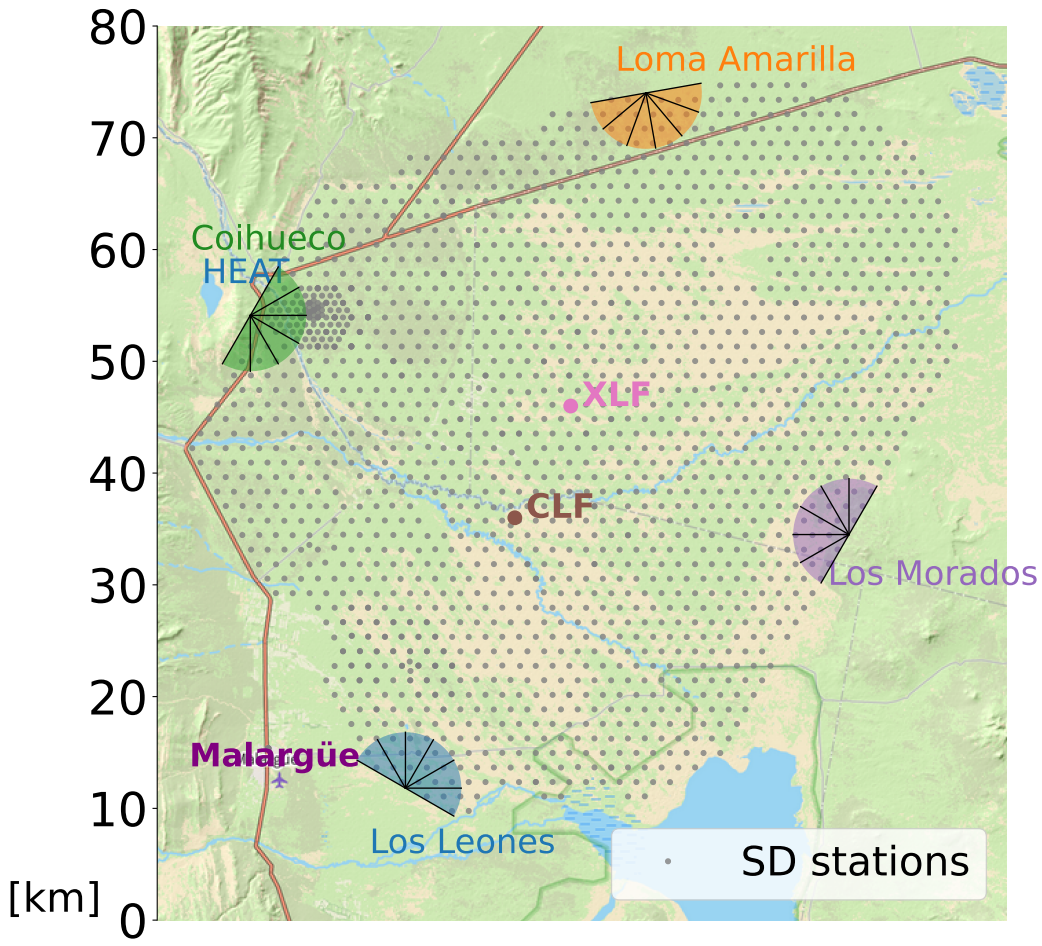

Figure 4.1: Layout of the Pierre Auger Observatory in Argentina. The black lines indicate the field of view of each telescope. Redone from [188].

The Pierre Auger Observatory [8] is the largest CR observatory in the world. Located outside Malargüe in the Argentinian *pampas*, the observatory spans across an area of 3000 km^2. Originally conceptualized in the 1990s, it was built in the early 2000s and fully completed in 2008. Geographically the site is located near the base of the Andes at an altitude of 1400 m above sea level and is relatively flat across its whole span. The observatory was designed to detect CR-induced EASs having primary energy of 10^{17}eV to 10^{20}eV and beyond. It does so by identifying the EAS via two different complementary detecting components: *Surface Detector* array (SD) and the *Fluorescence Detector* (FD). A schematic of the observatory is shown in Fig. 4.1. The SD consists of 1660 water Cherenkov tanks spread in a triangular grid with 1.5 km spacing. The FD consists of four sites with 27 telescopes located at the edges of the ground array and overlooking the sky above. The observatory also consists of various atmospheric monitoring devices such as LIDARs [189], laser facilities [190, 191] and other weather sensors to constantly monitor the atmosphere which is important for FD operation. With the AugerPrime upgrade of the observatory which is scheduled to be finished in 2024 two new detecting components are being added: The *Radio Detector* (RD) [192] and the *Underground Muon Detector* (UMD) [193]. The tanks are also being upgraded with the addition of a scintillator on top [194]. The individual components of the new upgrade are not discussed in detail since they are not used in the context of this thesis but only AugerPrime as a whole and its potential for detecting neutrinos at the Pierre Auger Observatory is discussed later.

Even though, the primary objective of the Pierre Auger Observatory is UHECR physics it is also sensitive to the neutrino induced EAS signature via both the SD and FD. The low neutrino interaction probability requires a detector that is always active. The high duty cycle of the SD $\simeq$ 100% compared to a limited duty cycle of the FD $\simeq$ 15% makes SD the more probable of the detector to detect neutrinos. This has already been shown in previous neutrino searches at Auger where the search with the SD provides the most stringent limits to the diffuse flux of ultra-high-energy neutrinos [18]. This chapter aims to provide a short review of the different components of the observatory with a focus on the SD and its trigger system since it is the primary detector used for the analysis presented in this thesis.

4.1 Fluorescence Detector

The Fluorescence Detector system at the Pierre Auger Observatory consists of an array of Fluorescence telescopes that are constantly looking inwards over the surface detector array trying to measure the nitrogen fluorescence induced by the EAS. The FD consists of 24 telescopes located at four different small hills (Coihueco, Los Morados, Loma Amarilla and Los Leones). The Coihueco site also consists of High Elevation Auger Telescope (HEAT) which can be tilted upwards to extend the field of view at the Coiheuco site. Each of the 24 telescopes has a field of view of $30^\circ \times 30^\circ$ in azimuth and elevation. The combination of the telescopes gives an azimuth coverage of 180°. The HEAT telescopes can extend the field of view by a further 30° in elevation. This gives a 100% triggering efficiency for EAS above

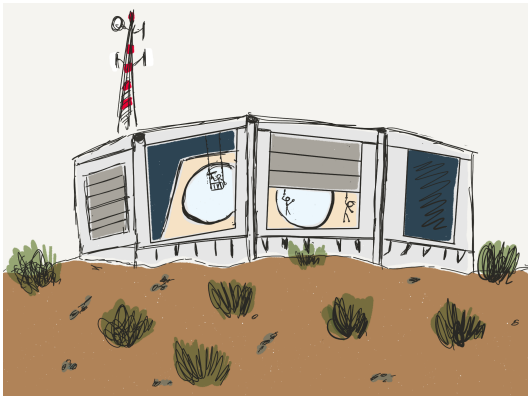

(a) An artistic drawing inspired by the FD building at Los Leones.

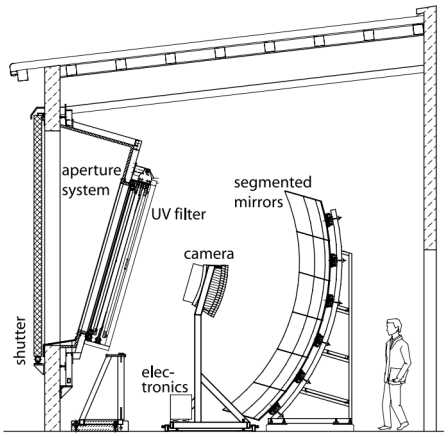

(b) Schematic view of a fluorescence telescope with a description of its main components. Taken from [8].

Figure 4.2: Fluorescence Telescope at Pierre Auger Observatory

10^{19}eV for FD and above 10^{17}eV with the inclusion of HEAT. Currently, the FD is always operated in combination with SD. As mentioned before the measured fluorescence light gives the deposited shower energy which is about 90% of the total. The remaining 10% which is carried by non-fluorescence producing particles such as neutrinos and muons is corrected with simulations [195]. The expected fluorescence yield (combined for all wavelengths) is affected by the temperature, pressure and humidity of air [196]. This is constantly monitored at the observatory via several monitoring instruments. Each FD site is equipped with a LIDAR station which continuously monitors the aerosol profile, cloud and sky cameras which photograph the sky to estimate the cloud coverage and wind and rain sensors for the safe functioning of the FD telescopes. Two laser facilities Central Laser Facility (CLF) and eXtreme Laser Facility (XLF) have also been functional since 2003 and 2008 respectively. These help provide hourly measurements of the atmospheric aerosol content and can also be used to measure FD performance.

Fig. 4.2 shows an FD site along with the schematic of an FD telescope. The fluorescence light enters through the UV filtered window which is surrounded by a corrector ring. A spherical segmented mirror is used to gather the incoming light and focus it onto a 440 pixeled PMT camera. The camera records the light pulses every 100ns and based on a hierarchical trigger [195] saves the event. For reconstructing the energy and the geometry of the shower the recorded information is combined with the information detected by the SD (hybrid) or other FD telescopes (stereo) [197]. A relative calibration of the PMTs is performed for each camera before and after each night of data taking [195]. A regular absolute calibration procedure called the X-Y scanner has also been developed and is currently being deployed at each FD telescope.

The FD acts as an important calibration tool for the SD, especially for the energy estimation where the hybrid detection of EAS is used to provide a simulation free primary energy estimate for the SD. It can also be useful for looking into high energy atmospheric phenomena such as ELVES [198]. The low duty cycle of the FD which is due to its operation being limited to clear moonless nights, limits its overall capabilities, especially for a neutrino analysis. However, the FD has been used for up-going neutrino searches (publication under review) and also has a potential use to look for atmosphere skimming CRs or neutrinos.

4.2 Surface Detector

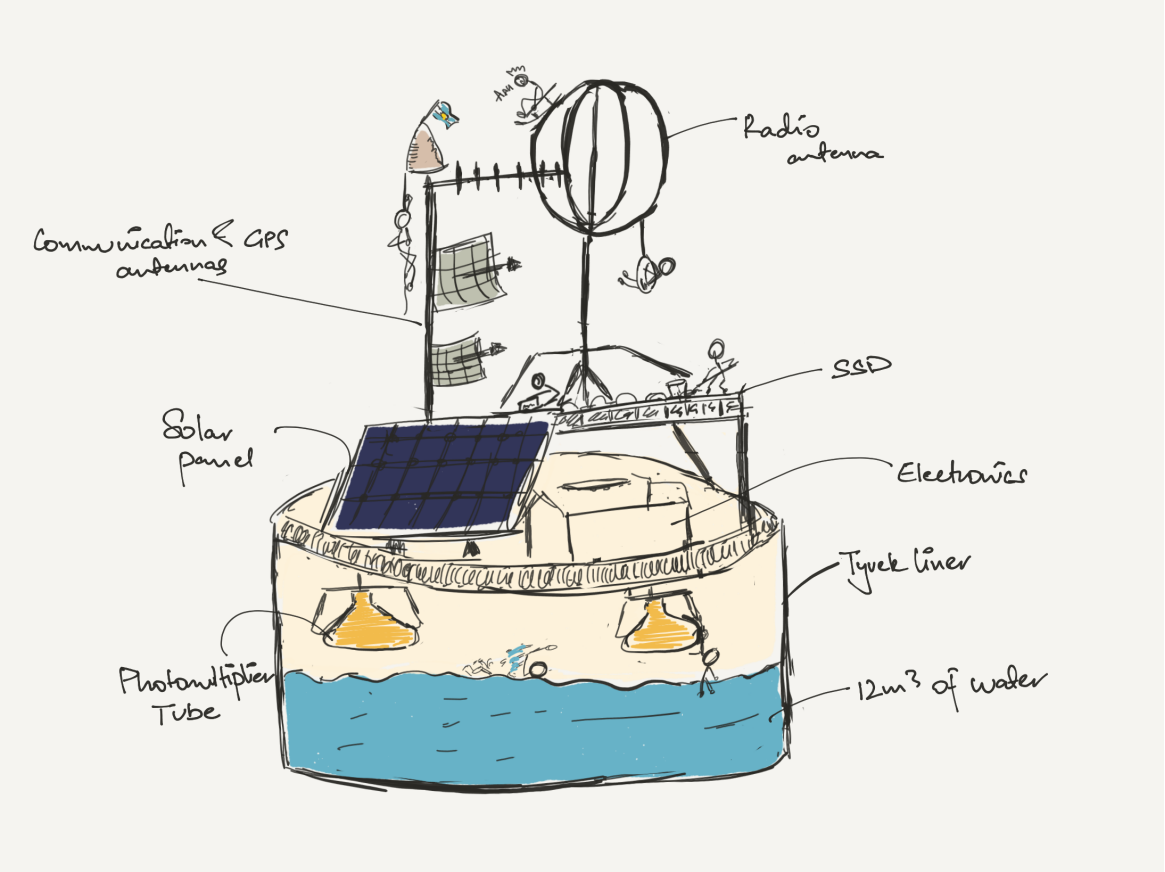

Figure 4.3: Artistic representation of a Surface Detector tank with all its components with the AugerPrime upgrade. The third PMT and the small PMT are not visible in the drawing. The water level is usually touching the PMTs.

The SD baseline design consisted of a Water Cherenkov Detector (WCD) array which is used to detect the EAS on the ground by detecting the shower particles that reach the ground. Each WCD comprises a tank with 3.6 m diameter and 1.2 m height [199]. It also consists

of a reflective inner liner containing 12,000 litres of ultrapure water. Three 9-in PMTs look into the water and detect the Cherenkov light produced by the charged shower particles as they traverse through the water. With the AugerPrime upgrade the WCDs have also been equipped with a scintillator, additional PMT and a radio antenna on top. These are described later in section 4.3. Each WCD tank also has its own electronics and communication system. All the components are powered using a solar panel. An artistic representation along with all the components is shown in Fig. 4.3.

The 1.5 km grid spacing is commonly referred to as SD-1500. There are further sub-arrays within the SD, SD-750 also called the infill and SD-433 with the numbers representing the distance between the tanks in the sub-arrays in meters. Each WCD can be operated on its own with each PMT signal first recorded at the station and then combined using a Central Data Acquisition System (CDAS) [8] which uses a ranked system of triggers to decide if the combination of all WCDs is a candidate for an EAS event. The data taking process of the SD is described in more detail in the following sections. Due to its autonomous nature, the SD array is easy to maintain and has a duty cycle $\simeq$100%. The array is only affected if there is a communication outage or if the solar panel cannot generate power for an extended time period both of which are rare at the site of the Pierre Auger Observatory. For this study whenever the SD is mentioned it refers to the SD-1500 array with only the WCD component unless specified otherwise.

4.2.1 Calibration of SD

The PMT signals in the WCDs are digitized by a 40 MHz 10 bit *flash analog-to-digital converters* (FADCs) [200]. One of the signals is taken from the anode of the PMT and is called the *low gain* channel and the other is taken by the last dynode and is amplified by a factor of 32 and is called the *high gain* channel. The two signals provide sufficient precision and range to record both the signals produced near the shower core ($\sim$1000 particles/µs) and those produced far from the core ($\sim$1 particles/µs). The signal trace is recorded at a sampling rate of 40 MHz with a total of 768 bins leading to each bin width corresponding to 25 ns. Due to varying PMT gains across the WCDs a robust procedure is needed to calibrate each station to a universal unit of measurement for the SD. Also, due to the remoteness of the WCDs such a procedure needs to be performed locally for each station to allow for its functioning even in the case of individual broken PMTs. The unit of measurement used to calibrate the SD stations is called *vertical equivalent muon* (VEM). This is the charge deposited by a vertically central through-going (VCT) muon in the WCD station. The SD station by itself cannot select these particular muons but the normal SD measurement of all atmospheric muons has been studied in comparison with a muon telescope that only triggers these VCTs for a reference tank [201]. This measurement is used to calibrate the SD.

To perform the calibration charge distribution, $Q^{\text{peak}}_{\text{VEM}}$, and the pulse height, $I^{\text{peak}}_{\text{VEM}}$, both for the individual PMTs and their sums, are compared to the measurements done with a muon telescope as shown in Fig. 4.4. The first peak in the figure for the PMT measurement is caused due to low energy particles while the second peak is produced by the atmospheric muons.

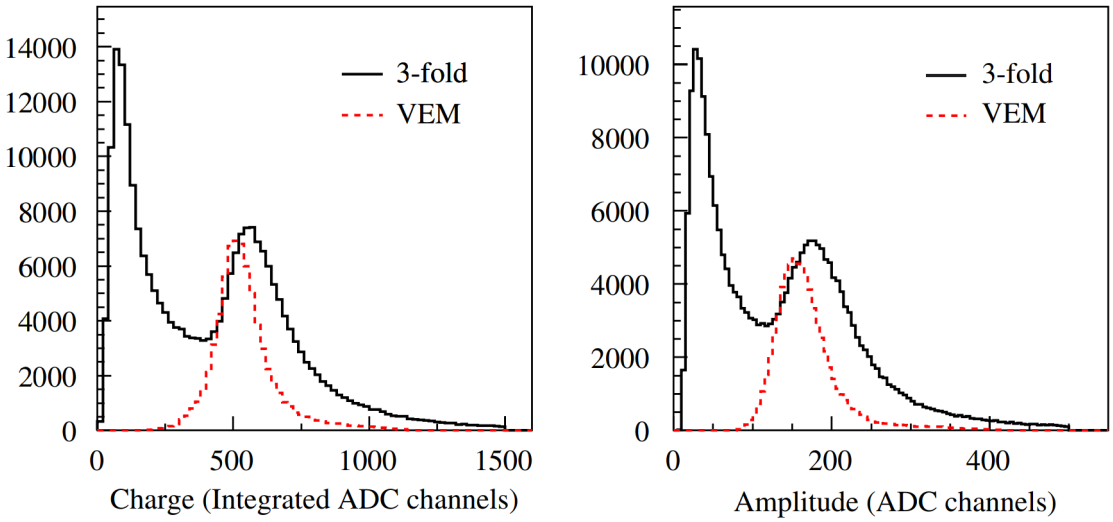

Figure 4.4: Left:The charge histogram (black), is the sum of the responses of all three PMTs above the electronic noise threshold, while the dashed red line represents the reference measurement done by an external muon telescope. The first peak in the charge histogram is noise from low-energy particles. The second peak is caused by the vertical-through going muons and is used to determine VEM. Right: The pulse height histogram (black) that is used to calibrate $I_{\mathrm{VEM}}^{\mathrm{peak}}$ which is used for trigger thresholds. The calibration is again performed using the reference measurements from the muon telescope. Taken from [200].

This peak corresponds to $Q_{\mathrm{VEM}}^{\mathrm{peak}} \simeq 1.03$ VEM for the sum and $\simeq$1.09 VEM for each PMT. The shift in comparison to the muon telescope measurement is caused by the convolution of photo-electron statistics on an asymmetric peak in the track length distribution and local light collection effects. Furthermore, the black histogram is integrated across all zenith angles with $< \theta > \sim 20^{\circ}$. This peak is used to obtain a conversion for the integrated signal of the PMT to VEM units. In addition to this, since the subsequent trigger for the SD also requires a measure of the current I_{VEM}, this value also needs to be converted and calibrated to VEM units [200]. The same technique as the charge calibration is employed since the VCTs also produce a peak in the pulse height histograms. The calibration is performed every 60 s and sent to CDAS thus for an incoming event, calibration data is available for the preceding minute ensuring high calibration accuracy.

4.2.2 SD Trigger system

A schematic of the logic of the trigger system is shown in Fig. 4.5. There are three types of different types of station level triggers scalar, calibration and shower trigger. The scalar trigger records signals for very low thresholds and is useful for supplementary physics such as space weather [202]. The calibration trigger, as explained in the previous section, helps store

and calculate the calibration parameters. The main shower trigger, used to record the EAS events is a hierarchical system consisting of two local triggers (T1 and T2) implemented at the station level, a third level trigger (T3) implemented by CDAS and further event selection triggers (T4 and T5) stored by the SD but only used depending on the analysis and the quality of data required by the said analysis. The hierarchical nature arises from the limits on the wireless communication network required for a vast autonomous array. The T3 trigger aims to reduce the rate especially for the expected muonic background and at the same time maximising the EAS event detection.

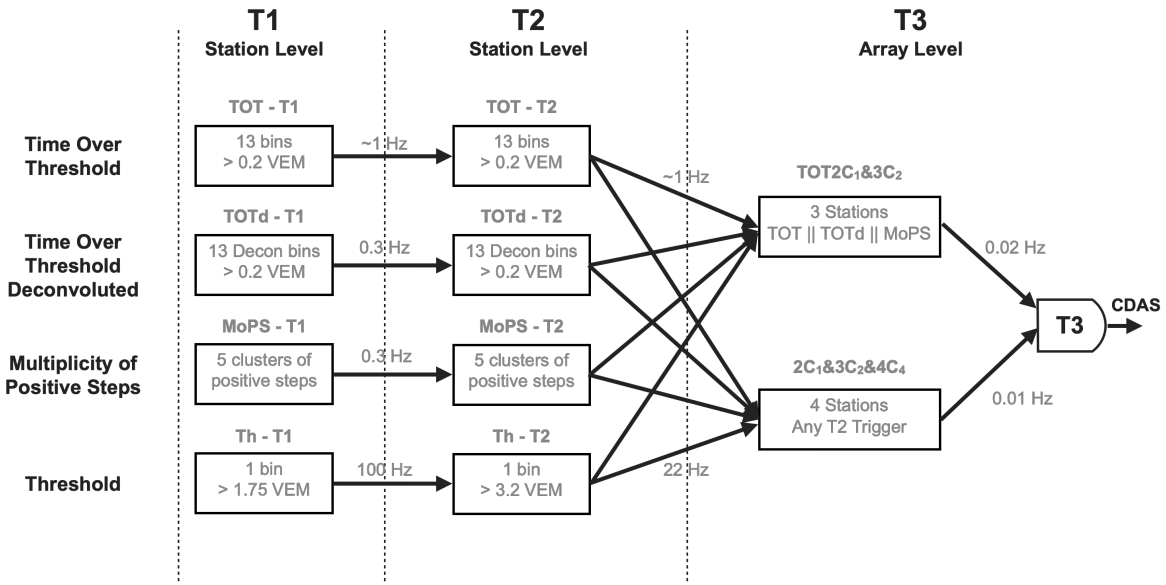

Figure 4.5: Schematics of the hierarchy of the trigger system of the Surface Detector array.

Old triggers

The T1 trigger consists of two parts/modes both of which need to be satisfied for an event to be checked for the possibility of higher level triggers. One of them is a basic threshold trigger (TH) that requires the signal for each of the three PMTs to be above $1.75I_{\mathrm{VEM}}^{\mathrm{peak}}$. If there are only one or two PMTs active then the requirement changes to $>2.8I_{\mathrm{VEM}}^{\mathrm{peak}}$ or $>2I_{\mathrm{VEM}}^{\mathrm{peak}}$ respectively. The TH mode is used to select large signals which are expected for very inclined CR induced showers ($\theta > 60^{\circ}$) which are predominantly muons. It reduces the rate for the atmospheric muons from 3 KHz to a 100 Hz. The second mode for the T1 trigger is called time-over-threshold (ToT). ToT requires 13 or more of the 25 ns time bins within a 3 μs window to be above a threshold of $0.2I_{\mathrm{VEM}}^{\mathrm{peak}}$ for at least two PMTs. Since this mode filters for signals spread in time it is sensitive to low energy vertical showers nearer to the core and also high energy inclined showers far from the shower core. It is also very effective in filtering random muonic background which typically has a spread of 150 ns compared to the

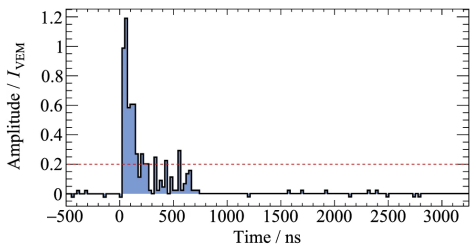

(a) Example waveform which passes the ToTd algorithm.

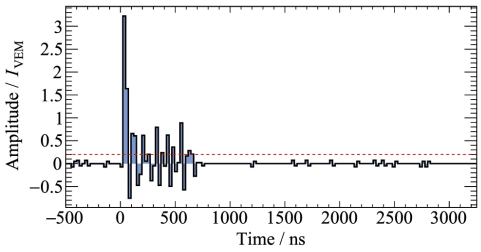

(b) The deconvolution of the initial ToTd waveform along with the required threshold in red dashed line

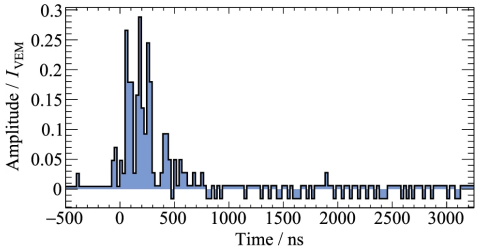

(c) Example waveform which passes the MoPS algorithm.

Figure 4.6: Functioning of ToTd trigger and an example of MoPS. Taken from [204].

325 ns spread for ToT fulfilment. The rate for ToT at each detector is ∼1.2 KHz with the main contribution being two consecutive muons arriving within the time window.

New triggers

In June 2013, two additional T1 trigger modes were implemented at the Pierre Auger Observatory to reduce the influence of atmospheric background muons and reduce the energy threshold of the array. The two modes both of which build upon the ToT condition are time-over-threshold-deconvolved (ToTd) and multiplicity-of-positive-steps (MoPS).

The ToTd trigger was first proposed internally in [203]. The trigger aims to deconvolve the FADC trace, suppressing the exponential tail of the diffusely reflected Cherenkov emission before applying the ToT condition. This helps in compressing the signal from a muon which typically has a fast rise time in one or two time bins before the application of the ToT condition. The trigger has an expected rate of 0.2 Hz-3 Hz. ToTd also requires the integrated signal to be above 0.5 VEM. An example of the functioning of the trigger is shown in Fig. 4.6.

The MoPS trigger [205] was implemented to achieve a similar goal as ToT and ToTd i.e. a better separation between the air shower signal from the mostly muonic background. It is designed to do so by counting the number of positive steps (cumulation of successive increases) in the flash analog-to-digital converter (FADC) trace within a 3 μs sliding window.

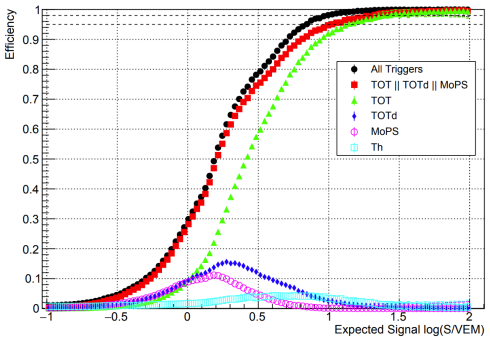

(a) Contribution to the different triggers to the efficiency as a function of the mean expected signal. Respectively green, blue, pink and cyan for ToT, ToTd, MoPS and TH.

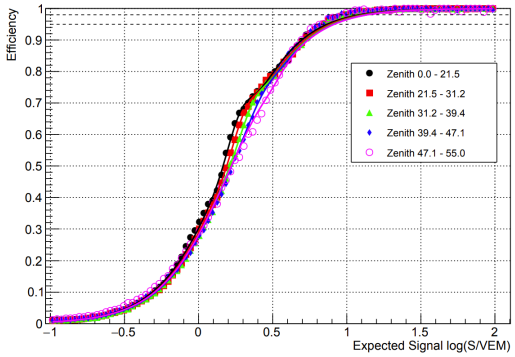

(b) The change in the triggering efficiency with zenith angle.

Figure 4.7: Trigger efficiency for different triggers implemented at the Pierre Auger Observatory calculated using the SD-750 array for zenith angles below 60°. Taken from [206].

These steps are expected to be above a certain threshold (5xRMS noise) and below a maximum value (~0.5 VEM). The MoPS trigger is satisfied if more than 4 positive steps are counted during the sliding window in at least 2 PMTs. The expected rates both from simulations and data taking are found to be <2 Hz. MoPS is even better at recovering lower signals compared to ToT and ToTd, thus improving the overall trigger efficiency. Both ToTd and MoPS are implemented as an OR logic with the ToT condition. An example of a signal that passes the MoPS trigger is shown in Fig. 4.6(c).

The trigger efficiencies for the different T1s implemented at the Pierre Auger Observatory along with the zenith dependence are shown in Fig. 4.7. The results are taken from a study [206] performed over three years using a special doublet hexagon which consisted of two hexagons of SD stations next to each other, one with new triggers active and one with new triggers inactive. Due to the small size of the hexagon the study was only performed for zenith angles less than 60°. However, the overall trend i.e. increase in efficiency holds for higher zenith angles. This is validated in sec. 5.4 where an overall increase in events is seen when new triggers are included in the neutrino analysis.

The new triggers particularly improve the trigger efficiency and sensitivity for photon and neutrino induced EAS. By rejecting the signals caused by muons or other low energetic particles the new triggers are expected to increase the low energy threshold for the detection of these particles. They also help in recording more low electromagnetic like signals which is the expected signature for photons and neutrinos.

Array Level Triggers

T2 level triggers aim to apply higher constraints to T1 triggers. A T1-ToT trigger is automatically updated to a T2-ToT trigger while a T1-TH trigger requires the signal to pass a higher

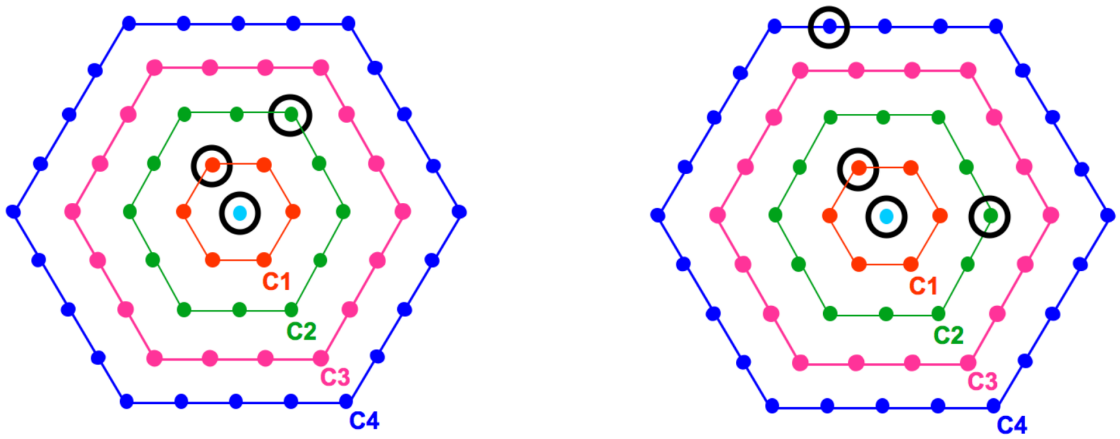

(a) ToT2C$_1$& 3C$_2$ **(b)** 2C$_1$&3C$_2$&4C$_4$

Figure 4.8: Example of two possible T3 configurations. Taken from [207].

threshold condition of $>3.2 I^{\text{peak}}_{\text{VEM}}$ for three coincident PMTs to get upgraded to T2-TH. For two (one) working PMTs the threshold is stricter at >3.8 $(4.5) I^{\text{peak}}_{\text{VEM}}$. After the T2 level, the expected station rate of events drops to ~23 Hz. The T2 level triggers from all stations are sent to the CDAS to form a global trigger.

The T3 level aims to build a condition based on both spatial and temporal combinations of stations that have passed the T2 condition. It again has two modes with only one needed to be satisfied to form a successful T3. Both of these conditions use a unit of detector called the crown, C_n. The crown as shown in Fig. 4.8 is a set of concentric hexagons centred around each station with n giving the order of the surrounding hexagons, 1 being the nearest. The first mode $ToT2C_1\&3C_2$ (4.8(a)) requires three SD stations which have passed T2-ToT criteria. It further requires at least one station to be located in the first crown denoted by $2C_1$ and the last to be located in the second crown ($3C_2$). The trigger is efficient in selecting compact vertical showers ($\theta < 60^\circ$) and selects about 90% of the physical events at the array. The second mode $2C_1\&3C_2\&4C_4$ (4.8(b)) is less restrictive and aims to select showers with moderate compactness. It requires a 4-fold coincidence of stations having any type of T2s (T2-ToT or T2-TH). The first two neighbouring stations must be again located in the first and second crown, but the last station can be as far as the fourth crown. This mode is more efficient in selecting inclined showers which typically being rich in muons have a sparse detector triggering pattern. Along with the spatial requirements both of the modes also require each of the T2 triggers in the stations to be within (3+5C$_n$) µs of the first one. Once either of the modes is satisfied all the FADC signals from the detectors passing T2 as well as signals from the detectors only passing T1 which are within 30 µs of the T3 are stored by CDAS as a part of the event. This process is described in more detail in [8]. With the present trigger setup, the observatory records about 3 million SD events per year [8].

The next two triggers T4 and T5 are used to improve the data quality. Unlike T1-T3 these

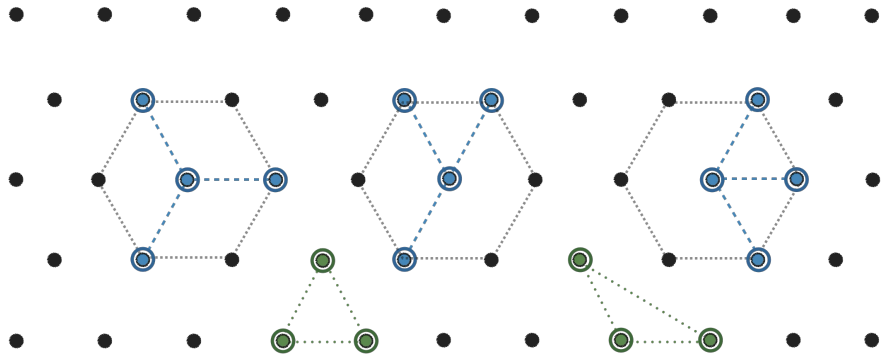

Figure 4.9: Different possible minimal T4 configurations. In blue are the three possible minimal $4C_1$ configurations while in green are the two possible minimal 3ToT configurations.

are implemented offline. Both check for the geometry and the timing compatibility to select showers in the T3 events. The T4 trigger uses either of the two different criteria to select showers. The first is the requirement of a 3-ToT compact configuration i.e. three nearby stations satisfying the T2-ToT condition in triangular patterns shown in green in Fig. 4.9. The second criterion, 4C1 requires the main triggered station to have at least three triggered tanks out of its six first neighbours as shown in blue in Fig. 4.9. Both the criteria work in collaboration with each other, 3ToT configuration has a selection efficiency of ~99% for showers below 60° and the 4C1 configuration helps to recover the rest ~1% showers lost below 60° and also selects low energy events above 60°. This trigger is not used for the neutrino analysis.

The T5 fiducial triggers help improve the quality of the showers selected, especially for an accurate energy and angular reconstruction. The trigger ensures the selection of showers that are well contained in the detector array to avoid miss-reconstruction of the core. There are two severity levels for the triggers called 6T5 and 5T5 as shown in Fig. 4.10. The former requires all six stations in the first crown around the station with the highest signal to be functional while the latter only requires five. The 6T5 condition helps negate the showers that might fall at any hole in the detector array. These holes can be due to natural obstacles or non-functional tanks. Since 6T5 also improves the angular resolution and improves the overall quality of the selected showers this criterion is used in the search for neutrinos, especially for angles below 75°. Above 75° since most of the events expected are elongated along a single line the fulfilment of the T5 criteria is very difficult, thus this trigger is not used.

4.3 AugerPrime

AugerPrime [63] also called Auger Phase 2, is the ongoing upgrade of the Pierre Auger Observatory to improve its sensitivity and detection capabilities. The upgrade aims to both improve the already present detector systems and also plans to add new components to the

observatory. One of the key aims of the *AugerPrime* upgrade is to improve the estimation of the primary CR mass measured by the SD. This is done by the installation of plastic scintillators, *Surface Scintillator Detectors* (SSDs) [194] on top of the WCD tanks. The differing responses of WCDs and the SSDs to the electromagnetic and muonic components help enhance the overall mass sensitivity of the detector for vertical showers. The upgrade also replaces the SD electronics (*unified board* and SD front-end board) with the *upgraded unified board* (UUB) [208] and adds a *small* PMT (sPMT) [209] to the WCD. The UUBs allow for better station level processing power to account for the SSD and also add a faster sampling rate and better timing accuracy for the SD. The sPMT helps increase the dynamic range of the WCD by reducing the saturated signals in the stations closest to the shower axis. The *AugerPrime* upgrade also includes the deployment of plastic scintillators underground in the vicinity of the WCD tanks, the UMD [193] as an extension of AMIGA [210] across the SD-750 and SD-433 sub arrays. The UMD is sensitive to the penetrating muon component of the EAS is very useful for extending the lower energy detection range of the observatory and can also help in photon searches [211]. Deployment of radio antennas on top of each WCD to form *Radio Detector* [192] is also a part of *AugerPrime*. This will allow for the measurement of the radio component of the EAS which originates primarily from the electromagnetic component. Such a measurement especially at very inclined zenith angles will allow for an improved mass estimation even for higher zenith angles where the SSD is insensitive. Additionally, increasing the duty cycle of the FD by operating the telescopes during higher night sky brightness periods with reduced PMT gain is also a part of the upgrade.

In the context of this thesis, the data from the ongoing upgrade and the preceding test array were not used. However, it is important to mention that the higher sampling rate available with the UUBs and the addition of RD could offer a way to improve the current neutrino analysis. The higher sampling rate could help in reducing the effect of the background muons especially at lower zenith angles ($\sim 60^{\circ}$) whereas the RD in conjunction with WCD could help improve the neutrino detection efficiency for higher zenith angles ($\gtrsim 75^{\circ}$) by improving the T3 efficiency. Also, a general increase in the statistics and continued data taking till the 2030s will help enhance the limits in case of non-detection of cosmogenic neutrinos which have further important implications for the CR spectrum especially for the cutoff as discussed before. The upgrade will also help improve the multi-messenger astronomy capabilities of the observatory.

4.4 The Offline Framework

The Offline framework [212, 213] is the C++ based software developed internally by the Pierre Auger Observatory to reconstruct air showers and perform cosmic ray analysis. It can process and reconstruct both air shower simulation outputs from generators such as CORSIKA [214], Aires [215] etc. and the data recorded at the observatory. Offline aims to standardize basic quantities such as detector response for simulations and important variables

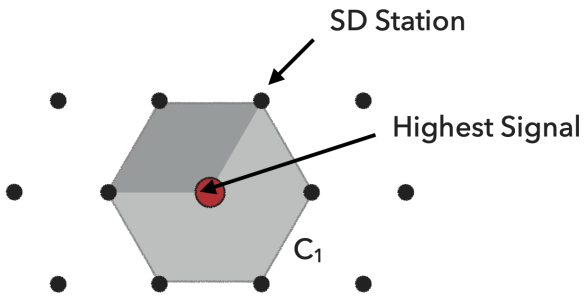

Figure 4.10: Two T5 configurations. The dark shaded hexagon represents the 5T5 condition while the entire shaded hexagons represents the 6T5 hexagon.

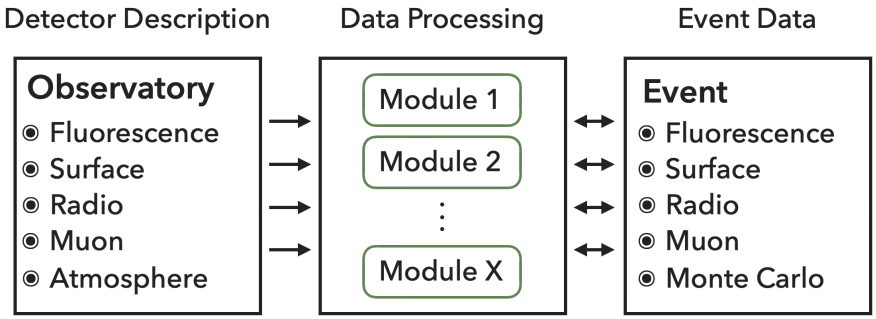

Figure 4.11: An Overview of the general structure of Offlineframework. Modified from [212].

inferred from reconstructing an EAS for the entire collaboration. This helps in providing the collaboration with a homogenous backbone to build physics analysis. It also allows for the physics analysis to be stored and implemented within the framework which helps in leading and optimizing productivity. The modular design allows it to be constantly updated for the addition of new functionality and detectors. The framework is available internally on GitLab to the entire Collaboration with regularly planned public releases. Offline consists of three fundamental constituents as shown in Fig. 4.11. These are summarized below:

Detector description: This part acts as an input and consists of information about the individual detector systems of the Pierre Auger Observatory. The information is available to the data processing modules as needed but cannot be modified. The static information such as the layout of the detector is stored in XML files whereas the time dependent information such as atmospheric conditions, hardware changes, calibration information etc. is stored in MySQL databases. For real events this allows for an almost perfect duplication of the conditions and for simulations it offers a vast range of available detector configurations.

Event data: This part is used to store the important event variables required by modules or the end physics analysis. This includes basic detector level information such as measured or reconstructed signal traces, trigger information etc. to reconstructed variables such as energy,

direction or $X_{\max}$. The information is transferred to the data processing modules based on the use case. For a simulation, the event information is first provided to the modules to generate the detector response which is then further reconstructed. In such cases true Monte Carlo (MC) values, detector response and the reconstructed quantities are all stored in the event data. Whereas, for real recorded data since the detector response is already present only the reconstruction is performed by the data processing modules. Event data acts as both an input and output for the data processing component of the framework.

Data processing: The type of task performed by the Offline is controlled using the data processing components. The different tasks are implemented using individual modules where each module is a self-contained algorithm with the ability to read the detector description. The modules can also read and write event data. Since the modules do not interact with each other they can be easily updated and new modules can be used in an analysis in a plug and play fashion. The different modules can be implemented sequentially in a chosen order based on the analysis. This is controlled via an XML file called Modulesequence.xml. The modules also have adjustable parameters which can either be controlled using individual XML steering files of each module or using a central XML file called bootstrap.xml. There are various standard pre-defined sets of module sequences and bootstraps available in the Offline framework which can be directly used without any alterations. For this analysis, one standard reconstruction SdDglNeutrinoReconstruction was tweaked to perform a neutrino search with MoPS and ToTd. Two new reconstruction modules SdDghNeutrinoReconstruction and SdNeutrinoSimulation based on previously done analyses were also adapted and added to the Offline framework. The exact modules used in the different neutrino analyses and a description of their functionality are mentioned in the following chapters.

4.4.1 Advanced Data Summary Tree

Advanced Data Summary Trees (ADSTs) are ROOT [216] based file structures developed internally within the Pierre Auger Collaboration to store the output of the reconstruction. Additionally, it can also be used to store low level information such as detector description, calibration information and also the configuration of the Offline framework used to produce the ADST. ADSTs can be used to browse through individual events via the Eventbrowser and carry out higher level physics analysis. Since the structure is based on ROOT ADSTs can be read through different programming languages. In the context of this analysis the ADSTs are interfaced within C++ directly and in python using modules such as Python Instrumentation Kit [217] and uproot [218] in Python.

CHAPTER 5

Neutrino Analysis $60^\circ < \theta < 75^\circ$

This chapter details the work done to improve the neutrino search performed for the zenith angle range $60^\circ < \theta < 75^\circ$ at the Pierre Auger Observatory. The chapter aims to cover the expected signature in terms of measurable quantities in the Pierre Auger Observatory for the particular angular range, a description of the neutrino simulation used to develop the analysis and the reconstruction chain used to reconstruct the neutrino simulations with the Offline framework. Further, the quality cuts used are analysed in more detail, especially in the context of improving the capability of the search by the usage of MoPS and ToTd triggers. In the end, the improvement to the neutrino detection efficiency with the inclusion of MoPS and ToTd is quantified.

5.1 SD Neutrino signature $60^\circ < \theta < 75^\circ$

The strategy and method to detect neutrino showers in this angular range with the SD remain the same as mentioned before in section 3.3.5 i.e. to try detecting showers that develop late and have an electromagnetic or "young" shower front at ground. In terms of signal in the SD array, the young shower is expected to be spread over a longer time period, typically hundreds of nanoseconds, and have a lower maximum peak compared to signal induced by older showers which are spread over tens of nanoseconds and have a higher maximum peak. A comparison of the difference between the induced SD signal from a young and old shower arriving from the same zenith angle is presented in Fig. 5.1. However, such differences in signals and the ability of the SD to differentiate between a neutrino induced and a proton/heavy nuclei induced shower disappear for vertical showers ($\theta < 60^\circ$). For vertical showers, a UHECR induced EAS does not have enough time to develop because of the limited thickness of the atmosphere. At these zenith angles a high energy UHECR induced EAS can mimic the expected young shower signature of a neutrino induced EAS at the ground. Thus, currently, the neutrino searches at the Pierre Auger Observatory are limited to zenith angles above 60° where it is much easier to separate a neutrino induced EAS from a UHECR induced EAS. Since the searches involve looking for young showers

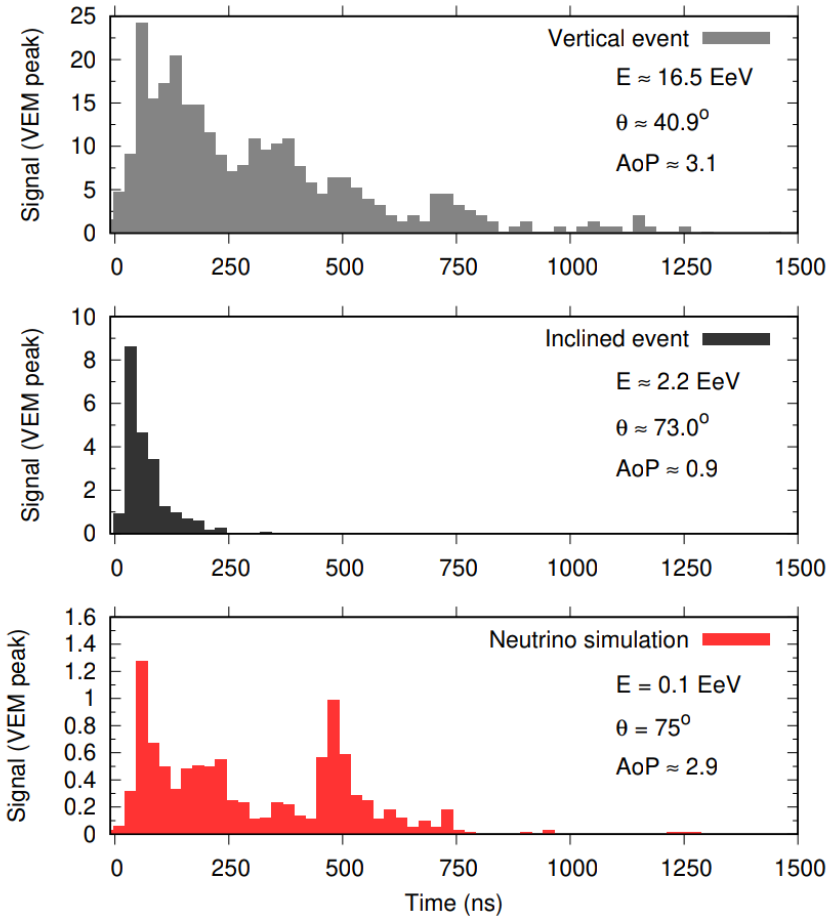

Figure 5.1: FADC trace comparison for stations at 1 km distance from the shower core. The first and second panel indicate a station belonging to a cosmic ray like event for two different zenith angles. The last panel indicates a station trace for a neutrino simulated event. The Area over Peak is also indicated for each event for comparison. Taken from [18].

which have not fully developed till they are detected at the ground, reconstructed energy cannot be used as a discrimination criterion.

To select the longer signals in the SD one of the variables that was used in erstwhile neutrino searches at Auger is the fraction of ToT-T2 triggered signals in the recorded event. As mentioned in the previous chapter this trigger is tuned to select broader signals, which for an inclined shower is evidence of a young shower. For the search presented in this thesis along with the ToT-T2, the ToTd and MoPS are also used. Both ToTd and MoPS as mentioned in section 4.2.2 help further increase the selection efficiency for broader signals by reducing the impact of low energy muons. These muons form the majority of the background at low zenith angles of the selected search range. Thus, these triggers are impactful in increasing the separation power for low energy ($\leq$ 1 EeV) neutrino showers. Another important variable that is used to judge the width of the signals is the Area over Peak (AoP). The AoP is defined

as the ratio of the integrated signal of each PMT of the station over the biggest value or peak of the signal in that particular PMT averaged over all active PMTs in a station. The AoP is calibrated in such a way that narrow or old shower signals, which are predominantly muons, have AoP ∼1 while broad/old shower signals have AoP ⩾ 1.

5.2 Neutrino Simulations

To characterize the neutrino search ability of the Pierre Auger Observatory MCsimulations of EASs induced by UHEνs are required. There are six possible neutrino interaction channels due to the three possible neutrino flavors with each having two possible channels (CC or NC). However, for simulations these are envisioned to be characterized by just two sets of simulations. For the NC channel since the EAS induced by three neutrino flavors has the exact same signature for our detector, only ν_e NC simulations were performed to estimate the NC contribution of all the three flavors to the final detection efficiency.

For the CC interactions, in the case of ν_μ the resulting high energy muon has a high probability of evading detection. This signature is very similar to the NC interaction where the resultant secondary neutrino also carries approximately 80% of the primary energy and probably evades detection. Thus, after taking into account the appropriate cross-section, in principle, the NC simulations can be used to also estimate the contribution of ν_μ CC channel to the detection efficiency.

In the case of ν_τ CC interactions, the resulting τ especially at higher energies (≥EeV) can decay and also initiate a secondary shower resulting in a "double bang" like signature in the observatory. In the context of this thesis, such signatures are not accounted for and the ν_τ CC interaction is treated in the same way as the ν_μ CC interaction resulting in a possible underestimation of the detection potential of the observatory to ν_τ events. A future ν_τ simulation library is currently being prepared by the Pierre Auger Collaboration Monte Carlo task and could help improve this analysis in the future.

Thus, in summary, ν_e CC and NC simulations can be considered to be good approximations to estimate the contributions of all the other channels to the overall exposure of the observatory. The simulations were produced in two parts by the Pierre Auger Collaboration Monte Carlo task based on the GAP note [23] and input from the author. The first part entails the simulation of the ν_e induced EAS in the atmosphere and the second consists of simulating the appropriate detector response for the corresponding shower.

5.2.1 Atmospheric Shower simulations

CORSIKA (COsmic Ray Simulations for KASCADE) [214], a simulation software for modelling extensive air showers in the Earth's atmosphere was used to generate the EAS initiated by a ν_e primary. The simulation parameters are defined through files known as input cards. An example of the input cards used to generate simulation for this analysis is provided in Appendix A. The first step involved simulating the primary neutrino-nucleon interaction

which is performed in CORSIKA using the HERWIG [219] code. Further, options such as CHARM to track charm secondaries are not used. Also since only ν_e simulations are simulated, the TAULEP option which handles ν_τ and $\overline{\nu_\tau}$ is also not used. The systematic uncertainties related to the primary interaction estimator are discussed later in section 6.2. CORSIKA further tracks and simulates the interactions of the primary interaction products as they travel in the atmosphere toward the ground constituting the air shower. It offers a wide variety of choices regarding the hadronic interaction models it uses to simulate these interactions. For the simulations used in this study, separate high and low energy hadronic interaction models were used. For energies higher than 200 GeV three high energy hadronic models QGSJETT-II.04 [220], SIBYLL 2.3d [221] and EPOS-LHC [222] were compared. The results of the comparison are mentioned in detail in Appendix B. Since the differences between the models are not that significant, for the neutrino analysis SIBYLL 2.3d was chosen as the high energy interaction model. For lower energies FLUKA [223, 224] was chosen. The systematic uncertainties arising from different models are discussed in section 6.2.

To account for the curvature of the Earth which is especially important for the zenith angle range studied, the EGS4 [225] Monte-Carlo method is chosen to simulate the electromagnetic component of the shower. The analytical NKG method based on eq. 3.3 which is also available but is not used for these simulations since it vastly underestimates the maximum of the electromagnetic component due to the fact it does not account for a curved atmosphere. Global Data Assimilation System (GDAS) measurements at Malargüe [226] were used for the atmospheric profile chosen for the simulations. The magnetic field components are taken to be the default values at the Malargüe site ($B_x = 19.52\,\mu T$ and $B_z = -14.17\,\mu T$).

Further, since the computing times taken for shower simulations scale roughly with the primary energy, for primary energies $>10^{16}$eV these times become extremely long ($\sim$ weeks). Though parallel computing provides a viable solution, the technique of "thin sampling" or thinning [227] offers an alternate way to reduce the computation times while simultaneously avoiding the waste of resources. The thinning algorithm is applied to all particles below the adjustable fraction of the primary energy that emerge from an interaction. Only one of these particles is followed, and a proper weight is assigned to this particle to account for the untracked ones which are dropped based on the thinning level ($\epsilon_{th} = E/E_0$). Additional information about the application and the improvements to this process can be found in [228, 229]. A thinning value of $\epsilon_{th} = 10^{-6}$ is used for the simulations in this study.

The simulations were performed using the GRID technology [230, 231]. Both CC and NC showers were simulated for fixed primary energy steps of $\log(E/\text{eV}) = 0.5$ in the range $10^{16.5} - 10^{20.0}$eV. The number of simulated showers was varied depending on the Energy (E), atmospheric depth of interaction or injected slant depth (X) and the injected zenith angle (θ_{MC}). More showers were simulated at lower energies and the energy dependent numbers are tabulated in table 5.1. Further, for both the interaction channels within the zenith angle range $60^\circ - 70^\circ$ the neutrinos were forced to interact at fixed atmospheric depths in steps of $100\,\text{g cm}^{-2}$. The injection points both close to the ground where a neutrino shower might have a lower trigger efficiency and close to the top of the atmosphere where a neutrino induced

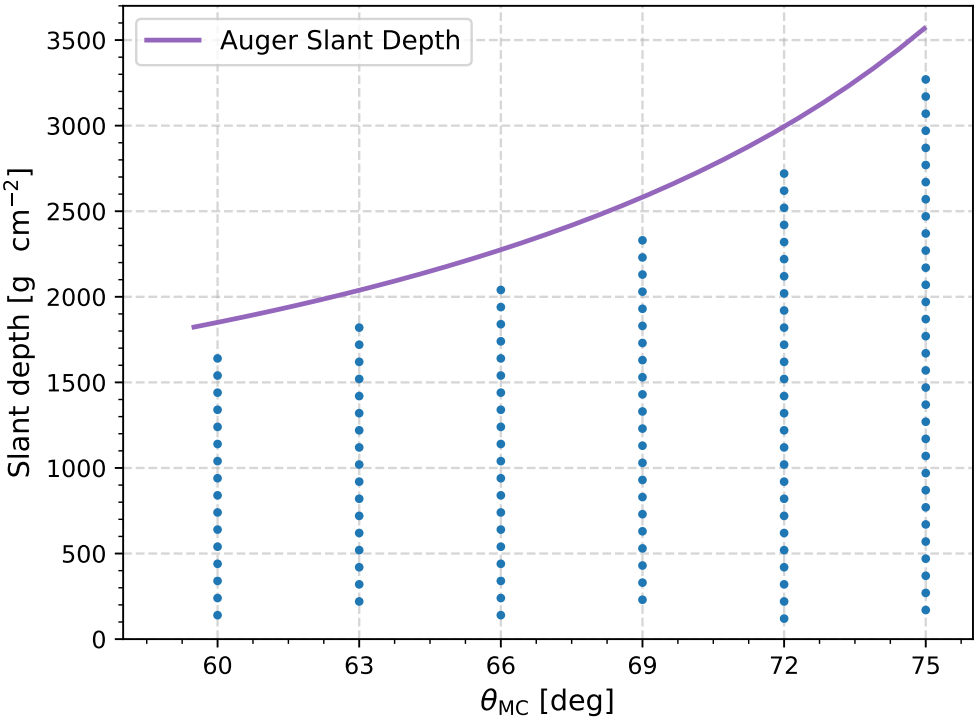

Figure 5.2: The different injected slant depths simulated for the different zenith angles in the range $60^\circ - 75^\circ$. The purple line represents the atmospheric slant depth at the Pierre Auger Observatory. The blue dots represent the simulated depths for the different zenith angles. The top of the atmosphere is at $y = 0$ g cm^{-2}.

shower might mimic one induced by a proton are rejected for the simulations. The azimuthal angle is left free and can take any value between 0° and 360°. The simulated depths for each zenith angle bin are also summarized in table 5.1. The values for the simulations are almost the same as used in the previous analysis [23] with the only change being the range for the primary energy which was simulated.

Based on the (E, θ_{MC}, X) bin the number of CORSIKA showers simulated vary. Higher values were chosen for lower energies to increase the statistics since at these energies the simulated showers have a lower chance of being detected by the detector.

After the simulation is completed, CORSIKA outputs a normal particle output file that contains information about the surviving particles at the ground level which is set based on the detector elevation. The file contains the relevant information such as energy, momentum, position, weight and timing all segregated for each particle based on its Particle Data Group Code [61]. It also produces a *".long"* file that contains the longitudinal distribution of various particle numbers along with the energy deposited which is relevant for analyses that use

$\log_{10}(E/\text{eV})$	16.5	17.0	17.5	18.0	18.5	19.0	19.5	20.0
Showers per (θ, X)	300	200	150	50	50	50	50	50
Resamplings in Offline CC (NC)	100 (200)	50 (100)	50 (100)	10 (50)	10 (50)	10 (50)	10 (50)	10 (50)

θ_{MC}	60°	63°	66°	69°	72°	75°
Interaction Depths (X)	13	14	17	19	23	29
Max interaction depth (g cm^{-2})	1640	1820	2040	2330	2720	3270
Min. interaction depth (g cm^{-2})	140	220	140	230	120	170

Table 5.1: Summary of the number of showers simulated for each (E,θ_{MC},X) bin. The number of resamplings for the Offline reconstruction is also given. The simulations are performed in steps of 100 g cm^{-2} between the minimum and maximum interaction depths for each zenith angle bin.

the FD. For this work, the normal particle output files were used for further processing to simulate a response in the Pierre Auger Observatory SD.

5.2.2 Surface Detector Response

The next step required to complete the ν-induced shower simulation is to generate an appropriate detector response in the SD array for each simulated atmospheric shower. This is done using the Offline framework (section 4.4). The framework can read in the CORSIKA output files, unfold the applied thinning, simulate the Cherenkov light which will be produced as the particles travel through the WCDs. It then also mimics the corresponding WCD electronics outputting the trigger and event information for each simulated shower akin to how real showers are measured at the observatory. Each step is performed using specific modules. Since Offline is an evolving framework a special tag "v4r0p2-pre3" was used to simulate the detector response and to reconstruct both the neutrino simulations and measured data. The module sequence used to simulate the detector response for ν-induced showers in this thesis is given below:

```
<sequenceFile>
<enableTiming/>
<moduleControl>
  <loop numTimes="unbounded" pushEventToStack="yes">
    <module> EventFileReaderOG </module>
    <!- increase numTimes if you want to throw the shower
    into the array more than once ->
    <loop numTimes="5" pushEventToStack="yes">
      <module> EventGeneratorOG </module>
      <!- simulation of muon background ->
      <module> SdAccidentalInjectorKG </module>
```

```
      <module> G4StationSimulatorOG </module>
      <loop numTimes="unbounded" pushEventToStack="no">
        <module> CachedShowerRegeneratorOG </module>
        <module> G4TankSimulatorOG </module>
      </loop>
      <module> SdSimulationCalibrationFillerOG </module>
      <module> SdPMTSimulatorOG </module>
      <module> SdFilterFADCSimulatorMTU </module>
      <module> SdBaselineSimulatorOG </module>
      <module> TankTriggerSimulatorOG </module>
      <module> TankGPSSimulatorOG </module>
      <module> CentralTriggerSimulatorXb </module>
      <module> CentralTriggerEventBuilderOG </module>
      <module> EventBuilderOG </module>
      <module> EventFileExporterOG </module>
    </loop>
  </loop>
</moduleControl>
</sequenceFile>
```

The *EventFileReaderOG* reads in the CORSIKA output file. The following steps are performed assuming an "ideal" SD array with every station operational and fully efficient within the design limits. The steps are also repeated for an individual shower between 10–300 times depending on the primary energy to further increase the statistics for each (E, θ, X) bin and to account for fluctuations depending on the detector simulation. The first module, *EventGeneratorOG*, sets the core position, time and event ID for MC events. In this analysis similar to [23] the core position is only allowed to be randomized over a $5 \times 5\,\mathrm{km}^2$ area around a fixed station at the centre of the array. The resampling is done to increase the overall simulation statistics for this study and also allows for an in depth study of how core position could impact the reconstruction which is discussed later. In the next step, the *CachedShowerRegeneratorOG* reads in the list of the shower particles and un-thins each particle injecting a set of new particles based on its unique weight [232]. It can then create a list of particles for each SD station which is then passed to the next module, *G4TankSimulatorOG*. *G4TankSimulatorOG* uses Geant4 [233–235] to simulate the particle trajectories in the WCD and the corresponding Cherenkov light produced by these particles. It also handles all possible absorption and reflections the light can suffer before it is measured by the PMT. Following this, the *SdSimulationCalibrationFillerOG* simulates the detector calibration constants described in section 4.2.1 and the *SdPMTSimulatorOG* takes in the information from the tank simulator and simulates a corresponding PMT signal (trace). *SdFilterFADCSimulatorMTU* and *SdBaselineSimulatorOG* further simulate the processing of the PMT signal by the electronics at each station with the former applying the filter response and the FADC sampling and the latter adding baseline and simulated noise to these traces.

The next two modules decide whether the simulated event fulfils the hierarchical trigger system of the observatory explained in section 4.2.2. *TankTriggerSimulatorOG* checks if the signal fulfils the local station criteria i.e. T1 and T2 condition. Following this the *CentralTriggerSimulatorXb* further combines all the stations which fulfil the T2 criteria to form the T3, simulating the task performed by CDAS for real data. The *CentralTriggerEventBuilderOG* and *EventBuilderOG* then facilitate the transfer of events passing the T3 criteria from the simulation container class to the event class with the last module *EventFileExporterOG* responsible for exporting all the processed showers now with the applied detector response in a file which can be used for further reconstruction.

5.3 Shower Reconstruction

The event reconstruction is needed before any further analysis can be performed. This procedure is developed first for neutrino simulations to enhance their identification efficiency and to study the possible background. Once fixed, the reconstruction is also applied on the measured data to look for neutrino like events. Shower reconstruction is also performed within the Offline framework with a module sequence that contains a combination of some standard reconstruction modules and some specific modules developed for neutrino identification in GAP note [23]. The reconstruction is again performed with the help of the MC task on the GRID framework based on the particular reconstruction chain developed for neutrinos. The module sequence used to reconstruct simulated neutrino showers is given below:

```
<sequenceFile>
<enableTiming/>
<moduleControl>
  <loop numTimes="unbounded" pushEventToStack="yes">
    <!- Event Reading and Pre-selection ->
    <module> EventFileReaderOG </module>
    <module> EventCheckerOG </module>
    <!- SD Calibration ->
    <module> SdGainRatioCorrectorKG </module>
    <module> SdStationCheckerOG </module>
    <module> SdHistogramFitterKG </module>
    <module> SdBaselineFinderKG </module>
    <module> SdTraceCalibratorOG </module>
    <module> SdSignalRecoveryKLT </module>
    <!- Event-selection ->
    <module> SdMonteCarloEventSelectorOG </module>
    <module> SdEventSelectorOG </module>
    <module> SdTopDownSignalSelectorUGR </module>
    <!- Angular Reconstruction ->
    <module> SdPlaneFitOG </module>
```

```
      <module> LDFFinderKG </module>
      <!- Post selection and export ->
      <module> DLECorrectionWG </module>
      <module> SdEventPosteriorSelectorOG </module>
      <module> RecDataWriterNG </module>
    </loop>
  </moduleControl>
  </sequenceFile>
```

The sequence remains similar to the one used in [23] apart from the iterative development performed by the Offline developers over the years. For data reconstruction, the *SdMonteCarloEventSelectorOG* is omitted from the sequence. The chain can be subdivided into three main parts which are "event reading and pre-selection," "angular reconstruction" and "posterior selection and export" which are discussed in the next few sections.

5.3.1 Event reading and pre-selection

The first module in this part of the reconstruction is again the *EventFileReaderOG* which depending on the input format can parse the file. In the reconstruction sequence, it is used to read in either the detector response simulated file for simulations or the measurement files obtained from the SD. The *EventCheckerOG* further checks if the stations in each read event have proper timing information. After this point, the FADC traces are processed with various modules to covert them to VEM units. The *SdGainRatioCorrectorKG* corrects for the gain ratio for the electronics followed by *TriggerTimeCorrection* which further corrects for differences in electronics especially related to timing for data over the course of its operation. The *SdStationCheckerOG* further checks the station quality and appropriately sets stations silent if they do not contribute to the final trigger formation. After this point the *SdHistogramFitterKG*, *SdBaselineFinderKG* and *SdTraceCalibratorOG* get the calibration constants from the calibration traces, fit the baseline and convert the traces to VEM units. Further, *SdStationPositionCorrection* corrects the positional differences that might arise due to faulty GPSs which is important for later reconstruction, *SdBadStationRejectorKG* sets known bad stations in the array to be non-operational and the *SdSignalRecoveryKLT* which tries to recover signals from the saturated PMTs, if any, by looking at the undershoot value [236, 237]. An extra module *SdPMTQualityCheckerKG* is also used in the case of data reconstruction to estimate the quality of the detector.

The next three modules are used to fine tune the selection of signals and later events, to improve both the quality of simulated and measured data especially for the specific case of neutrino detection. The first one is the *SdEventSelectorOG* which applies a basic SD event selection which is also used in other analyses. The module sets conditions based on T4, T5 and other station based parameters if appropriate. The different operations performed by the module are as follows:

- **Bottom-up Selection:** This selection helps in flagging the non-participating stations if the stations are not compatible with a planar shower front propagating at the speed of light hypothesis [238]. Such stations can arise due to random noise in the array or due to random coincidences between non-air shower like events with actual air showers. The selection requires a minimum of three stations that fit the planar front of the shower within lenient time tolerances. It also removes isolated stations by checking the distances to the nearest neighbours. In this analysis this selection is not used since it is not very effective for inclined showers (>60°) as the showers above these angles are not geometrically compact. Thus, this selection is replaced by another approach known as the Top-down selection implemented in *SdTopDownSignalSelectorUGR* which is discussed later.

- **T4 and T5 trigger:** The module also calculates the T4 and T5 criteria discussed in section 4.2.2. It then further discards events if they do not fulfil these criteria. In this study, the T4 criterion was not used but a stringent 6T5 criterion was required for the selection.

- **Lightning Rejection:** The lightning events can be detected in the SD stations by looking for an oscillatory signal in the FADC traces of all three PMTs [239]. For this analysis, if any lightning like signal is detected in any one of the stations the whole event is rejected from the analysis.

- **ToTd and MoPS trigger:** The module can also silence particular triggers before applying the selection. This feature is used to produce two sets of reconstruction files one with the triggers turned off and one with them turned on to check the impact of the new triggers for some energies. This functionality and the usage of the new triggers can impact the number of events fulfilling the 6T5 conditions and thus the overall number of events which can be seen later in section 5.4.1.

The *MonteCarloEventSelectorOG* further removes stations with distance in shower plane coordinates smaller than the inner radius used in the CORSIKA simulations. It also removes dense stations i.e. virtual stations which are sometimes used for MC studies since these are not representative of the regular SD array.

The *SdTopDownSignalSelectorUGR* is a module developed specifically to carry out a Top-down selection and accidental signal rejection for neutrino like events. A summarized overview of what this module aims to accomplish is given next with a detailed description of the module already published in [240]. The Top-down procedure is applicable for both the simulations and measured data whereas the accidental signal treatment is only applied for measured data. The procedure is based on [241]. Top-down selection requires a minimum of three stations with the shower front time tolerance compatibility dependent on the zenith angle. If the fit does not converge stations are successively removed and re-tested until a satisfactory fit is achieved. At the end of the procedure stations which do not contribute to the final fit are rejected while the others are marked as candidate stations. Further, the

Top-down procedure also takes into account the individual traces and uses the shape for 3-fold topologies. It also rejects isolated signals akin to the Bottom-up selection but with larger tolerances to account for the wider footprint of inclined events. The module also applies an accidental signal rejection procedure before the Top-down procedure is applied to account for the atmospheric muon background based on [242]. The atmospheric muons and also local showers can either trigger isolated stations or even real event stations affecting the start times and in turn the zenith angle reconstruction. This mis-reconstruction can either cause problems with the fitting of the Top-down procedure and can also lead to a worsening neutrino detection efficiency by improper background rejection. The module discards stations with total signals below 3 VEM which rejects the muonic background which typically peaks at 1 VEM. The discarding procedure is implemented only till the minimal number of stations present in the event is below 6.

Since the parameters of the module were evaluated without the consideration of MoPS and ToTd, especially for the segment selection and accidental stations removal procedure, slight changes were made to the module in this analysis. The segmentation procedure was not applied to the stations which had a MoPS/ToTd trigger. These stations were only subjected to the Top-down selection procedure. Some more details about this choice are presented in Appendix C. Further, the accidental station cut was lowered till the minimum number of stations present in the event are below 5 compared to 6 to account for the increased number of randomly triggered stations expected with the inclusion of new triggers. This was done after the partial unblinding of the test sample and is described in more detail in section 6.3.1. These changes were only implemented for the sample where the new triggers are included and the sample where the new triggers are not used remains unchanged.

5.3.2 Angular Reconstruction

The angular reconstruction forms the basis for neutrino detection using the SD especially since for inclined neutrinos the primary energy estimation algorithms typically used for UHECRs become unreliable. The angular reconstruction is performed by the *SdPlaneFitOG* and *LDFFinderKG*. The primary energy estimation using the SD is typically done using the *LDFFinderKG* which fits a lateral distribution function to the SD signal based on the NKG approximation. The NKG approximation is typically inaccurate for inclined showers above a zenith of 60° thus alternate methods based on muon maps are used for UHECR like inclined showers. These also fail for neutrino induced showers which in our detection scenario usually have a large electromagnetic component. Thus, without a reliable energy reconstruction, angular reconstruction becomes vital for neutrino induced shower detection with the SD. A summary of the method and the procedure is presented below based on a detailed description which can be found in [237].

The angular reconstruction procedure uses the timing information from the stations to fit either a plane or a spherical shower front. A schematic of the procedure is shown in Fig. 5.3. The axis of a shower, $\hat{a}$ is initially assumed to intersect the ground at some time using a signal weighted barycenter x_b and bary-time t_b of selected stations located at x_i with start

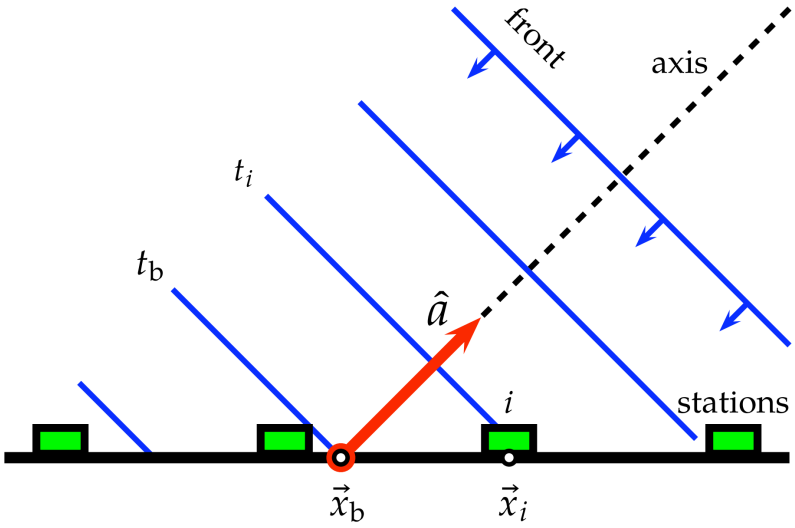

Figure 5.3: Schematic of plane-front approximation. Taken from [237].

time t_i given by :

$$\vec{x_b} = \frac{\sum_i \sqrt{S}_i x_i}{\sum_i \sqrt{S}_i} \quad \text{and} \quad t_b = \frac{\sum_i \sqrt{S}_i t_i}{\sum_i \sqrt{S}_i}. \tag{5.1}$$

The choice of the weights, taken as $\sqrt{S}$ with S being the signal of the stations, has been previously evaluated using MC studies to give the best results. The barycenter also serves as the first estimate of the impact position of *shower core* at the ground but is later estimated more accurately. The shower core is assumed to be moving in the $-\hat{a}$ direction. Under the plane-front assumption the particles in the shower front move in a plane perpendicular to the shower axis (*shower plane*) with the same speed as the core of the shower which is the speed of light, c, the time, $t(\vec{x})$ when the shower plane passes through some chosen point, $\vec{x}$ (e.g. a station on the ground) can be inferred through a simple projection onto the shower axis as,

$$c\, t(\vec{x}) = c\, t_b - (\vec{x} - \vec{x_b}) \cdot \hat{a}. \tag{5.2}$$

Assuming a minimal change in altitude which is true for the SD location and precise knowledge of station locations the deviations in estimating the geometrical shower parameters can be due to the uncertainty of the observed start times σ_t. Thus, the following function needs to be minimized to fit the model for the measured signal start times

$$\chi^2 = \sum_i \left(\frac{t_i - t(\vec{x_i})}{\sigma_{t_i}} \right)^2, \tag{5.3}$$

where t_i are the start time of the signals of station i located at $x_i = \vec{x} - \vec{x_b}$. The minimization of the χ^2 is performed using MINUIT [243]. For the start time variance determination the standard model described in [237] is used. Replacing the axis with $a = (u, v, w)$ and the station coordinates with $\vec{x} = (x, y)$ (ignoring altitude z). Adding the constraint $u^2 + v^2 + w^2 = 1$ the χ^2 can be easily solved. The solution only fails if the stations used while fitting have a linear dependence (three stations in a line) but for higher station multiplicity this is highly improbable, especially for the theta range explored for the DG_{low} channel.

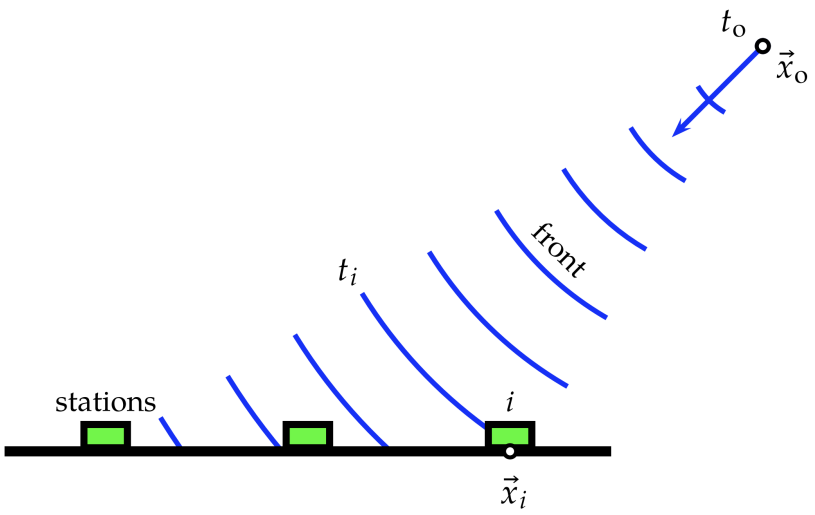

Figure 5.4: Schematic of spherical-front approximation. Taken from [237].

Another shower front estimation technique based on a curved shower front approximation is also used to fit the measured stations. A schematic of the procedure is shown in Fig. 5.4. The reconstruction called the *Observer*, assumes the shower development starting at time t_o from a point of origin x_o propagating toward the ground as a concentrically expanding sphere with the speed of light, c. The arrival time of the shower front at point $\vec{x}$ can thus be estimated as:

$$t(\vec{x}) = t_o + \frac{|\vec{x} - \vec{x_o}|}{c} \tag{5.4}$$

As can be seen by the equation, the spherical fit is decoupled from any prior knowledge of the shower core or the shower axis. It is only dependent on the point of origin. Quantities such as the shower axis can be determined later when the impact point, $\vec{x_c}$ has been estimated as $\hat{a} = (\vec{x_o} - \vec{x_c})/|\vec{x_o} - \vec{x_c}|$. The expected solid angle differences between the two fits are of the order of half a degree. The curvature shower front fit is only used for station multiplicities greater than five. This is so because for lower station multiplicities the degrees of freedom are not enough to solve for the shower-front curvature. A side by side comparison for an event for both plane fit and spherical fit is shown in Fig. 5.5.

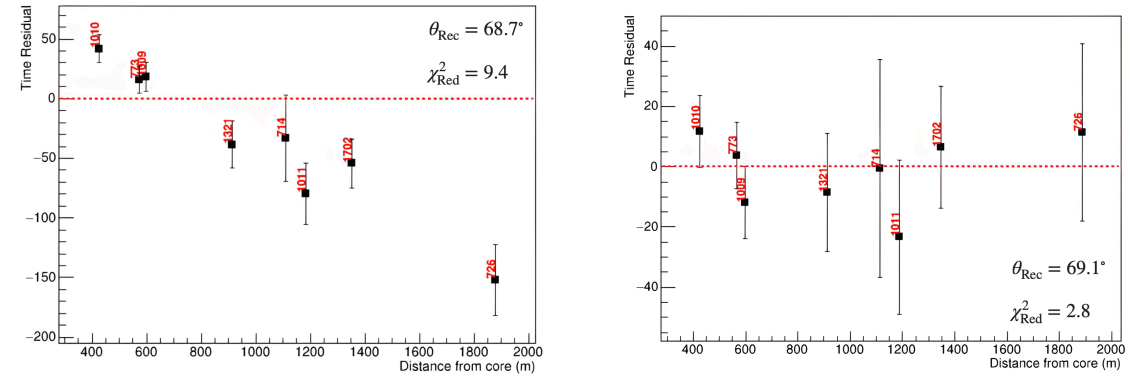

(a) Plane wavefront assumption.

(b) Spherical wavefront assumption.

Figure 5.5: Comparison for the Plane and Spherical wavefront fit for the same event. The black points indicated the time residuals calculated under the two assumptions plotted against the distance of each station from the core or hottest station. The red numbers indicate the Stations IDs of the stations used for the fit. The two approximations agree within uncertainties for the zenith angle.

5.3.3 Posterior selection and Export

The last part of the shower reconstruction chain includes the application of the *SdEventPosteriorSelectorOG* module which computes the 6T5 *posterior* trigger differing from the 6T5 criteria mentioned earlier. The 6T5 posterior requires the 6 stations in the first crown from the nearest station to the reconstructed shower axis to be active or alive during the event. The events which do not pass this criterion are rejected. The last module *RecDataWriterNG* exports all the relevant information to ADST 4.4.1 files. In the case of reconstructed simulations, both the simulated and reconstructed information are stored while for measured data only the reconstructed information is stored.

5.4 Reconstructed ν simulations

This section includes some sanity checks to examine and verify the quality of the ν simulations. Fig. 5.6 shows the efficiency of the reconstructed showers as a function of the zenith angle and the injected slant depth. It is clear from the figure that the WCD is more sensitive to neutrino showers that interact in the atmosphere midway between the top of the atmosphere and the detector. This is so since if the neutrino interacts at the very top of the atmosphere the electromagnetic component of the EAS is attenuated by the time it reaches the detector. On the other hand if the neutrino interacts too close to the detector it is very difficult to reconstruct the EAS due to the compactness of the shower and saturation of the detector. Fig. 5.7 shows the frequency of reconstructed events based on the MC core position. The non-uniform distribution with minimal events for core positions close to the stations can

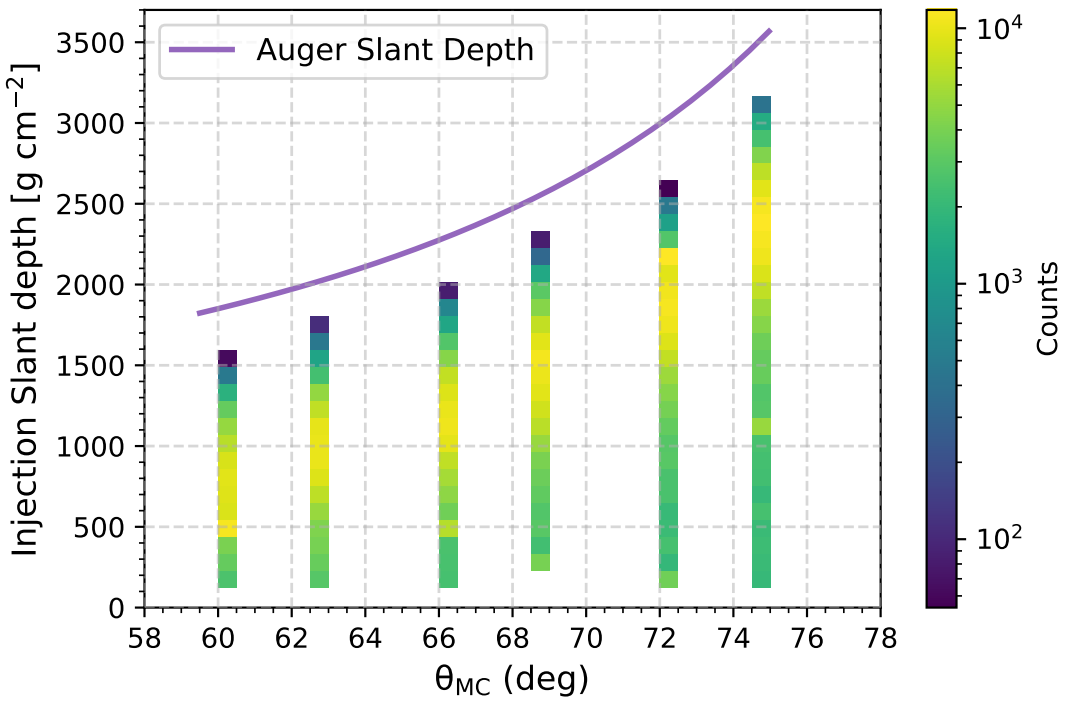

Figure 5.6: Number of showers reconstructed for each MC injected slant depth as a function of θ_{MC}. The colour scale represents the number of showers reconstructed. The purple line represents the apparent slant depth for the detector. The y = 0 line represents the top of the atmosphere at 0 g cm^{-2}.

be explained arising due to two reasons. The first is the removal of stations if the PMTs for the particular station are saturated. This saturation can occur for stations very close to the core. The second reason is that the efficiency of reconstruction is the highest when the mean distance to the three closest stations to the core is maximized.

Fig. 5.8 shows the reconstructed zenith angle distributions for the CC and NC neutrino simulations. The peaks in both the distributions correspond to the simulated MC angles. It is also clear that the distribution of the NC channel (Fig. 5.8(b)) is slightly wider than that of the CC channel (Fig. 5.8(a)) pointing towards a worse resolution. This can be attributed to the reduced total detectable energy carried by an NC shower in comparison to a CC shower. It can also be seen that the distributions of both the channels (open histogram) have a long tail extending towards small values of zenith angle. This is caused due to two reasons. The angular reconstruction used in this analysis is tuned to work best for UHECR showers initiated at the top of the atmosphere with zenith angles below 60°. For neutrinos which can be initiated at any point in the atmosphere the reconstruction is not as efficient. This has been checked by only plotting showers having an injection slant depth < 350 g cm^{-2} as shown in the filled histograms (purple). The second cause of this tail and the worsened resolution is also partially due to the inclusion of ToTd and MoPS. It was seen that the inclusion of

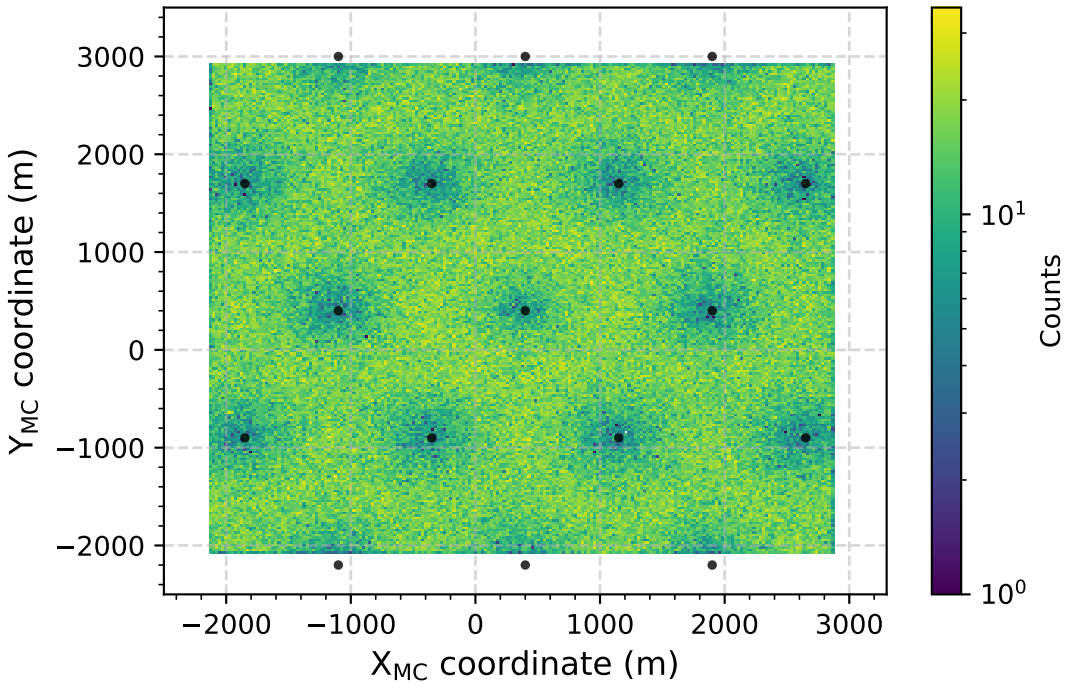

Figure 5.7: Number of showers reconstructed for each MC core position for $\log_{10}(E/\text{eV}) = [16.5, 20.0]$, $\theta_{\text{MC}} = [60^\circ, 75^\circ]$ and all simulated interaction depths. The colour scale represents the number of showers reconstructed. The black dots represent the stations in the array.

these triggers can lead to a worsening of the resolution especially for inclined showers. This effect is more visible when these distributions are compared to reconstructions obtained without the inclusion of these triggers as shown in Fig. 5.10 later. The effect is due to a lack of tuned accidental signal rejection for these new triggers which affect the quality of the angular reconstruction as mentioned before. To mitigate this effect an angular fit quality cut is introduced in the analysis which significantly improves the resolution but comes at a cost of reduced efficiency.

The angular resolution can be determined via the residual distributions ($\theta_{\text{Rec}} - \theta_{\text{MC}}$) shown in Fig. 5.9. It is given by the standard deviation of the residual distribution. For the CC channel the angular resolution is $\sim 3^\circ$ when all events are considered (blue open histogram). The resolution improves to $\sim 1^\circ$ when only events with slant depth $< 350\,\text{g}\,\text{cm}^{-2}$ are considered (purple filled histogram). The angular resolution is $\sim 2^\circ$ with the proposed angular fit quality cut is also shown in Fig. 5.9(b).

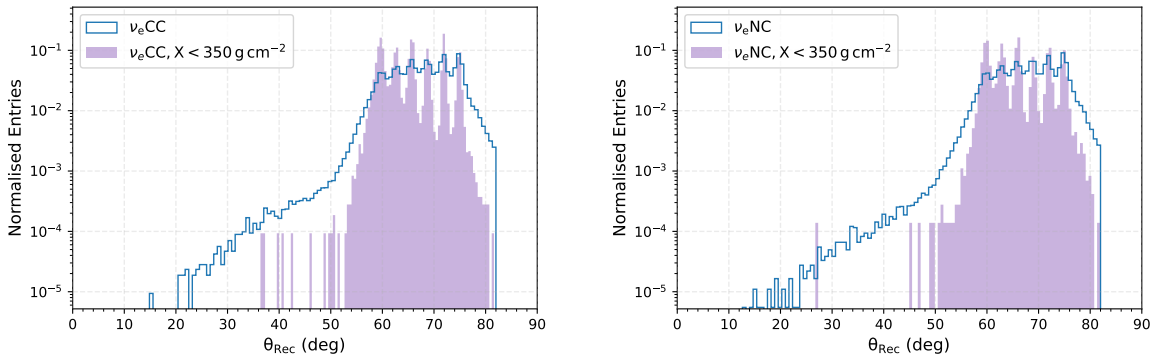

(a) ν_e CC simulations.

(b) ν_e NC simulations.

Figure 5.8: Reconstructed zenith angle distributions for CC and NC neutrino simulations. The open histograms represent all events while the purple filled histograms represent events with slant depth < 350 g cm^{-2}. The peaks correspond to the discrete values of zenith angles simulated which are smeared due the angular resolution.

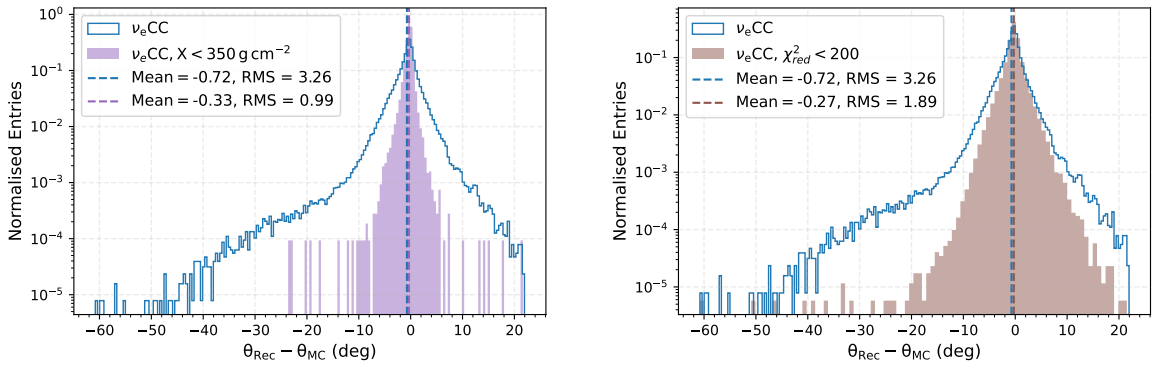

(a)

(b)

Figure 5.9: Residual distributions for the CC channel. The figure on the left (5.9(a)) shows the residual distribution for all events (blue open histogram) and events with slant depth <350 g cm^{-2} (purple filled histogram). The figure on the right (5.9(b)) shows the effect on residual distribution due to the proposed angular fit quality cut. The RMS value represents the angular resolution.

5.4.1 Comparison to reconstruction with old triggers

In this subsection the impact of the inclusion of the new triggers to the total reconstructed events is discussed in more detail. The comparison is done with a sample reconstructed from the same CORSIKA showers using the same reconstruction chain described above. Stations with the new triggers were silenced via the option in the *SdEventSelectorOG* module and thus were not used in the reconstruction. Two more small subsample was also simulated for low energies (10^{17} – $10^{18.5}$eV) each with either ToTd or MoPS active in addition to the old

triggers to quantify their individual impact.

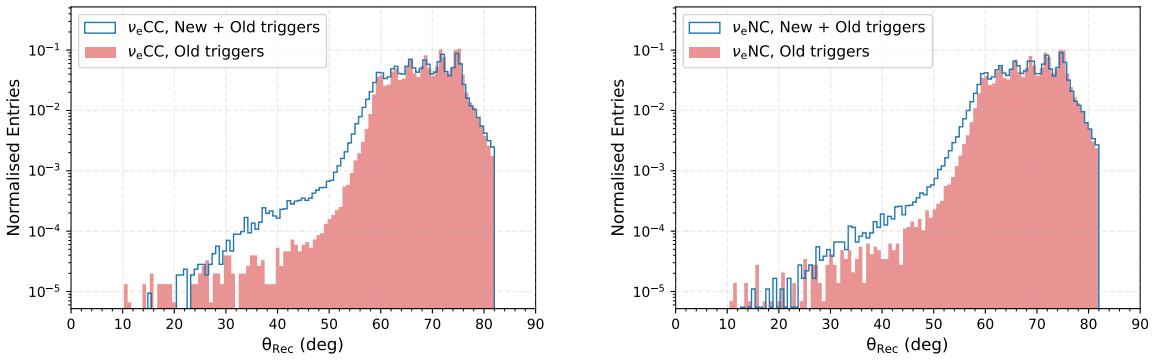

(a) ν_e CC simulations.

(b) ν_e NC simulations.

Figure 5.10: Comparison of the reconstructed zenith angle distributions for CC and NC neutrino simulations with and without the new triggers. The blue open histograms represent all events from the sample where both new and old triggers are used while the red filled histograms represents events from the sample with only the old triggers.

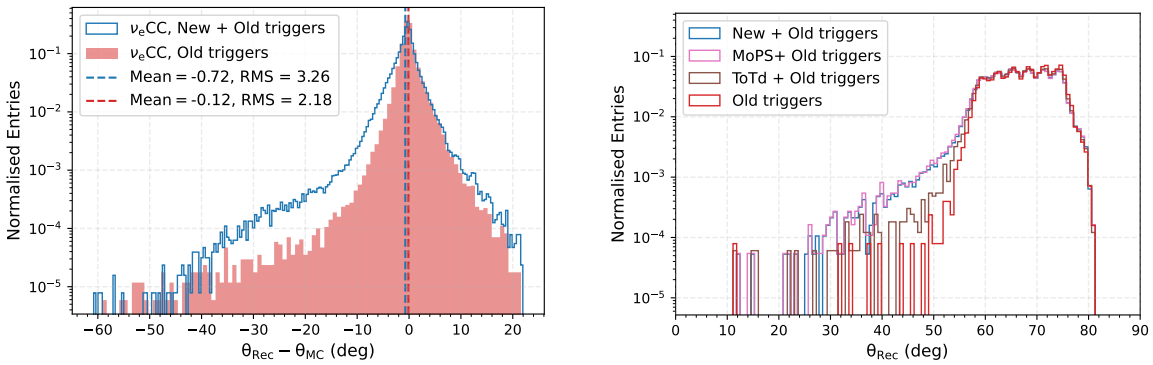

(a) $\theta_{\text{Rec}} - \theta_{\text{MC}}$ comparison.

(b) Contributions of ToTd and MoPS.

Figure 5.11: (Left) The effect of the inclusion of the new triggers on the residual distribution for ν_e CC showers. The RMS value gives the angular resolution. (Right) The individual contribution of ToTd and MoPS to the reconstructed zenith angle for all channels in the energy range E= 10^{17} – $10^{18.5}$eV. The pink histograms represent the sample with only MoPS active while the brown histograms represent the sample with only ToTd active.

Fig. 5.10 shows the comparison for reconstructed zenith angle distributions for the CC and NC channels. The blue histogram is the sample with both the new triggers and old triggers included while the red histogram is the sample with only the old triggers active. The distributions look very similar other than the higher number of events in the tails for the sample with new triggers. This increase is more significant for CC in comparison to NC channel since the inclusion of new triggers adds more overall events to the CC channel in

comparison to NC. A worsening of the residual is also seen in Fig. 5.11(a) but as mentioned before is corrected with the angular fit quality or goodness of fit cut, $\chi^2/\text{ndf} = \chi^2_{\text{red}}$. The individual contribution of the MoPS and ToTd to the reconstructed theta for all channels in the energy range E= $10^{17} - 10^{18.5}$eV is shown in Fig. 5.11(b). It can be clearly seen that both ToTd and MoPS contribute to the higher extended tails. The contribution of MoPS is higher than that of ToTd. The magnitude difference can also be due to higher number of stations with MoPS (2x) in comparison to ToTd.

The angular bias and the evolution of angular resolution with energy, slant depth and MC zenith angle is shown in figures. 5.12(a), 5.12(b) and 5.12(c) respectively. The angular bias is usually small within $\sim 2^\circ$ and is comparable to the one observed in the sample with only old triggers. The resolution seems to improve with energy and worsens with the injected slant depth which is as expected. The variable used for discrimination, AoP of all the T5 stations is also compared in Fig. 5.12(d). No significant differences are observed between the two samples.

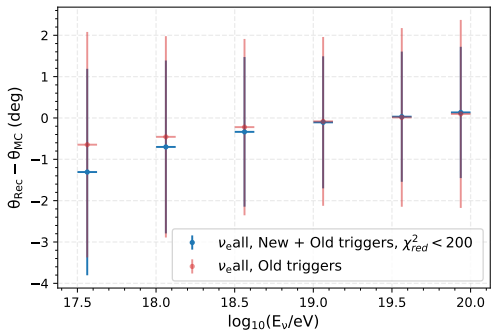

(a) $\theta_{\text{Rec}} - \theta_{\text{MC}}$ vs E_{MC}.

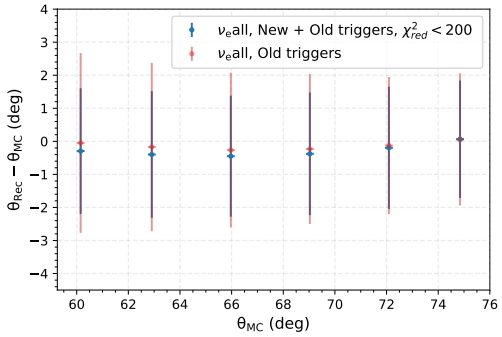

(b) $\theta_{\text{Rec}} - \theta_{\text{MC}}$ vs θ_{MC}

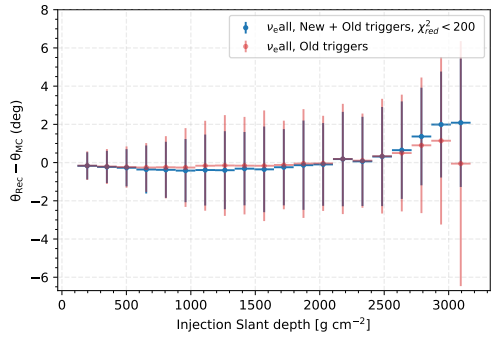

(c) $\theta_{\text{Rec}} - \theta_{\text{MC}}$ vs X_{MC}.

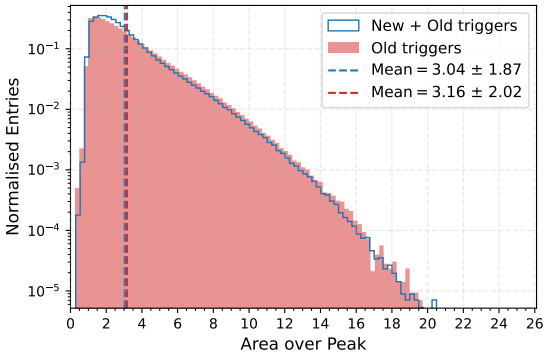

(d) Area over Peak distribution.

Figure 5.12: The residual dependence on energy (a), zenith angle (b) and slant depth (c) for all reconstructed simulations. The error bars signify the spread of the distribution. (d) The AoP distribution for the T5 stations for the sample with new triggers (open blue histogram) and old triggers (filled red histogram) is also shown.

The overall summary of the reconstructed events for both the sample for all energies, channels (CC + NC) as a function of zenith angle is given in Fig. 5.13. The disproportionate total number of events at lower energies in comparison are due to differences in resampling. The gain in total events is higher for lower energies and decreases fast as the energy increases. This is because the ToTd and MoPS were designed to be sensitive to small air shower signal which is typically the case of a neutrino induced shower of low energy. The ToTd and MoPS also have a zenith dependence and are more effective for lower zenith angles. This is because at lower zenith angles the neutrino induced shower still has significant electromagnetic component which ToTd and MoPS are more sensitive to. As the zenith angle increases ToTd and MoPS help in increasing the identification efficiency for neutrinos which interact closer to the array and still have a significant electromagnetic component. Due to the large atmospheric depth at these angles for the farther interaction points the neutrino induced shower becomes older and more muonic reducing the positive effect of the new triggers. Although not shown the overall gain in events is also higher for the CC channel in comparison to the NC channel.

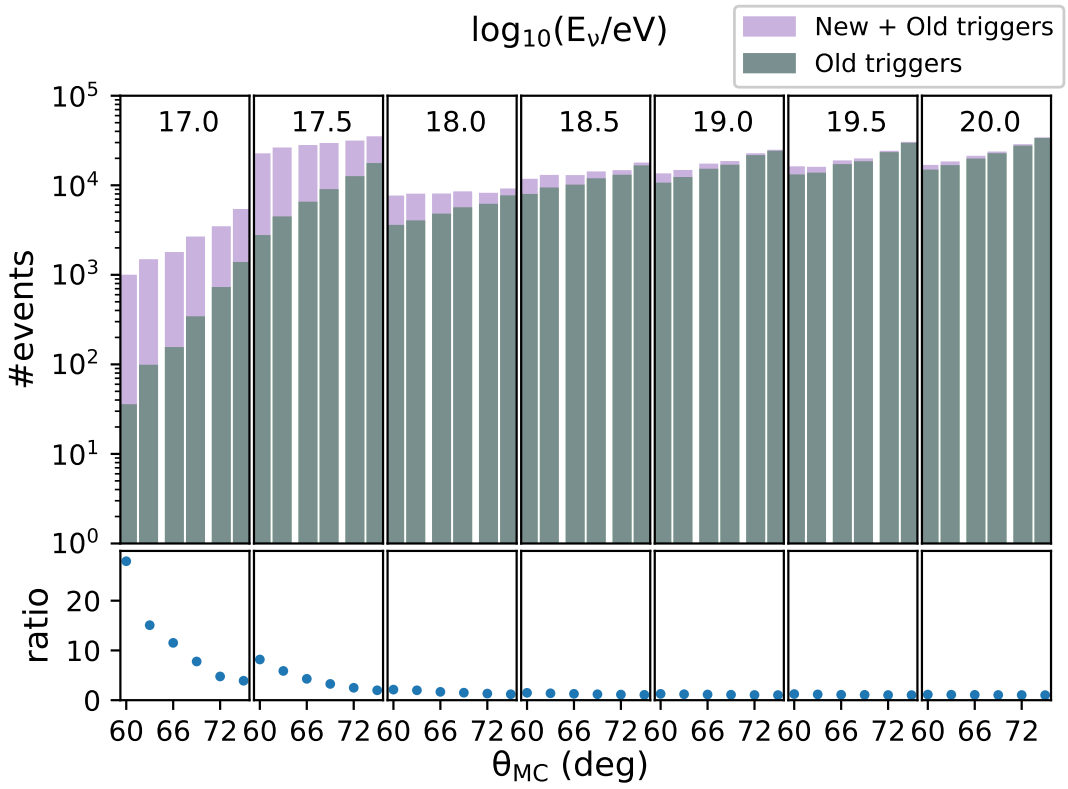

Figure 5.13: An overall comparison of the reconstructed events for all energies and channels as a function of zenith angle for the sample with new and old triggers (purple bars) and old triggers (dark green bars). The plot below shows the ratio of the two samples.

5.5 ν selection

This section describes the decisions made to select ν induced air showers. The selection is optimized and evaluated on the above-mentioned neutrino simulations and a part of the measured data which is used as an estimate for the expected background. Since a *blind search* strategy is envisioned for the search. The rest of the measured data forms the *search sample* and will be used to look for neutrino like events during the *unblinding*. In the first part, the selection used to identify ν showers is described in more detail. The selection consists of some pre-selection cuts applied to enhance the reconstruction quality of the selected events followed by a Fisher Linear Discriminant [244] based on AoP which is the main criteria of differentiation between a ν induced air shower and background. In the second part, the performance of the selection is further evaluated based on temporal changes such as ageing in the surface detector and the neutrino detection efficiency is quantified. Comparisons to previously used selection are also presented especially in the context of the performance improvements achieved by using new triggers for neutrino detection.

5.5.1 Samples Used

As mentioned above to devise an efficient neutrino selection good quality training samples for both signal and background are required. Monte-Carlo simulations described in section 5.2 are used for the signal sample. For the background sample a portion of real data (20%) is used. Due to the low flux prediction of neutrinos a large portion of the measured data if not all is expected to be nucleonic air showers. Simulated showers could also serve as background sample, but this is not done to due to the following reasons. For the energies that are investigated in this search the high uncertainties observed for the air shower simulations, particularly due to hadronic interaction models could lead to errors. Further, the simulations are still incomplete i.e. they tend to sometimes ignore some physical processes and also do not account for all the possible and sometimes even unknown detector effects which could be important for the neutrino search. Using measured data as background is advantageous here as it already contains all the possible effects. Also, due to the vast parameter space looked at for the neutrino search such a simulated background sample would require huge amount of computing resources.

The number, 20% of the measured data sample for the time period 01.01.2014-31.12.2021, which is from here on referred to as 2014-2021, is arrived at to keep the search sample i.e. the rest 80% large enough to look for neutrinos but still have enough events in the training sample for the Fisher analysis. The dataset is chosen at random by only selecting reconstructed events with SD event IDs divisible by 5. The training data for the time period corresponds to 1.29 ± 0.01 years of the continuous measurement of a full array composed of 1420 T5 hexagons. Periods of instability or large outages marked as "BadPeriods" are rejected. The time period is chosen to be starting from the year 2014 since by this time the array had full coverage of MoPS and ToTd. The end date of December 31, 2021 was decided in discussions with the collaboration as the end of Phase 1 of data taking of the Pierre Auger Observatory

since after this point significant changes were made to the electronics of the SD tanks as a part of AugerPrime activities as previous mentioned in section 4.3.

The remaining sample was unblinded in two parts: A 20% test sample was unblinded first to check if there was any need for further optimization of the analysis and the rest 60% constituted the search sample and was used to look for neutrino candidates.

Samples Used	
MC ν *training* sample	Simulated events Detailed info in table 5.1
Analysed data period - 01.01.2014 till 31.12.2021	
Background *training* sample	20% analysed data 1.29 ± 0.01 yr of full Auger equivalent exposure (SD event IDs divisible by 5)
Signal *search* sample	20% + 60% analysed data 4.94 ± 0.04 yr of full Auger equivalent exposure (SD event IDs non-divisible by 5)

Table 5.2: A summary of the samples used for the neutrino selection procedure.

5.5.2 Pre-selection Cuts

The pre-selection cuts are applied based on the unique properties of "young" neutrino like showers in comparison to older nucleon like showers. The cuts are the same as used in [23] with a slight modification to include MoPS and ToTd. These pre-selection cuts are applied in the same way to both the neutrino and background training samples.

Inclined Shower Selection: This cut aims to select showers which fall in the given angular window. The reconstructed zenith angle of each event is required to be in the range $58.5^\circ < \theta_{\mathrm{Rec}} < 76.5^\circ$. The range is extended by 1.5° on both sides in comparison to the simulated values from the simulations to account for the angular resolution of the detector. Further, the error on the reconstructed angle, $\delta\theta_{\mathrm{Rec}}$ is required to be smaller than 3° to ensure the quality of angular reconstruction. The efficiency of this cut is found to be 89 (90)% without the cut on $\delta\theta_{\mathrm{Rec}}$ and the efficiency decreases to 72 (70)% for CC (NC) neutrinos with the restriction on $\delta\theta_{\mathrm{Rec}}$. The angular distribution of the background sample is shown in Fig. 5.14.

Fiducial Quality Cut: This cut also remains unchanged when compared to the previous analysis. The main aim of the cut is to ensure that the shower core for the selected event is completely contained inside the array and the stations which are used for the analysis of the event are operational. This is ensured by requiring the event to satisfy the 6T5 trigger condition. The efficiency of the cut is 100% for the neutrino simulations

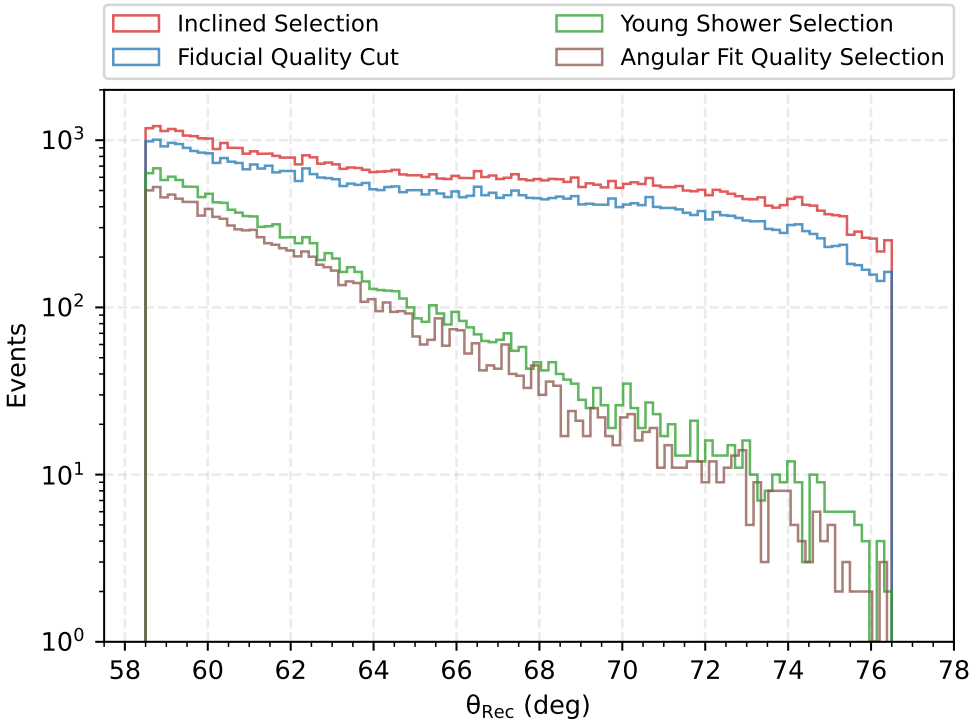

Figure 5.14: Histogram representing the reconstructed angular distribution of the background training sample after each pre-selection cut. The cuts are applied sequentially in the order as described in the text.

by design and for the background sample this cut leads to a reduction of ~ 20% events across the zenith range as shown in Fig. 5.14

Young Shower Selection: This cut tries to ensure the selection of events with a high electromagnetic component at ground. For this purpose events with stations having FADC traces spread in time need to be selected. As mentioned previously ToT, ToTd and MoPS triggers being more sensitive to the presence of high electromagnetic component can be used for this young shower selection. This cut ensures that more than 75% of stations in the T5 hexagon satisfy the ToT/MoPS/ToTd condition. The 75% fraction is calculated on a per-event basis and the hexagon could have stations with mixtures of these triggers. The cut retains most of the neutrino events and at the same time is highly effective in rejecting background especially for high angles as shown in the Fig. 5.14.

Angular Fit Quality: A few erroneous events were discovered to have a bad geometric fit. This problem though discovered with the analysis with new triggers has always affected the neutrino analysis. To mitigate this problem a fit quality cut based on the goodness of the geometry fit was devised. The cut only accepts events which have a goodness of geometrical fit or χ^2_{Red} less than 200. The efficiency of the cut if applied

simultaneous to the station cut used to select stations for the Fisher analysis is ~99% for the neutrino simulations and for the background sample this cut leads to a reduction of <0.1% of events. The change in background events with the application of the cut is shown in Fig. 5.14. Although the cut has minimal impact it, it ensures that one of the fundamental pillars of the analysis i.e. the geometry of the shower especially the zenith angle is well reconstructed.

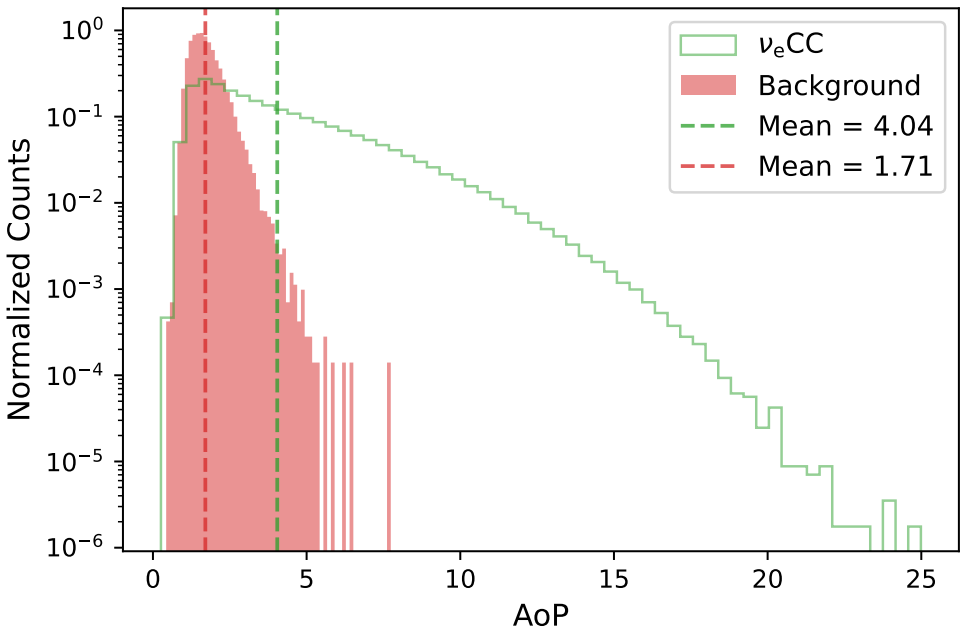

Figure 5.15: Histogram of Area over Peak of all stations that pass the pre-selection cuts. The distribution of the background training sample is represented in red while for the CC neutrino sample is represented in green.

5.5.3 Fisher linear discriminant analysis

The last step for the ν selection and identification involves Fisher Discriminant Analysis (FDA) also known as Linear Discriminant Analysis (LDA). This is a statistical method used to find a linear combination of features i.e. Fisher polynomial that characterizes and separates the two classes, in our case, signal and background training distributions. The goal of FDA is to find a projection that maximizes the distance between the projected class means while minimizing the variance within each class. This ensures that the classes are well-separated in the reduced space. Mathematically, if we have a signal class represented by X_s with mean μ_s and a background class X_b with mean μ_b then the optimal discriminating hyperplane represented by w can be found by solving the equation $S_B w = \lambda S_W w$. The solution is the

eigenvector corresponding to the largest eigenvalue λ. S_B is called the between-class matrix and represented as follows:

$$S_B = \sum_{i=X_s,X_b} n_i(\mu_i - \mu)(\mu_i - \mu)^T \tag{5.5}$$

with $\mu = \frac{n_s\mu_s + n_B\mu_b}{n_s+n_b}$ is the overall mean

The within-class matrix S_W is given as

$$S_W = \sum_{i=X_s,X_b} \sum_{j=n_s,n_b} (x_j^{(i)} - \mu_i)(x_j^{(i)} - \mu_i)^T \tag{5.6}$$

After finding the weight vector, the projected data for each sample is given as $z_i = w^T x_i$, z_i from here on is referred to as Fisher value, $\mathcal{F}$. The elements of the normalised transposed weight vector are called Fisher coefficients. The method has been implemented in a standalone python program with the help of [245] and has been verified with the inbuilt LDA module of python [246] with both results agreeing within 0.01%.

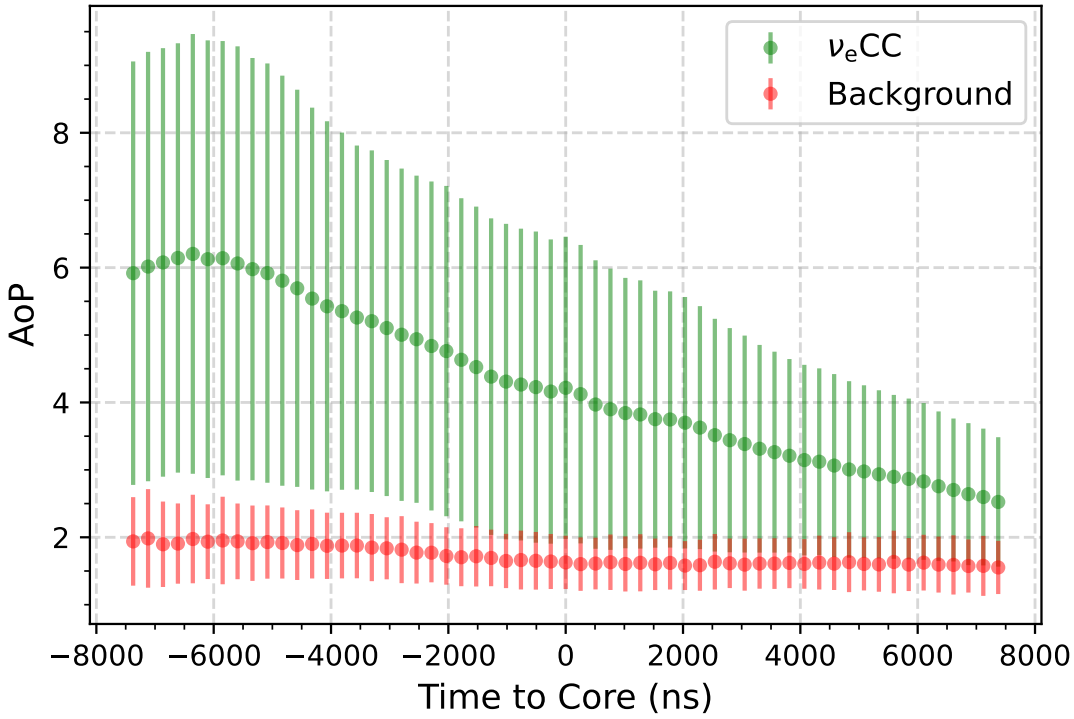

Figure 5.16: Distribution of the Area over Peak of all stations as a function of their relative time to the core for all events in the background training sample that pass the pre-selection cuts. The background sample is represented by the red points while the CC neutrino sample is represented by the green points. The error bars represent the spread of the distribution.

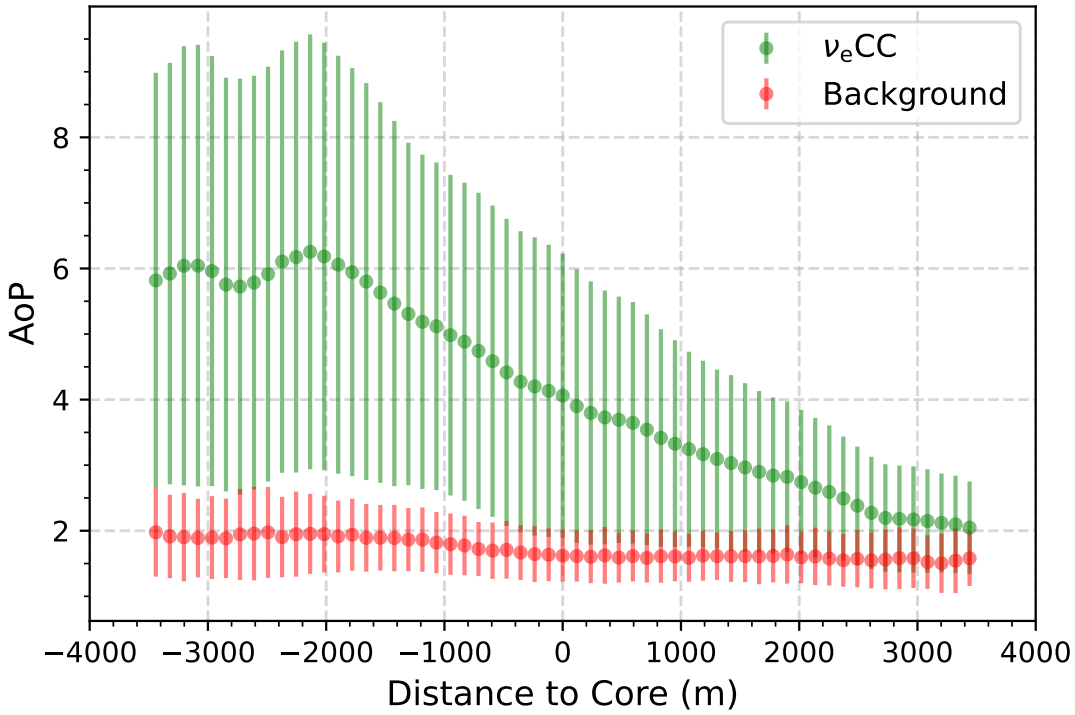

Figure 5.17: Distribution of the Area over Peak of all stations as a function of their projected distance to the core for all events in the background training sample that pass the pre-selection cuts. The background sample is represented by the red points while the CC neutrino sample is represented by the green points. The error bars represent the spread of the distribution.

Fisher polynomials and training

It is really important to find the correct features or variables to train the algorithm to achieve the best possible separation. Various combinations of input features were tested and evaluated based on the level of separation along with the shape of the tail of the background description which is important for the cut evaluation procedure. As mentioned before, AoP (Fig. 5.15) will remain the primary feature used for discrimination. It was also shown in [23] that for the DG_{low} channel AoPs of the earliest stations closest to the core provide the best level of discrimination between data and background. This also visualized in figs. 5.16,5.17. Further, the zenith angle range for the search, $58.5^\circ < \theta < 76.5^\circ$ is subdivided into five sub-regions similar to [23] as shown in Fig. 5.19. This is done to incorporate shower age while training the Fisher polynomial. The first four angular regions are 3° each whereas the last region is 6°. This is due to the small amount of statistics observed for higher angles in the background training sample which required a larger window size. For each angular window the Fisher polynomial is trained separately to maximize the analysis performance.

Different forms of the Fisher polynomial were tested, and their performance was evaluated

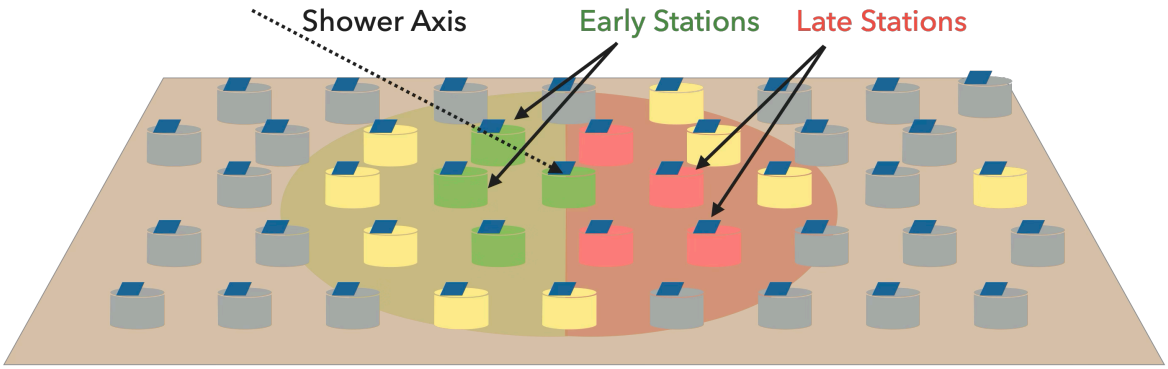

Figure 5.18: An illustration to depict the station selection process for the Fisher polynomial. The AoPs of the green stations are used to build the Fisher polynomial i.e. stations triggered earliest in the first crown. Stations in yellow are the ones triggered by the EAS and take part in the shower reconstruction.

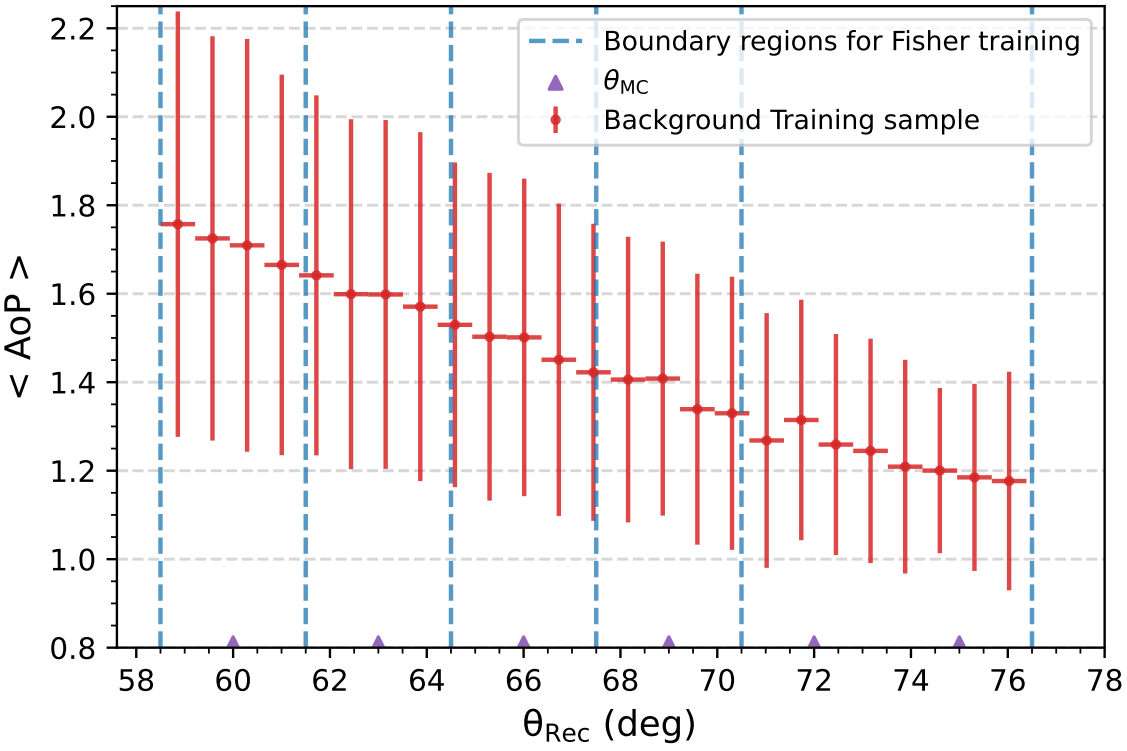

Figure 5.19: Distribution of the Area over Peak of all T5 stations as a function of their reconstructed zenith angle. The vertical dashed blue lines mark the five sub-regions split for individual analysis. The error bars represent the spread of the distribution. The purple triangles mark the simulated zenith angle values for the simulations.

based on the MC neutrinos passing the evaluated Fisher cut which is described in the next section. In this section the two forms compared are mentioned, the baseline polynomials were taken to be the one described in the previous analysis [23]. For the first three angular regions ($58.5^\circ \leq \theta_{\mathrm{Rec}} < 67.5^\circ$) a more stringent criterion which requires the AoPs of the first five triggered T5 stations along with their product was used to build the Fisher polynomial. For the remaining two angular regions ($67.5^\circ \leq \theta_{\mathrm{Rec}} < 76.5^\circ$) only the AoPs of the first four triggered T5 stations along with their product were required. The form of the Fisher polynomial used in the previous analysis is given below:

$$\mathcal{F} = \sum_{i=1}^{4\,\mathrm{or}\,5} C_i \mathrm{AoP}_i + C_p \prod_{i=1}^{4\,\mathrm{or}\,5} \mathrm{AoP}_i \,, \tag{5.7}$$

where C_i and C_p are the corresponding Fisher coefficients.

A modified version of this baseline polynomial was used for this analysis. The product term was found to not have a significant contribution to the separation and was thus removed for this analysis. Further, the requirement of five stations for lower angular regions was also eliminated which effectively lowered the minimum number of stations required for each event. The form of the polynomial used is :

$$\mathcal{F} = \sum_{i=1}^{4} C_i \mathrm{AoP}_i \tag{5.8}$$

The performance comparison of the two polynomials is discussed in the next section.

As mentioned before to train the Fisher polynomial 20% of the measured data sample for the time period 2014-2021 is used as the background training sample. Since this is measured data at the detector it is already weighted by energy (cross-section is a function of primary energy) and zenith angle (affects available detection area). For the MC neutrino events (signal sample) which do not have this natural weighting, each event is weighted by a factor of $\omega = E_{\mathrm{MC}}^{-1} \cdot \sin(\theta_{\mathrm{MC}}) \cdot \cos(\theta_{\mathrm{MC}})$. The Fig. 5.20 shows the Fisher value, $\mathcal{F}$ distributions for both signal and background training distributions for all five angular regions. An excellent separation is achieved for all angular regions.

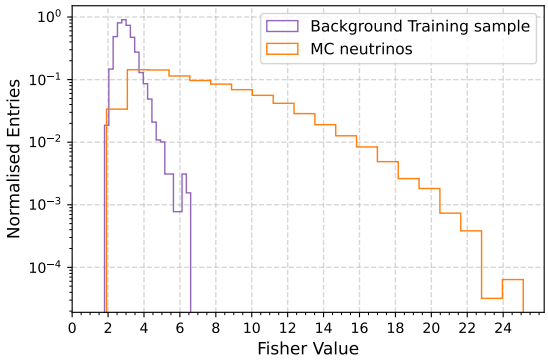

(a) $58.5^\circ < \theta_{\text{Rec}} \leq 61.5^\circ$

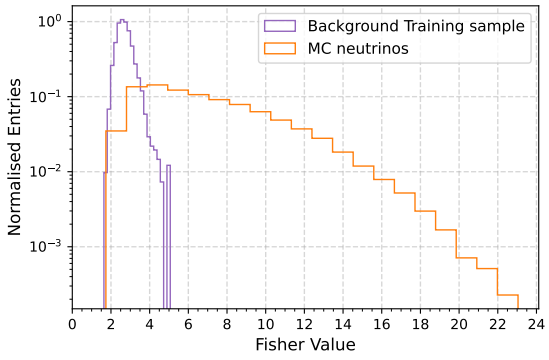

(b) $61.5^\circ < \theta_{\text{Rec}} \leq 64.5^\circ$

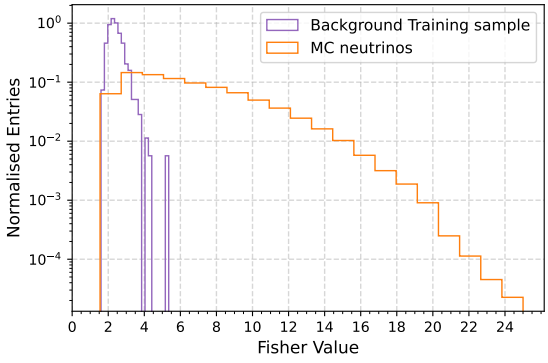

(c) $64.5^\circ < \theta_{\text{Rec}} \leq 67.5^\circ$

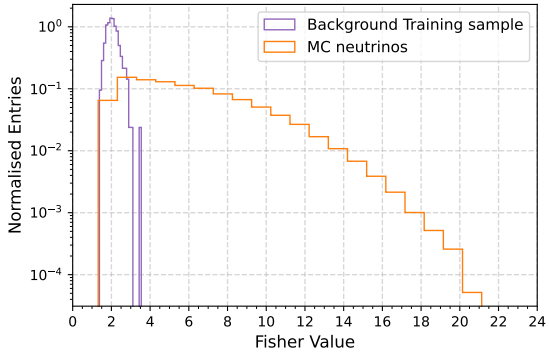

(d) $67.5^\circ < \theta_{\text{Rec}} \leq 70.5^\circ$

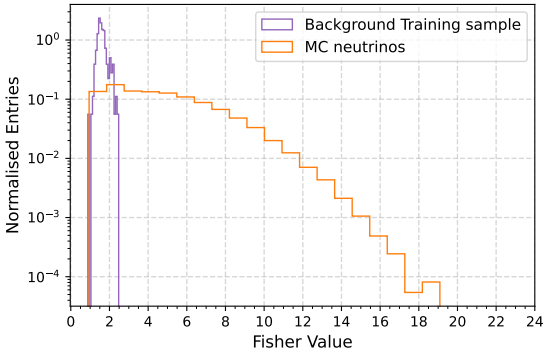

(e) $70.5^\circ < \theta_{\text{Rec}} \leq 76.5^\circ$

Figure 5.20: Fisher polynomial distributions ($\mathcal{F}$) for the signal (MC neutrinos) and background training samples (20% data) for the different angular sub-regions.

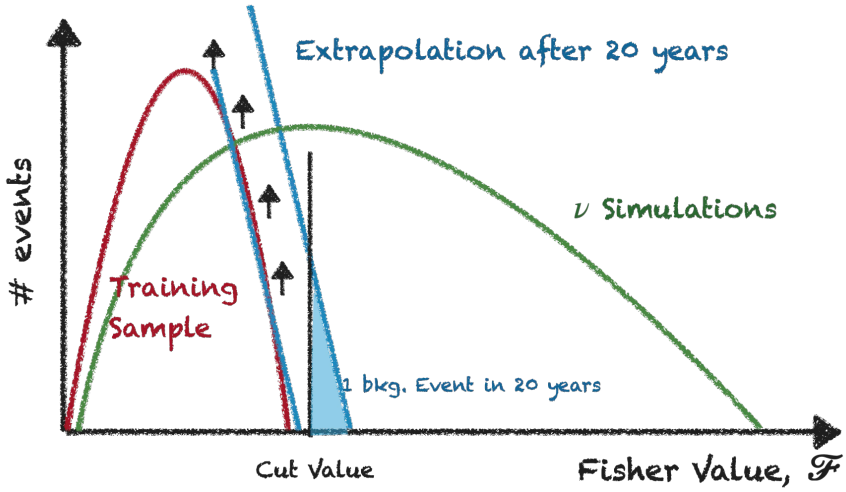

Figure 5.21: Schematic representation of the Fisher cut determination procedure.

Fisher Cut and background estimation

After the training process a cut criterion is still needed to be established to best separate the signal and background distribution. This cut is evaluated by analysing the tail of the Fisher value distribution of the background.

The tail is fit using an exponential function in the logarithmic scale ($A\mathcal{F} + B$). The fitting is done between $\mu + \sigma$ and $\mu + 4\sigma$ where μ is the mean and σ is the RMS value of the distribution. The exponential assumption is only a reasonable guess especially due to the low statistics of the last few bins. The bin size can also affect the fit and is determined for each angular region by minimizing the residual fit. This bin size is also verified with the Freedman-Diaconis method available in python to negate the possibility of over binning or under binning. Table 5.3 shows the *observed* and *predicted* values for the exponential fit procedure. The values are calculated by integrating over the range starting from the initial point specified in the first column and extending up to $+1\sigma$. The estimate using the exponential fit mostly agrees with the observed values. It agrees the best near the mean of the distribution and becomes slightly worse near the tails. In the higher angular regions a secondary bump like structure is also seen. This is attributed to the form of the Fisher polynomial and the lack of the product term. The predicted values also include the uncertainties of the fit which slightly increases the predicted number of the background events. The cut, $\mathcal{F}_{\text{cut}}$ is calculated such that after 20 years of data taking with a full SD array 0.2 events are expected to pass for each angular sub-regions with a total of 1 background event for the full search angular range.

$$\mathcal{F}_{\text{cut}} = \frac{\log[1.25 \cdot \text{B} \cdot 0.2 \cdot \Delta(\mathcal{F})/20] - \text{A}}{\text{B}} \tag{5.9}$$

Fig. 5.22 shows the $\mathcal{F}_{\text{cut}}$ obtained for the different angular regions.

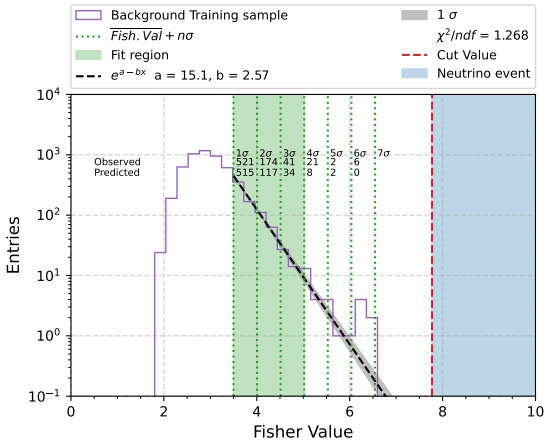

(a) $58.5^\circ < \theta_{\text{Rec}} \leq 61.5^\circ$

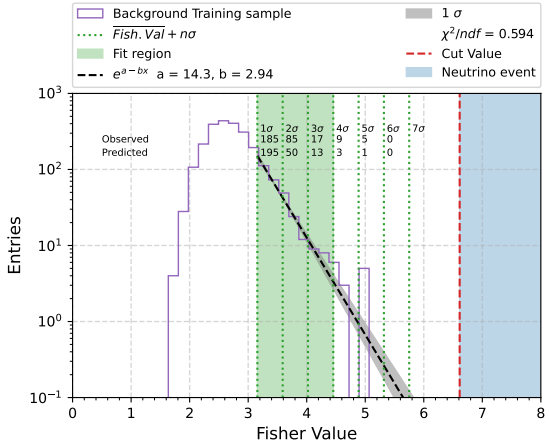

(b) $61.5^\circ < \theta_{\text{Rec}} \leq 64.5^\circ$

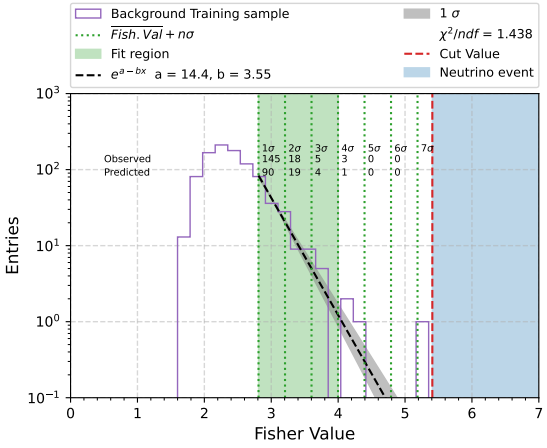

(c) $64.5^\circ < \theta_{\text{Rec}} \leq 67.5^\circ$

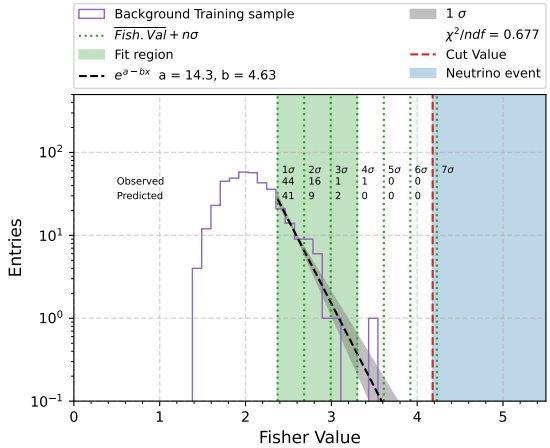

(d) $67.5^\circ < \theta_{\text{Rec}} \leq 70.5^\circ$

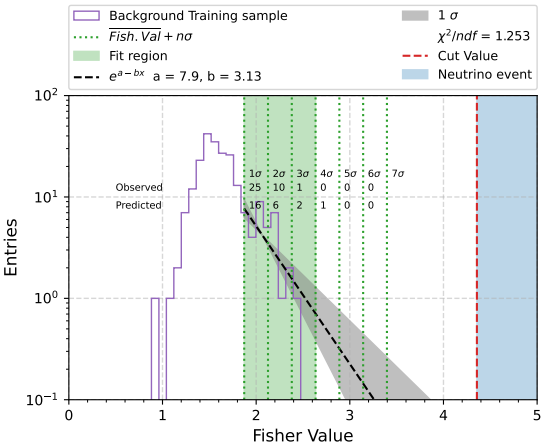

(e) $70.5^\circ < \theta_{\text{Rec}} \leq 76.5^\circ$

Figure 5.22: Fisher Cut determination for the different angular sub-regions. The $\mathcal{F}$ distributions of the background training sample are plotted in purple. The exponential fit is shown in black with green marking the fitting region for the fit. The numbers in text indicate the comparison for Observed and Predicted events in each region, see text for more details. The red line indicates the $\mathcal{F}_{\text{cut}}$ obtained from the fit.

Fit Range	Number of events in $\mathcal{F}$ tails Observed - Predicted				
	Region 1 (58.5°-61.5°]	Region 2 (61.5°-64.5°]	Region 3 (64.5°-67.5°]	Region 4 (67.5°-70.5°]	Region 5 (70.5°- 76.5°]
$\mu + 1\sigma$	521 - 514.5	185 - 195.1	145 - 90.2	44 - 40.7	25 - 15.6
$\mu + 2\sigma$	174 - 116.8	85 - 49.8	18 - 18.8	16 - 8.6	10 - 5.6
$\mu + 3\sigma$	41 - 33.6	17 - 12.7	5 - 3.9	1 - 1.5	1 - 2.04
$\mu + 4\sigma$	21 - 7.6	9 - 3.2	3 - 0.8	1 - 0.3	0 - 0.7
$\mu + 5\sigma$	2 - 2.2	5 - 0.8	0 - 0.2	0 - 0.1	0 - 0.3
$\mu + 6\sigma$	6 - 0.5	0 - 0.2	0 - 0.0	0 - 0.0	0 - 0.0

Table 5.3: Evaluation of the exponential fit for the Fisher cut determination. The observed and predicted (from the fit) number of events in the tail of the Fisher distribution are shown for each angular sub-region. The numbers are calculated by integrating from the start point mentioned in the first row till the $+1\sigma$.

The final coefficients obtained are tabulated in Appendix D and the cut value for each angular region is presented in table 5.4. The two polynomials mentioned in the above section are evaluated based on the fraction of neutrino events passing the $\mathcal{F}_{\text{cut}}$. The numbers are calculated relative to the number of surviving events right before the Fisher analysis. As can be seen in Fig. 5.23 the simplified Fisher polynomial either matches or outperforms the polynomial used in the previous analysis. The comparison is done only for the case where new triggers are included. The much higher number of events in this sample are required to achieve a sufficiently high background-signal separation especially in the low zenith angular regions of the selected range where previously a more stringent number of station cut was needed to reduce noise. However, the new Fisher polynomial seems to perform better even for higher angles which could lead to an overall improvement of neutrino detection efficiency irrespective of energy. This is proved later in section 6.1. Based on this comparison the polynomial given in eq. 5.8 was used for signal-background separation is this analysis.

A two-dimensional plot with the Fisher values on an event by event basis as a function of the zenith angle is shown in Fig. 5.24. The black dots represent the background events and the 2-D histogram represents the signal events. The red line is obtained by setting the $\mathcal{F}_{\text{cut}}$ to the mid-value of the bin and extrapolating for a particular angular sub-region. The background events seem to be distributed non-uniformly within the angular subsamples. The linear interpolation ensures that the effective number of events is almost constant with the zenith angle. Anything above the cut line is considered as a neutrino candidate.

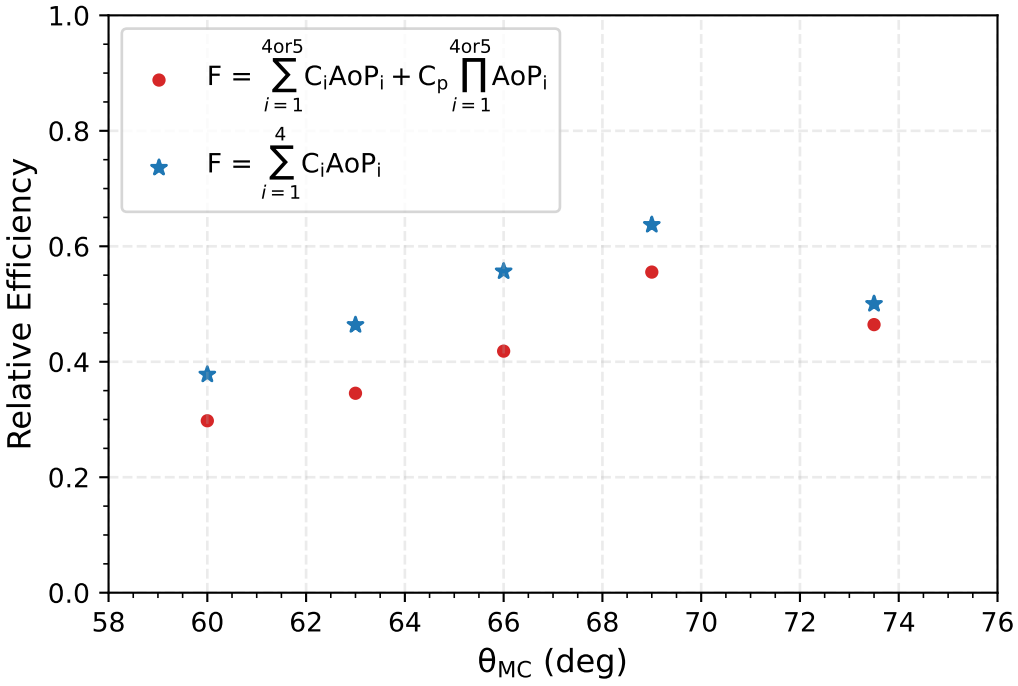

Figure 5.23: A comparison of the two different forms of Fisher polynomials tested in this analysis. The blue stars represent the efficiency of the new Fisher polynomial and the red dots represent the efficiency of the polynomial used in the previous analysis. The efficiency is calculated as the fraction of neutrino events passing the $\mathcal{F}_{\text{cut}}$ relative to the number of surviving events right before the Fisher analysis.

ν selection summary					
Inclined Sel. $\theta_{\text{Rec}} \in$	Region 1 (58.5°-61.5°]	Region 2 (61.5°-64.5°]	Region 3 (64.5°-67.5°]	Region 4 (67.5°-70.5°]	Region 5 (70.5°- 76.5°]
	$\delta\theta_{\text{Rec}} < 3^{\circ}$				
Fiducial Quality	6T5				
Young Shower Sel.	75 % of T5 stations to be ToT/ToTd/MoPS				
Angular Fit Quality	$\chi^2_{\text{red}} < 200$				
Fisher Discrim. $\mathcal{F}$	$\sum_{i=1}^{4} C_i AoP_i$ i = number of first T5 triggered stations				
$(\theta, \mathcal{F}_{\text{cut}})$	(60°, 7.772)	(63°, 6.613)	(66°, 5.408)	(69°, 4.180)	(73.5°, 4.357)

Table 5.4: Summary of the selection procedure along with the $\mathcal{F}_{\text{cut}}$ values for the different angular sub-regions.

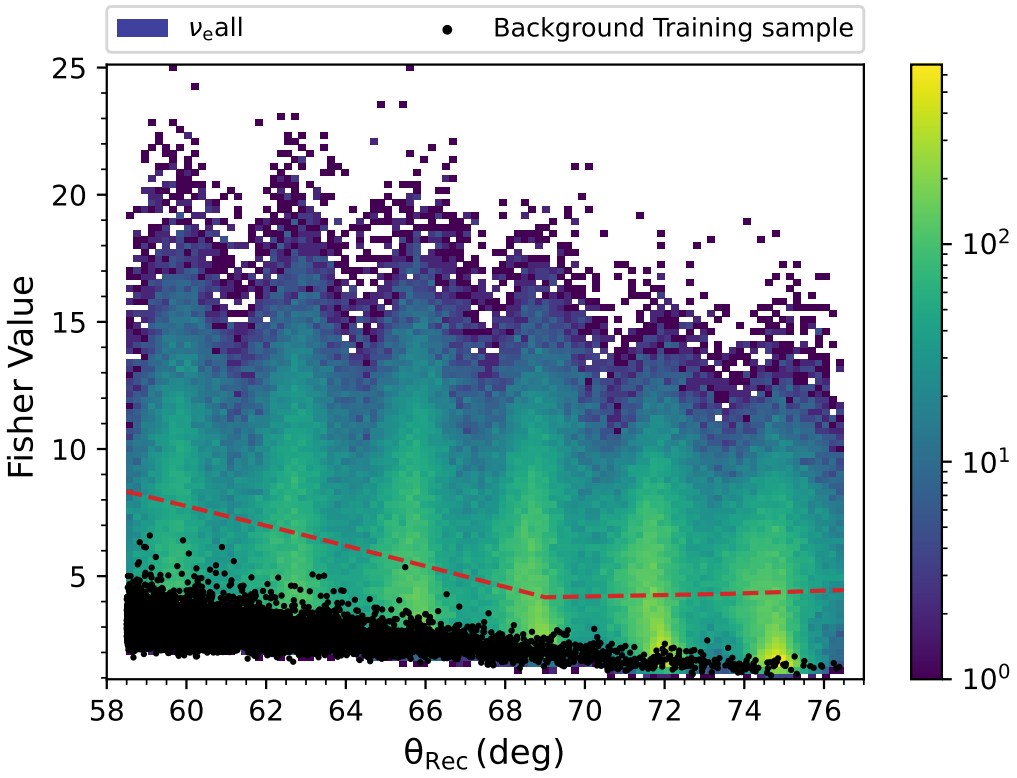

Figure 5.24: Distribution of the Fisher values for the signal (MC neutrinos) and background training samples as a function of θ_{Rec}. The black dots represent the background events and the 2-D histogram represents the signal events. The red line represents the interpolated $\mathcal{F}_{\text{cut}}$.

5.5.4 Time evolution of selection parameters

A time evolution study of the selection parameters used in the ν analysis is very important as any missed non-physical phenomenon which impacted data taking with the SD can erroneously affect the training procedure. Since the search sample is kept "blind" and the analysis is fixed based on the training samples, any missed error during the training procedure could result in fake neutrino candidates when the search sample is unblinded.

The first step that is taken to mitigate such instances is in the way the background training sample is chosen. Since the 20% background sample is chosen randomly over the same time period as that of the search sample it already should be a good representative of the search sample. The check is still performed to look for specific features for the selection parameters such as AoP, Fisher value and the Long signal fraction.

The values for these parameters are extracted from the background training sample and are plotted vs the SD Event ID which is correlated to time (higher ID, later time) and represents the time evolution of the array. Fig. 5.25 shows the evolution of the Long signal fraction with respect to the SD Event ID number. The Long signal fraction is likely to be time-

dependent [247] as the signal threshold for the triggers can be affected by changes in the SD stations (PMT degradation, change in linear reflectivity etc.). A decrease of $\sim 8\%$ is observed for the Long signal fraction which is similar to the one observed for the ToT fraction which is a discriminating variable used in the old analysis. There is an ongoing effort to include the effect of ageing of the detector for future detector simulations [248]. Since, this work is still ongoing it was not used for this analysis.

Fig. 5.26 show the evolution of AoP of the T5 stations selected for the Fisher analysis. AoP shows a slight modulation which could be related to the effect mentioned in [247] and was also observed in the previous DG_{low} analysis. This modulation was also observed to have a slight zenith angle dependence. Overall, this effect is very small and is not expected to affect the analysis.

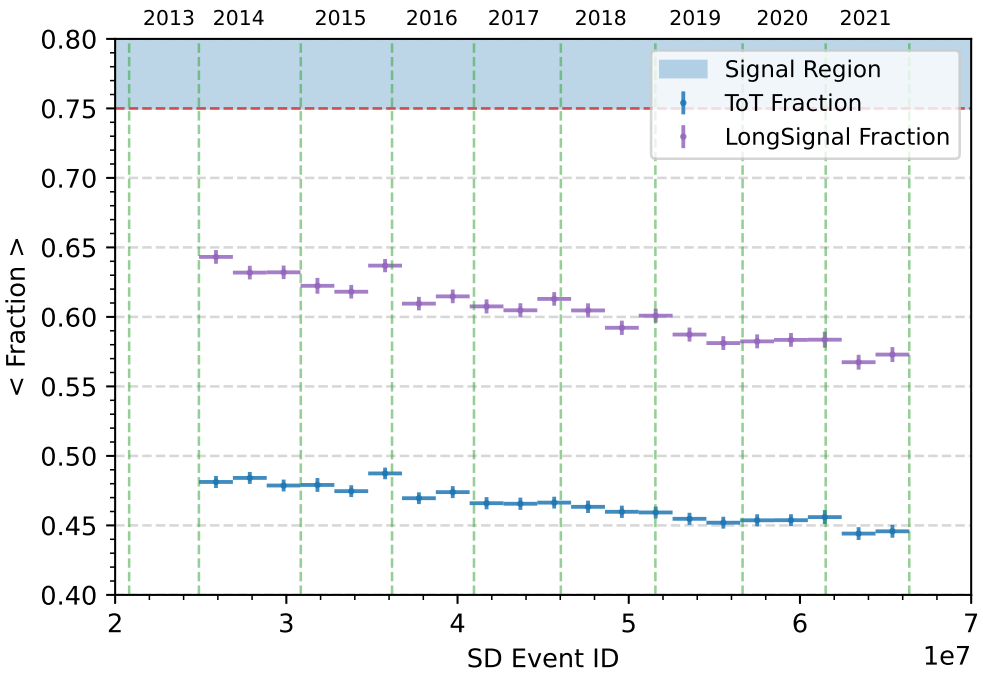

Figure 5.25: Comparison of average fraction of stations with ToT/ToTd/MoPS triggers (Long Signal fraction, purple) and stations with ToT triggers (ToT fraction, blue) for the background training sample. The fraction is calculated for the T5 stations that are used in the Fisher analysis.

Further the evolution of the Fisher value with respect to the SD Event ID is shown in Fig. 5.27. The Fisher value is seen to be stable, within the errors, over the entire time period and the overall effect of the variation of AoP is less significant though still present for the Fisher value.

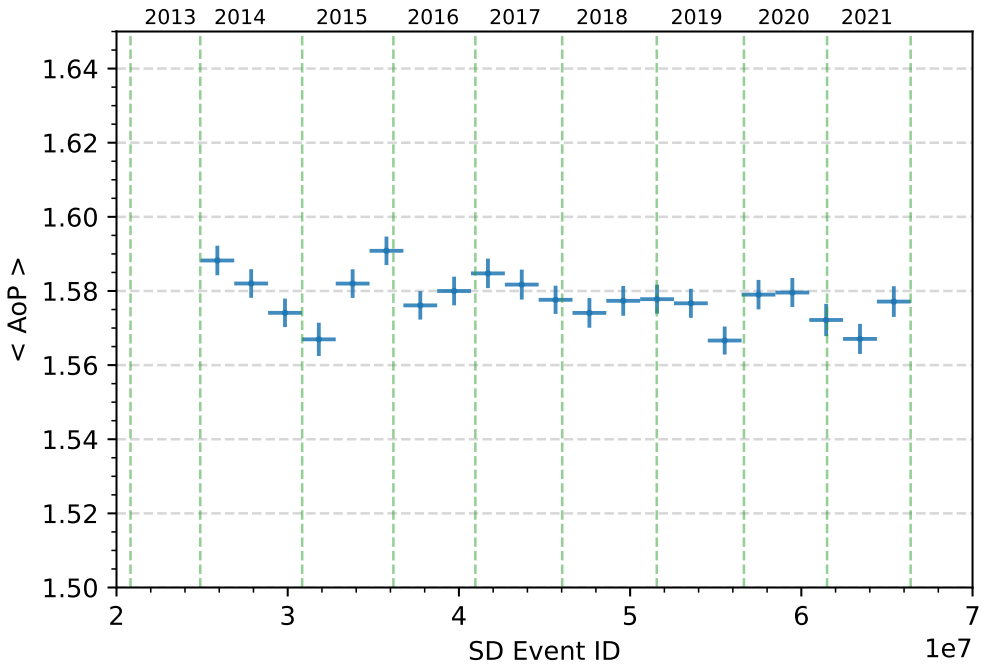

Figure 5.26: Evolution of average Area over Peak of the T5 stations used in the Fisher analysis for the background training sample with time.

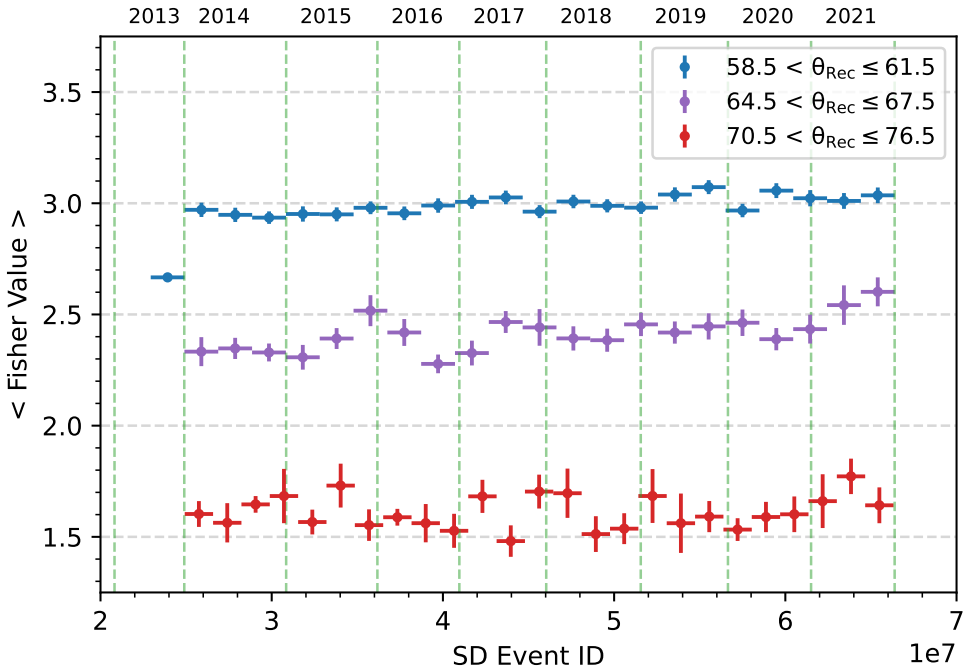

Figure 5.27: Evolution of the average Fisher value for the background training sample with time.

5.5.5 Neutrino Detection Efficiency

In this section, the detection efficiency at each stage of the ν selection procedure is determined and discussed. The efficiency is affected by a myriad of factors such as neutrino flavour, NC or CC interaction, energy, zenith angle and slant depth of interaction. The list is presented in table 5.5. The numbers are calculated with respect to the events remaining after the precedent cut except for the inclined selection where they are calculated against the number of reconstructed events. They are presented sequentially ordered according to the application of the cut in the selection chain. The values are obtained from MC simulations assuming a fully functional surface detector array.

ν selection efficiencies			
Cut		Efficiency	
		CC	NC
Inclined Selection	$58.5^\circ < \theta_{\text{Rec}}, \geq 76.5^\circ$	90.1%	89.5%
Quality Cuts	6T5 + $\delta\theta_{\text{Rec}} < 3^\circ$	79.25%	78.4%
Young Shower Selection	75 % of T5 stations to be ToT/ToTd/MoPS	84.9%	79.9%
Angular Fit Quality	χ^2/ndof < 200	88.7%	82.6%
Station Cut	No. of T5 triggered stations ≥ 4	86.7%	76.0%
Neutrino Selection	$\mathcal{F}_{\text{cut}}$	69.1%	37.1%

Table 5.5: The table shows the selection efficiencies for the MC sample across different cuts in the ν analysis. Efficiencies are computed relative to the events remaining after each preceding cut, except for the inclined selection, where they are calculated against the total number of reconstructed events. The results include efficiencies for both CC and NC interaction channels.

Relative efficiency for CC (NC) (%)					
Angular Region	$(58.5^\circ$-$61.5^\circ]$	$(61.5^\circ$-$64.5^\circ]$	$(64.5^\circ$-$67.5^\circ]$	$(67.5^\circ$-$70.5^\circ]$	$(70.5^\circ$- $76.5^\circ]$
Quality Cuts	70.9 (72.7)	71.3 (74.4)	73.2 (74.86)	88.1 (78.02)	88.5 (83.5)
Fit + T5 Candidates	75.0 (60.9)	74.6 (61.7)	74.9 (61.2)	75.6 (62.1)	79.9 (65.3)
Fisher Selection	58.6 (11.5)	69.6 (18.5)	75.3 (27.8)	80.3 (41.5)	64.3 (29.2)

Table 5.6: Relative efficiency of the most important selection cuts for the MC sample across different angular regions. The values in the brackets are the efficiencies for the NC channel.

The inclined shower selection removes $\sim$ 10% of showers. These showers were previously discussed in section 5.4. Most of these events are showers which interact very close to the ground which can lead to a mis-reconstructed zenith angle. Further, calculating the impact of $\delta\theta_{\mathrm{Rec}}$ both CC and NC events observe a strong reduction. Comparing to the analysis with old triggers this decrease is $\sim$10% higher for CC but similar for the one observed for NC interactions.

The errors associated with NC events tend to worsen with increasing zenith angle and decreasing shower energy which was also shown in the previous analysis. These conditions hinder the performance of the reconstruction algorithm, as both scenarios result in a limited number of triggered stations. Additionally, in the case of lower energies, certain geometric patterns, such as linear alignments, can adversely affect zenith angle determination.

The error distribution for the CC channel is shown in Fig. 5.28. For CC events, the significant decline in reconstruction performance with the inclusion of new triggers is primarily due to a deterioration in angular reconstruction. This issue may stem from several factors, such as the absence of a tuned segment selection algorithm for the new triggers or the susceptibility of these triggers to noise. It was also seen that neutrino events with a lower primary energy, where new triggers perform the best, have a higher absolute error on zenith angle further cementing this fact. Future improvements to the angular reconstruction algorithm, which were beyond the scope of this thesis, are proposed in chapter 8 to address these challenges and enhance performance.

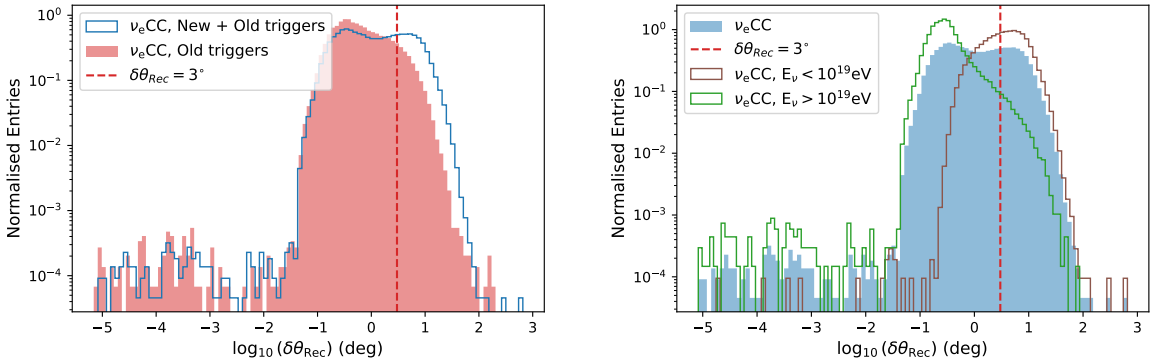

(a) $\delta\theta_{\mathrm{Rec}}$ comparison.

(b) $\delta\theta_{\mathrm{Rec}}$ for different primary energies.

Figure 5.28: Error distribution of the reconstructed zenith angle for the ν_e CC neutrino simulations. On the left the error distribution (blue) is compared to the one obtained from the sample with just old triggers (red). On the right the error distribution is compared for low (brown) and high energy (green) events for the sample with new triggers included.

The fiducial quality cut is inherently integrated into the reconstruction algorithm and, therefore, is not evaluated separately in this section.

The T5 candidate cut has a more pronounced effect on the NC channel than on the CC channel. This difference arises because the NC channel typically involves fewer triggered stations compared to the CC channel.

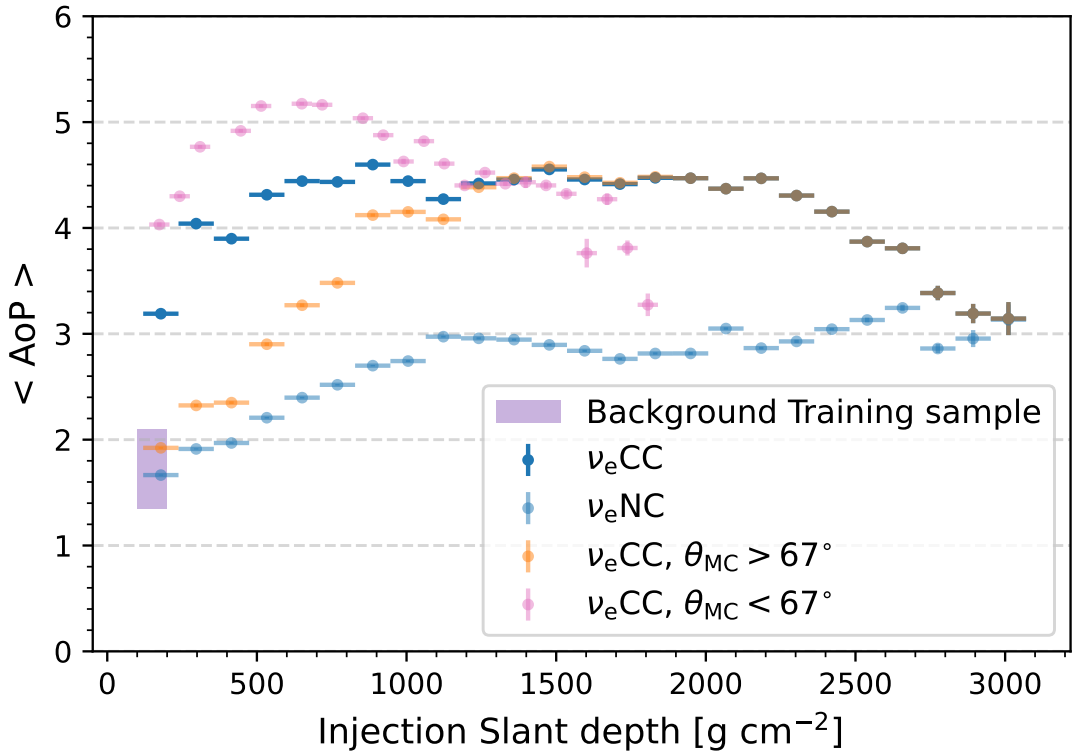

Figure 5.29: Average Area over Peak of the T5 stations used in the Fisher analysis for the signal training sample as a function of the injected slant depth. The AoP values for the ν_e CC channels are also subdivided into two angular regions for comparison. The AoP value range for the background training sample is shown as the purple box.

Additionally, the Fisher discrimination efficiency varies between the channels, performing better for the CC channel than for the NC channel as seen in table 5.5. This discrepancy is further investigated through the AoP distributions for the two channels (see Fig. 5.29). On average, CC events exhibit higher AoP values compared to NC events. Notably, the AoP values for NC events tend to fall between those of CC and background events, resulting in less effective separation for the NC channel. Overall, NC channel events retain a lower electromagnetic component when reaching the ground compared to CC events, a feature already highlighted in previous analyses.

Figure 5.30 compares the neutrino detection efficiency as a function of zenith angle for the CC channel for various primary energies. The efficiency generally increases with energy, reaching its maximum around $E \sim 10^{20}$ eV. As a function of zenith angle, the efficiency peaks near $\theta_{MC} \sim 70^\circ$ but begins to decline for angles exceeding $\sim 73^\circ$. This decline is attributed to the reduced electromagnetic component at the ground for highly inclined showers, which impacts the identification efficiency. Another contributing factor is the $\delta\theta_{Rec}$ quality cut, which disproportionately affects events with very high zenith angles due to limitations in the

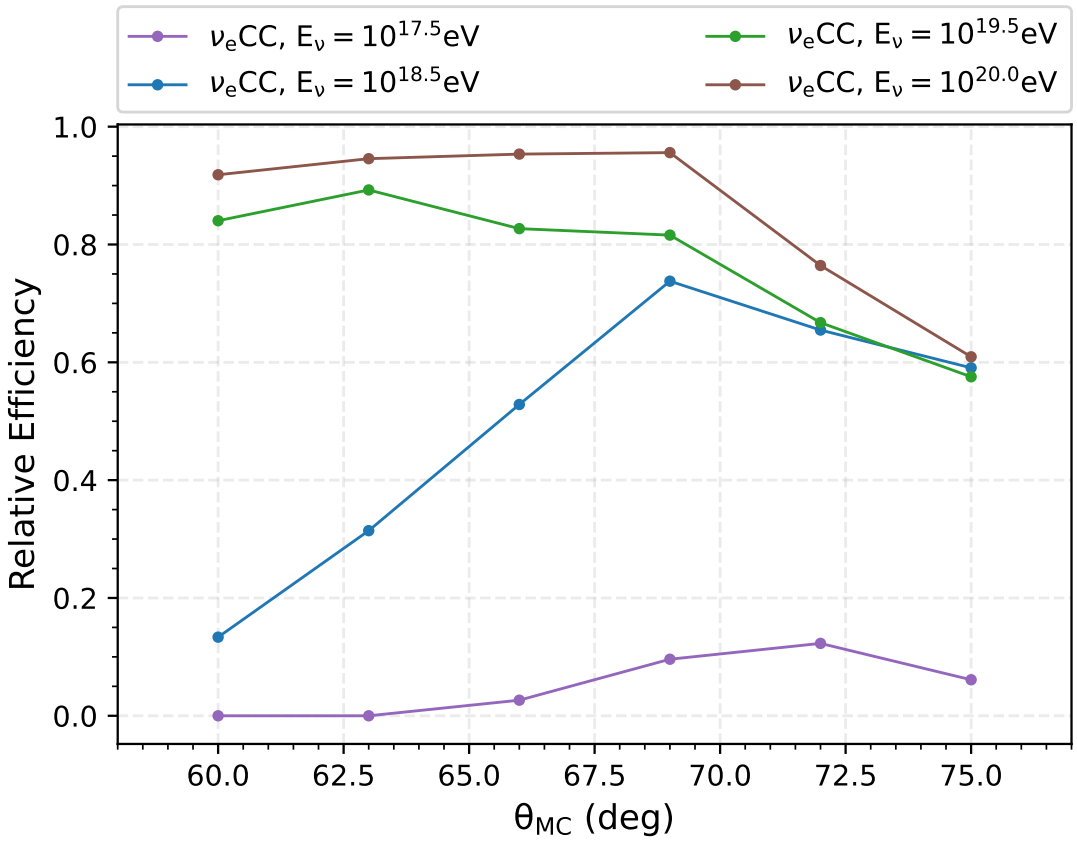

Figure 5.30: Relative fraction of CC events passing the selection cuts as a function of θ_{MC} for four different E_{MC} (different colours). The values are calculated relative to the events remaining after the preceding cut.

angular reconstruction algorithm for extremely inclined showers. Further it is also seen that since the efficiency for higher energies is already pretty high the effect of the new triggers is less pronounced for higher energies. This can also be further visualized in Fig. 5.31 where the trigger efficiency and the neutrino identification efficiency for two different primary energies and zenith angles are compared. As it is seen in the figure on the right for higher energies the trigger efficiency is ~ 1 for the injection slant depths close to the top of the atmosphere and decreases close to the detector where the shower does not get enough time to develop and trigger the stations for a good reconstruction. For lower energies such as the one presented on the left at low zenith angles of the explored range the new triggers can significantly improve the trigger efficiency.

The implementation of new triggers leads to a 20-50% improvement per simulated zenith angle in the neutrino detection efficiency for the DG_{low} channel, particularly for the CC channel, as illustrated in Fig. 5.32. The numbers for the sample with just old triggers are calculated relative to the events of the sample with new triggers which is significantly higher.

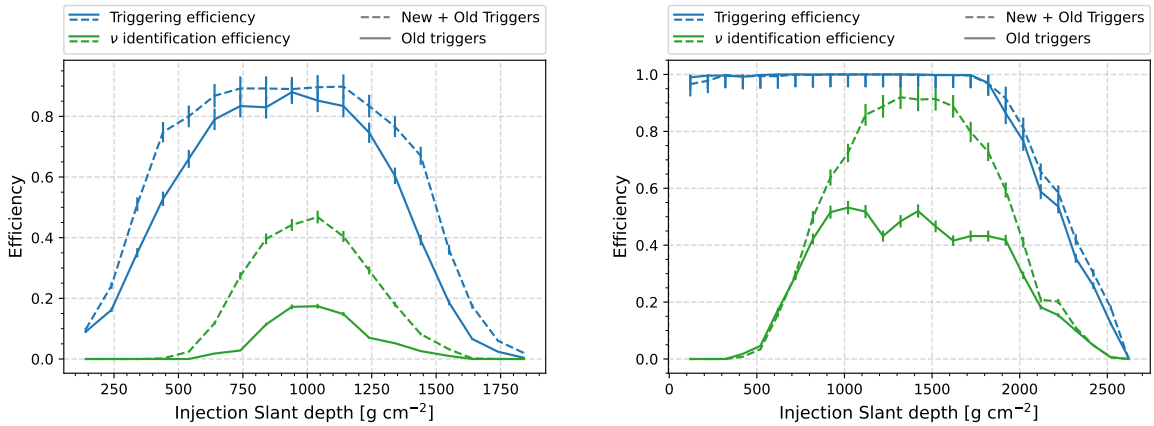

(a) $\log_{10}(E_\nu/eV) = 18.5$, $\theta_{MC} = 66^\circ$.

(b) $\log_{10}(E_\nu/eV) = 19.5$, $\theta_{MC} = 72^\circ$.

Figure 5.31: Comparison of the trigger (blue) and neutrino identification (green) efficiency as a function of injected slant depth for two different angles and energies for ν_e CC sample. The top of the atmosphere is at 0 g cm^{-2} and the SD depth changes according to the angle as shown in Fig. 5.6.

This is done to ensure a fair comparison since even though the relative efficiency of the sample with just the old triggers could be higher, the absolute efficiency i.e. the number of surviving events after all the cuts is way lower.

This improvement is most significant for energies up to $10^{18.5}$ eV and diminishes at higher energies. Several factors contribute to this enhancement. The new triggers increase the total number of detectable events, especially at lower energies, as demonstrated earlier in Fig. 5.13. Additional factors, such as reducing the minimal T5 station requirement for low angular regions and modifying the Fisher polynomial, also play key roles in improving the overall neutrino detection efficiency compared to previous analyses. While similar trends are observed for the NC channel, the overall efficiency remains lower than that of the CC channel.

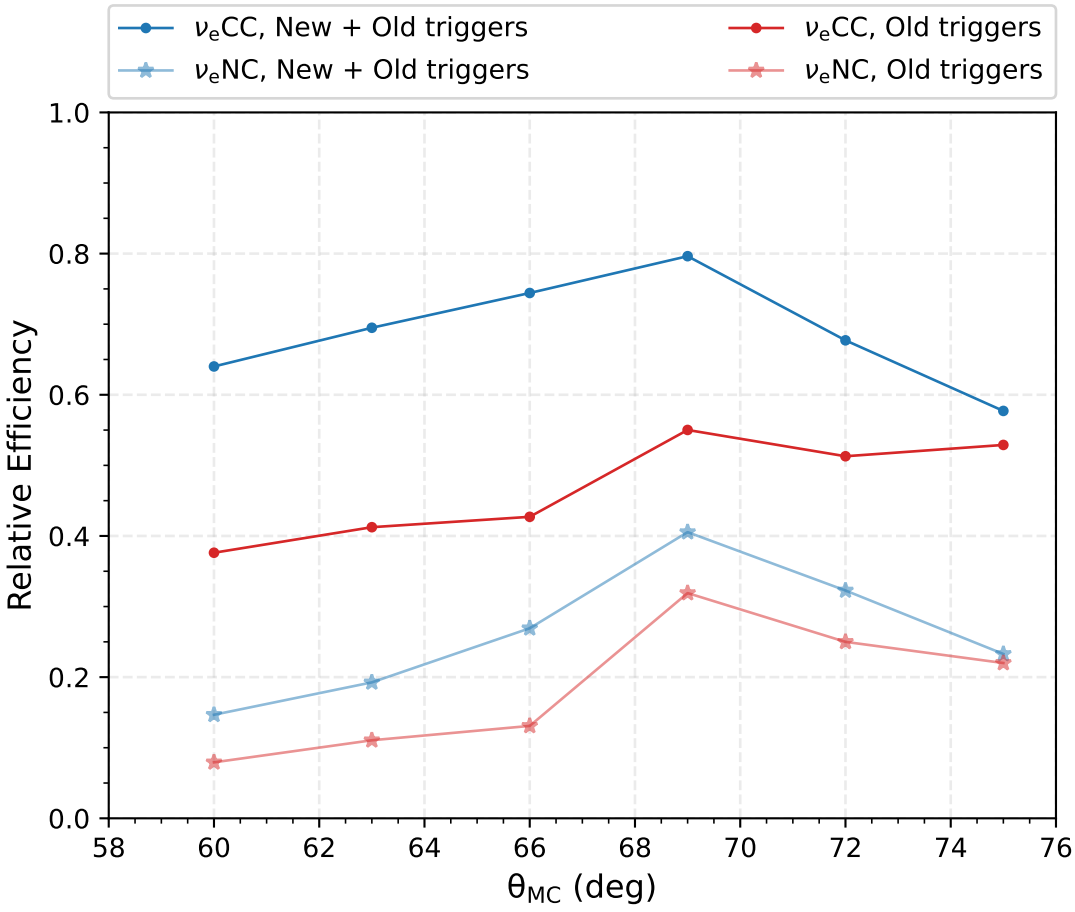

Figure 5.32: Comparison of the neutrino identification efficiency for both neutrino channels for the sample with the new triggers (blue) to the one without (red). For both the samples the efficiency is calculated relative to the events remaining after the precedent cuts in the sample with new triggers.

CHAPTER 6

Detector Exposure and Limits to the Diffuse Flux of UHEνs

This chapter aims to detail the procedure used to calculate the detector exposure or sensitivity to neutrinos for the DG_{low} region. The efficiencies calculated in the last chapter are used and the final expected neutrino rates are calculated. The first part of the chapter describes the exposure calculation along with the exposure contribution from different channels. Systematic uncertainties which can arise during the full analysis along with their contribution to the exposure are also discussed. The second part of the chapter details the results of the unblinding where no possible neutrino candidates were found for the investigated angular range. Using this information an upper limit on the incoming flux of UHEνs is calculated. This limit is further compared to the one obtained by the previous analysis for the same time period but without the contribution of new triggers. The overall improvement to this limit is a crucial result of this work.

6.1 Exposure Calculation

Exposure refers to the effective observation capability of a detector or observational setup over a specific time period, accounting for its sensitivity, the area it covers, and the duration of the observation. One of the most accurate techniques used at Auger to calculate the exposure of the SD array to UHEνs is through extensive simulations of different detector configurations. In this method MC neutrino showers are thrown over varied detector configuration to calculate the effective or active area at each instant of time. Since the detector configuration of the SD array is constantly changing (*faulty tanks, regular maintenance etc.*), sometimes on a daily basis, this technique requires a large amount of computational time and resources making it less desirable for use in this analysis.

A different approach based on the 6T5 condition, which is required for each selected event for this study, is used for the exposure calculation. For this calculation, the 6T5 hexagon is taken to be the smallest possible detection unit for the ν event. The effective area i.e. the area

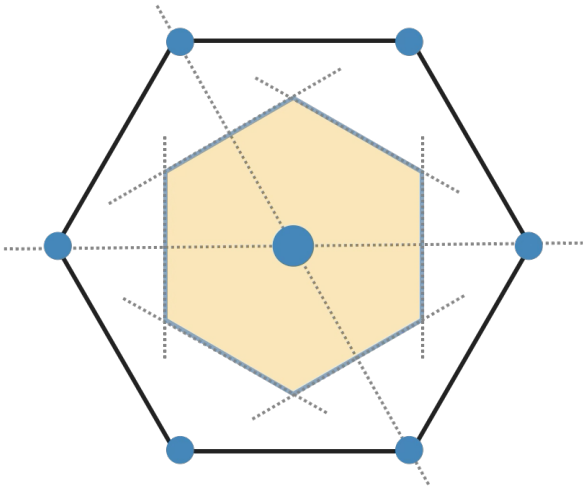

Figure 6.1: Sketch of a 6T5 hexagon of the SD array. The shaded area in yellow represents the Brillouin effective area (A_{6T5}) of the hexagon for a neutrino event.

where the neutrino can be observed for this detection unit at full efficiency is given by the Brillouin area [207], $A_{6T5} = 1.95\,\mathrm{km}^2$ as shown by the shaded area in Fig. 6.1. The aperture for this detector unit is dependent on the energy of the primary neutrino, the slant depth in the atmosphere of the first interaction, X, neutrino flavor (cross-section), type of the interaction (CC or NC), zenith angle, azimuth angle and the point of impact of the shower on the ground. The effective *acceptance* of the detector unit can be written as follows:

$$A_{hex}(E_\nu, X) = \int_{\phi=0}^{\phi=2\pi} d\phi \int_{\theta_{min}=58.5^\circ}^{\theta_{max}=76.5^\circ} A_{6T5} \cdot \varepsilon(E_\nu, X, \theta) \cdot \sin\theta \cos\theta \cdot d\theta, \quad [\mathrm{cm}^2\mathrm{sr}] \qquad (6.1)$$

where $\varepsilon(E_\nu, X, \theta)$ is the neutrino detection efficiency for each simulated energy, slant depth and zenith angle discussed in the last chapter. An example for a particular combination is given in Fig. 5.31 in the last chapter. Plots for efficiency for each combination can be found as part of the git repository made available for this analysis.

The next step involves integrating the *acceptance* over the different simulated injected slant depths (as given in Tab. 5.1) to account for the *effective mass* target for the neutrino identification over the 6T5 hexagon unit. It is calculated as follows:

$$M_{\mathrm{hex}}(E_\nu) = \int_X A_{\mathrm{hex}}(E_\nu, X) \cdot dX. \qquad (6.2)$$

Fig. 6.2 shows the effective mass for both CC and NC interaction channels for a single 6T5 hexagon unit. Like the detection efficiency it increases with energy.

Exposure calculation still needs to account for the detector configuration and its evolution over time. We reduced our array to units of 6T5 hexagons and a full SD array with 1660

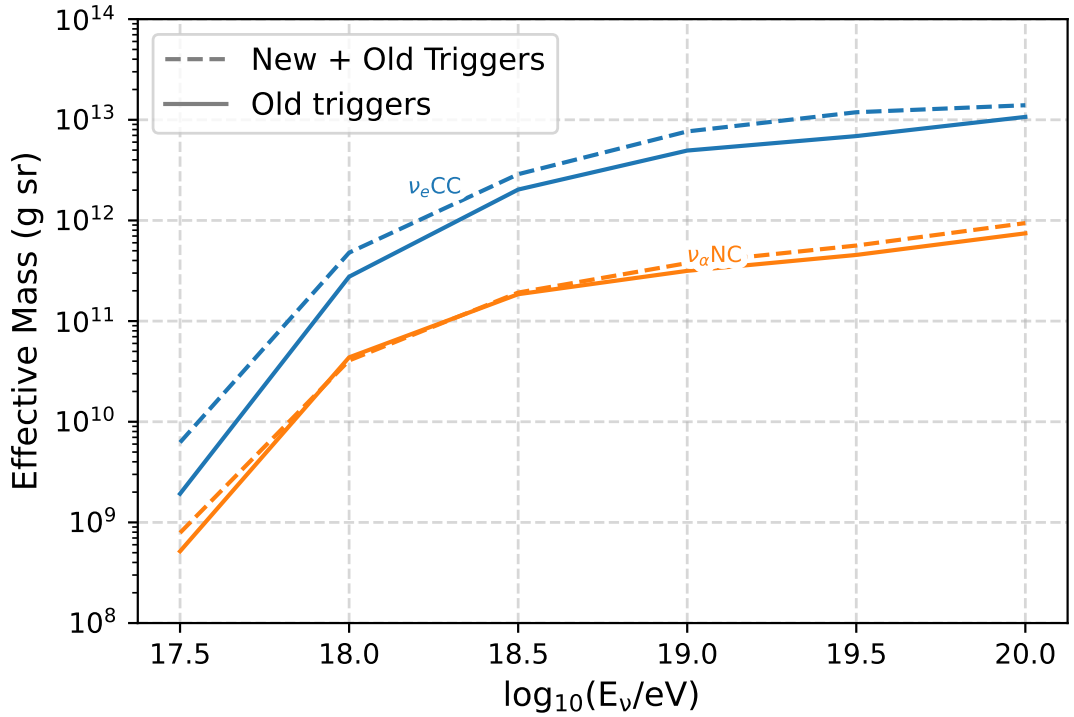

Figure 6.2: Effective mass for one 6T5 hexagon of the SD array for different neutrino flavors and interaction channels. The dashed lines are the calculated effective mass for this analysis and the solid lines is the effective mass calculated for the analysis performed without including new triggers.

stations consists 1420 of these hexagons. Since the establishment of the Pierre Auger Observatory the active number of 6T5 hexagons are monitored every second. This forms a very good indicator for the time evolution of the SD array since any non-working station or large periods of instability are intrinsically recorded in the number of active 6T5 hexagons at that time. The instantaneous number of hexagons, $n_{\text{hex}}(t)$ thus can be used as an indicator of detector configurations over time. The $n_{\text{hex}}(t)$ were updated and calculated every minute and have an uncertainty of about 1.5% as mentioned in [207] and also confirmed in this study. To calculate the energy dependent exposure, the effective mass of one 6T5 hexagon is multiplied by the instantaneous number of hexagons and integrated in time. Further, the ν interaction probability for each flavour (i = ν_e, ν_μ, ν_τ) and channel (c = CC, NC) is also folded in. The exposure is given as:

$$\xi^{i,c}(E_\nu) = \frac{\sigma^{i,c}(E_\nu)}{m_N} \int_t M^{i,c}_{\text{hex}}(E_\nu) \cdot n_{\text{hex}}(t) \cdot dt = \frac{\sigma^{i,c}(E_\nu)}{m_N} \cdot M^{i,c}_{\text{hex}}(E_\nu) \cdot N_{\text{hex}}, \tag{6.3}$$

$\sigma^{i,c}(E_\nu)$ is the neutrino nucleon cross-section taken from [249] and N_{hex} is the total number of active 6T5 hexagons integrated in time over the search period. The value for N_{hex} calculated

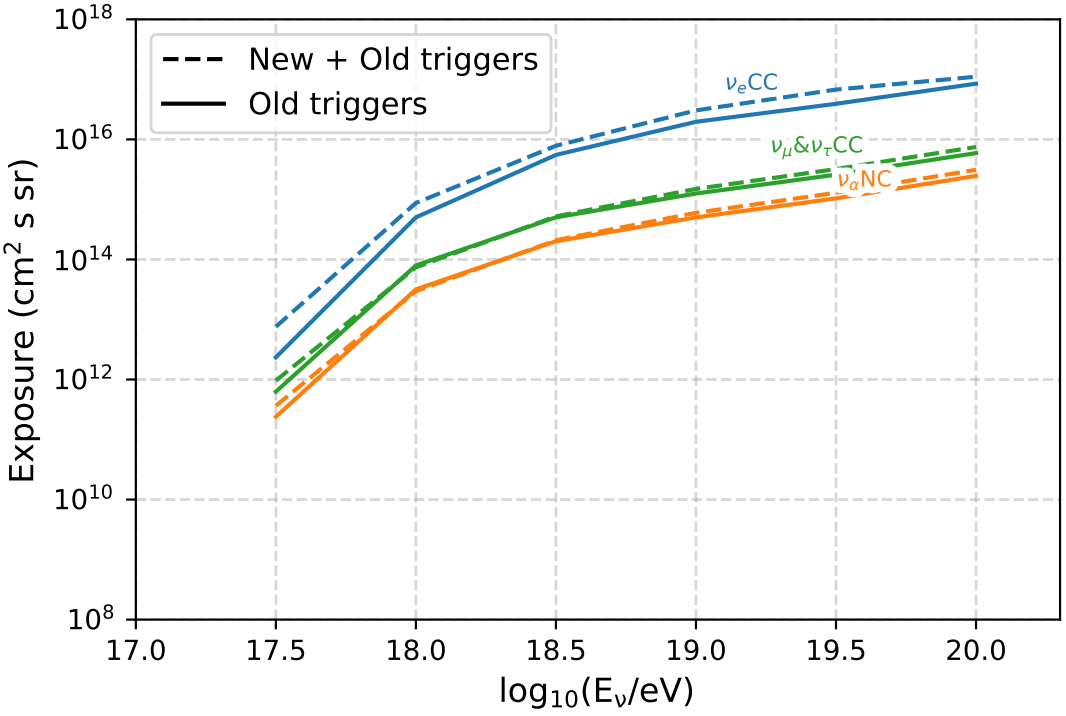

Figure 6.3: Exposure of the Pierre Auger Observatory for different neutrino flavors and interaction channels in the DG_{low} angular range for the time period 2014-2021. The dashed lines are the calculated exposures for this analysis and the solid lines is the exposure calculated for the analysis performed without including new triggers for the same time period.

for the period analysed is 2.8 $\times 10^{11}$ which is about ~6.75 equivalent years of a fully functional SD array. The energy dependent exposure for different flavors and interaction channels is shown in Fig. 6.3. It is necessary to point out again that the double bang showers which can be produced by ν_{tau} are not taken into account for this analysis.

An effective or total exposure, $\xi_{tot}(E_\nu) = \sum_i \sum_c \xi^{i,c}(E_\nu)$ is calculated by summing all the interaction channels and assuming a 1:1:1 flavour ration at earth (large propagation distances combined with neutrino oscillations) as shown by the red line in Fig. 6.4.

As seen in the figure, the ν_e CC channels contributes the most to the total neutrino exposure (~85%). The exposure rises rapidly at lower energies and then mostly flattens with just a slight increase which is due to the energy dependence of the neutrino cross-section. The shape is due to the neutrino detection efficiency which is small for lower energies as shown in Fig. 5.30 in the previous chapter. The next dominant channels are the ν_τ and ν_μ CC which are assumed to have a similar detection efficiency as the NC channel but have a higher value of cross-section. The NC channel contribution is not significant (~5%) due to the reasons discussed in section 5.5.5.

The exposure calculated in this analysis is also compared to the one calculated using

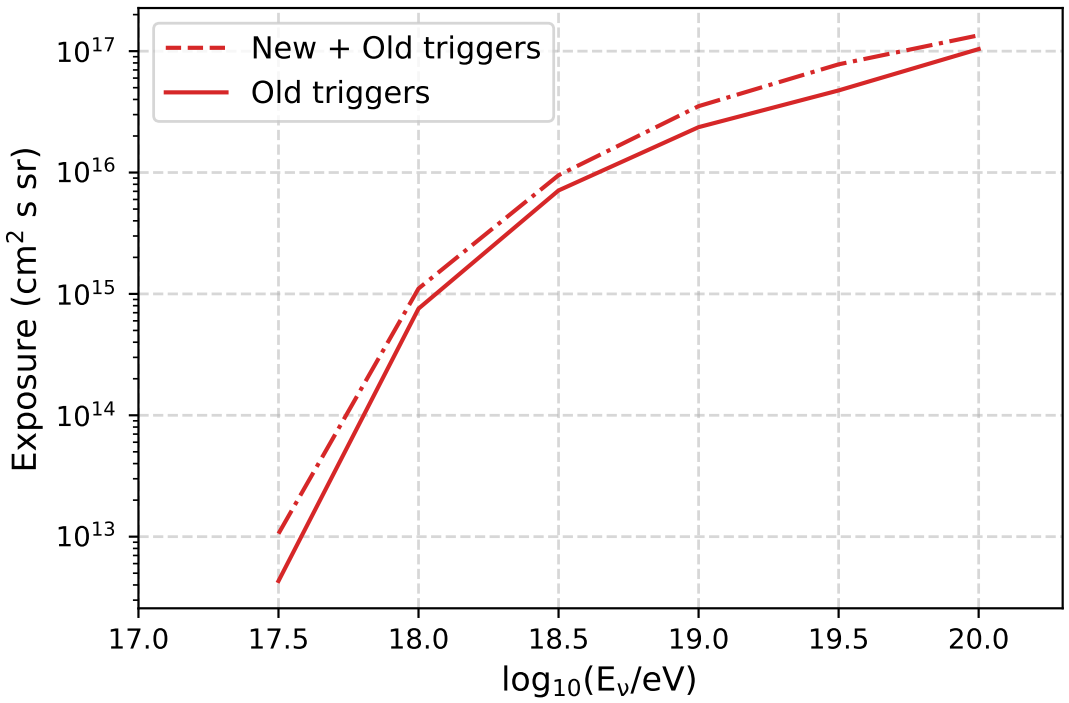

Figure 6.4: Comparison of the total exposure of the Pierre Auger Observatory for the time period 2014-2021. The dashed dotted line is the exposure calculated for this analysis and the solid line is the exposure calculated for the analysis performed without including new triggers for the same time period.

the previous analysis for the same time period in Fig. 6.3. For the CC channel a $\sim$ 5$\times$ improvement is seen at lower energies and a $\sim$ 2$\times$ improvement at higher energies. For NC this improvement is not that significant. There is a 2$\times$ improvement at lower energies and a 1.5$\times$ improvement at higher energies. The improvement at lower energies is due to the inclusion of the new triggers MoPS and ToTd which enhance the detection efficiency at lower energies. The improvement at higher energies is mainly due to the improved Fisher analysis. Since the ν_e CC contribution to the total exposure is significantly higher than other channels, the overall improvement to the total exposure is only slightly less than the improvement to the ν_e CC channel.

6.2 Systematic uncertainties

This section aims to detail the systematic uncertainties which can arise during the course analysis and their contribution to the exposure. The systematic uncertainties in an analysis can arise at any point. The investigations start already at the simulation level where the uncertainties from the primary interaction, hadronic interaction models, thinning etc. can

lead to uncertainties in the neutrino detection efficiency. At the next step the uncertainties in the reconstruction algorithms could also affect the final exposure. The cross-sections used for the final calculation of exposure could also prove to be a source of systematic uncertainties. Other parameters such as the number of hexagons are very well-defined parameters and are not expected to have a contribution to the systematic uncertainties in the exposure. For this analysis the systematic uncertainties are either sourced through previous analysis [250] or are calculated for certain cases. Since the analysis has been done once before, albeit without the new triggers, the sources of systematic uncertainties are sufficiently similar to [23]. The sources of systematic uncertainties considered for this analysis are discussed below:

Primary interaction generator: For the simulations used in this analysis which is based on CORSIKA 7.2 the only available option for the primary interaction generator is the HERWIG [219] code. Thus, it was not possible to compare the differences that could arise due to the use of different primary interaction generators. These systematic uncertainties were taken from [250] where PYTHIA [251] and several versions of HERWIG are compared for CORSIKA 6. The uncertainties were found to be [+2.6%, 3.7%].

Parton Distribution function: Again the uncertainties are taken from [250] since this functionality is not available in CORSIKA 7. The systematic uncertainties on exposure quoted by the source are [+4%, -5%].

Hadronic interaction models: The choice of the hadronic model used for the simulations can also lead to systematic uncertainties since most of these models are tuned on different accelerator datasets measured at much lower energies than the ones investigated in this analysis. Since the systematic uncertainties due to the hadronic models calculated in this analysis were found to be below the statistic uncertainties. A realistic estimate of the systematic uncertainties due to the hadronic models was taken from [250], particularly the uncertainty between QGSJET-II and SIBYLL which is the closest analogy to this study where SIBYLL 2.3d was chosen as the reference model. The systematic uncertainties were chosen to be +1%.

Shower simulator and thinning algorithm: The systematic uncertainties due to the differing shower simulation programs was estimated through the comparison quoted in [252] for both hadronic cascades and electromagnetic showers. The differences seen in different softwares are of the order $\sim$ 15% which agrees with the results from [250]. The uncertainties due to thinning were also calculated in [250] and were found to be $\sim$ 7%.

Detector simulation: The differences in the detector simulation software i.e. a GEANT4 based approach used in this analysis to other approaches is already compared in [253]. The systematic uncertainties were found to be ±5%. Further, in this analysis the simulated showers were reconstructed using two different Offline tags with no significant differences observed in the final exposure.

Number of Hexagons: To calculate the total numbers of hexagons it is implicitly assumed that all stations contribute equally. However, if the new triggers are not active due to problems with two PMTs in a given station, such a hexagon might not contribute the same as the other. This points to a systematic error associated with using the hexagon files as they are, as a station with one PMT is counted full but likely should not. For a neutrino analysis with new triggers, the unique situation of an active WCD station which is unable to use these triggers needs to be accounted for. The systematic uncertainty associated with this effect was calculated by looking at the average number of stations with only one functional PMT over time. The uncertainty associated with this effect was found to be $\leq \pm 2\%$.

Reconstruction algorithm: The effect of different reconstruction algorithm were also tested in this analysis. Two modules HASReconstructionOG and the normal top-down selection module were tested. Though the total number of events that are reconstructed by these modules can differ the difference in the final exposure is found to be $< \pm 1\%$.

Neutrino cross-sections: The systematic uncertainties due to the neutrino cross-sections were taken from [249] which are of the order $\pm 7\%$.

Table 6.1 summarizes the source of systematic uncertainties and their contribution to the total exposure. The total systematic uncertainties are calculated by adding them in quadrature. As discussed later in section 6.4.3 the uncertainties are directly incorporated in the limit by applying the Conrad method [254] to calculate the confidence intervals.

Source of systematic uncertainty	Contribution
Primary interaction generator	+3% -4%
Parton Distribution function	+4% -5%
Hadronic interaction models	+1%
Shower simulator	+15%
Thinning algorithm	+7% -7%
Detector simulation	+5% -5%
Number of Hexagons	+2% -2%
Reconstruction algorithm	+1% -1%
Neutrino cross-sections	+7% -7%
Total uncertainty	+19.5% -13%

Table 6.1: Systematic uncertainties and their contribution to the exposure.

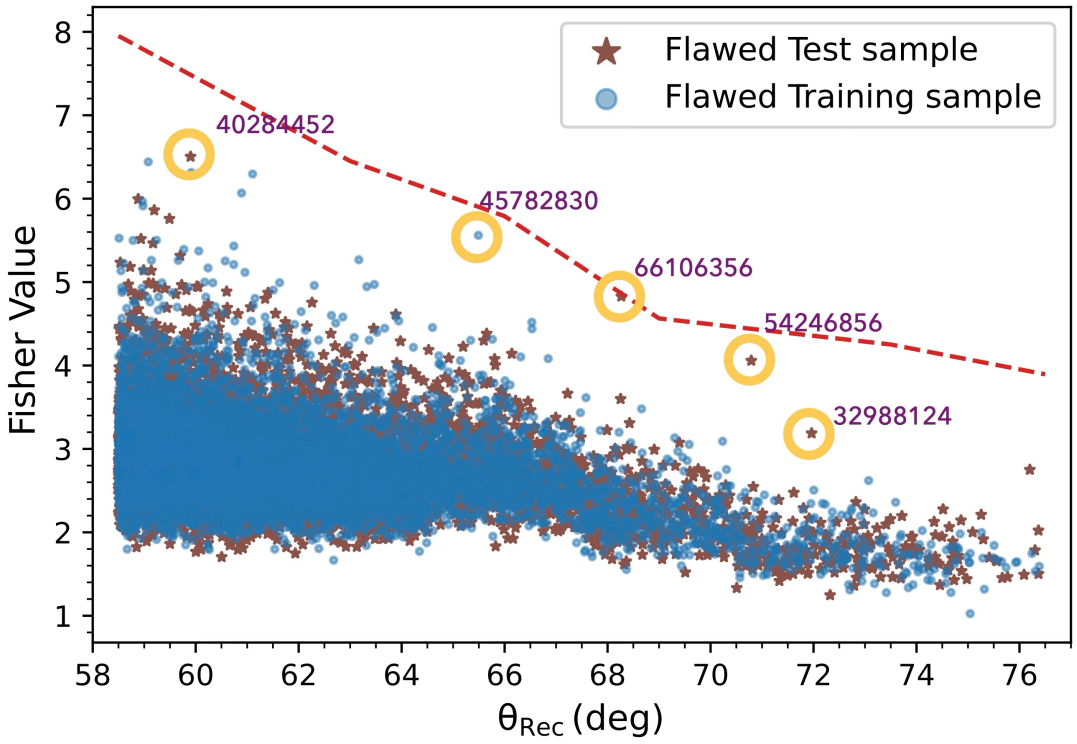

Figure 6.5: Distribution of the Fisher values for the background training sample (blue) and the test sample (brown) as a function of θ_{Rec} for the sample before the last fixes to the reconstruction were applied. The red line represents the interpolated $\mathcal{F}_{cut}$. The interesting events are marked with circles.

6.3 Data unblinding

As mentioned before in section 5.5.1 the search data consists of all events recorded at the Observatory between 2014-2021 which have a SD ID number non-divisible by 5 i.e. 80% of all SD data recorded between 2014-2021. This search data sample was further split into a 20% test sample such that from the 80% sample only those events where SD ID numbers were divisible by 4 were taken to be a part of the test sample while the rest became the part of the 60% search sample. This split was done to perform the unblinding in two stages. The first, where only the test sample in unblinded to detect any remaining flaws in the analysis. This exercise turned out to be useful as a slight error was uncovered during the unblinding process of the 20% test sample and was corrected. Said flaw, which is described in more detail later, required the whole reconstruction process along with the training of the Fisher polynomial to be performed again. This also effectively led to the unblinded 20% test sample to be re-blinded since the reconstruction was altered. The splitting procedure was repeated

SD Event ID	θ_{Rec}	Reason
32988124	71.96°	MoPS peak selection
40284452	58.88°	No particular feature
45782830	65.50°	No particular feature
54246856	70.79°	MoPS Peak selection
66106356	68.30°	Accidental station cut

Table 6.2: Summary of the vents analysed in more detail from the flawed 20% test sample. Some of these events are also discussed in App. C.

and the total unblinding was performed again in parts. It is important to mention in all of unblinding procedure **0 neutrino events survive** the analysis selection. This section is thus split into two subsections. The first describing the unblinding of the 20% test sample along with the changes brought about by this unblinding. The second section details the full unblinding of the redone search samples (test + remaining) and discusses the interesting features of the unblinded search samples.

6.3.1 Flawed 20% test sample

The Fisher value distribution for the test sample is shown in Fig. 6.5 where it is clear that no event passes the Fisher cut in any angular region. However, there are a few events which come very close to the cut line. Five events marked with a red circle were analysed in more detail. Each of them has its own unique reason with the one with zenith angle of 68.30° and SD Event ID of "66106356" being the most interesting. After investigating the event in detail it was found that the accidental station cut used is insufficient. Previously, the accidental cut (rejection of stations with Total signal < 3 VEM) is only applied to the event if there are more than 5 stations in the event. Since for this analysis due to the inclusion of MoPS and ToTd an overall increase in events is expected, which also increases the overall number of stations with accidental stations, this cut needs to be modified a bit to take this overall increase into account. The cut was modified and applied for events with more than 4 stations. This reduction decreases the total events passing the analysis cut by ∼5% for the background training sample and $1-2\%$ for the signal training sample. The Fisher coefficients and cuts change slightly. After this change in the reconstruction the test sample was obtained again and compared to the background sample as shown in Fig. 6.6. The other interesting events which have $\mathcal{F}$ values close to the $\mathcal{F}_{\text{cut}}$ with their respective IDs are tabulated in Tab. 6.2. These events were individually evaluated. Some of these were found to have a bad time residual fit primarily because of multiple peaks observed in stations triggered by the new triggers. Since no segmentation algorithm was used for stations with MoPS and ToTd triggers, sometimes a wrong peak was selected, affecting the reconstruction for these events. A future analysis with a corrected segmentation algorithm which is functional for the new triggers MoPS and ToTd is envisaged as the next step. Such events are expected to be limited to less than ∼1% of total events but still require a careful look for future analysis upgrades. A further detailed analysis

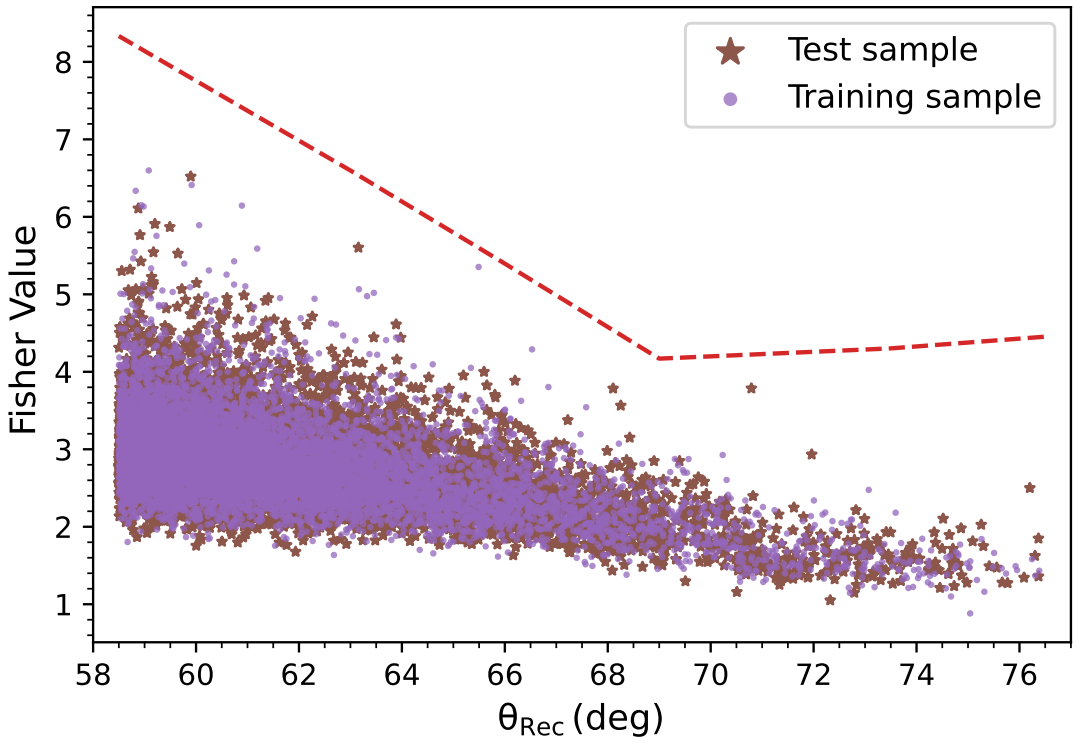

Figure 6.6: Distribution of the Fisher values for the background training sample (purple) and the test sample (brown) as a function of θ_{Rec}. The red line represents the interpolated $\mathcal{F}_{\text{cut}}$.

where the primary mass composition is extracted via the muon production distributions, as mentioned in [255], could not be performed for these events since the event had too few stations (~ 4) and the shower had a very low reconstructed energy both of which hinder the ability to extract any information about the primary. Such events were also seen in previous analysis albeit not these many. For the other events no particular feature worth mentioning was observed. Some figures with more information about the interesting events from this section are also included as a part of App. C.

6.3.2 Reevaluated 20% test search sample and 60% search sample

After the errors discovered in the initial partial unblinding were fixed by altering the reconstruction, the final unblinding was again performed in two stages. Initially a 20% part was unblinded and then the remaining 60% blinded sample was analysed. Again **0 neutrino candidates** were found after candidate selection. The Fisher value distributions as a function of reconstructed zenith angle for both the test and search samples are presented in Fig. 6.6 and Fig. 6.7 respectively. The results of the test sample (brown) and search sample (green) are overlaid over the background training sample (purple) in each plot with the dashed lines in-

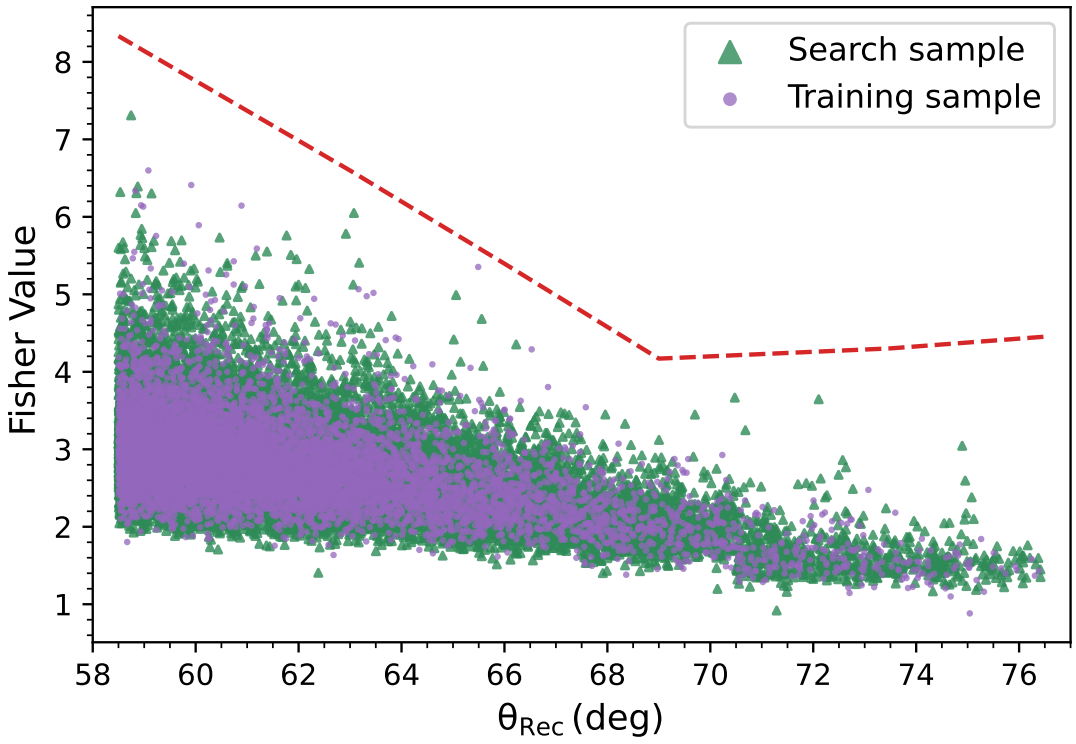

Figure 6.7: Distribution of the Fisher values for the background training sample (purple) and the search sample (green) as a function of θ_{Rec}. The red line represents the interpolated $\mathcal{F}_{\text{cut}}$.

dicating the value of the $\mathcal{F}_{\text{cut}}$ obtained according to Eq. 5.9. As it can be seen the distributions are compatible with each other within statistical fluctuations. The results of the unblinding for each angular sub-region for a combination of test and search samples is presented in Fig. 6.8. The distribution is scaled by the ratio of the integrals and the exponential fit is reevaluated again by comparing the Observed values to the predicted values from the fit. This comparison confirms that the exponential tail assumption is reasonable enough to determine the $\mathcal{F}_{\text{cut}}$. The goodness of the fit is once against presented in Tab. 6.3 in the form similar to Tab. 5.3. This time for the observed values the numbers are calculated from the much larger search sample. It is found that the tails of the distributions which typically seemed to have fit badly also fit reasonably well. The events in the search sample that have $\mathcal{F}$ values close to the $\mathcal{F}_{\text{cut}}$ were again carefully checked and were found to be either due to the issues with the segmentation algorithm or known issues such as partial shower containment or large number of non-working PMTs both issues have also been seen in previous analysis.

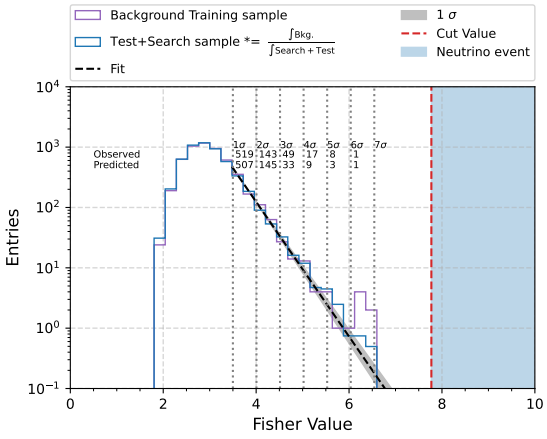

(a) $58.5^\circ < \theta_{\text{Rec}} \leq 61.5^\circ$

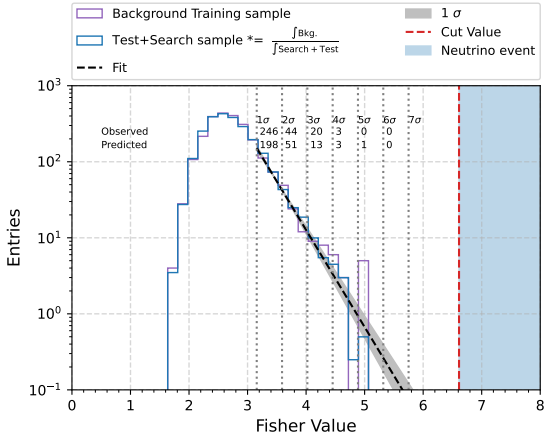

(b) $61.5^\circ < \theta_{\text{Rec}} \leq 64.5^\circ$

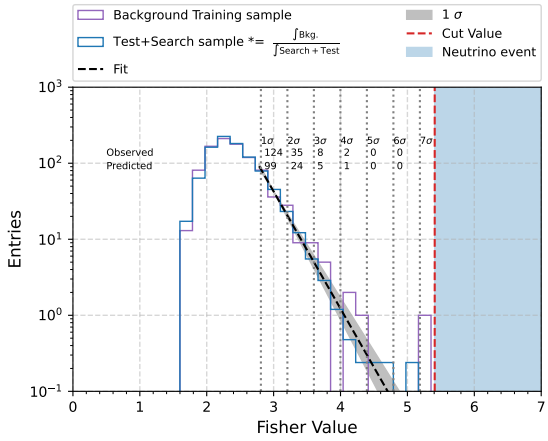

(c) $64.5^\circ < \theta_{\text{Rec}} \leq 67.5^\circ$ [1]

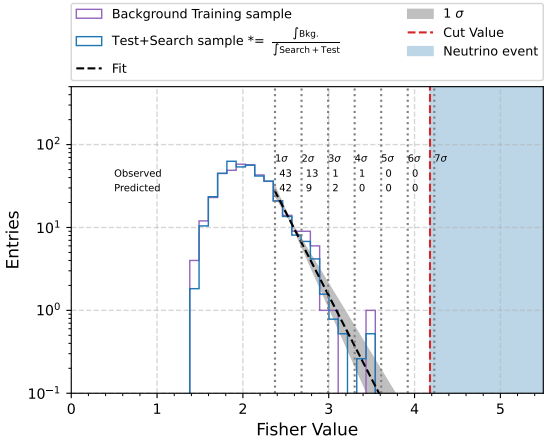

(d) $67.5^\circ < \theta_{\text{Rec}} \leq 70.5^\circ$

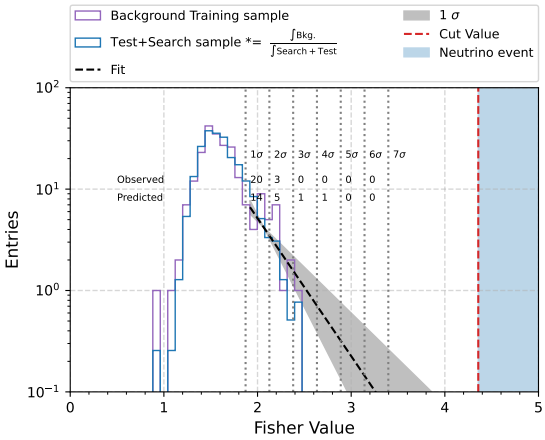

(e) $70.5^\circ < \theta_{\text{Rec}} \leq 76.5^\circ$

Figure 6.8: Comparison of the $\mathcal{F}$ value distributions for the background training (purple) and the test+search samples (blue) for the different angular sub-regions. The test+search sample is scaled by the ratio of the integrals of the background training and test+search samples. The black dashed line indicates the exponential fit to the tail of the distribution. The red dashed line indicates the value of the $\mathcal{F}_{\text{cut}}$ obtained from the fit. For the test+search sample the observed values are compared to the predicted values from the fit.

[1]

Fit Range	Number of events in $\mathcal{F}$ tails Observed - Predicted				
	Region 1 (58.5°-61.5°]	Region 2 (61.5°-64.5°]	Region 3 (64.5°-67.5°]	Region 4 (67.5°-70.5°]	Region 5 (70.5°- 76.5°]
$\mu + 1\sigma$	518.6 - 506.7	245.9 - 198.4	124.1 - 99.1	42.5 - 41.6	20.0 - 14.0
$\mu + 2\sigma$	143.5 - 145.2	43.6 - 50.5	35.4 - 24.2	12.5 - 8.8	2.6 - 4.5
$\mu + 3\sigma$	48.6 - 32.8	19.9 - 12.9	8.4 - 4.8	1.3 - 1.6	0.0 - 1.5
$\mu + 4\sigma$	16.6 - 8.9	3.2 - 3.3	1.7 - 1.1	0.8 - 0.3	0.0 - 0.5
$\mu + 5\sigma$	1.2 - 0.5	0.5 - 0.8	0.5 - 0.3	0.0 - 0.0	0.0 - 0.0
$\mu + 6\sigma$	0.0 - 0.1	0.0 - 0.0	0.2 - 0.0	0.0 - 0.0	0.0 - 0.0

Table 6.3: Evaluation of the exponential fit on the $\mathcal{F}$ distributions for test+search samples. The observed and predicted (from the fit) number of events in the tail of the Fisher distribution are shown for each angular sub-region. The numbers are calculated by integrating from the start point mentioned in the first row till the $+1\sigma$.

6.4 Diffuse limit for the UHE neutrino flux

Since no neutrino candidate was found in this analysis, an upper limit to the flux of the incoming UHEνs can be estimated. Let flux per unit area, A, energy, solid angle Ω and time be denoted by $\phi(E_\nu) = \frac{d^6 N_\nu}{dE_\nu\, d\Omega\, dA\, dt}$. The expected number of detected neutrinos can be calculated by folding in the total exposure $\xi_{\rm tot}(E_\nu)$ with flux as follows,

$$N_{\rm expected} = \int_{E_{\nu_{\rm min}}}^{E_{\nu_{\rm max}}} \phi(E_\nu) \cdot \xi_{\rm tot}(E_\nu) \cdot dE_\nu \tag{6.4}$$

Assuming a differential UHEν flux $\phi = k \cdot E_\nu^{-2}$, the integrated upper limit on the value of k is given by:

$$k_{\rm up} = \frac{N_{\rm up}}{\int_{E_{\nu{\rm min}}}^{E_{\nu{\rm max}}} E_\nu^{-2} \cdot \xi_{\rm tot}(E_\nu) \cdot dE_\nu}\,, \tag{6.5}$$

the value of $N_{\rm up}$ for a given confidence level can be determined based on the number of observed events and the number of expected background events. Different statistical methods can be used to obtain the value for $N_{\rm up}$ based on the confidence interval. In the next sections some of these different statistical approaches are discussed in more detail. The Feldman and Cousins limit with an extension that incorporates the systematic uncertainties discussed above is chosen as a final estimate for $N_{\rm up}$.

[1] The events close to the Fisher cut in this plot do not show up as the printed values on the plot because it is a part of the 7σ interval.

6.4.1 Feldman and Cousins limit

Feldman-Cousins method [256] is a statistical technique used to construct confidence intervals, particularly for Poisson distributed data. This approach addressed the key shortcomings of traditional methods used to construct confidence intervals especially for cases where the number of observed events are low or zero. Traditional methods such as Gaussian approximation, which assume that data follows a normal distribution and are used to calculate confidence intervals can often lead to incorrect intervals particularly in rare event searches where the data is better described by a Poisson distribution. This can also lead to unphysical values e.g. negative value for rate of expected events. The Feldman-Cousins approach solves this problem by giving a unified method for constructing confidence intervals. The method ensures that the intervals are unbiased and do not favour one outcome over the other. It also ensures a natural transition from two-sided intervals (where there is significant data) to one-sided upper limits (when there is little to no data). The method also respects physical constraints, such as non-negative values for expected event rates. It also provides intervals with more accurate coverage probabilities, reducing over-coverage issues common in other methods.

The Feldman & Cousins approach is implemented as a part of *gammapy* in python [257] which was used to get the interval for this analysis. The information was also verified with look-up tables in [256]. For a 90% confidence interval, in case of zero signal and background events, the upper and lower limits are given as $N_{\rm up}^{90\%} = 2.44$ and $N_{\rm low}^{90\%} = 0$ respectively. If one signal event is seen with zero background then this interval shifts to [4.36, 0.11]. It is important to note that both statistical and systematic uncertainties are not included for the intervals calculated in the Feldman & Cousins method.

6.4.2 Rolke approach

The Feldman & Cousins treatment is a frequentist method which requires the background source to be known precisely. Such a method can fail if the uncertainties are too high [258]. To solve this problem one can also use the Rolke method [259] which incorporates prior information in this case signal with a Poisson distribution and background with either a Poisson or Gaussian distribution. The method is implemented as a ROOT class under TRolke [260]. For a 90% confidence interval in the case of zero signal and background events the interval is given as [2.21, 0] assuming a Poisson distribution for both signal and background. As it is seen the interval is smaller in comparison to the Feldman & Cousins approach. This can be explained much more clearly for the case where there is one signal event and no background where the Rolke interval is [3.65,0]. In this case according to the Feldman & Cousins approach the event has to be a signal since the lower limit is > 0 but in the Rolke approach it is still possible that such an event in the signal region could be a background event i.e. in the Rolke approach the absence of background does not imply zero background, but it only means that the background is not too large. This is because the background is treated as a Poisson number. Thus, the overall upper and lower limits in the

Rolke approach are always smaller in comparison to the Feldman & Cousins method.

6.4.3 Conrad approach

The Conrad method for calculating confidence intervals allows the inclusion of systematic uncertainties in the evaluation. Using this approach the uncertainties in the background prediction, background detection and the signal detection efficiencies can be incorporated in the confidence interval calculation by integrating over the PDFs of these parameters [254]. The method computes the upper limit based on a likelihood ratio between the observed data and the null hypothesis (no signal). For this work the interval was calculated using POLE++ [261] which is a C++ program that implements the Conrad method. The systematic uncertainty on exposure was estimated to be as [+20%, -14%] as mentioned in section 6.2. Using a uniform PDF to characterize the exposure and a Gaussian assumption for background, for a 90% confidence interval in the case of zero signal and background events the upper and lower limits are given as:

$$N_{up}^{90\%} = 2.39,\ N_{\mathrm{low}}^{90\%} = 0 \tag{6.6}$$

The interval is smaller in comparison to the Feldman & Cousins method due to the uneven interval for the systematic uncertainty.

6.4.4 Final calculation

After the determination of N_{up} using the Conrad approach the equation 6.5 can be solved to determine the upper limit to the diffused flux of UHEνs. The integral goes from $E_{\mathrm{min}} = 10^{17.5}$eV till $E_{\mathrm{max}} = 10^{20.5}$eV which is the total energy range explored in the simulations. It is also important to note that the limit is only valid for a smaller energy window. The single flavour 90% C.L. integrated limit is given by

$$k_{90} < 1.9 \times 10^{-7}\mathrm{GeVcm}^{-2}\mathrm{s}^{-1}\mathrm{sr}^{-1}. \tag{6.7}$$

It applies to an energy range of $E_\nu \epsilon [1.3 \times 10^{18} - 2.5 \times 10^{19.5}]$ which is the energy range for which ~90% total event rate is expected in the case of E_ν^{-2} flux. The value along with the 90% energy range is plotted as a dashed purple line in Fig. 6.9.

The other dashed purple lines with central dots are the *differential limits*. These are calculated by integrating the denominator of eq. 6.5 in bins of width $\Delta = 0.5$ eV in $\log_{10}(E_\nu)$. Mathematically for the i^{th} bin this can be represented as follows:

$$\text{Differential limit } (i^{\mathrm{th}}\ E_\nu \text{ bin}) = \frac{N_{\mathrm{up}}}{\int_{\log_{10}(E^i-(\Delta \log_{10} E)/2)}^{\log_{10}(E^i+(\Delta \log_{10} E)/2)} E_\nu^{-1} \cdot \xi(E_\nu) \cdot \ln(10) \cdot d(\log_{10}(E_\nu))} \tag{6.8}$$

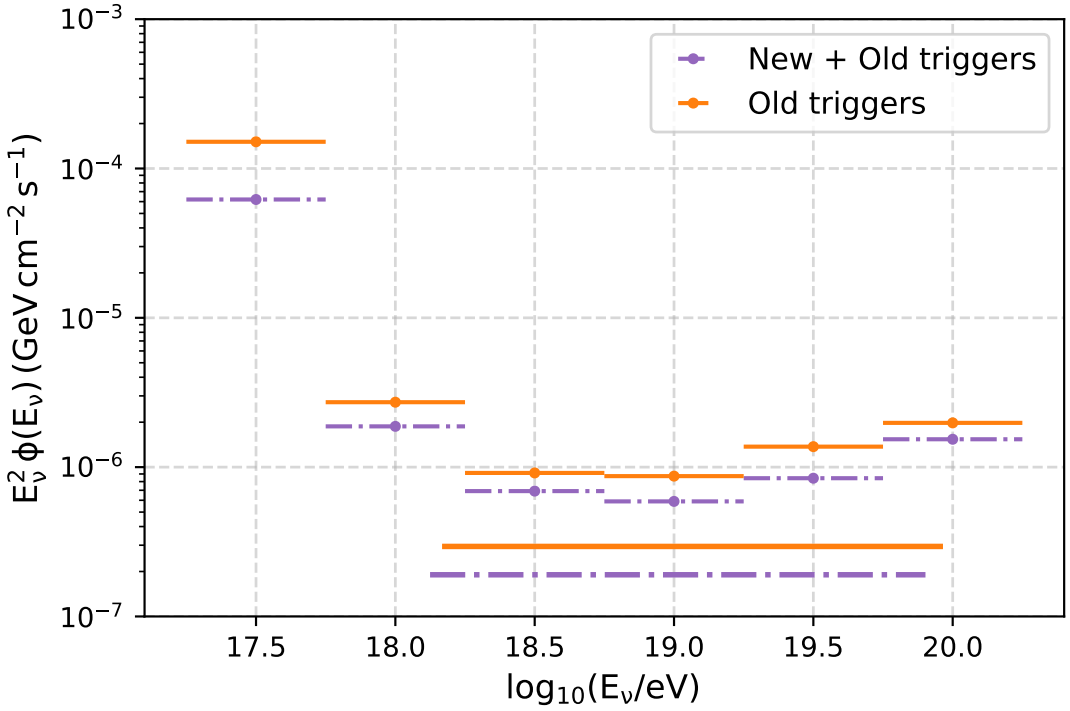

Figure 6.9: Integral (90% C.L., long purple dashed lines) and differential upper limits (short purple segments) for the UHEνs diffuse flux in the DG_{low} region. The limits for an analysis without the new triggers are also plotted in orange for comparison. Both the limits are calculated for the time period 2014-2021.

Assuming constant exposure and flux in each energy bin the differential limit can be estimated as:

$$\text{Approx. Differential limit } (i^{\text{th}}\ E_\nu \text{ bin}) = \frac{N_{\text{up}}}{E_\nu^{-1} \cdot \xi(E_\nu) \cdot \ln(10) \cdot \Delta(\log_{10}(E_\nu))} \tag{6.9}$$

These limits provide a way to denote the sensitivity of the detector for different energies. As it can be seen from the Fig. 6.9 for the Down-going Low analysis the Pierre Auger Observatory is the most sensitive for energies ~10 EeV.

Both limits are also compared to the results from the previous analysis in Fig. 6.9. As it was seen in the exposure comparison it is clear that the new triggers help improve the sensitivity at lower energies. For higher energies the improvements to the upper-limit for the diffuse flux of UHEνs though not as significant is still substantial. This improvement can be attributed to the changes in the Fisher analysis. The integral flux limit sees an improvement of $\sim 40\%$.

Furthermore, the limits obtained in this analysis are combined with the limits obtained using the old analysis. The total exposure for the time period 2004-2013 is calculated using

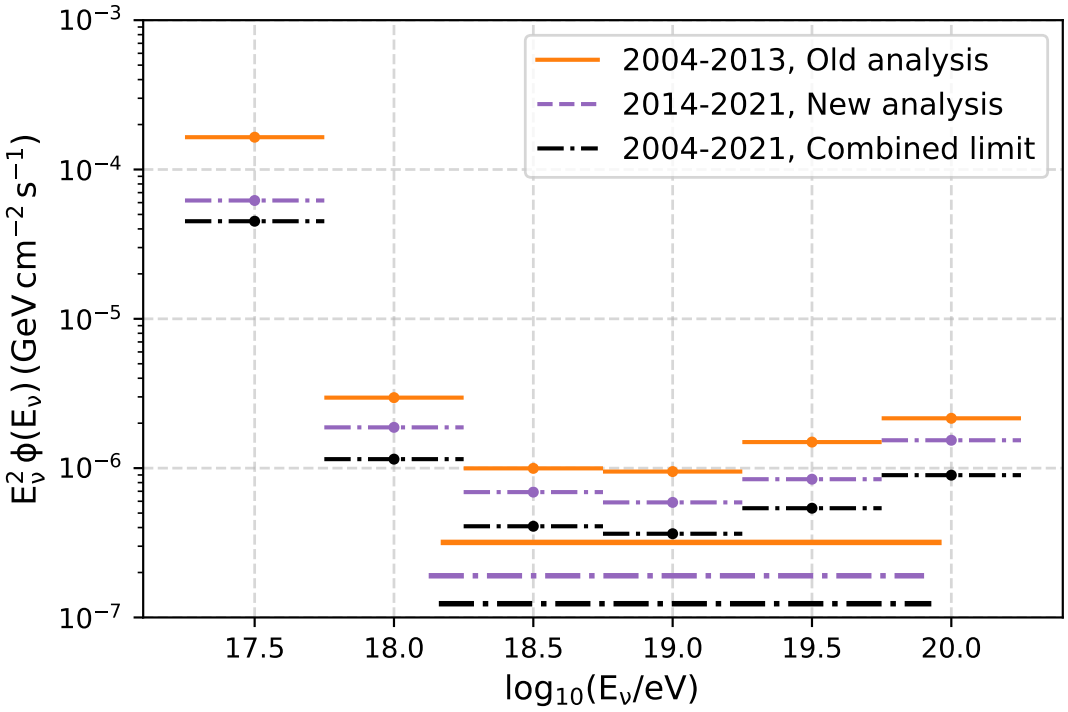

Figure 6.10: Combination of Integral and differential upper limits for a UHEνs diffuse flux in the angular range, $58.5^\circ < \theta_{\mathrm{Rec}} \leq 61.5^\circ$, for the time period 2004-2021. The limits for the time period 2004-2013 are plotted in orange and the limits for the time period 2014-2021 are plotted in purple. The combined limits are plotted in black.

the old analysis and selection as ToTd and MoPS were not implemented for this time period. This exposure is combined with the exposure obtained in this study with the inclusion of new triggers for the time period 2014-2021. This combination is only done under the assumption that the systematics for both the analysis are very similar. The combined exposure is then used to calculate the overall differential and integral limits for the $\mathrm{DG_{low}}$ region in the time period 2004-2021. This is shown in Fig. 6.10. Further this combination is also compared to the expected limit if only the old analysis is applied to the time period 2004-2021. This is shown in Fig. 6.11.

The diffuse flux limit and sensitivity for Auger is dominated by the Earth-skimming channel as shown in [18]. This limit is significantly lower than the $\mathrm{DG_{low}}$ channel and is the main driver to constrain astrophysical and cosmogenic models. A comparison of the limits obtained in this study to the overall limit set at the Pierre Auger Observatory along with the flux predictions from some popular cosmogenic and astrophysical models is shown in Fig. 6.12. The aim of this study was to evaluate the improvement, but it was always known that unless huge, the inclusion of new triggers does not improve the overall diffuse flux limits set using the data collected by the Pierre Auger Observatory. However, the improvements

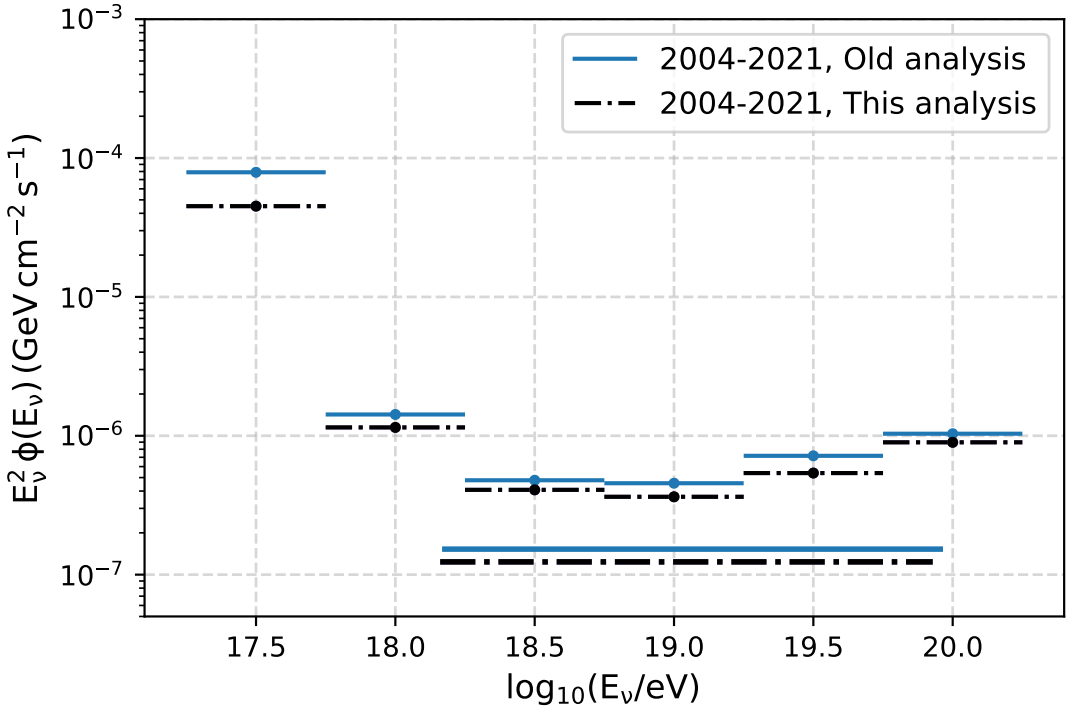

Figure 6.11: Comparison of the combined limits to the expected limits if only the old analysis is applied to the time period 2004-2021. The limits obtained in this study are plotted in black while the limits obtained from the old analysis for the same time period are plotted in blue.

shown in this analysis are more important in the context of point source searches. This is discussed more in the next chapter.

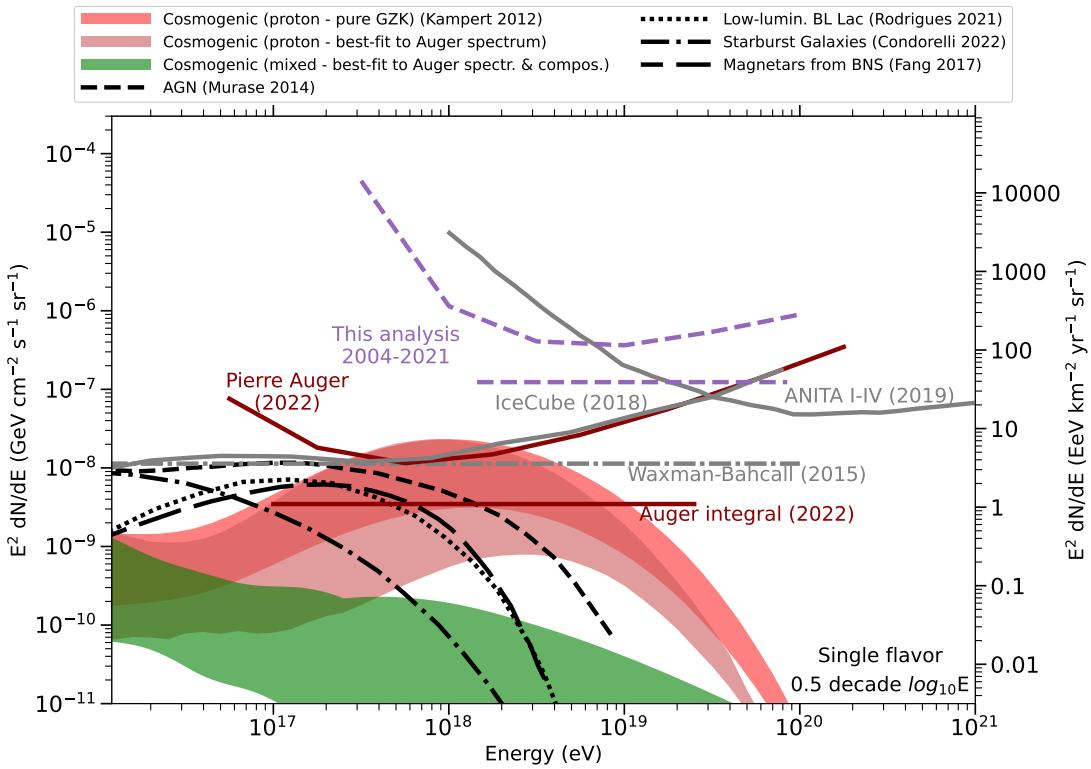

Figure 6.12: Comparison of the combined limits obtained in this analysis to the current upper limits on the diffuse flux of cosmogenic neutrinos. The predicted fluxes from a few cosmogenic and astrophysical models is also shown for comparison. The plot has been modified to add the limits of this analysis using code provided by J. Muñiz and is originally taken from [141].

CHAPTER 7

Search for point-like sources of UHEνs in the DG_{low} range

One of the most exciting fields of modern day neutrino astrophysics involves scanning the observable sky to look for neutrino sources. As mentioned in section 2.2.4 the reported evidence of TXS 0506+056 [17] and NGC 1068 [16] which are examples of a transient source and a steady state of neutrinos has brought unprecedented excitement to the field. Any observation of a neutrino source offers a chance to significantly increase our overall knowledge about astroparticle physics. Since the Pierre Auger Observatory is one of the few experiments in the world sensitive to UHEνs ($E > 10^{16}$eV), any improvement in its point source sensitivity increases its capability for neutrino detection.

In this chapter, the point source sensitivity to ν events of the SD array is discussed for the zenith angular range explored in this thesis, DG_{low}. Based on the zero neutrino candidates found in the search performed in this work, a source declination (δ) dependent neutrino flux is calculated. This process includes calculating the declination dependent exposure and then converting it to a limit on the flux. The improvements to this exposure and sensitivity by the inclusion of new triggers is also discussed. Finally, the new limit is used to scan a few interesting sources which lie in the most sensitive range for the DG_{low} region.

7.1 Procedure to look for a point like steady source of UHEνs

7.1.1 Source visibility

The field of view (FOV) of the Observatory and the corresponding neutrino efficiency is related to the zenith angle which in turn is related to the declination. For a given point-like source at declination, δ and right ascension, α (in equatorial coordinates), the time zenith

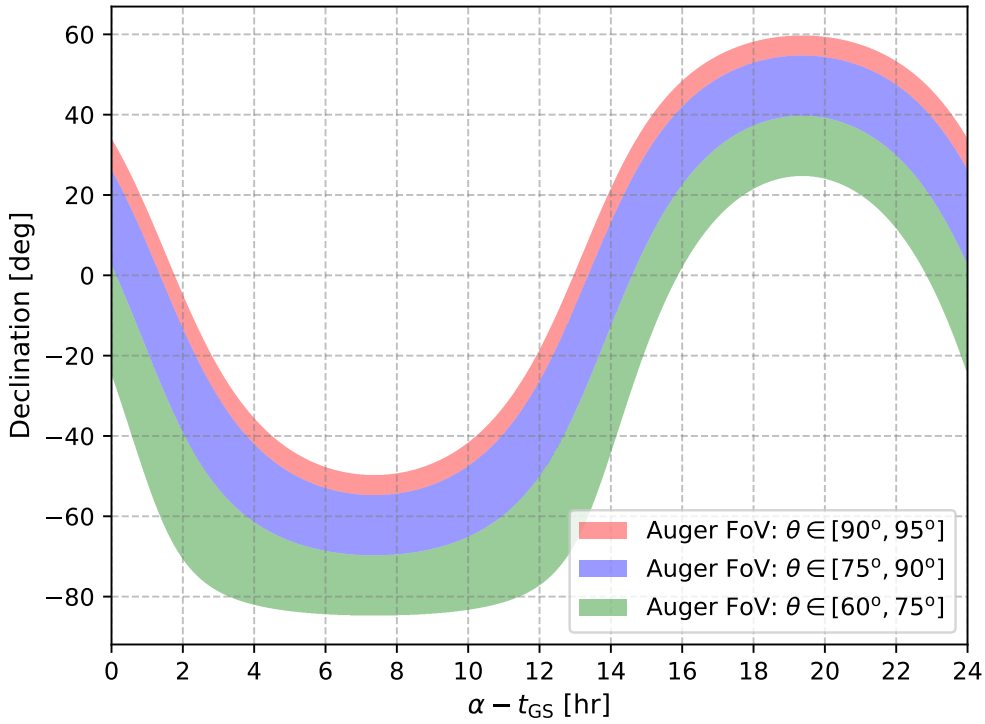

Figure 7.1: Instantaneous field of view for different neutrino searches performed at the Pierre Auger Observatory. The declination is plotted as a function of $\alpha - t_{GS}$ where t_{GS} is the Greenwich Sidereal Time converted to the mean longitude of the Observatory. The bands show the sensitive declination ranges for different neutrino searches (ES: red, DGH: blue, DGL: green) which are separated based on zenith angle ranges.

angle which is the θ dependence at a certain time, t is given by:

$$\cos\theta(t) = \sin\lambda \sin\delta + \cos\lambda \cos\delta \sin(2\pi\frac{t}{T} - \alpha) \tag{7.1}$$

where T is the duration of one sidereal day and λ is the latitude of the observer ($\lambda = -35.2^\circ$ for Pierre Auger Observatory).

Figure 7.1 shows the FOV bands for different neutrino search channels (DG_{low}, DG_{high}, ES). These bands are plotted in equatorial coordinates as a function of $\alpha - t_{GS}$ where t_{GS} is the Greenwich Sidereal Time (GST) converted to angle for a mean longitude of the Observatory, l calculated as $t_{GS} = 2\pi t/T + l$. The sensitive declination ranges for different t_{GS} can be read from the plot which is very useful for real-time transient follow-up. For DG_{low} showers the SD of the Pierre Auger Observatory is sensitive to declinations between $\delta \simeq [-85^\circ - 40^\circ]$. Another way to denote sky coverage for different neutrino searches at Auger is by calculating

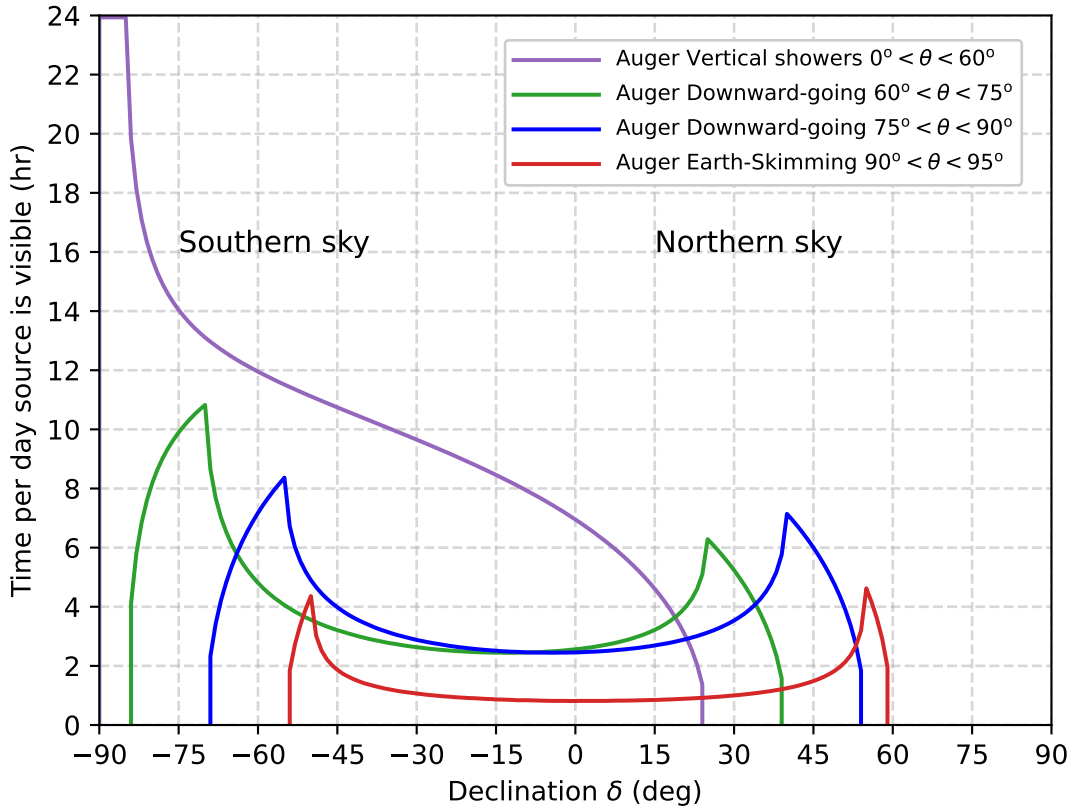

Figure 7.2: Total time per sidereal day a source is visible to the Pierre Auger Observatory for different neutrino searches. The time is plotted as a function of declination. The ES channel is shown in red while the DG_{low} and DG_{high} channels are shown in green and blue respectively. The fraction of time a source is visible for vertical showers is also shown in purple.

the time a source is visible to the Observatory for a particular declination. This is plotted in Fig. 7.2 for all three search channels. As it can be seen from the plot all three channels are the most sensitive at two ends of their sensitive declination ranges (DG_{low}-$\delta \simeq [-70^{\circ}, 35^{\circ}]$) which is a consequence of smaller variation in zenith angle in time for certain directions. The sensitivity sharply decreases beyond these declination values. In the middle of these *two horns* is a plateau like region. It is also seen that generally the fraction of time in which a source is visible is comparable in the DG_{low} and DG_{high} channel with both being higher than the ES channel due to the size of the zenith angle windows. The fraction of visible time for vertical showers is also plotted. Even though this fraction of time is significantly high, currently no neutrino search is performed for this region as it is very difficult to differentiate between a cosmic ray and neutrino EAS for this zenith angle range.

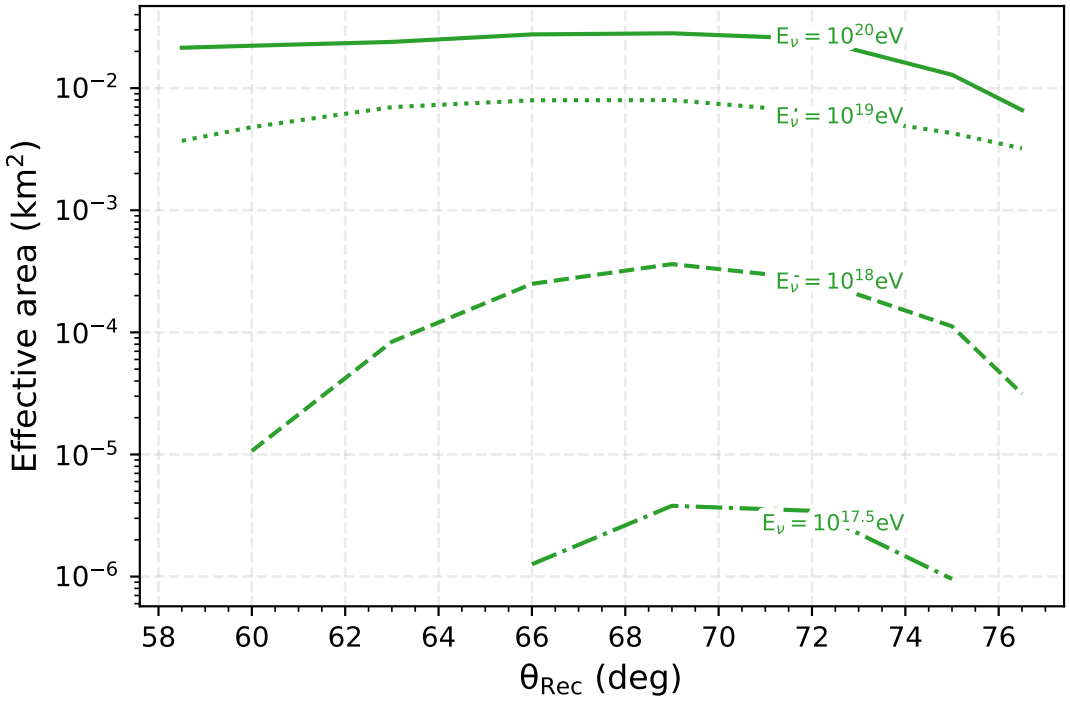

Figure 7.3: Instantaneous effective area for ν_e CC neutrinos as a function of zenith angle for different neutrino energies. The effective area is calculated for the DG_{low} channel.

7.1.2 Effective area and Exposure

Following this to calculate point source sensitivity, the declination dependent SD exposure is evaluated. This is done by first calculating an effective area to neutrinos of flavours i and energy E_ν is defined in the following way. For a point source spectral flux of flavour i given by $\phi_i(E_\nu) = \frac{d^4N_\nu}{dE_\nu dAdt}$ the expected number of detected events is given by

$$\frac{dN_i}{dt} = \int_{E_{\nu_{\min}}}^{E_{\nu_{\max}}} dE_\nu \, \phi(E_\nu) \, \mathcal{A}_i(E_\nu) \tag{7.2}$$

The effective area is flavour dependent since for each flavour the shower development and the primary interaction (c = NC, CC) is substantially different. The effective area is for the DG_{low} region is given as follows:

$$\mathcal{A}_{\rangle,\rfloor}(E_\nu, \theta(t), t) = \frac{\sigma^{i,c}(E_\nu)}{m_N} \int_X \varepsilon_{i,c}(E_\nu, \theta(t), t) \, A_{6T5} n_{\text{hex}}(t) \, dX \,, \tag{7.3}$$

where $\varepsilon_{i,c}$ is the neutrino identification efficiency for a 6T5 unit. The declination dependence is taken into account by the $\theta(t)$ dependence of the efficiency. The instantaneous effective area for electron neutrinos with CC interactions in km^2 for different zenith angles

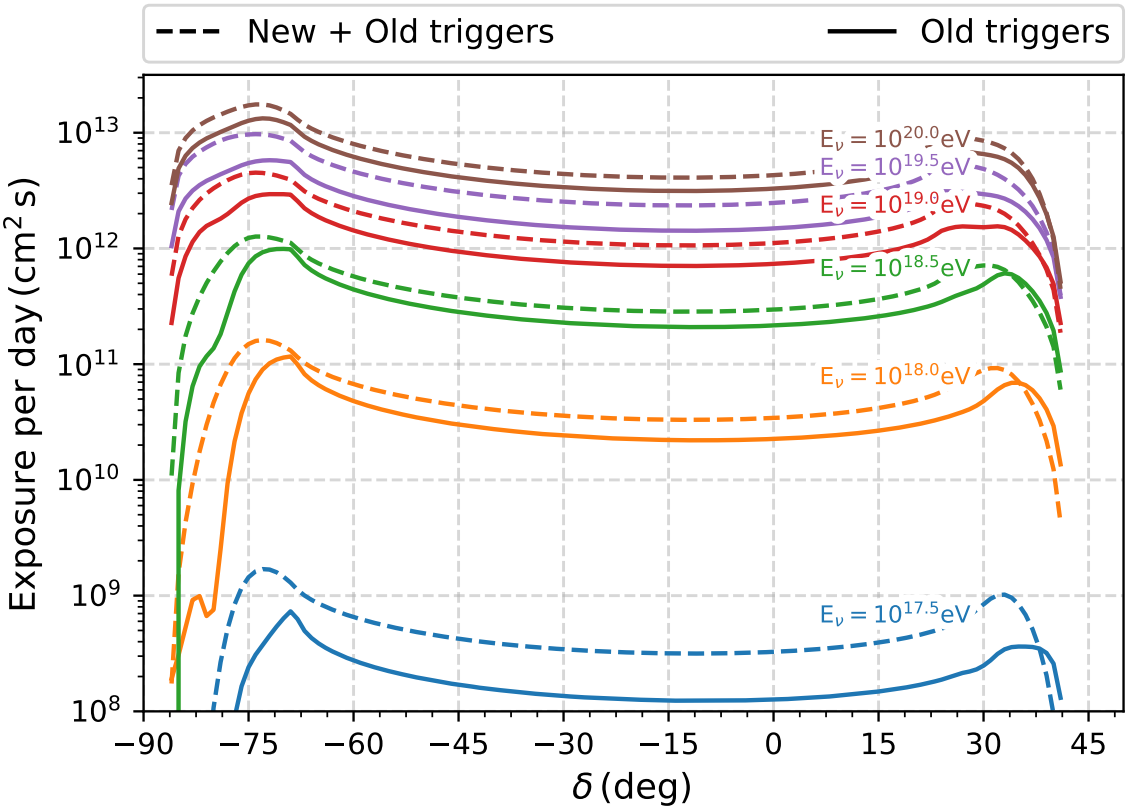

Figure 7.4: Average exposure for different neutrino energies as a function of declination for the DG_{low} channel. The exposure is calculated for the time period 2014-2021. The solid lines show the exposure calculated with the previous analysis while the dashed lines show the exposure calculated with the inclusion of new triggers.

is plotted in Fig. 7.3. The effective area increases with increasing primary energy. It also increases with zenith angles until ~70° beyond which there is a slight decrease in the effective area due to the decrease in neutrino sensitivity at higher zenith angles (section 5.5.5).

The exposure to point-like sources of UHE neutrinos can then be calculated by integrating the effective area for a given time interval and summing over the different flavours (1:1:1 expectation at Earth) and channels as follows:

$$\xi(E_\nu, \delta) = \sum_{i,c} \int_t \mathcal{A}_{\rangle,\rfloor}(E_\nu, \theta(t), t)\, dt. \tag{7.4}$$

The exposure is δ dependent due to the dependence of effective area on $\theta(t)$. The effective area can also change with time due to the changes in the number of hexagons $n_{hex}(t)$. This change is represented in Fig. 7.5. As it can be seen in the plot the number is relatively stable especially in the period of one sidereal day apart from a few outages which are removed

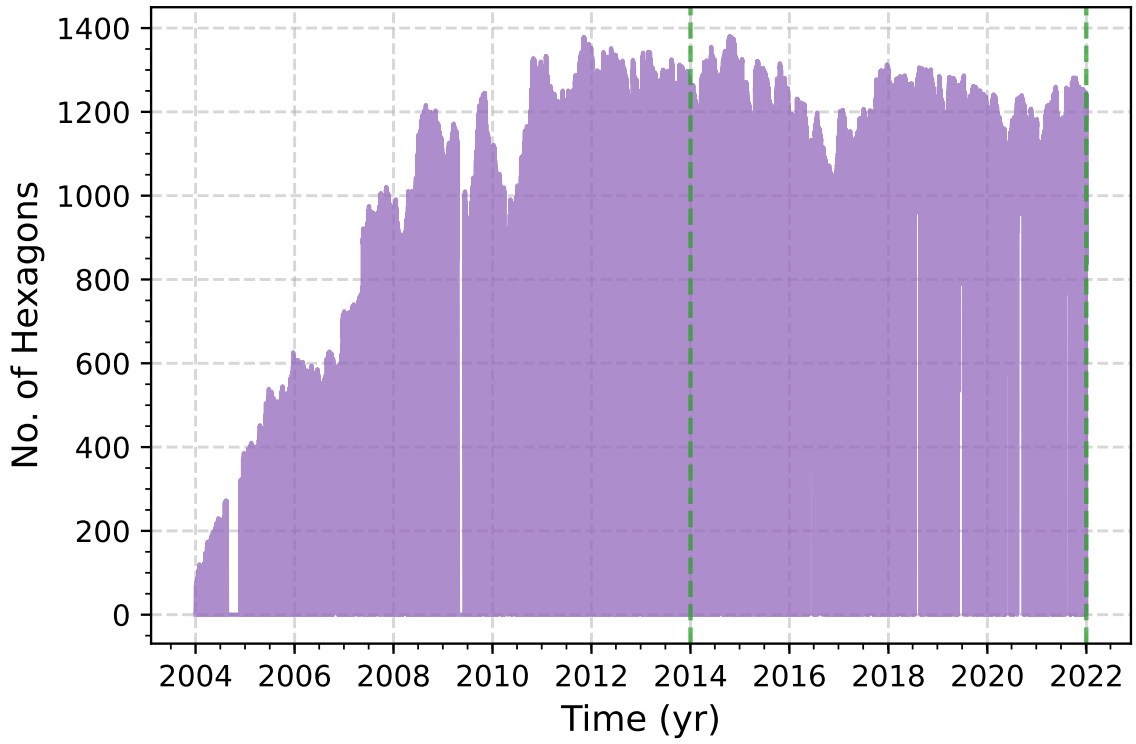

Figure 7.5: Number of 6T5 hexagons as a function of time. The white regions show the outages which are removed from the searches. The area between the green lines shows the time period of this search.

from the searches. The directional exposure for the DGL channels for different fixed energies between 2014-2021 is shown in Fig. 7.4. The dashed line shows the exposure calculated in this study by including the new triggers while the solid line shows the exposure calculated with the previous analysis for the same time period. Similar to the one calculated for the diffuse flux, the exposure is significantly improved for lower energies with the improvement decreasing for higher energies. The shape of the exposure is similar to the observation time plot in Fig. 7.2 with the maximum exposure peaks seen at the same declinations. It is also interesting to note that the exposure at a given energy for any given point source can be estimated as the ratio between the diffuse exposure (Fig. 6.9) and the solid angle covered by the DG_{low} analysis multiplied by the fraction of time the source is visible 7.2. The solid angle covered by the DG_{low} analysis is given by $2\pi \int_{60^\circ}^{75^\circ} \sin\theta \, d\theta \sim 1.515$sr.

7.2 Flux limits for point-like sources of UHEνs

Since no neutrino candidate was discovered in the search window, an upper limit to a point-like source of UHE neutrinos can be calculated. Similar to the calculation for the diffuse flux,

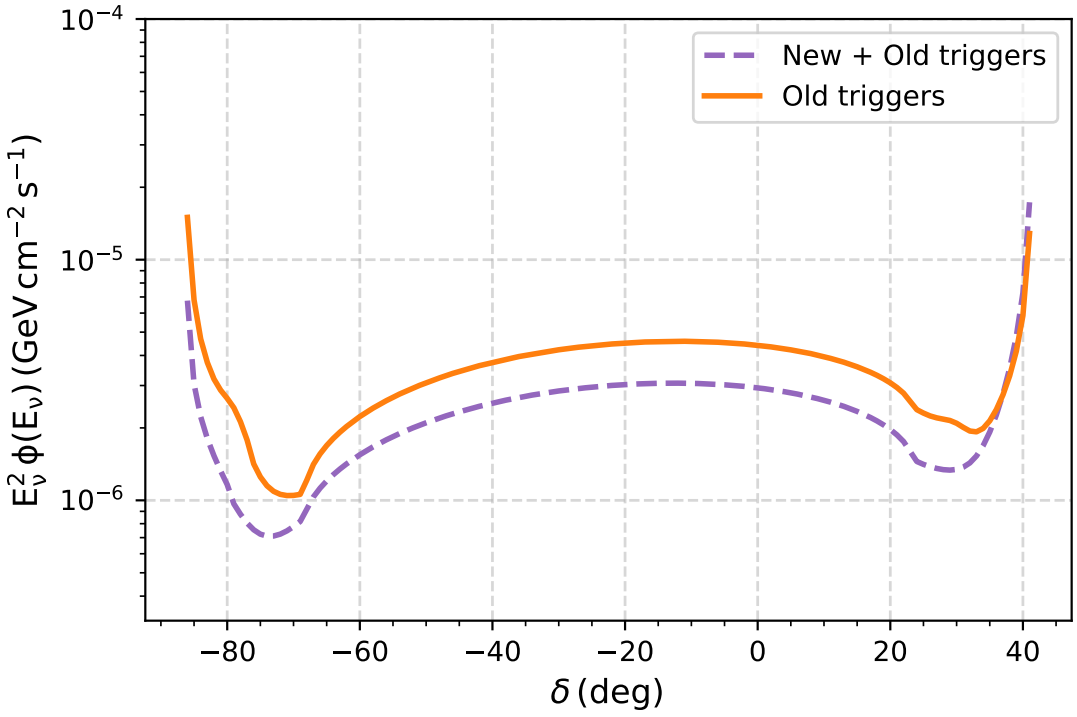

Figure 7.6: Comparison of the 90% C.L. declination dependent upper-limit (01.01.2014–31.12.2021) for the DG_{low} channel of a single flavor point-like flux of UHE. The limit (dashed line) is compared to the limit obtained from the previous analysis (solid line) for the same time period.

the number of expected neutrino events from a point like source at a given declination can be written as:

$$N_{\text{expected}}(\delta) = \int_{E_{\text{min}}}^{E_{\text{max}}} \phi(E_\nu)\, \xi(E_\nu, \delta)\, dE_\nu \tag{7.5}$$

The point source flux is assumed to be independent of time and is characterized as a power law, $\phi(E_\nu) = k_{\text{PS}} E_\nu^{-2}$ for all declinations. The integrated upper-limit from each source can then be further calculated as follows:

$$k_{\text{PS}}^{90\%CL} = \frac{N_{\text{up}}}{\int_{E_{\text{min}}}^{E_{\text{max}}} E_\nu^{-2}\, \xi(E_\nu, \delta)\, dE_\nu}. \tag{7.6}$$

For this study initially a time period from 1 Jan 2014 till 31 December 2021 is selected. The $N_{\text{up}} = 2.39$ is calculated according to the Conrad approach as mentioned in section 6.4.3. The exposure is assumed to be uniform within ±0.6% for the time period of search as shown in [262].

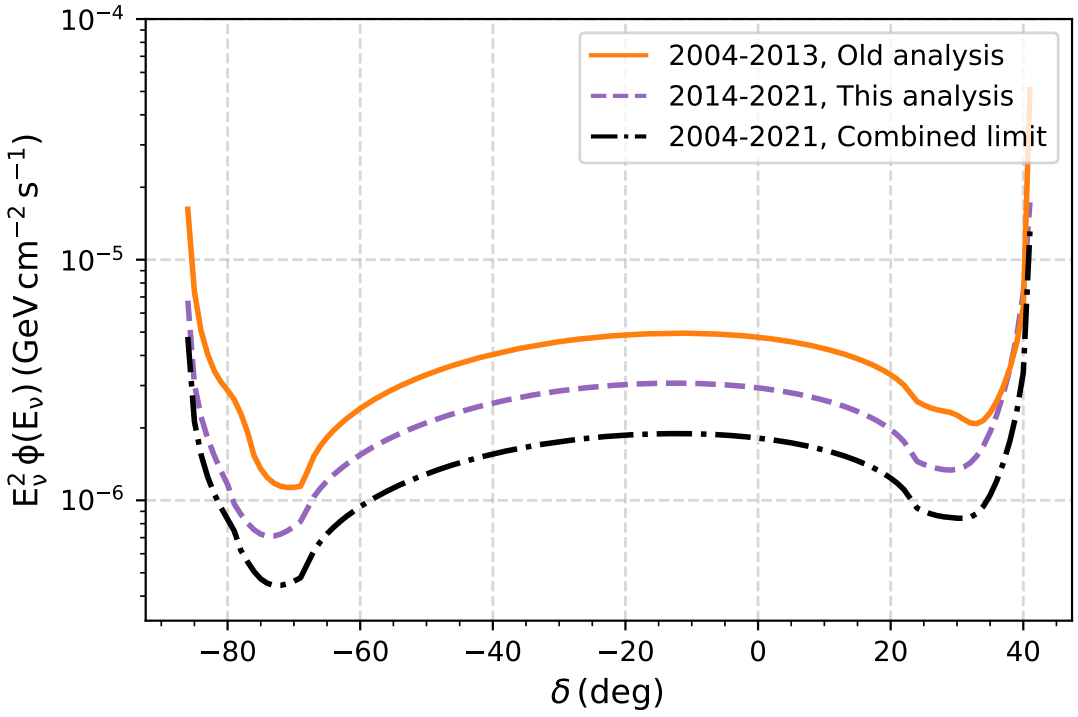

Figure 7.7: 90% C.L. declination dependent upper-limit for different time periods for the DG_{low} channel of a single flavor point-like flux of UHE. The limit for 01.01.2004-31.12.2013 obtained with the previously done analysis (solid, orange) is combined with the limit obtained in this analysis for 01.01.2014-31.12.2021 (dashed, purple) to give the combined limit for 01.01.2004-31.12.2021 (dashed dotted, black).

The 90% C.L. declination dependent upper-limit for the DG_{low} channel is shown in Fig. 7.6. The limit is the most stringent for the times the source is seen the longest. The limit is calculated for the energy range $\sim$ 1.2 $\times 10^{18}$eV - 2.5 $\times 10^{19.5}$eV. The dependence of energy intervals is minimal. This limit is also compared to the limit obtained from the previous analysis for the same time period in the same figure. As it can be seen the limit is significantly improved with new triggers fulfilling one of the primary objectives of this thesis. Furthermore, a combined limit is calculated where the old analysis is applied for the time period 01.01.2004–31.12.2013 and the analysis presented in this thesis is applied for the time period 01.01.2014–31.12.2021. This limit is only computed under the assumption that the systematics for both the time periods are similar, and no neutrino candidates were found in both time periods. The combined limit along with the limits from the separate time periods is shown in Fig. 7.7. Furthermore, the limit is also compared to the point-like source limit calculated with the old analysis for the time period 01.01.2004-31.12.2021. This is presented in Fig. 7.8. For the best declination range of the DG_{low} channel (-74°) the limit is improved by a factor of $\sim$ 1.5 for the time period where both the new triggers and old triggers were

active i.e. 2014-2021. Since the exposure at high energies is a few magnitudes larger than the one at low energies, the new triggers do not improve the overall limit significantly. The improvement is primarily due to the changes in the Fisher discriminant analysis which were proposed and implemented in this thesis.

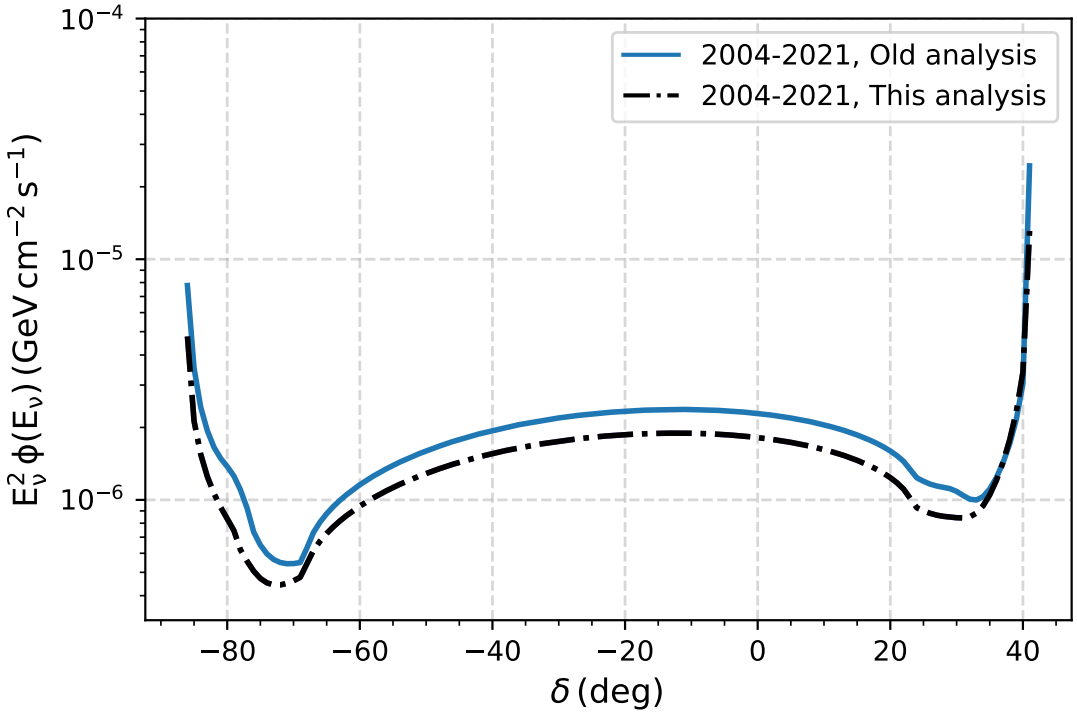

Figure 7.8: Comparison of the 90% C.L. declination dependent upper-limit (01.01.2004–31.12.2021) for the $\mathrm{DG_{low}}$ channel of a single flavor point-like flux of UHE. The limit (dashed dotted) is compared to the limit obtained from the previous analysis (solid line) for the same time period.

A cross-check of the diffuse limit is obtained from the point source analysis by performing double integration of the exposure, $\xi(E_\nu, \delta)$ similar to what was done in [23].

The diffuse limit can be written as:

$$k_{\mathrm{PS}}^{90\%\mathrm{CL}} < \frac{N_{\mathrm{up}}}{\int_{\log_{10} E_{\mathrm{min}}}^{\log_{10} E_{\mathrm{max}}} \int_{-\pi/2}^{\pi/2} 2\pi \cdot \cos(\delta) \cdot E_\nu^{-1} \cdot \xi(E_\nu, \delta) \cdot \ln(10) \cdot d(\log_{10}(E_\nu)) \cdot d\delta}. \tag{7.7}$$

The diffuse limit from point source analysis is given as:

$$k_{\mathrm{PS}}^{90\%\mathrm{CL}} < 2.06 \times 10^{-7} \mathrm{GeV\ cm^{-2} s^{-1} sr^{-1}}\,, \tag{7.8}$$

which agrees with the value obtained in eq. 6.7.

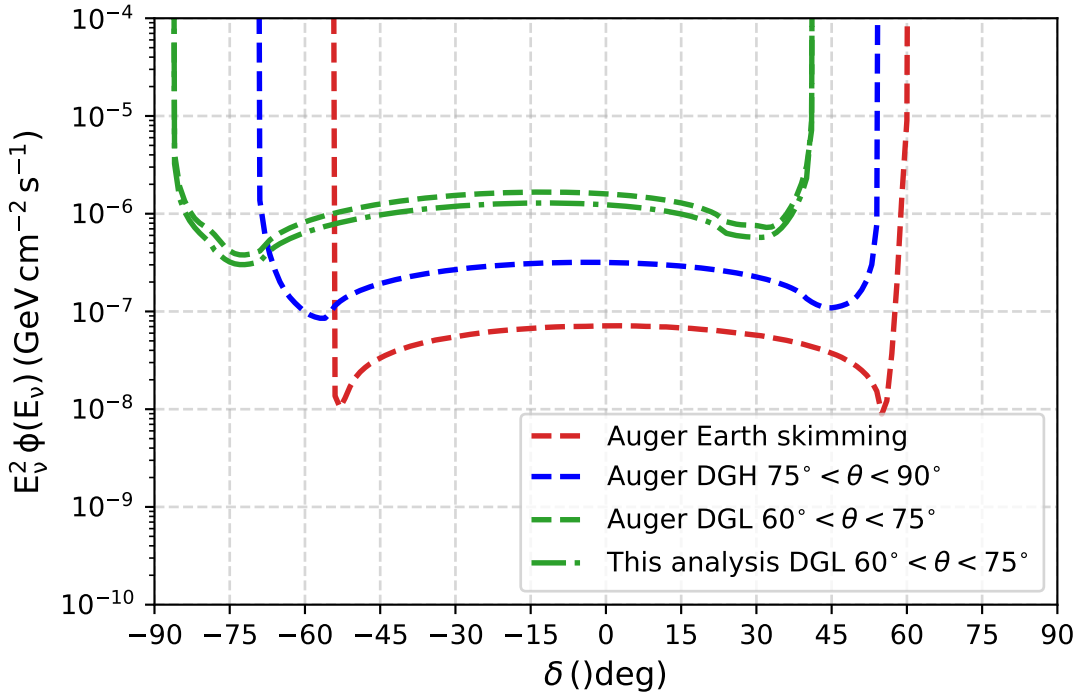

Figure 7.9: The upper limits (01.01.2004–31.12.2021) at 90% C.L. for different neutrino searches performed at the Pierre Auger Observatory of a single flavor point-like flux of UHE. The limit obtained in this analysis (dashed dotted, green) for the DG_{low} channel is compared to the limits obtained for the DG_{high} and ES channels.

It is also important to mention that even though the overall sensitive declination range for the DG_{low} analysis is small in comparison to other channels [11], the improvement presented in this thesis is still important as the sensitive declination ranges are not fully overlapping. Thus, if there is a point source between declinations $\delta \in [-80^\circ, -68^\circ]$ then DG_{low} channel offers the only window at Auger to see UHEνs from such a source.

The limit obtained in this analysis was then used to constraint some interesting sources which exclusively lie in the DG_{low} sensitive range. The sources were selected based on their declination and expected energies of neutrinos they could produce which could lie in the region explored. The upper limits on the expected neutrino flux are given under the assumption of an E^{-2} like neutrino flux constant in time. The sources were selected from the Roma-BZCAT catalogue [263], Fermi 4LAC catalogue [264] and from [265]. The sources along with their type, declination and right ascension (equatorial coordinates) and the 90% C.L. upper limits on the fluxes obtained are listed in table 7.1.

Source	Type	Dec. (deg)	R.A. (deg)	$k_{PS}^{90\%\mathrm{CL}} \times 10^{-7}$ (GeV cm^{-2} s^{-1} sr^{-1})
NGC 2060	SNR	-69.2	84.4	4.73
30 Dor C	SB	-69.8	83.6	4.64
BZQ J0102-7546	FSRQ	-75.4	15.3	4.85
BZQ J0102-8012	FSRQ	-80.1	15.3	8.44
BZB J0127-8108	BLL	-81.1	21.5	9.47
BZQ J0217-7347	FSRQ	-73.8	34.26	4.50
BZQ J0143-6813	FSRQ	-68.1	25.5	5.34
BZQ J0947-7731	FSRQ	-77.3	146.6	5.75
BZQ J1058-8003	FSRQ	-80.1	164.4	8.44
BZQ J1733-7935	FSRQ	-79.4	263.2	7.81
BZB J1843-7430	BLL	-74.3	280.5	4.58
BZQ J2147-7536	FSRQ	-75.3	326.5	4.82
BZQ J2356-6820	FSRQ	-68.2	359.0	5.28
BZB J0028-7045	BLL	-70.5	7.10	4.55
PKS 0637-752	FSRQ	-75.2	98.6	4.78
LHA120-N-157B	PWN	-69.16	84.43	4.74
4FGL J0524.7-8304	BLL	-83.1	81.2	12.80
PSR J1036-8317	PUL	-83.3	159.2	13.39

Table 7.1: Upper limits on the expected neutrino flux at 90% C.L. for different sources. The limits are calculated for the $\mathrm{DG}_{\mathrm{low}}$ channel. BLL = BL Lac, FSRQ = Flat Spectrum Radio Quasar, PWN = Pulsar Wind Nebula, SB = Super Bubble.

CHAPTER 8

Conclusion and Outlook

Besides detecting UHECRs, the Pierre Auger Observatory with its large Surface Detector array offers a remarkable exposure to neutrinos above 10^{17}eV. Any potential observation of such UHEνs will further our knowledge about the observable universe. Since neutrinos are not deflected as they travel towards us at Earth, they offer a direct line of sight to the sources where they were produced. They are also some of the earliest particles to arrive from a transient source which makes their detection an important beacon for other astronomical instruments to perform a multi-messenger observation. The Pierre Auger Observatory is constantly monitoring the sky for the presence of such UHEνs. The idea behind the detection remains the same as previous analysis, detecting Extensive Air Showers close to the ground with a large electro-magnetic component at ground ("young" showers). This strategy is only employed for horizontal showers ($\theta > 60^{\circ}$). Two new SD triggers, time-over-threshold-deconvolved and multiplicity of positive steps were installed in 2014 to further increase the detection efficiency for low energy neutrino induced EASs. This thesis presents the first analysis of this improved efficiency for low energy neutrino showers in the zenith angle range $\theta \in [60^{\circ}, 75^{\circ}]$ also known as Down-going low or $\mathrm{DG_{low}}$ range. In this thesis the effect of the new triggers was evaluated for two types of searches, the searches for the diffuse flux of UHEνs and search for point-like sources of UHEνs. For both searches an overall improvement of efficiency is observed when information from the new triggers is incorporated in the analysis. A short summary of the three main contributions of this thesis along with an outlook detailing potential improvements are detailed in the next sections.

Incorporating new triggers in the $\mathrm{DG_{low}}$ UHEνs searches

In this thesis each facet of the $\mathrm{DG_{low}}$ analysis was examined. An effort was made to maximize the potential of the analysis. A blind search strategy similar to [18, 23] was followed to avoid any bias in the analysis. The first step in this process was to include the information from the new triggers in the neutrino searches. About ~7 years of recorded data was available for this task. The effect of the new triggers was first evaluated on neutrino simulations by including

them in the analysis chain as described in section 5.5.3. By the inclusion of new triggers an overall increase in reconstructed events was observed as shown in Fig. 5.13. This increase was most significant for lower energy neutrinos and decreased with increase in primary energy. This was an expected consequence due to the design of the new triggers. The overall increase also allowed for further modifications to the analysis which included lowering some stringent cuts as described in section 5.5.5. For the final step of the analysis a Fisher discriminate polynomial was built and trained using the simulations (signal training sample) and a small fraction of recorded data, ~20% from the Observatory (background training sample). The polynomial is built with Area over Peaks of the stations and a differentiation between the background and signal is performed based on a cut on the Fisher value as given in eq. 5.9. After fixing the selection, a test sample was unblinded to catch any remaining flaws in the analysis. This proved worthwhile as a small error in the reconstruction was discovered during this process. The error was promptly corrected, and the whole selection procedure was re-evaluated, and the Fisher was retrained. Since the correction involved a change to the reconstruction procedure, the blind search was redone from the start. After this correction the unblinding was again performed in two stages. The new test sample and the full blinded sample, 20% + 60% of recorded data between the period of 1 Jan 2014 to 31 December 2012 was analysed to search for neutrinos. **No neutrino candidates** were found in the search performed using the analysis described in this thesis.

Outlook

Even though a concerted effort was made to maximize the potential of the analysis presented in this thesis, certain improvements could not be implemented and are thus summarized here for future studies. The segmentation algorithm used for reconstruction of events for neutrino searches was found to be not properly tuned for the new triggers, ToTd and MoPS. Thus, for this analysis the new triggers were completely removed from the segmentation algorithm. The primary purpose of the segmentation algorithm is to evaluate the correct start times for the WCD signals to decrease the effect of accidental muons which in turn affects the zenith angle estimation. A better tuned segmentation algorithm could thus further improve the neutrino search with new triggers. A more detailed summary of this topic along with examples of events where the segmentation algorithm fails and where it could help are presented in Appendix C. This tuning could not be explored in this thesis but could be implemented in the future. Further, as seen in this analysis, the angular reconstruction used for neutrinos is not particularly calibrated for EASs which originate deep in the atmosphere. This could also be rectified for the future to improve this analysis. Other techniques which involved computing the zenith angle via measuring the footprint of the shower cannot not be applied here due to the compact nature of EASs expected for the angular range explored. In this thesis a cut on the saturated and active PMTs was also explored but not implemented in the final analysis. A detailed study on such a cut could also be useful to increase the efficiency of the analysis.

In addition, this thesis also includes ongoing work to adapt the DG_{high} analysis to the

current $\overline{\text{Off}}\underline{\text{line}}$ version, which is described in detail in Appendix E. This work aims to evaluate and test potential improvements to the analysis. Although the impact of incorporating new triggers for this analysis is expected to be minimal due to their decreasing efficiency with increasing zenith angle, there is still potential for the new triggers to enhance the efficiency for neutrinos in the angular range of $E \sim 10^{17} - 10^{17.5}$eV.

Improvements to the diffuse flux limit for UHEνs with new triggers

With no neutrino candidate detected, a 90% C.L. upper limit on the diffuse flux of UHEνs for the DG_{low} channel was evaluated under the assumption of a diffuse flux given by $\phi \propto E_{\nu}^{-2}$ with a 1:1:1 neutrino flavour ratio at earth. The integrated limit is given as:

$$k_{90} < 1.9x10^{-17}\text{GeVcm}^{-2}\text{s}^{-1}\text{sr}^{-1}, \tag{8.1}$$

in the energy range $E_{\nu} \in [1.3 \times 10^{18} - 2.5 \times 10^{19.5}]$eV. The limit represents the value of the normalization of the differential flux needed to predict ~2.39 expected events. The number 2.39 was evaluated using a semi Bayesian extension of the Feldman & Cousins treatment accounting for systematic uncertainties on exposure [254]. This limit is ~ 40% stricter than the one obtained without the new triggers for the same time period. Even though this improvement is significant the overall effect on the sensitivity of the Observatory to the diffuse flux of UHEνs is minimal.

Improvements to the point source searches for UHEνs with new triggers

The sensitivity to a point like source of UHEνs was also calculated to evaluate the improvements for such searches with the inclusion of new triggers. The methodology was adopted from [11] and an energy and declination dependent exposure was evaluated for the DG_{low} range. Using the no neutrino candidate detection ansatz, a 90% C.L. upper limit on the neutrino flux from point-like sources as a function of source declination, δ was evaluated and presented in Fig. 7.6. This limit was also shown to improve with the inclusion of new triggers. The improvement, though small, has an impact in the overall sensitivity since the different searches (DG_{low}, DG_{high}, ES) have different FOVs. It must also be stressed that Auger is one of the constantly running experiments sensitive to Energy ranges > 10^{18}eV thus any improvement to its sensitivity is an important step for the potential future detection of UHEνs.

Bibliography

[1] T. Wulf, *Beobachtungen über die Strahlung hoher Durch-dringungsfähigkeit auf dem Eiffelturm*, Phys. Z.**11** 811–813.

[2] V. F. Hess, *Über Beobachtungen der durchdringenden Strahlung bei sieben Freiballonfahrten*, Phys. Z. **13** (1912) 1084–1091.

[3] J. Clay, *Penetrating radiation*, Acad. Amsterdam Proc. **30** (1927) 1115–1127.

[4] J. Clay, *Penetrating radiation II*, Acad. Amsterdam Proc. **31** (1928) 1091–1097.

[5] B. Rossi, *Über die Eigenschaften der durchdringenden Korpuskularstrahlung im Meeresniveau*, Zeitschrift für Physik **82** no. 3, (1933) 151–178.

[6] K. Schmeiser and W. Bothe, *Die harten ultrastrahlschauer*, Annalen der Physik **424** no. 1-2, (1938) 161–177.

[7] P. Auger, P. Ehrenfest, R. Maze, J. Daudin, and A. F. Robley, *Extensive cosmic ray showers*, Rev. Mod. Phys. **11** (1939) 288–291.

[8] Pierre Auger Collaboration, A. Aab et al., *The Pierre Auger Cosmic Ray Observatory*, Nucl. Instrum. Meth. A **798** (2015) 172–213, arXiv:1502.01323 [astro-ph.IM].

[9] Pierre Auger Collaboration, R. Mussa and A. Vasquez, *Classification and Reconstruction of single and multiple ELVES in AUGER*, J. Phys. Conf. Ser. **2398** no. 1, (2022) 012006.

[10] Pierre Auger Collaboration, P. Abreu et al., *Limits to Gauge Coupling in the Dark Sector Set by the Nonobservation of Instanton-Induced Decay of Super-Heavy Dark Matter in the Pierre Auger Observatory Data*, Phys. Rev. Lett. **130** no. 6, (2023) 061001, arXiv:2203.08854 [astro-ph.HE].

[11] Pierre Auger Collaboration, A. Aab et al., *Limits on point-like sources of ultra-high-energy neutrinos with the Pierre Auger Observatory*, JCAP **11** (2019) 004, arXiv:1906.07419 [astro-ph.HE].

[12] Pierre Auger Collaboration, P. Abreu et al., *Searches for Ultra-High-Energy Photons at the Pierre Auger Observatory*, Universe **8** no. 11, (2022) 579, arXiv:2210.12959 [astro-ph.HE].

[13] T. Bister, G. R. Farrar, and M. Unger, *The Large-scale Anisotropy and Flux (de)magnification of Ultrahigh-energy Cosmic Rays in the Galactic Magnetic Field*, Astrophys. J. Lett. **975** no. 1, (2024) L21, arXiv:2408.00614 [astro-ph.HE].

[14] D. Allard, *Extragalactic propagation of ultrahigh energy cosmic-rays*, Astropart. Phys. **39-40** (2012) 33–43, arXiv:1111.3290 [astro-ph.HE].

[15] IceCube, Pierre Auger, Telescope Array Collaboration, M. G. Aartsen et al., *Search for correlations between the arrival directions of IceCube neutrino events and ultrahigh-energy cosmic rays detected by the Pierre Auger Observatory and the Telescope Array*, JCAP **01** (2016) 037, arXiv:1511.09408 [astro-ph.HE].

[16] IceCube Collaboration, R. Abbasi et al., *Evidence for neutrino emission from the nearby active galaxy NGC 1068*, Science **378** no. 6619, (2022) 538–543, arXiv:2211.09972 [astro-ph.HE].

[17] IceCube Collaboration, M. G. Aartsen et al., *Neutrino emission from the direction of the blazar TXS 0506+056 prior to the IceCube-170922A alert*, Science **361** no. 6398, (2018) 147–151, arXiv:1807.08794 [astro-ph.HE].

[18] Pierre Auger Collaboration, A. Aab et al., *Probing the origin of ultra-high-energy cosmic rays with neutrinos in the EeV energy range using the Pierre Auger Observatory*, JCAP **10** (2019) 022, arXiv:1906.07422 [astro-ph.HE].

[19] LIGO Scientific, Virgo Collaboration, B. P. Abbott et al., *Observation of Gravitational Waves from a Binary Black Hole Merger*, Phys. Rev. Lett. **116** no. 6, (2016) 061102, arXiv:1602.03837 [gr-qc].

[20] LIGO Scientific, Virgo, Fermi GBM, INTEGRAL, IceCube, AstroSat Cadmium Zinc Telluride Imager Team, IPN, Insight-Hxmt, ANTARES, Swift, AGILE Team, 1M2H Team, Dark Energy Camera GW-EM, DES, DLT40, GRAWITA, Fermi-LAT, ATCA, ASKAP, Las Cumbres Observatory Group, OzGrav, DWF (Deeper Wider Faster Program), AST3, CAASTRO, VINROUGE, MASTER, J-GEM, GROWTH, JAGWAR, CaltechNRAO, TTU-NRAO, NuSTAR, Pan-STARRS, MAXI Team, TZAC Consortium, KU, Nordic Optical Telescope, ePESSTO, GROND, Texas Tech University, SALT Group, TOROS, BOOTES, MWA, CALET, IKI-GW Follow-up, H.E.S.S., LOFAR, LWA, HAWC, Pierre Auger, ALMA, Euro VLBI Team, Pi of Sky, Chandra Team at McGill University, DFN, ATLAS Telescopes, High Time Resolution Universe Survey, RIMAS, RATIR, SKA South Africa/MeerKAT Collaboration, B. P. Abbott et al., *Multi-messenger Observations of a Binary Neutron Star Merger*, Astrophys. J. Lett. **848** no. 2, (2017) L12, arXiv:1710.05833 [astro-ph.HE].

[21] IceCube, Fermi-LAT, MAGIC, AGILE, ASAS-SN, HAWC, H.E.S.S., INTEGRAL, Kanata, Kiso, Kapteyn, Liverpool Telescope, Subaru, Swift NuSTAR, VERITAS,

VLA/17B-403 Collaboration, M. G. Aartsen et al., *Multimessenger observations of a flaring blazar coincident with high-energy neutrino IceCube-170922A*, Science **361** no. 6398, (2018) eaat1378, arXiv:1807.08816 [astro-ph.HE].

[22] IceCube Collaboration, R. Abbasi et al., *Observation of high-energy neutrinos from the Galactic plane*, Science **380** no. 6652, (2023) adc9818, arXiv:2307.04427 [astro-ph.HE].

[23] J. L. Navarro Quirante, *Search for ultra-high energy neutrinos at the Pierre Auger Observatory*, 2013. http://hdl.handle.net/10481/26377.

[24] V. Hess, *On the Observations of the Penetrating Radiation during Seven Balloon Flights*, 2018. https://arxiv.org/abs/1808.02927.

[25] B. Rossi, *On the Magnetic Deflection of Cosmic Rays*, Phys. Rev. **36** (1930) 606–606, https://link.aps.org/doi/10.1103/PhysRev.36.606.

[26] T. H. Johnson, *The Azimuthal Asymmetry of the Cosmic Radiation*, Phys. Rev. **43** (1933) 834–835, https://link.aps.org/doi/10.1103/PhysRev.43.834.

[27] L. Alvarez and A. H. Compton, *A Positively Charged Component of Cosmic Rays*, Phys. Rev. **43** (1933) 835–836, https://link.aps.org/doi/10.1103/PhysRev.43.835.

[28] Telescope Array Collaboration, R. U. Abbasi et al., *An extremely energetic cosmic ray observed by a surface detector array*, Science **382** no. 6673, (2023) abo5095, arXiv:2311.14231 [astro-ph.HE].

[29] A. M. Hillas, *The Origin of Ultrahigh-Energy Cosmic Rays*, Ann. Rev. Astron. Astrophys. **22** (1984) 425–444.

[30] R. D. Blandford, *Acceleration of ultrahigh-energy cosmic rays*, Phys. Scripta T **85** (2000) 191–194, arXiv:astro-ph/9906026.

[31] J. P. Rachen and P. L. Biermann, *Extragalactic ultrahigh-energy cosmic rays. 1. Contribution from hot spots in FR-II radio galaxies*, Astron. Astrophys. **272** (1993) 161–175, arXiv:astro-ph/9301010.

[32] P. Bhattacharjee and G. Sigl, *Origin and propagation of extremely high-energy cosmic rays*, Phys. Rept. **327** (2000) 109–247, arXiv:astro-ph/9811011.

[33] N. Busca, D. Hooper, and E. W. Kolb, *Pierre auger data, photons, and top-down cosmic ray models*, Phys. Rev. D **73** (2006) 123001, arXiv:astro-ph/0603055.

[34] E. Fermi, *On the Origin of the Cosmic Radiation*, Phys. Rev. **75** (1949) 1169–1174.

[35] K. Murase and H. Takami, *Implications of Ultra-High-Energy Cosmic Rays for Transient Sources in the Auger Era*, Astrophys. J. Lett. **690** (2009) L14–L17, arXiv:0810.1813 [astro-ph].

[36] Pierre Auger Collaboration, A. Aab et al., *Combined fit of spectrum and composition data as measured by the Pierre Auger Observatory*, JCAP **04** (2017) 038, arXiv:1612.07155 [astro-ph.HE], [Erratum: JCAP 03, E02 (2018)].

[37] R. Alves Batista et al., *Open Questions in Cosmic-Ray Research at Ultrahigh Energies*, Front. Astron. Space Sci. **6** (2019) 23, arXiv:1903.06714 [astro-ph.HE].

[38] P. Blasi, *Cosmic Ray Acceleration in Supernova Remnants*, in *ICATPP Conference on Cosmic Rays for Particle and Astroparticle Physics*. 2011. arXiv:1012.5005 [astro-ph.HE].

[39] F. M. Rieger, *Active Galactic Nuclei as Potential Sources of Ultra-High Energy Cosmic Rays*, Universe **8** no. 11, (2022) 607, arXiv:2211.12202 [astro-ph.HE].

[40] K. Kotera, *Ultrahigh energy cosmic ray acceleration in newly born magnetars and their associated gravitational wave signatures*, Phys. Rev. D **84** (2011) 023002, arXiv:1106.3060 [astro-ph.HE].

[41] B. Cerutti and G. Giacinti, *A global model of particle acceleration at pulsar wind termination shocks*, Astron. Astrophys. **642** (2020) A123, arXiv:2008.07253 [astro-ph.HE].

[42] K. Murase, S. Inoue, and S. Nagataki, *Cosmic Rays Above the Second Knee from Clusters of Galaxies and Associated High-Energy Neutrino Emission*, Astrophys. J. Lett. **689** (2008) L105, arXiv:0805.0104 [astro-ph].

[43] A. Condorelli, J. Biteau, and R. Adam, *Impact of Galaxy Clusters on the Propagation of Ultrahigh-energy Cosmic Rays*, Astrophys. J. **957** no. 2, (2023) 80, arXiv:2309.04380 [astro-ph.HE].

[44] J. G. Kirk, A. W. Guthmann, Y. A. Gallant, and A. Achterberg, *Particle acceleration at ultrarelativistic shocks: an eigenfunction method*, Astrophys. J. **542** (2000) 235, arXiv:astro-ph/0005222.

[45] A. Achterberg, Y. A. Gallant, J. G. Kirk, and A. W. Guthmann, *Particle acceleration by ultrarelativistic shocks: Theory and simulations*, Mon. Not. Roy. Astron. Soc. **328** (2001) 393, arXiv:astro-ph/0107530.

[46] R. Aloisio and F. Tortorici, *Super Heavy Dark Matter and UHECR Anisotropy at Low Energy*, Astropart. Phys. **29** (2008) 307–316, arXiv:0706.3196 [astro-ph].

[47] L. Marzola and F. R. Urban, *Ultra High Energy Cosmic Rays \& Super-heavy Dark Matter*, Astropart. Phys. **93** (2017) 56–69, arXiv:1611.07180 [astro-ph.HE].

[48] P. Bhattacharjee and G. Sigl, *Origin and propagation of extremely high-energy cosmic rays*, Phys. Rept. **327** (2000) 109–247, arXiv:astro-ph/9811011.

[49] V. Berezinsky, B. Hnatyk, and A. Vilenkin, *Gamma-ray bursts from superconducting cosmic strings*, Phys. Rev. D **64** (2001) 043004, arXiv:astro-ph/0102366.

[50] V. Berezinsky and A. Vilenkin, *Cosmic necklaces and ultrahigh-energy cosmic rays*, Phys. Rev. Lett. **79** (1997) 5202–5205, arXiv:astro-ph/9704257.

[51] Pierre Auger Collaboration, P. Abreu et al., *Testing effects of Lorentz invariance violation in the propagation of astroparticles with the Pierre Auger Observatory*, JCAP **01** no. 01, (2022) 023, arXiv:2112.06773 [astro-ph.HE].

[52] XENON Collaboration, E. Aprile et al., *First Dark Matter Search with Nuclear Recoils from the XENONnT Experiment*, Phys. Rev. Lett. **131** no. 4, (2023) 041003, arXiv:2303.14729 [hep-ex].

[53] LZ Collaboration, J. Aalbers et al., *First Dark Matter Search Results from the LUX-ZEPLIN (LZ) Experiment*, Phys. Rev. Lett. **131** no. 4, (2023) 041002, arXiv:2207.03764 [hep-ex].

[54] K. Greisen, *End to the cosmic ray spectrum?*, Phys. Rev. Lett. **16** (1966) 748–750.

[55] G. T. Zatsepin and V. A. Kuzmin, *Upper limit of the spectrum of cosmic rays*, JETP Lett. **4** (1966) 78–80.

[56] K.-H. Kampert and P. Tinyakov, *Cosmic rays from the ankle to the cutoff*, Comptes Rendus Physique **15** (2014) 318–328, arXiv:1405.0575 [astro-ph.HE].

[57] C. Evoli, *The Cosmic-Ray Energy Spectrum*, Dec., 2018. https://doi.org/10.5281/zenodo.2360277.

[58] Telescope Array Collaboration, H. Kawai et al., *Telescope array experiment*, Nucl. Phys. B Proc. Suppl. **175-176** (2008) 221–226.

[59] AMS Collaboration, M. Aguilar et al., *First Result from the Alpha Magnetic Spectrometer on the International Space Station: Precision Measurement of the Positron Fraction in Primary Cosmic Rays of 0.5–350 GeV*, Phys. Rev. Lett. **110** (2013) 141102.

[60] KASCADE Collaboration, G. Schatz et al., *The KASCADE experiment*, Nucl. Phys. B Proc. Suppl. **60** (1998) 151–160.

[61] Particle Data Group Collaboration, S. Navas et al., *Review of particle physics*, Phys. Rev. D **110** no. 3, (2024) 030001.

[62] Pierre Auger Collaboration, A. Aab et al., *Inferences on mass composition and tests of hadronic interactions from 0.3 to 100 EeV using the water-Cherenkov detectors of the Pierre Auger Observatory*, Phys. Rev. D **96** no. 12, (2017) 122003, arXiv:1710.07249 [astro-ph.HE].

[63] Pierre Auger Collaboration, G. A. Anastasi, *AugerPrime: The Pierre Auger Observatory upgrade*, Nucl. Instrum. Meth. A **1044** (2022) 167497.

[64] A. A. Garcia, K. Bondarenko, A. Boyarsky, D. Nelson, A. Pillepich, and A. Sokolenko, *Ultrahigh energy cosmic ray deflection by the intergalactic magnetic field*, Phys. Rev. D **104** no. 8, (2021) 083017, arXiv:2101.07207 [astro-ph.HE].

[65] Pierre Auger Collaboration, C. Bonifazi, *The angular resolution of the Pierre Auger Observatory*, Nucl. Phys. B Proc. Suppl. **190** (2009) 20–25, arXiv:0901.3138 [astro-ph.HE].

[66] Pierre Auger Collaboration, P. Abreu et al., *Arrival Directions of Cosmic Rays above 32 EeV from Phase One of the Pierre Auger Observatory*, Astrophys. J. **935** no. 2, (2022) 170, arXiv:2206.13492 [astro-ph.HE].

[67] Pierre Auger Collaboration, A. Aab et al., *Cosmic-ray anisotropies in right ascension measured by the Pierre Auger Observatory*, Astrophys. J. **891** (2020) 142, arXiv:2002.06172 [astro-ph.HE].

[68] T. P. Li and Y. Q. Ma, *Analysis methods for results in gamma-ray astronomy*, Astrophys. J. **272** (1983) 317–324.

[69] Telescope Array, Pierre Auger Collaboration, A. di Matteo et al., *UHECR arrival directions in the latest data from the original Auger and TA surface detectors and nearby galaxies*, PoS **ICRC2021** (2021) 308, arXiv:2111.12366 [astro-ph.HE].

[70] Pierre Auger Collaboration, A. Aab et al., *A Targeted Search for Point Sources of EeV Neutrons*, Astrophys. J. Lett. **789** (2014) L34, arXiv:1406.4038 [astro-ph.HE].

[71] Pierre Auger Collaboration, A. Abdul Halim et al., *Search for evidence of neutron fluxes using Pierre Auger Observatory data*, PoS **ICRC2023** (2023) 246.

[72] Pierre Auger Collaboration, A. Abdul Halim et al., *Search for photons above* 10^{18} *eV by simultaneously measuring the atmospheric depth and the muon content of air showers at the Pierre Auger Observatory*, Phys. Rev. D **110** no. 6, (2024) 062005, arXiv:2406.07439 [astro-ph.HE].

[73] G. Pühlhofer, F. Leuschner, and H. Salzmann, *H.E.S.S.: The High Energy Stereoscopic System*, arXiv:2405.11104 [astro-ph.IM].

[74] D. J. Thompson and C. A. Wilson-Hodge, *Fermi Gamma-ray Space Telescope*, arXiv:2210.12875 [astro-ph.HE].

[75] CTA Consortium Collaboration, B. S. Acharya et al., *Science with the Cherenkov Telescope Array*. WSP, 11, 2018. arXiv:1709.07997 [astro-ph.IM].

[76] Pierre Auger Collaboration, P. Abreu et al., *Searches for Ultra-High-Energy Photons at the Pierre Auger Observatory*, Universe **8** no. 11, (2022) 579, arXiv:2210.12959 [astro-ph.HE].

[77] L. M. Brown, *The idea of the neutrino*, Phys. Today **31N9** (1978) 23–28.

[78] F. Reines and C. L. Cowan, *Detection of the free neutrino*, Phys. Rev. **92** (1953) 830–831.

[79] Super-Kamiokande Collaboration, Y. Fukuda et al., *Evidence for oscillation of atmospheric neutrinos*, Phys. Rev. Lett. **81** (1998) 1562–1567, arXiv:hep-ex/9807003.

[80] SNO Collaboration, A. Bellerive, J. R. Klein, A. B. McDonald, A. J. Noble, and A. W. P. Poon, *The Sudbury Neutrino Observatory*, Nucl. Phys. B **908** (2016) 30–51, arXiv:1602.02469 [nucl-ex].

[81] X. Qian and P. Vogel, *Neutrino Mass Hierarchy*, Prog. Part. Nucl. Phys. **83** (2015) 1–30, arXiv:1505.01891 [hep-ex].

[82] Katrin Collaboration, M. Aker et al., *Direct neutrino-mass measurement based on 259 days of KATRIN data*, arXiv:2406.13516 [nucl-ex].

[83] A. de Gouvêa, *Neutrino mass puzzle*, https://cerncourier.com/a/the-neutrino-mass-puzzle/#:~:text=Though%20there%20are%20too%20many,or%20through%20a%20different%20mechanism.

[84] E. Vitagliano, I. Tamborra, and G. Raffelt, *Grand Unified Neutrino Spectrum at Earth: Sources and Spectral Components*, Rev. Mod. Phys. **92** (2020) 45006, arXiv:1910.11878 [astro-ph.HE].

[85] Kamiokande-II Collaboration, K. Hirata et al., *Observation of a Neutrino Burst from the Supernova SN 1987a*, Phys. Rev. Lett. **58** (1987) 1490–1493.

[86] IceCube Collaboration, M. G. Aartsen et al., *First observation of PeV-energy neutrinos with IceCube*, Phys. Rev. Lett. **111** (2013) 021103, arXiv:1304.5356 [astro-ph.HE].

[87] IceCube Collaboration, M. G. Aartsen et al., *Evidence for High-Energy Extraterrestrial Neutrinos at the IceCube Detector*, Science **342** (2013) 1242856, arXiv:1311.5238 [astro-ph.HE].

[88] IceCube Collaboration, R. Abbasi et al., *Measurement of atmospheric neutrino mixing with improved IceCube DeepCore calibration and data processing*, Phys. Rev. D **108** no. 1, (2023) 012014, arXiv:2304.12236 [hep-ex].

[89] M. Prado Rodriguez, *Neutrino Mass Ordering with IceCube DeepCore*, Phys. Sci. Forum **8** no. 1, (2023) 7.

[90] D. Scott, *The Cosmic Neutrino Background*, in *International School of Physics "Enrico Fermi" in collaboration with the summer schools ISAPP: Neutrino Physics, Astrophysics and Cosmology*. 2, 2024. arXiv:2402.16243 [astro-ph.CO].

[91] M. Ahlers, *ISAPP lecture on high energy neutrino astronomy*, 2022. https://indico.ijclab.in2p3.fr/event/7633/contributions/25553/attachments/18579/24903/Ahlers_ISAPP2022_Saclay.pdf.

[92] B. Pontecorvo, *Inverse beta processes and nonconservation of lepton charge*, Zh. Eksp. Teor. Fiz. **34** (1957) 247.

[93] Z. Maki, M. Nakagawa, and S. Sakata, *Remarks on the unified model of elementary particles*, Prog. Theor. Phys. **28** (1962) 870–880.

[94] P. Lipari, M. Lusignoli, and D. Meloni, *Flavor Composition and Energy Spectrum of Astrophysical Neutrinos*, Phys. Rev. D **75** (2007) 123005, arXiv:0704.0718 [astro-ph].

[95] IceCube Collaboration, R. Abbasi et al., *Characterization of the astrophysical diffuse neutrino flux using starting track events in IceCube*, Phys. Rev. D **110** no. 2, (2024) 022001, arXiv:2402.18026 [astro-ph.HE].

[96] IceCube Collaboration, R. Abbasi et al., *Constraining High-energy Neutrino Emission from Supernovae with IceCube*, Astrophys. J. Lett. **949** no. 1, (2023) L12, arXiv:2303.03316 [astro-ph.HE].

[97] A. Condorelli, D. Boncioli, E. Peretti, and S. Petrera, *Testing hadronic and photohadronic interactions as responsible for ultrahigh energy cosmic rays and neutrino fluxes from starburst galaxies*, Phys. Rev. D **107** no. 8, (2023) 083009, arXiv:2209.08593 [astro-ph.HE].

[98] K. Murase and F. W. Stecker, *High-Energy Neutrinos from Active Galactic Nuclei*, http://dx.doi.org/10.1142/9789811282645_0010.

[99] B. Zhang, Z. G. Dai, and P. Meszaros, *High-energy neutrinos from magnetars*, Astrophys. J. **595** (2003) 346–351, arXiv:astro-ph/0210382.

[100] J. Heinze, A. Fedynitch, D. Boncioli, and W. Winter, *A new view on Auger data and cosmogenic neutrinos in light of different nuclear disintegration and air-shower models*, Astrophys. J. **873** no. 1, (2019) 88, arXiv:1901.03338 [astro-ph.HE].

[101] V. S. Berezinsky and G. T. Zatsepin, *Cosmic neutrinos of superhigh energy*, Yad. Fiz. **11** (1970) 200–205.

[102] D. Ehlert, A. van Vliet, F. Oikonomou, and W. Winter, *Constraints on the proton fraction of cosmic rays at the highest energies and the consequences for cosmogenic neutrinos and photons*, JCAP **02** (2024) 022, arXiv:2304.07321 [astro-ph.HE].

[103] R. Aloisio, D. Boncioli, A. di Matteo, A. F. Grillo, S. Petrera, and F. Salamida, *Cosmogenic neutrinos and ultra-high energy cosmic ray models*, JCAP **10** (2015) 006, arXiv:1505.04020 [astro-ph.HE].

[104] K.-H. Kampert and M. Unger, *Measurements of the Cosmic Ray Composition with Air Shower Experiments*, Astropart. Phys. **35** (2012) 660–678, arXiv:1201.0018 [astro-ph.HE].

[105] R. Alves Batista, R. M. de Almeida, B. Lago, and K. Kotera, *Cosmogenic photon and neutrino fluxes in the Auger era*, JCAP **01** (2019) 002, arXiv:1806.10879 [astro-ph.HE].

[106] Z. Myers and A. Nusser, *Searching for Neutrinos from WIMP Annihilations in the Galactic Stellar Disk*, Mon. Not. Roy. Astron. Soc. **387** (2008) 1712, arXiv:0804.0554 [astro-ph].

[107] C. A. Argüelles, D. Delgado, A. Friedlander, A. Kheirandish, I. Safa, A. C. Vincent, and H. White, *Dark matter decay to neutrinos*, Phys. Rev. D **108** no. 12, (2023) 123021, arXiv:2210.01303 [hep-ph].

[108] J. A. Formaggio and G. P. Zeller, *From eV to EeV: Neutrino Cross Sections Across Energy Scales*, Rev. Mod. Phys. **84** (2012) 1307–1341, arXiv:1305.7513 [hep-ex].

[109] S. L. Glashow, *Resonant Scattering of Antineutrinos*, Phys. Rev. **118** (1960) 316–317.

[110] IceCube Collaboration, M. G. Aartsen et al., *Detection of a particle shower at the Glashow resonance with IceCube*, Nature **591** no. 7849, (2021) 220–224, arXiv:2110.15051 [hep-ex], [Erratum: Nature 592, E11 (2021)].

[111] A. Garcia Soto, D. Garg, M. H. Reno, and C. A. Argüelles, *Probing quantum gravity with elastic interactions of ultrahigh-energy neutrinos*, Phys. Rev. D **107** no. 3, (2023) 033009, arXiv:2209.06282 [hep-ph].

[112] A. Cooper-Sarkar, P. Mertsch, and S. Sarkar, *The high energy neutrino cross-section in the Standard Model and its uncertainty*, JHEP **08** (2011) 042, arXiv:1106.3723 [hep-ph].

[113] H1, ZEUS Collaboration, F. D. Aaron et al., *Combined Measurement and QCD Analysis of the Inclusive e+- p Scattering Cross Sections at HERA*, JHEP **01** (2010) 109, arXiv:0911.0884 [hep-ex].

[114] G. Altarelli and G. Parisi, *Asymptotic Freedom in Parton Language*, Nucl. Phys. B **126** (1977) 298–318.

[115] Y. L. Dokshitzer, *Calculation of the Structure Functions for Deep Inelastic Scattering and e+ e- Annihilation by Perturbation Theory in Quantum Chromodynamics.*, Sov. Phys. JETP **46** (1977) 641–653.

[116] V. N. Gribov and L. N. Lipatov, *Deep inelastic electron scattering in perturbation theory*, Phys. Lett. B **37** (1971) 78–80.

[117] C. A. Argüelles, F. Halzen, and N. Kurahashi, *From the Dawn of Neutrino Astronomy to A New View of the Extreme Universe*, arXiv:2405.17623 [hep-ex].

[118] IceCube Collaboration, M. G. Aartsen et al., *The IceCube Neutrino Observatory: Instrumentation and Online Systems*, JINST **12** no. 03, (2017) P03012, arXiv:1612.05093 [astro-ph.IM], [Erratum: JINST 19, E05001 (2024)].

[119] E. Andres et al., *The AMANDA neutrino telescope: Principle of operation and first results*, Astropart. Phys. **13** (2000) 1–20, arXiv:astro-ph/9906203.

[120] K. Arisaka et al., *KAMIOKA Nucleon Decay Experiments; status and performance*, AIP Conf. Proc. **114** (1984) 54–76.

[121] ANTARES Collaboration, A. Creusot, *The Antares detector*, Nucl. Instrum. Meth. A **718** (2013) 489–491.

[122] KM3NeT Collaboration, A. Margiotta, *The KM3NeT deep-sea neutrino telescope*, Nucl. Instrum. Meth. A **766** (2014) 83–87, arXiv:1408.1392 [astro-ph.IM].

[123] Baikal-GVD Collaboration, Y. Malyshkin, *Baikal-GVD neutrino telescope: Design reference 2022*, Nucl. Instrum. Meth. A **1050** (2023) 168117.

[124] P-ONE Collaboration, M. Agostini et al., *The Pacific Ocean Neutrino Experiment*, Nature Astron. **4** no. 10, (2020) 913–915, arXiv:2005.09493 [astro-ph.HE].

[125] G. A. Askar'yan, *Excess negative charge of an electron-photon shower and its coherent radio emission*, Zh. Eksp. Teor. Fiz. **41** (1961) 616–618.

[126] J. Alvarez-Muniz, A. Romero-Wolf, and E. Zas, *Practical and accurate calculations of Askaryan radiation*, Phys. Rev. D **84** (2011) 103003, arXiv:1106.6283 [astro-ph.HE].

[127] ANITA Collaboration, P. W. Gorham et al., *The Antarctic Impulsive Transient Antenna Ultra-high Energy Neutrino Detector Design, Performance, and Sensitivity for 2006-2007 Balloon Flight*, Astropart. Phys. **32** (2009) 10–41, arXiv:0812.1920 [astro-ph].

[128] H. Schoorlemmer et al., *Energy and Flux Measurements of Ultra-High Energy Cosmic Rays Observed During the First ANITA Flight*, Astropart. Phys. **77** (2016) 32–43, arXiv:1506.05396 [astro-ph.HE].

[129] RNO-G Collaboration, J. A. Aguilar et al., *Design and Sensitivity of the Radio Neutrino Observatory in Greenland (RNO-G)*, JINST **16** no. 03, (2021) P03025, arXiv:2010.12279 [astro-ph.IM], [Erratum: JINST 18, E03001 (2023)].

[130] IceCube-Gen2 Collaboration, M. G. Aartsen et al., *IceCube-Gen2: the window to the extreme Universe*, J. Phys. G **48** no. 6, (2021) 060501, arXiv:2008.04323 [astro-ph.HE].

[131] ANTARES Collaboration, R. Lahmann, *Status and Recent Results of the Acoustic Neutrino Detection Test System AMADEUS*, Nucl. Instrum. Meth. A **662** (2012) S216–S221, arXiv:1104.3041 [astro-ph.IM].

[132] IceCube Collaboration, T. Karg, *Status and recent results of the South Pole Acoustic Test Setup*, Nucl. Instrum. Meth. A **662** (2012) S36–S41, arXiv:1010.2025 [astro-ph.IM].

[133] A. Marinelli, P. Migliozzi, and A. Simonelli, *Acoustic neutrino detection in a Adriatic multidisciplinary observatory (ANDIAMO)*, Astropart. Phys. **143** (2022) 102760, arXiv:2109.15199 [astro-ph.IM].

[134] Radar Echo Telescope Collaboration, S. Prohira et al., *The Radar Echo Telescope for Cosmic Rays: Pathfinder experiment for a next-generation neutrino observatory*, Phys. Rev. D **104** no. 10, (2021) 102006, arXiv:2104.00459 [astro-ph.IM].

[135] IceCube Collaboration, M. G. Aartsen et al., *Search for a diffuse flux of astrophysical muon neutrinos with the IceCube 59-string configuration*, Phys. Rev. D **89** no. 6, (2014) 062007, arXiv:1311.7048 [astro-ph.HE].

[136] ANTARES Collaboration, A. Albert et al., *ANTARES Search for Point Sources of Neutrinos Using Astrophysical Catalogs: A Likelihood Analysis*, Astrophys. J. **911** no. 1, (2021) 48, arXiv:2012.15082 [astro-ph.HE].

[137] IceCube Collaboration, R. Abbasi et al., *Search for Point Sources of High Energy Neutrinos with Final Data from AMANDA-II*, Phys. Rev. D **79** (2009) 062001, arXiv:0809.1646 [astro-ph].

[138] Baikal-GVD Collaboration, V. A. Allakhverdyan et al., *Search for directional associations between baikal gigaton volume detector neutrino-induced cascades and high-energy astrophysical sources*, Mon. Not. Roy. Astron. Soc. **526** no. 1, (2023) 942–951, arXiv:2307.07327 [astro-ph.HE].

[139] D. Eichler, *High-energy neutrino astronomy-A probe of galactic nuclei?*, Astrophys. J. **232** (1979) 106–112.

[140] V. Berezinsky and V. Ginzburg, *On high-energy neutrino radiation of quasars and active galactic nuclei*, Monthly Notices of the Royal Astronomical Society **194** no. 1, (1981) 3–14.

[141] Pierre Auger Collaboration, A. Abdul Halim et al., *Latest results from the searches for ultra-high-energy photons and neutrinos at the Pierre Auger Observatory*, PoS **ICRC2023** (2023) 1488.

[142] LIGO Scientific Collaboration, J. Abadie et al., *Implications For The Origin Of GRB 051103 From LIGO Observations*, Astrophys. J. **755** (2012) 2, arXiv:1201.4413 [astro-ph.HE].

[143] ANTARES, IceCube, Pierre Auger, LIGO Scientific, Virgo Collaboration, A. Albert et al., *Search for High-energy Neutrinos from Binary Neutron Star Merger GW170817 with ANTARES, IceCube, and the Pierre Auger Observatory*, Astrophys. J. Lett. **850** no. 2, (2017) L35, arXiv:1710.05839 [astro-ph.HE].

[144] SNEWS Collaboration, S. Al Kharusi et al., *SNEWS 2.0: a next-generation supernova early warning system for multi-messenger astronomy*, New J. Phys. **23** no. 3, (2021) 031201, arXiv:2011.00035 [astro-ph.HE].

[145] M. W. E. Smith et al., *The Astrophysical Multimessenger Observatory Network (AMON)*, Astropart. Phys. **45** (2013) 56–70, arXiv:1211.5602 [astro-ph.HE].

[146] Pierre Auger Collaboration, A. Aab et al., *Multi-Messenger Physics with the Pierre Auger Observatory*, Front. Astron. Space Sci. **6** (2019) 24, arXiv:1904.11918 [astro-ph.HE].

[147] IceCube, Pierre Auger, Telescope Array, Auger, ANTARES Collaboration, A. Albert et al., *Search for Spatial Correlations of Neutrinos with Ultra-high-energy Cosmic Rays*, Astrophys. J. **934** no. 2, (2022) 164, arXiv:2201.07313 [astro-ph.HE].

[148] *Wikipedia article: Multimessenger astronomy*, https://en.wikipedia.org/wiki/Multimessenger_astronomy.

[149] W. Heitler, *The quantum theory of radiation*, vol. 5 of *International Series of Monographs on Physics*. Oxford University Press, Oxford, 1936.

[150] J. Matthews, *A Heitler model of extensive air showers*, Astropart. Phys. **22** (2005) 387–397.

[151] J. Alvarez-Muniz, R. Engel, T. K. Gaisser, J. A. Ortiz, and T. Stanev, *Hybrid simulations of extensive air showers*, Phys. Rev. D **66** (2002) 033011, arXiv:astro-ph/0205302.

[152] T. Pierog and K. Werner, *Muon Production in Extended Air Shower Simulations*, Phys. Rev. Lett. **101** (2008) 171101, arXiv:astro-ph/0611311.

[153] J. Linsley, *Proc. 15th ICRC, Plovdiv, Bulgaria, vol. 12, p.89*,.

[154] J. W. Fowler, L. F. Fortson, C. C. H. Jui, D. B. Kieda, R. A. Ong, C. L. Pryke, and P. Sommers, *A Measurement of the cosmic ray spectrum and composition at the knee*, Astropart. Phys. **15** (2001) 49–64, arXiv:astro-ph/0003190.

[155] T. Wibig, *Testing the superposition model in small CORSIKA shower simulations*, J. Phys. G **49** no. 3, (2022) 035201, arXiv:2107.11591 [astro-ph.HE].

[156] J.-S. Li, D.-H. Zhang, H.-L. Li, and N. Yasuda, *Projectile fragmentation of 500 A MeV 56Fe in nuclear emulsion*, Nuclear Instruments and Methods in Physics Research B **307** (2013) 503–506.

[157] J. Albrecht et al., *The Muon Puzzle in cosmic-ray induced air showers and its connection to the Large Hadron Collider*, Astrophys. Space Sci. **367** no. 3, (2022) 27, arXiv:2105.06148 [astro-ph.HE].

[158] L. D. Landau and I. Pomeranchuk, *Limits of applicability of the theory of bremsstrahlung electrons and pair production at high-energies*, Dokl. Akad. Nauk Ser. Fiz. **92** (1953) 535–536.

[159] A. B. Migdal, *Bremsstrahlung and pair production in condensed media at high-energies*, Phys. Rev. **103** (1956) 1811–1820.

[160] CORSIKA Collaboration, A. Sandrock, J.-M. Alameddine, and F. Riehn, *Validation of Electromagnetic Showers in CORSIKA 8*, PoS **ICRC2023** (2023) 393, arXiv:2308.07112 [astro-ph.HE].

[161] T. K. Gaisser and A. M. Hillas, *Reliability of the Method of Constant Intensity Cuts for Reconstructing the Average Development of Vertical Showers*, in *International Cosmic Ray Conference*, vol. 8. Jan., 1977.

[162] Mayotte, Sonja, *Study of the cosmic ray composition sensitivity of AugerPrime: probing the prospects of the upgrade to the Pierre Auger Observatory with a deep learning approach*. thesis, Bergische Universität Wuppertal, Wuppertal, June 2021.

[163] K. Greisen, *Cosmic ray showers*, Ann. Rev. Nucl. Part. Sci. **10** (1960) 63–108.

[164] K. Kamata and J. Nishimura, *The Lateral and the Angular Structure Functions of Electron Showers*, Prog. Theor. Phys. Suppl. **6** (1958) 93–155.

[165] A. M. Hillas, *Angular and energy distributions of charged particles in electron-photon cascades in air*, Journal of Physics G: Nuclear Physics **8** no. 10, (1982) 1461.

[166] A. Fedosimova, P. Kharchevnikov, I. Lebedev, and A. Temiraliev, *Applying universality in the development of cascade processes for the research of high energy cosmic particles in space experiments*, EPJ Web Conf. **145** (2017) 10004.

[167] A. Bridgeman, *Shower universality reconstruction of data from the Pierre Auger Observatory and validations with hadronic interaction models*, PoS **ICRC2017** (2017) 323.

[168] L. Cazon, R. Conceição, M. A. Martins, and F. Riehn, *Proton-air interactions at ultra-high energies in muon-depleted air showers with different depths*, Phys. Lett. B **859** (2024) 139115, arXiv:2406.08620 [astro-ph.HE].

[169] R. Ulrich, J. Blumer, R. Engel, F. Schussler, and M. Unger, *On the measurement of the proton-air cross section using air shower data*, New J. Phys. **11** (2009) 065018, arXiv:0903.0404 [astro-ph.HE].

[170] H. E. Bergeson, G. L. Cassiday, T. W. Chiu, D. A. Cooper, J. W. Elbert, E. C. Loh, D. Steck, W. J. West, J. Linsley, and G. W. Mason, *Measurement of Light Emission from Remote Cosmic Ray Air Showers*, Phys. Rev. Lett. **39** (1977) 847–849.

[171] R. M. Baltrusaitis et al., *The Utah Fly's Eye detector*, Nucl. Instrum. Meth. A **240** (1985) 410–428.

[172] R. M. Baltrusaitis, G. L. Cassiday, R. Cooper, B. R. Dawson, J. W. Elbert, B. E. Fick, D. F. Liebing, E. C. Loh, P. Sokolsky, and D. Steck, *The Fly's Eye Detector: Present and Future*, Nucl. Instrum. Meth. A **264** (1988) 87–92.

[173] P. A. Cherenkov, *Visible luminescence of pure liquids under the influence of γ-radiation*, Dokl. Akad. Nauk SSSR **2** no. 8, (1934) 451–454.

[174] M. Dyakonov, S. Knurenko, V. Kolosov, D. Krasilnikov, F. Lischenyuk, I. Sleptsov, and S. Nikolsky, *The use of Cherenkov detectors at the Yakutsk cosmic ray extensive air shower array*, Nuclear Instruments and Methods in Physics Research Section A: Accelerators, Spectrometers, Detectors and Associated Equipment **248** no. 1, (1986) 224–226.

[175] L. Kuzmichev et al., *Cherenkov EAS arrays in the Tunka astrophysical center: From Tunka-133 to the TAIGA gamma and cosmic ray hybrid detector*, Nucl. Instrum. Meth. A **952** (2020) 161830.

[176] MAGIC Collaboration, J. Cortina, F. Goebel, and T. Schweizer, *Technical Performance of the MAGIC Telescopes*, arXiv:0907.1211 [astro-ph.IM].

[177] KASCADE Collaboration, K. H. Kampert et al., *Cosmic rays in the energy range of the knee: Recent results from KASCADE*, in *30th International Symposium on Multiparticle Dynamics*. 2, 2001. arXiv:astro-ph/0102266.

[178] F. D. Kahn and I. Lerche, *Radiation from Cosmic Ray Air Showers*, Proceedings of the Royal Society of London Series A **289** no. 1417, (1966) 206–213.

[179] H. R. Allan, R. W. Clay, and J. K. Jones, *Radio Pulses from Extensive Air Showers*, Nature (London) 227: 1116-18 (12 Sep 1970). (1970).

[180] T. Huege, *Radio detection of cosmic ray air showers in the digital era*, Phys. Rept. **620** (2016) 1–52, arXiv:1601.07426 [astro-ph.IM].

[181] LOFAR Collaboration, M. P. van Haarlem et al., *LOFAR: The LOw-Frequency ARray*, Astron. Astrophys. **556** (2013) A2, arXiv:1305.3550 [astro-ph.IM].

[182] Pierre Auger Collaboration, A. Aab et al., *Energy Estimation of Cosmic Rays with the Engineering Radio Array of the Pierre Auger Observatory*, Phys. Rev. D **93** no. 12, (2016) 122005, arXiv:1508.04267 [astro-ph.HE].

[183] K. Fang et al., *The Giant Radio Array for Neutrino Detection (GRAND): Present and Perspectives*, PoS **ICRC2017** (2018) 996, arXiv:1708.05128 [astro-ph.IM].

[184] W. Galbraith and J. V. Jelley, *Light Pulses from the Night Sky associated with Cosmic Rays*, Nature **171** no. 4347, (1953) 349–350.

[185] E. Bagge, E. Böhm, R. Fritze, U. J. Roose, M. Samorski, C. Schnier, R. Staubert, K. O. Thielheim, J. Trümper, L. Wiedecke, and W. Wolter, *The extensive air shower experiment at Kiel.*, in *International Cosmic Ray Conference*, vol. 1. Jan., 1965. https://ui.adsabs.harvard.edu/abs/1965ICRC....2..738B.

[186] J. Linsley, L. Scarsi, and B. Rossi, *Extremely energetic cosmic-ray event*, Phys. Rev. Lett. **6** (1961) 485–487.

[187] A. Bueno, A. Gascon, J. I. Illana, and M. Masip, *Propagation of B mesons in the atmosphere*, JCAP **02** (2012) 028, arXiv:1109.4337 [hep-ph].

[188] Pawlowsky, J. and Kampert, K-H. and Nelles, A., *Search for inclined photon air showers with the AugerPrime Radio Detector*. thesis, Bergische Universität Wuppertal, Wuppertal, August 7, 2024.

[189] S. Y. BenZvi et al., *The Lidar System of the Pierre Auger Observatory*, Nucl. Instrum. Meth. A **574** (2007) 171–184, arXiv:astro-ph/0609063.

[190] B. Fick, M. Malek, J. A. J. Matthews, J. Matthews, R. Meyhandan, M. Mostafá, M. Roberts, P. Sommers, and L. Wiencke, *The Central Laser Facility at the Pierre Auger Observatory*, JINST **1** no. 11, (2006) P11003–P11003.

[191] Pierre Auger Collaboration, L. Wiencke, *Atmospheric Calorimetry above 10^{19} eV: Shooting Lasers at the Pierre Auger Cosmic-Ray Observatory*, J. Phys. Conf. Ser. **160** (2009) 012037, arXiv:0807.2884 [astro-ph].

[192] J. R. Hörandel, *Status and prospects of the Auger Radio Detector*, PoS **ECRS** (2023) 095.

[193] Pierre Auger Collaboration, A. Abdul Halim et al., *Status and Performance of the Underground Muon Detector of the Pierre Auger Observatory*, PoS **ICRC2023** (2023) 267.

[194] Pierre Auger Collaboration, G. Cataldi, *The upgrade of the Pierre Auger Observatory with the Scintillator Surface Detector*, PoS **ICRC2021** (2021) 251.

[195] Pierre Auger Collaboration, J. Abraham et al., *The Fluorescence Detector of the Pierre Auger Observatory*, Nucl. Instrum. Meth. A **620** (2010) 227–251, arXiv:0907.4282 [astro-ph.IM].

[196] J. Rosado, F. Blanco, and F. Arqueros, *On the absolute value of the air-fluorescence yield*, Astropart. Phys. **55** (2014) 51–62, arXiv:1401.4310 [astro-ph.IM].

[197] Pierre Auger Collaboration, F. Salamida, *The analysis of hybrid events in the Pierre Auger Observatory*, Nucl. Instrum. Meth. A **588** (2008) 207–210.

[198] Pierre Auger Collaboration, A. Aab et al., *A Three Year Sample of Almost 1600 Elves Recorded Above South America by the Pierre Auger Cosmic-Ray Observatory*, Earth Space Sci. **7** no. 4, (2020) e2019EA000582.

[199] Pierre Auger Collaboration, I. Allekotte et al., *The Surface Detector System of the Pierre Auger Observatory*, Nucl. Instrum. Meth. A **586** (2008) 409–420, arXiv:0712.2832 [astro-ph].

[200] Pierre Auger Collaboration, X. Bertou et al., *Calibration of the surface array of the Pierre Auger Observatory*, Nucl. Instrum. Meth. A **568** (2006) 839–846, arXiv:2102.01656 [astro-ph.HE].

[201] Pierre Auger Collaboration, M. Aglietta et al., *Response of the Pierre Auger Observatory water Cherenkov detectors to muons*, in *29th International Cosmic Ray Conference*. 7, 2005.

[202] Pierre Auger Collaboration, S. Dasso and H. Asorey, *The scaler mode in the Pierre Auger Observatory to study heliospheric modulation of cosmic rays*, Adv. Space Res. **49** (2012) 1563–1569, arXiv:1204.6196 [astro-ph.SR].

[203] P. Billoir, *Proposition to improve the local trigger of the Surface Detector for low energy showers*, Tech. Rep. GAP-2009-179, Pierre Auger Observatory, 2009. https://www.auger.org/gap-notes/. (key protected).

[204] Pierre Auger Collaboration, P. Abreu et al., *The energy spectrum of cosmic rays beyond the turn-down around* 10^{17} *eV as measured with the surface detector of the Pierre Auger Observatory*, Eur. Phys. J. C **81** no. 11, (2021) 966, arXiv:2109.13400 [astro-ph.HE].

[205] P. Billoir, *New proposal to improve local trigger of the Surface Detector*, Tech. Rep. GAP-2011-089, Pierre Auger Observatory, 2011. https://www.auger.org/gap-notes/. (key protected).

[206] A. Coleman, P. Ghia, and M. Mostafa, *The Station Triggering Efficiency Using the New Triggers*, Tech. Rep. GAP-2018-017, Pierre Auger Observatory, 2018. https://www.auger.org/gap-notes/. (key protected).

[207] Pierre Auger Collaboration, J. Abraham et al., *Trigger and Aperture of the Surface Detector Array of the Pierre Auger Observatory*, Nucl. Instrum. Meth. A **613** (2010) 29–39, arXiv:1111.6764 [astro-ph.IM].

[208] Pierre Auger Collaboration, P. Abreu et al., *AugerPrime Upgraded Electronics*, PoS **ICRC2021** (2021) 230.

[209] Pierre Auger Collaboration, A. Abdul Halim et al., *The dynamic range of the upgraded surface-detector stations of AugerPrime*, PoS **ICRC2023** (2023) 343.

[210] Pierre Auger Collaboration, A. Aab et al., *Design and implementation of the AMIGA embedded system for data acquisition*, JINST **16** no. 07, (2021) T07008, arXiv:2101.11747 [astro-ph.IM].

[211] Pierre Auger Collaboration, A. Abdul Halim et al., *Search for primary photons at tens of PeV with the Pierre Auger Observatory*, PoS **ICRC2023** (2023) 238.

[212] S. Argiro, S. L. C. Barroso, J. Gonzalez, L. Nellen, T. C. Paul, T. A. Porter, L. Prado, Jr., M. Roth, R. Ulrich, and D. Veberic, *The Offline Software Framework of the Pierre Auger Observatory*, Nucl. Instrum. Meth. A **580** (2007) 1485–1496, arXiv:0707.1652 [astro-ph].

[213] Pierre Auger Collaboration, A. Abdul Halim et al., *Update on the Offline Framework for AugerPrime and production of reference simulation libraries using the VO Auger grid resources*, PoS **ICRC2023** (2023) 248.

[214] D. Heck, J. Knapp, J. N. Capdevielle, G. Schatz, and T. Thouw, *CORSIKA: A Monte Carlo code to simulate extensive air showers*, Tech. Rep. FZKA-6019, Forschungszentrum Karlsruhe, 2, 1998.

[215] S. J. Sciutto, *AIRES: A system for air shower simulations*, arXiv:astro-ph/9911331.

[216] R. Brun and F. Rademakers, *ROOT: An object oriented data analysis framework*, Nucl. Instrum. Meth. A **389** (1997) 81–86.

[217] *Python Instrumentation Kit*, https://github.com/HDembinski/pyik.

[218] J. Pivarski et al., *Uproot*,.

[219] G. Corcella, I. G. Knowles, G. Marchesini, S. Moretti, K. Odagiri, P. Richardson, M. H. Seymour, and B. R. Webber, *HERWIG 6: An Event generator for hadron emission reactions with interfering gluons (including supersymmetric processes)*, JHEP **01** (2001) 010, arXiv:hep-ph/0011363.

[220] S. Ostapchenko, *Monte Carlo treatment of hadronic interactions in enhanced Pomeron scheme: I. QGSJET-II model*, Phys. Rev. D **83** (2011) 014018, arXiv:1010.1869 [hep-ph].

[221] F. Riehn, R. Engel, A. Fedynitch, T. K. Gaisser, and T. Stanev, *Hadronic interaction model Sibyll 2.3d and extensive air showers*, Phys. Rev. D **102** no. 6, (2020) 063002, arXiv:1912.03300 [hep-ph].

[222] T. Pierog, I. Karpenko, J. M. Katzy, E. Yatsenko, and K. Werner, *EPOS LHC: Test of collective hadronization with data measured at the CERN Large Hadron Collider*, Phys. Rev. C **92** no. 3, (2015) 034906, arXiv:1306.0121 [hep-ph].

[223] A. Ferrari, P. R. Sala, A. Fasso, and J. Ranft, *FLUKA: A multi-particle transport code (Program version 2005)*, Tech. Rep. CERN-2005-010, SLAC-R-773, INFN-TC-05-11, CERN-2005-10, CERN, 10, 2005.

[224] G. Battistoni et al., *Overview of the FLUKA code*, Annals Nucl. Energy **82** (2015) 10–18.

[225] W. R. Nelson, H. Hirayama, and D. W. O. Rogers, *The EGS4 Code System*, Tech. Rep. SLAC-0265, SLAC-265, SLAC-R-0265, SLAC-R-265, SLAC, 12, 1985.

[226] Pierre Auger Collaboration, P. Abreu et al., *Description of Atmospheric Conditions at the Pierre Auger Observatory using the Global Data Assimilation System (GDAS)*, Astropart. Phys. **35** (2012) 591–607, arXiv:1201.2276 [astro-ph.HE].

[227] A. M. Hillas, *Shower simulation: Lessons from MOCCA*, Nucl. Phys. B Proc. Suppl. **52** (1997) 29–42.

[228] D. Heck and J. Knapp, *Upgrade of the Monte Carlo Code CORSIKA to simulate extensive air showers with energies* $> 10^{20}$ *eV*, Tech. Rep. FZKA-6097, Forschungszentrum Karlsruhe, 1998.

[229] Pierre Auger Collaboration, M. Kobal, *A thinning method using weight limitation for air-shower simulations*, Astropart. Phys. **15** (2001) 259–273.

[230] *EGI, European Grid Infrastructure.*, http://www.egi.eu/.

[231] Pierre Auger Collaboration, J. Lozano Bahilo, *Mass production of extensive air showers for the Pierre Auger Collaboration using Grid technology*, J. Phys. Conf. Ser. **368** (2012) 012015.

[232] B. T. Stokes, R. Cady, D. Ivanov, J. N. Matthews, and G. B. Thomson, *Dethinning Extensive Air Shower Simulations*, Astropart. Phys. **35** (2012) 759–766, arXiv:1104.3182 [astro-ph.IM].

[233] GEANT4 Collaboration, S. Agostinelli et al., *GEANT4–A simulation toolkit*, Nucl. Instrum. Meth. A **506** (2003) 250–303.

[234] J. Allison et al., *Geant4 Developments and Applications*, IEEE Trans. Nucl. Sci. **53** (2006) 270.

[235] J. Allison et al., *Recent developments in Geant4*, Nucl. Instrum. Meth. A **835** (2016) 186–225.

[236] D. Veberic, *Estimation of the Total Signal in Saturated Stations of Pierre Auger Surface Detector*, in *33rd International Cosmic Ray Conference*. 2013.

[237] Pierre Auger Collaboration, A. Aab et al., *Reconstruction of events recorded with the surface detector of the Pierre Auger Observatory*, JINST **15** no. 10, (2020) P10021, arXiv:2007.09035 [astro-ph.IM].

[238] C. Medina and X. Bertou, *Using compact 3 TOT as a starting point for SD reconstruction*, Tech. Rep. GAP-2004-030, Pierre Auger Observatory, 2004. https://www.auger.org/gap-notes/. (key protected).

[239] Pierre Auger Collaboration, R. Colalillo, *The observation of lightning-related events with the Surface Detector of the Pierre Auger Observatory*, EPJ Web Conf. **197** (2019) 03003.

[240] P. Billoir, J. Navarro, and S. Navas, *An Offline Module for Injection of Random Accidental Signals in SD Stations*, Tech. Rep. GAP-2011-038, Pierre Auger Observatory, 2011. https://www.auger.org/gap-notes/. (key protected).

[241] P. Billoir, *Top-down Selection of Events and Stations*, Tech. Rep. GAP-2006-072, Pierre Auger Observatory, 2006. https://www.auger.org/gap-notes/. (key protected).

[242] P. Billoir, *FADC trace cleaning in Surface Detector through a segmentation procedure*, Tech. Rep. GAP-2005-074, Pierre Auger Observatory, 2005. https://www.auger.org/gap-notes/. (key protected).

[243] F. James and M. Roos, *Minuit: A System for Function Minimization and Analysis of the Parameter Errors and Correlations*, Comput. Phys. Commun. **10** (1975) 343–367.

[244] *An illustrative example of Fisher's linear discriminant*, https://sthalles.github.io/fisher-linear-discriminant/.

[245] *Conversations with Jaime Alvarez-Muñiz,*.

[246] *Scikit-learn: Linear Discriminant Analysis*, https://scikit-learn.org/0.16/modules/generated/sklearn.lda.LDA.html.

[247] Pierre Auger Collaboration, R. Sato, *Long term performance of the surface detectors of the Pierre Auger Observatory*, in *32nd International Cosmic Ray Conference*, vol. 3. 8, 2011.

[248] Pierre Auger Collaboration, A. Abdul Halim et al., *The Time Evolution of the Surface Detector of the Pierre Auger Observatory*, PoS **ICRC2023** (2023) 266.

[249] A. Cooper-Sarkar, P. Mertsch, and S. Sarkar, *The high energy neutrino cross-section in the Standard Model and its uncertainty*, JHEP **08** (2011) 042, arXiv:1106.3723 [hep-ph].

[250] J. Navarro et al., *An extensive review on the down-going neutrino systematic uncertainties from the Pierre Auger Observatory*, Tech. Rep. GAP-2010-027, Pierre Auger Observatory, 2010. https://www.auger.org/gap-notes/. (key protected).

[251] T. Sjostrand, S. Mrenna, and P. Z. Skands, *PYTHIA 6.4 Physics and Manual*, JHEP **05** (2006) 026, arXiv:hep-ph/0603175.

[252] CORSIKA Collaboration, T. Huege, *CORSIKA 8 - the next-generation air shower simulation framework*, SciPost Phys. Proc. **13** (2023) 028, arXiv:2208.14240 [astro-ph.IM].

[253] O. B. Bigas, *Study of systematic uncertainties for skimming tau neutrinos*, Tech. Rep. GAP-2006-054, Pierre Auger Observatory, 2006. https://www.auger.org/gap-notes/. (key protected).

[254] J. Conrad, O. Botner, A. Hallgren, and C. Perez de los Heros, *Including systematic uncertainties in confidence interval construction for Poisson statistics*, Phys. Rev. D **67** (2003) 012002, arXiv:hep-ex/0202013.

[255] Pierre Auger Collaboration, A. Aab et al., *Muons in Air Showers at the Pierre Auger Observatory: Measurement of Atmospheric Production Depth*, Phys. Rev. D **90** no. 1, (2014) 012012, arXiv:1407.5919 [hep-ex], [Addendum: Phys.Rev.D 90, 039904 (2014), Erratum: Phys.Rev.D 92, 019903 (2015)].

[256] G. J. Feldman and R. D. Cousins, *A Unified approach to the classical statistical analysis of small signals*, Phys. Rev. D **57** (1998) 3873–3889, arXiv:physics/9711021.

[257] Gammapy Collaboration, A. Donath et al., *Gammapy: A Python package for gamma-ray astronomy*, Astron. Astrophys. **678** (2023) A157, arXiv:2308.13584 [astro-ph.IM].

[258] W. A. Rolke and A. M. Lopez, *Confidence intervals and upper bounds for small signals in the presence of background noise*, Nucl. Instrum. Meth. A **458** (2001) 745–758, arXiv:hep-ph/0005187.

[259] W. A. Rolke, A. M. Lopez, and J. Conrad, *Limits and confidence intervals in the presence of nuisance parameters*, Nucl. Instrum. Meth. A **551** (2005) 493–503, arXiv:physics/0403059.

[260] *TRolke Class Reference*, https://root.cern/doc/v628/classTRolke.html.

[261] J. Conrad and F. Tegenfeldt, *Likelihood ratio intervals with Bayesian treatment of uncertainties: Coverage, power and combined experiments*, arXiv:physics/0511055.

[262] Pierre Auger Collaboration, A. Aab et al., *Observation of a Large-scale Anisotropy in the Arrival Directions of Cosmic Rays above* 8×10^{18} *eV*, Science **357** no. 6537, (2017) 1266–1270, arXiv:1709.07321 [astro-ph.HE].

[263] E. Massaro, P. Giommi, C. Leto, P. Marchegiani, A. Maselli, M. Perri, S. Piranomonte, and S. Sclavi, *Roma-BZCAT: A multifrequency catalogue of Blazars*, Astron. Astrophys. **495** (2009) 691, arXiv:0810.2206 [astro-ph].

[264] Fermi-LAT Collaboration, J. Ballet, T. H. Burnett, S. W. Digel, and B. Lott, *Fermi Large Area Telescope Fourth Source Catalog Data Release 2*, arXiv:2005.11208 [astro-ph.HE].

[265] S. P. Wakely and D. Horan, *TeVCat: An online catalog for Very High Energy Gamma-Ray Astronomy*, in *30th International Cosmic Ray Conference*, vol. 3. 7, 2007.

[266] T. Schulz et al., *New Baseline Algorithm for UB Traces*, Tech. Rep. GAP-2022-045, Pierre Auger Observatory, 2022. https://www.auger.org/gap-notes/. (key protected).

[267] Pierre Auger Collaboration, P. Abreu et al., *A Search for Ultra-High Energy Neutrinos in Highly Inclined Events at the Pierre Auger Observatory*, Phys. Rev. D **84** (2011) 122005, arXiv:1202.1493 [astro-ph.HE], [Erratum: Phys.Rev.D 84, 029902 (2011)].

Appendix

APPENDIX A

CORSIKA steer file

An example of a CORSIKA steer file used to produce neutrino simulations for this analysis is presented below. The parameters used along with a brief description of their use is given below. The file was used to simulate a CC neutrino shower having a primary energy of $10^{17.5}$eV, a zenith angle of 63° and the interaction slant depth (X) of 1750 g cm^{-2}. The example shower used FLUKA as the low energy and SIBYLL 2.3d as the high energy hadronic interaction model. The file was kindly provided by E. Santos from the MC task of the Pierre Auger Observatory.

```
RUNNR 1626                                                    number of run
NSHOW 1                                        number of showers to generate
EVTNR 1                                         number of first shower event
PRMPAR 66                primary particle code:  electron neutrino (66)
NUSLCT 1               type of interaction (0 - NC/ 1 - CC/ 2 - random)
FIXHEI 215132.421773 1          fix the height of the first interaction
ERANGE 3.162278E+08 3.162278E+08          energy range of primary (GeV)
THETAP 63 63                               range of zenith angle (degree)
PHIP -180.0 180.0                        range of azimuth angle (degree)
SEED 16261 0 0                                   seed for hadronic part
SEED 16262 0 0                                       seed for EGS4 part
SEED 16263 0 0                                 seed for Cherenkov part
SEED 16264 0 0                                                seed for ...
SEED 16265 0 0                                                seed for ...
THIN 1.000E-06 3.162278E+02 5.000E+3        parameters for the thinning
THINH 1.000E+00 1.000E+02           relation between thin em.  and had.
SIBYLL T 0                     SIBYLL 2.3d for high energy & debug level
SIBSIG T                            SIBYLL 2.3d cross-sections enabled
ATMOD 27     US Standard - 0 / Malargue GDAS model (18 - 29 Jan to Dec)
OBSLEV 1.452E+05                                 observation level (in cm)
MAGNET 19.5083 -14.2163                            magnetic field Malargue
```

```
ECUTS 5.00E-02 1.00E-02 2.50E-04 2.50E-04    energy cuts:  hadr., muon,
                                                      elect., phot.  (GeV)
MUADDI T                                      additional info for muons
MUMULT T                                   muon multiple scattering angle
HADFLG 0 0 0 0 0 2              flags hadr.  interact.  & fragmentation
ELMFLG F T                             em.  interaction flags (NKG,EGS)
STEPFC 1.0                          mult.  scattering step length fact.
RADNKG 5.0E+05                outer radius for NKG lat.  dens.  distr.
LONGI T 5.0 T T               longit.  distr.  & step size & fit & out
ECTMAP 2.5E+05                         cut on gamma factor for printout
HILOW 200                              transition energy between models
MAXPRT 1                                 max.  number of printed events
DATBAS T                                              write .dbase file
PAROUT T T                                                 output files
FLATOUT F                                 for backward compatibility
DIRECT /mnt/                            directory of particle output
DATDIR /mnt/                       directory with CORSIKA input tables
USER santos                                username for database file
HOST condor                                hostname for database file
DEBUG F 6 F 100000                   debug flag and log.  unit for out
EXIT
```

APPENDIX B

Testing the impact of high and low energy hadronic interaction models for neutrino simulations

This appendix contains an overview of the efforts done to check the dependence of the low and high hadronic interaction models used to simulate neutrino showers. The check was performed before the full library was simulated by the MC task. For the choice of the low energy hadronic interaction model UrQMD and FLUKA were compared and for the high energy model QGSJET-II-04,EPOS-LHC and SIBYLL 2.3d were compared. The comparison was done by simulating 20 neutrino showers for each model for five different injected slant depths. The comparison was only done for ν_e CC showers with a primary energy of 10^{19}eV for a zenith angle of 72° was considered for the comparison. These three choices were made since such neutrinos are expected to give a good idea of the performance of the models and their effect to the overall analysis. The showers were simulated with CORSIKA 7.7.2 and the output was fed to the Offline analysis framework for the detector response simulation and reconstruction in the same way as described in chapter. 5.

The comparison was done by calculating the ratio of the surviving events for both the models at each simulated slant depth. The T3 and ν identification efficiency was calculated. The T3 efficiency was calculated as a ratio of the number of reconstructed events to the number of simulated events. The ν identification efficiency was not calculated according to the method presented in this thesis but rather with a less stringent cut where the AoP of the three earliest stations were required to be above 1.5. The efficiency was calculated relative to the total simulated events and was plotted against the different injected slant depths which were simulated. This was also done to attempt to calculate the systematic uncertainties which can arise due to the choice of the hadronic interaction model. This comparison is shown in Fig. B.1. As seen in the figure the ration ~ 1 within the error bars which are high due to lack of statistics. After this comparison FLUKA was chosen as the main low energy hadronic model used in the simulations mainly because of ease of use with CORSIKA.

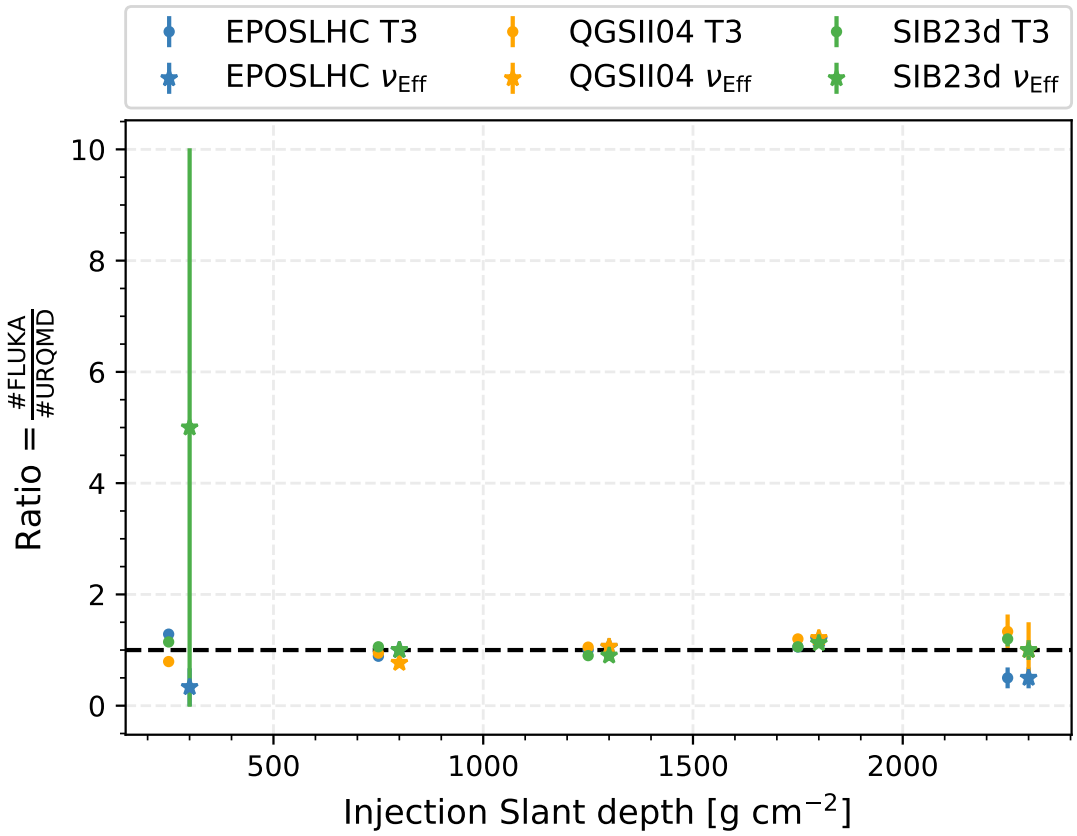

Figure B.1: Comparison of ratio of total reconstructed events between FLUKA and UrQMD for ν_e CC showers with a primary energy of 10^{19}eV for a zenith angle of 72° for five different injected slant depths. The ratio of the surviving events for both the models at each simulated slant depth is shown for different identification efficiencies. The ν identification efficiency has been shifted for better visualization. The error bars signify the statistical error.

For the choice of high energy interaction model the systematic uncertainties were calculated as the difference between the integral of efficiencies of the different models. Taking SIBYLL 2.3d as the reference model A, to test any other model the uncertainty is given by $\frac{\int A - \int B}{\int B}$. The results of the comparison are shown in Fig. B.2. The calculated systematic uncertainties are below 5% for the T3 efficiency and below 10% for the ν identification efficiency. The relative uncertainty for the T3 efficiency for SIBYLL 2.3d in comparison to the EPOS-LHC was found to be $\sim$ +3% and for QGSJETTII04 was found to be $\sim$ +7% and the uncertainty on ν identification was found to be $\sim$ +10% for both the models. However, due to the limited statistics and the statistical errors being way higher ($\sim$ 20%) than the systematic differences no real differences were seen between the three models. However, a conservative choice of $\sim$ +5% was chosen as systematic uncertainties related to the choice of the hadronic

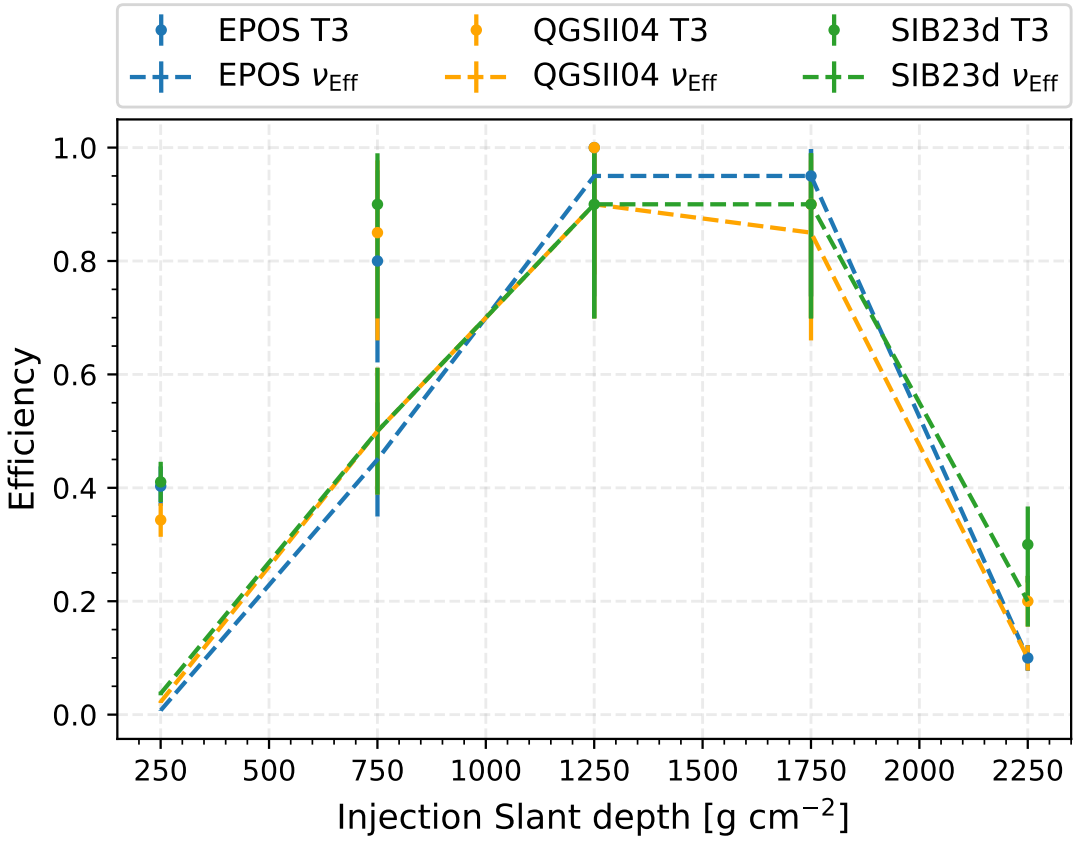

Figure B.2: Comparison of the T3 and ν identification efficiency for SIBYLL 2.3d, EPOS-LHC and QGSJET-II-04 for ν_e CC showers with a primary energy of 10^{19}eV for a zenith angle of 72° for five different injected slant depths. The error bars signify the statistical error.

interaction model in this analysis by comparing with other sources mentioned before.

APPENDIX C

Challenges with segment selection algorithm for new triggers

This appendix aims to present some interesting reconstructed events that were observed in the background training sample when new triggers were used for the neutrino analysis. As mentioned before in sec. 5.3.1 and described in more detail in [240] a segment selection process is applied to improve the quality of angular reconstruction. A small example of the working of the process is shown in Fig. C.1. It was observed while performing the neutrino analysis with new triggers some events were mis-reconstructed due to an untuned segment selection algorithm. These events were further checked and reconstructed using the standard reconstruction used for inclined UHECRs at the Pierre Auger Observatory which classified most of these as noise. It was also noticed that the problems with the segment selection algorithm for the new triggers could primarily arise from the presence of multiple peaks with similar amplitudes in the waveform. There is also an argument that the primary purpose of the segment selection algorithm i.e. the reduction of accidental muons which change the start time of the signal might already be addressed with the design of the new triggers thus decreasing the overall need for such an algorithm. However, these are only hypothesis and need to be confirmed with further studies. Thus, due to the inability to confirm the validity of the segment selection process for the new triggers, the algorithm was not applied to stations with these triggers in a way that the reconstruction for stations with old triggers remained unaffected. Some pictures of events which were investigated are shown below. The pictures are taken from the GUI display available to look at events within the collaboration.

Fig. C.2 shows an event where the segmentation algorithm failed to find the correct segment for the station with the MoPS trigger.

As mentioned before in Outlook a properly tuned segmentation algorithm could also help the neutrino search with new triggers. Fig. C.3 shows an event where the MoPS signal is selected with a start time of 200ns but is out of time with other stations with start times close to 240ns. A segment selection algorithm could help in this case to select the correct segment for the station with MoPS trigger.

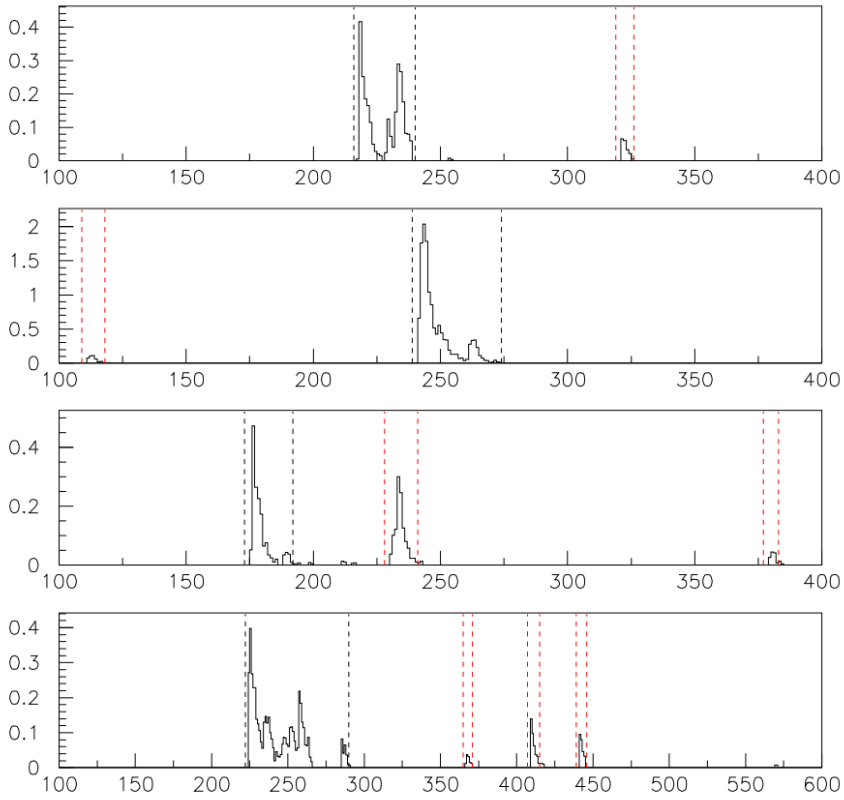

Figure C.1: Examples of the segment selection process applied on FADC traces. The main segment is enclosed within black lines. The red lines enclose the secondary segments found by the algorithm. Only the black segment is used for top-down selection. The x-scale is in VEM units and the y-axis denotes time in ns. Taken from [242].

Fig. C.4 shows an example of an event with a bad angular fit. The indication of the bad quality can only be gauged via the χ^2_{red} and does not show up in the error on zenith angle. Such events though small in number are essential to be excluded from the analysis to avoid any bias in the final result. This is done with the Angular fit quality cut described before.

The event shown in Fig. C.5 shows an example of an event which had an evaluated Fisher value close to the cut value. The event had no peculiar feature which could classify it as a neutrino or otherwise.

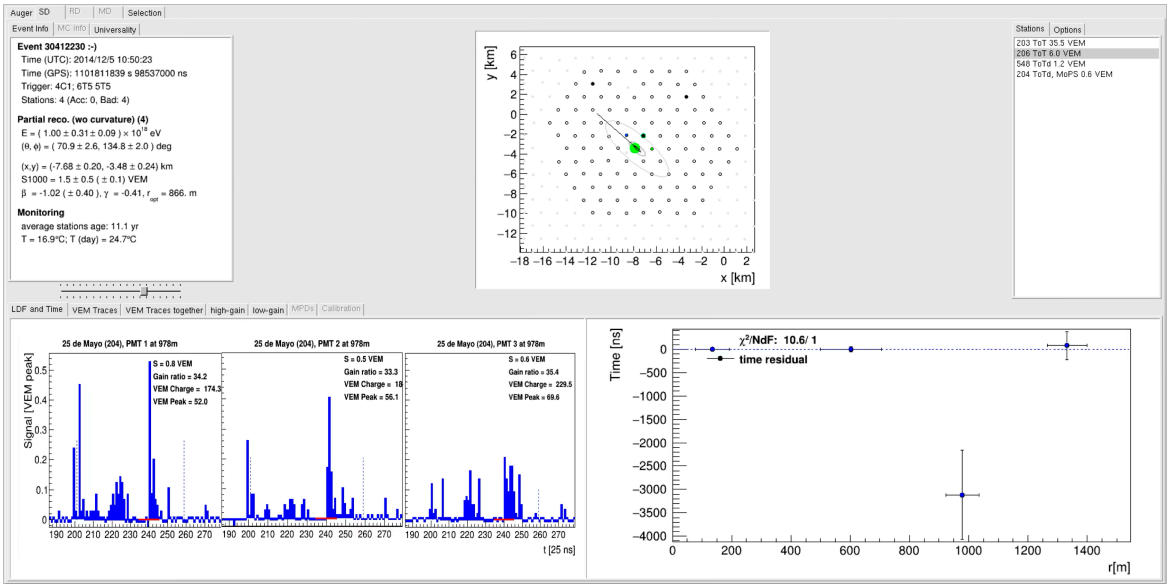

Figure C.2: An example of an event where segment selection did on a station with the MOPS trigger. Due to the two similar peaks seen in MoPS trace for the station 204, the segment selection algorithm could not find the correct segment and led to a mis-reconstruction of zenith angle.

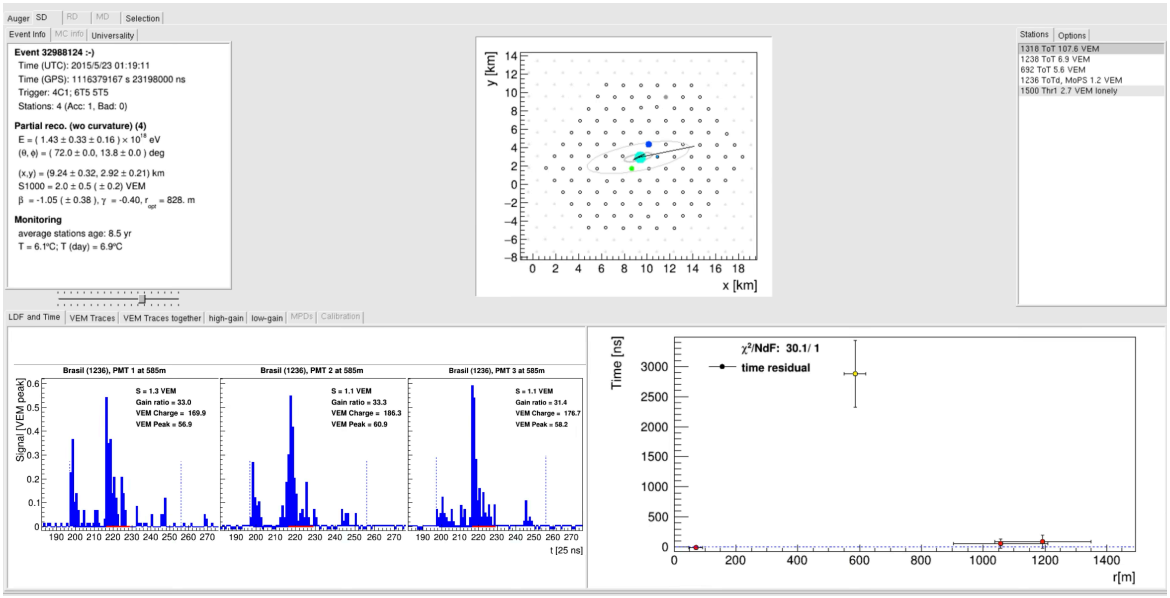

Figure C.3: An example of an event where segment selection could help in the reconstruction. The MoPS signal is selected with a start time of 200ns but is out of time with other stations (240ns). A segment selection algorithm could help in this case to select the correct segment for the station with MoPS trigger.

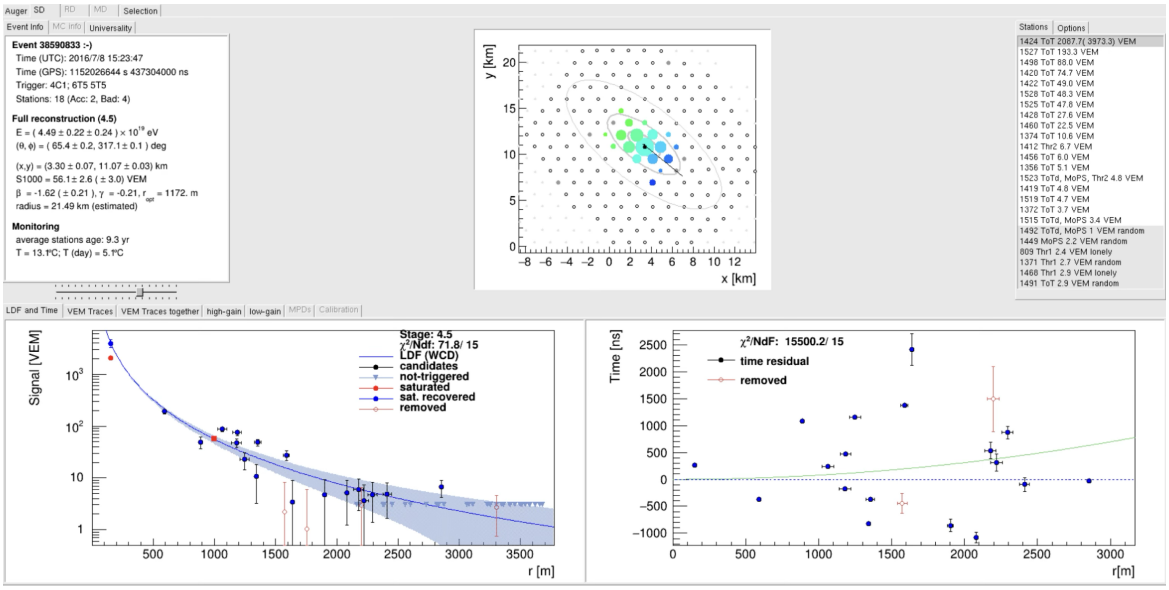

Figure C.4: Example of an event with a bad angular fit. The indication of the bad quality can only be gauged via the χ^2_{red}.

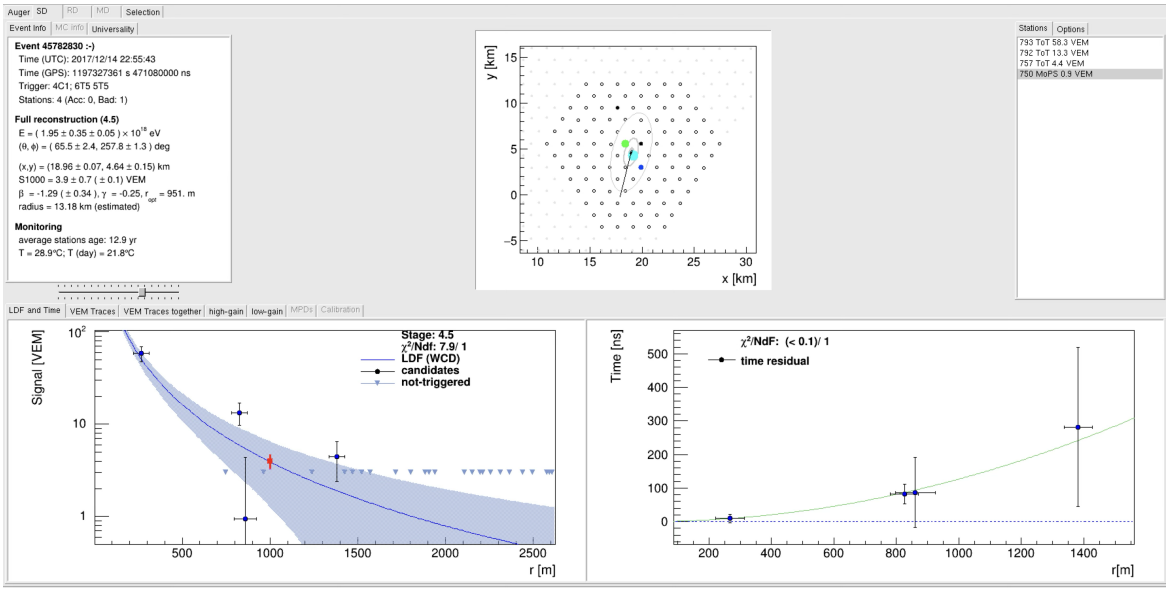

Figure C.5: An example of an event which had an evaluated Fisher value close to the cut value. No particular feature was found for this event which classified it as a neutrino like event or otherwise.

APPENDIX D

Supplementary results from Fisher Linear Discriminant Analysis

As mentioned before the Fisher Linear Discriminant analysis with a standalone python program (available on internal Gitlab) and checked against the inbuilt scikit-learn library. The Fisher polynomial of the form described in eq. 5.8 which was trained separately for five angular sub-regions. The results of the Fisher Coefficients, C_i for each angular region is given below in D.1(a). Further, as mentioned before the cut to establish the separation between the background and training sample is evaluated by fitting the tail of the background distribution to an exponential function in each angular region such that 0.2 events are expected to pass the cut in 20 years as mentioned in section 5.5.3. The fit parameters obtained after fitting e^{a-bx} to the tail of the Fisher distribution are given in D.1(b). The cut values were already mentioned before in table 5.4.

Evaluated Fisher Coefficients					
	Region 1 (58.5°-61.5°]	Region 2 (61.5°-64.5°]	Region 3 (64.5°-67.5°]	Region 4 (67.5°-70.5°]	Region 5 (70.5°- 76.5°]
C_1	$3.06 \cdot 10^{-1}$	$5.48 \cdot 10^{-1}$	$7.36 \cdot 10^{-1}$	$8.40 \cdot 10^{-1}$	$9.61 \cdot 10^{-1}$
C_2	$5.05 \cdot 10^{-1}$	$3.75 \cdot 10^{-1}$	$2.57 \cdot 10^{-1}$	$1.40 \cdot 10^{-1}$	$1.99 \cdot 10^{-2}$
C_3	$8.03 \cdot 10^{-1}$	$7.47 \cdot 10^{-1}$	$6.22 \cdot 10^{-1}$	$5.00 \cdot 10^{-1}$	$2.74 \cdot 10^{-1}$
C_4	$7.92 \cdot 10^{-2}$	$-3.90 \cdot 10^{-2}$	$-6.90 \cdot 10^{-2}$	$-7.90 \cdot 10^{-2}$	$-2.27 \cdot 10^{-2}$

(a) Normalised Fisher coefficients obtained for each angular region

	Region 1	Region 2	Region 3	Region 4	Region 5
a	15.1 ± 0.5	14.3 ± 0.8	14.2 ± 1.4	14.3 ± 1.7	7.8 ± 2.0
b	2.57 ± 0.12	2.94 ± 0.22	3.50 ± 0.44	4.63 ± 0.65	3.11 ± 0.96

(b) Fit parameters obtained after fitting e^{a-bx} to the tail of the Fisher distribution.

Table D.1: Summary of Fisher Linear Discriminant analysis.

APPENDIX E

Adapting DGH analysis to current Offline

This section aims to present the work done during this thesis to adapt the Down Going High neutrino analysis as a Standard Application to work with the current Offline version. The Down going high neutrino analysis was first created in 2011 and has not been updated since then. This has led to the ModuleSequence used in the erstwhile analysis to be incompatible with the new Offline versions. The work involved creating a Modulesequence that mimics the old analysis but is compatible with the new structure of Offline. This work has required a lot of input from J. Muñiz who was one of the authors of the original analysis. In the next few paragraphs the changes made to the original ModuleSequence are discussed along with the reasons for the choices made. The new ModuleSequence is then tested on a few events to check if the output is consistent with the old analysis. The work is still in progress and requires further testing and validation before it can be used for the analysis.

The previous version of the Module sequence is presented below:

```
<sequenceFile>
  <enableTiming/>
  <moduleControl>
    <loop numTimes="unbounded" pushEventToStack="yes">
      <!- Event Reading and Pre-selection ->
      <module> EventFileReaderOG </module>
      <module> EventCheckerOG </module>
      <!- SD Calibration previously SdCalibratorOG->
      <module> SdGainRatioCorrectorKG </module>
      <module> SdStationCheckerOG </module>
      <module> SdHistogramFitterKG </module>
      <module> SdBaselineFinderKG </module>
      <module> SdTraceCalibratorOG </module>
      <module> SdSignalRecoveryKLT </module>
```

```
      <!-Special Module to handle station with double peaks->
      <module> doublePeakDetector </module>
      <!- Rerunning SD Calibration ->
      <module> SdCalibratorUSC </module>
      <!- Event-selection ->
      <module> SdMonteCarloEventSelectorOG </module>
      <module> SdEventSelectorUBA </module>
      <module> SdTopDownSelectorUBA </module>
      <!- Angular Reconstruction ->
      <module> simpleRec </module>
    </loop>
  </moduleControl>
</sequenceFile>
```

The new version of the Module sequence is presented below:

```
<sequenceFile>
  <enableTiming/>
  <moduleControl>
    <loop numTimes="unbounded" pushEventToStack="yes">
      <!- Event Reading and Pre-selection ->
      <module> EventFileReaderOG </module>
      <module> EventCheckerOG </module>
      <!- SD Calibration ->
      <module> SdGainRatioCorrectorKG </module>
      <module> SdStationCheckerOG </module>
      <module> SdHistogramFitterKG </module>
      <module> SdBaselineFinderKG </module>
      <module> SdTraceCalibratorOG </module>
      <module> SdSignalRecoveryKLT </module>
      <!- Special Module to handle station with double peaks ->
      <module> doublePeaketector </module>
      <!- Rerunning SD Calibration ->
      <module> SdGainRatioCorrectorKG </module>
      <module> SdStationCheckerOG </module>
      <module> SdHistogramFitterKG </module>
      <module> SdBaselineFinderKG </module>
      <module> SdTraceCalibratorOG </module>
      <module> SdSignalRecoveryKLT </module>
      <!- Event-selection ->
      <module> SdMonteCarloEventSelectorOG </module>
      <module> SdEventSelectorOG </module>
      <module> SdTopDownSelector </module>
```

```
      <!- Angular Reconstruction ->
      <module> SdPlaneFitOG </module>
      <module> LDFFinderKG </module>
      <!- Post selection and export ->
      <module> DLECorrectionWG </module>
      <module> SdEventPosteriorSelectorOG </module>
      <module> RecDataWriterNG </module>
    </loop>
  </moduleControl>
</sequenceFile>
```

Since 2011 the modules in Offline have gone through a considerable amount of changes. The old *SdCalibratorOG* module was split into six separate modules for better future adaptability. This change also came with some improvements in the calibration process which can be found in more detail in [266]. The *doublePeakDetector* was also slightly updated by the author to fit the coding style of the Offline framework. The earlier used *SdCalibratorUSC* is no longer a part of the current framework but was thoroughly checked against the currently use calibration modules. The only difference that was observed was a snippet of code setting stations with multiple peaks to a specific error code and rejected the station with the error code. This functionality is envisioned to be transferred to other modules to simplify the analysis. For the result presented in this section this change has not been implemented yet and the standard calibration modules are used. *SdEventSelectorUBA* was found to be very similar to the currently used *SdEventSelectorOG* while *SdTopDownSelectorUBA* has been replaced by *SdTopDownSelector*. The last replacement is not perfect and is currently being improved to mimic the old module. The last change involved breaking down the *simpleRec* module which was responsible for some of the quality cuts implemented in the DG_{high} and also implemented a plane and curved angular reconstruction. The angular reconstruction part was replaced by the *SdPlaneFitOG* and *LDFFinderKG* modules to do the plane and curved shower front-fit respectively. The other analysis cuts from the module were implemented in a standalone program which analyses the ADSTs produced after detector reconstruction.

After all the changes were implemented to the *Modulesequence* and the DG_{high} analysis was rewritten in the exact same way as [267]. The neutrino identification efficiency was evaluated using a simulation sample having a primary energy of 10^{19}eV with zenith angle of 75° which is the last bin of the DG_{low} analysis range. The identification efficiency was found to be **0.52**. This is very close to the identification efficiency of ***0.58*** which was evaluated with the previous implementation of the analysis for the same energy and the same zenith angle. This shows that the new implementation of the analysis is consistent with the old implementation and can be used for the analysis. The next steps involve testing the analysis on a larger sample of events and comparing the results with the old analysis. The analysis will also be tested on the data to check if the results are consistent with the old analysis. The work is still in progress and requires further testing and validation before it can be used for the analysis.

List of Figures

Acronyms

ADST Advanced Data Summary Tree.

AGN Active Galactic Nuclei.

AoP Area over Peak.

CC Charged Current.

CLF Central Laser Facility.

CMB Cosmic Microwave Background.

CNB Cosmic Neutrino Background.

CR cosmic ray.

CTA Cherenkov Telescope Array.

DG_{high} down-going high.

DG_{low} down-going low.

DIS Deep Inelastic Scattering.

EAS extensive air shower.

EBL extragalactic background light.

ES Earth-skimming.

eV electronvolts.

FADC flash analog-to-digital converter.

FD Fluorescence Detector.

FDA Fisher Discriminant Analysis.

FOV field of view.

GDAS Global Data Assimilation System.

GHz gigahertz.

GZK Greisen–Zatsepin–Kuzmi.

HEAT High Elevation Auger Telescope.

HESS High Energy Stereoscopic System.

IACT Imaging Cherenkov telescope.

ISM interstellar medium.

LDA Linear Discriminant Analysis.

LDF lateral distribution function.

MC Monte Carlo.

MHz megahertz.

MoPS Multiplicity-of-Positive-Steps.

NC Neutral Current.

PMT photomultiplier tube.

QCD quantum chromodynamics.

RD Radio Detector.

SD Surface Detector.

TA Telescope Array.

TH threshold trigger.

ToT time-over-threshold.

ToTd Time-over-Threshold-deconvolved.

UHE ultra high energy.

UHEν Ultra high energy neutrino.

UHECR ultra-high energy cosmic ray.

UMD Underground Muon Detector.

UUB upgraded unified board.

UV ultraviolet.

VCT vertically central through-going.

VEM vertical equivalent muon.

WCD Water Cherenkov Detector.

WIMP Weakly Interacting Massive Particle.

XLF eXtreme Laser Facility.